University of Southampton

THE SYNTHESIS, CHARACTERISATION, AND CATALYTIC ACTIVITY OF URANIUM COMPOUNDS SUPPORTED ON LIQUID CRYSTAL TEMPLATED MESOPOROUS SILICA

TOM CAMPBELL

Submitted in partial fulfillment of the requirements for the Doctor of Philosophy at the University of Southampton

Department of Chemistry   August 2001

UNIVERSITY OF SOUTHAMPTON

ABSTRACT

FACULTY OF SCIENCE

CHEMISTRY

Doctor of Philosophy

THE SYNTHESIS, CHARACTERISATION, AND CATALYTIC ACTIVITY OF URANIUM COMPOUNDS SUPPORTED ON LIQUID CRYSTAL TEMPLATED MESOPOROUS SILICA

By Tom Campbell

Mesoporous silica with a regular hexagonal array of pores has been synthesised by a liquid crystal templating route, using a variety of surfactants. The mesostructure in all cases is retained on surfactant removal. The structure of these materials is typified by the Brij76 surfactant-templated silica, for which the nitrogen adsorption data showed a type IV isotherm with no hysteresis, giving a specific surface area of $870m^2g^{-1}$, a pore volume of $0.7cm^3g^{-1}$ and an average pore diameter of 3.6nm. X-ray powder diffraction patterns for this silica show an intense peak at low 2θ value corresponding to a d_{100} value of 4.9nm, as well as secondary peaks indicative of a hexagonal array of pores and extended long range order. The hydroxyl concentration is found to be 1.21 $OHnm^{-2}$. Heating in oxygen at temperatures up to 950°C reveals a slow decline in surface area and pore size up to 800°C, whereafter these values fall sharply to $300m^2g^{-1}$, and 2.2nm respectively at 850°C. A similar effect on the (100) reflection intensity is noted by X-ray powder diffraction. The surface hydroxyl concentration undergoes a similar non-linear reduction with calcination temperature, but this occurs between 700 and 800°C.

Uranyl nitrate hexahydrate and uranium tetrachloride have been supported on mesoporous silica, amorphous silica and alumina at 30wt% U. The temperature of supported uranium compound decomposition increases in the order amorphous silica $\leq$ amorphous alumina $<$ mesoporous silica $<$ unsupported bulk material forming a UO_3-type phase, which converts to U_3O_8 at higher temperatures. The U_3O_8 formation temperature has the opposite support dependence, and occurs at lower temperatures for the tetrachloride derivative materials compared to the nitrate analogues.

The activity of these systems towards the catalytic oxidation of CO, and the selective catalytic reduction of NO with CO has been determined. For both reactions, the activity of supported uranyl nitrate materials increases with decreasing catalyst pre-treatment temperature, whereas the uranium tetrachloride derivatives typically achieve a maximum in activity after pre-treatment at 600°C in oxygen. Generally, the activity increases with a decrease in either the size of supported uranium oxide particles, or, for the tetrachloride derivatives, the amount of chlorine retained. For the NO reduction reaction, the most active catalysts achieve 100% selectivity towards nitrogen at 360°C, and 90% NO conversion at 450°C. This reaction was found to be zero order with respect to NO, and have an order of 1.4 with respect to CO.

The organometallic complexes $[(C_5H_5)_3UCl]$, $\{N[CH_2-CH_2N(SiMe_2{}^tBu)]_3UOBu^t\}$, and $\{N[CH_2-CH_2N(SiMe_2{}^tBu)]_3UNEt_2\}$, have been deposited on mesoporous silica at 6wt% U. The supported species have been characterised, and the effect of thermal treatment investigated.

Contents

Chapter 3. Synthesis and Characterisation of Mesoporous Silica

Chapter 4. Characterisation of Supported Uranium Oxide Material

Chapter 5. Catalytic Oxidation of Carbon Monoxide

Chapter 6. Catalytic Selective Reduction of Nitrogen Monoxide

Chapter 7. Characterisation of Supported Organouranium Materials

Chapter 8. Conclusions

Abbreviations

BET	Brunauer Emmett Teller
CP	Cross Polarisation
DR	Diffuse Reflectance
DRIFTS	Diffuse Reflectance Infrared Fourier Transform Spectroscopy
DTA	Differential Thermal Analysis
EXAFS	Extended X-ray Absorption Fine Structure
FTIR	Fourier Transform Infrared
HPDEC	High Power Decoupling
MASNMR	Magic Angle Spinning Nuclear Magnetic Resonance
SEM	Scanning Electron Microscopy
STA	Simultaneous Thermal Analysis
TEM	Transmission Electron Microscopy
TGA	Thermogravimetric Analysis

Bu^t	Tertiary Butyl
Et	Ethyl
Me	Methyl
NO_x	Nitrogen Oxides
Pr	Propyl
thf	Tetrahydrofuran

Acknowledgements

I thank Judith Corker, for setting up this project and giving me the opportunity to spend three years of my life doing something that has given me great enjoyment and a sense of achievement. I hope very much that she would be happy to have her name associated with this thesis. Sadly missed, warmly remembered.

I thank John Evans for taking over the supervision of this work, and especially for allowing me independence to develop my own ideas, whilst providing guidance and support. This has enabled me to simultaneously learn much about science, and about myself, and will forever be appreciated.

I thank Mark Newton for the countless ways in which he has helped me through the technical aspects of this work. Without his support, and his constant willingness to discuss the project in detail, it would probably have taken me six years to complete my PhD rather than three. In addition, he demonstrated truly immense constancy as a smoking and drinking partner throughout this time.

I thank the whole of our group for creating such a pleasant environment in which to work. The willingness to help each other meant that our laboratory was always a relaxed place to be. Very special thanks to the synchrotron crew, who somehow managed to make expeditions to Daresbury and Grenoble more than a lesson in sensory deprivation. In particular, I would like to thank Steven Fiddy, Sandra Turin, Graham Rayner and Peter Bolton who, along with Mark, completed an awesome experimental team and a superb bunch of friends.

I want to thank all past and present on the seventh/second floor for making my PhD such a good laugh. This extends to all those unfortunates who have shared the comedic experience that is Stanley Matthews FC. Sunday afternoons will never, one hopes, be quite the same. Many thanks to all those who participated in SUSA FC, and I would like to take this opportunity to apologise for my consistently hungover state.

I wish to thank Matt, a brilliant friend who put a roof over my head for nearly seven years. Thanks to Ruth; just mad enough to keep me sane.

I want to thank my family, for everything else.

Chapter 1. Introduction

The subject of catalysis may be easily divided into two broad areas, with the distinction between these subsections made with respect to the number of phases present in the catalytic process; one for homogeneous catalysis, and two or three for heterogeneous catalysis. Homogeneous catalysts often provide better (a) product selectivity and (b) activity than their heterogeneous analogues, but (c) separation of catalyst from products is often much more difficult in a single phase process.

(a) This may be explained in part by the fact that solid surfaces have defects intrinsically present, and, sometimes, other material adsorbed on them. This indicates the presence of more than one type of site at which a reaction can take place, and the result is often the formation of more than one product.

(b) This can be best reconciled in terms of contact area and mass transport between catalyst and reactant. Homogeneous catalysts are discrete molecular units, and as such have the maximum possible surface area available for reaction. The homogeneous nature of the system also implies a greater ease in mixing reactants and catalyst.

(c) The catalyst is often the most cost intensive reagent in a process, and so, even if the product need not be completely pure (such as for general use polymers), it is very desirable to be able to recover and reuse it. For this reason the search for effective heterogeneous catalysts has intensified over time.

The ideal scenario would then be to obtain heterogeneous catalysts with a single type of catalytic site, and very large surface areas, whilst allowing diffusion of reactants and products through the system at a rate which does not make mass transport the rate limiting step. In practice, the target of research in this area is to obtain the closest approximation to these properties. An estimate of 70% of all industrial chemicals produced have required a catalyst on at least one occasion during their manufacture,[1] and, due to the ease of separation of products from catalyst, heterogeneous systems account for the majority of those employed.

The general approach of much of the work reported here is to disperse a heterogeneous catalyst on a well-defined, high surface area support, in an attempt to increase the activity of this catalyst by increasing the active surface area available for reaction. This chapter will introduce the nature of the support, the material that is to be dispersed on it, and the catalytic processes for which the activity of these systems is to be tested.

1.1 Porous Materials with Long Range Order

1.1.1 Zeolite and Zeotype Materials

The very large surface areas that are desirable may be achieved most effectively with the use of highly ordered porous materials, where much of the surface area is internal. If the pores are well defined this might also allow some shape and size selectivity of reactants and products. There are many porous materials with long range order, both naturally occurring and synthetic. By far the largest and most well understood group within this class of materials is the crystalline, open framework, aluminosilicate zeolite structures. The primary structure of zeolites consists of SiO_4 and AlO_4 tetrahedra. These tetrahedra may then be vertex-linked via bridging oxygen atoms, excluding Al-O-Al bridges,[2] to generate a large number of possible structures termed secondary building units. These secondary building units are then further joined together to produce the 3-D framework. Group I or II metal ions are also often incorporated, in order to balance the net negative charge caused by the presence of Al^{3+} as well as Si^{4+} in the framework. The general formula is then $M^{+}_{x/n}(AlO_2)_x(SiO_2)_y.mH_2O$, and an illustration of the type of open framework generated is given in figure 1.1, where MO_4 tetrahedra are shown as solid shapes.
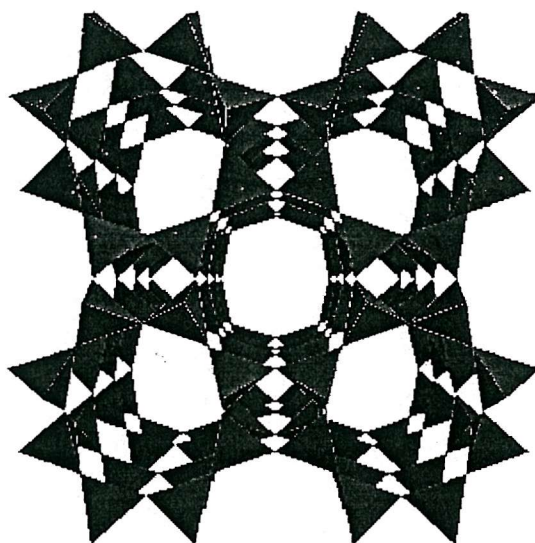

Figure 1.1 The structure of zeolite P[3]

The regular framework of pores in these materials affords excellent size selective adsorption properties, and zeolites have been extensively used as molecular sieves for many years.[4] The same types of systems have been exploited as heterogeneous catalysts, and are used for many industrial processes such as the employment of zeolite A in the

cracking of crude petroleum,[5] and ZSM-5 in the formation of octane from methanol.[6] In the last twenty years the range of synthetic microporous materials has been extended beyond these aluminosilicates, to include a number of examples of other zeotype systems such as aluminophosphates,[7] silicoaluminophosphates,[8] and gallophosphates.[9] However, the limit of pore size of these materials infers intrinsic problems in their use for some catalytic processes. It introduces a size limitation on the reactants that may be used, and the rate of diffusion of solution phase reactants through the pore structure is prohibitively slow. For these reasons there has been a growing interest in the synthesis and use of mesoporous materials with pore sizes between 2 and 50nm.[10]

1.1.2 Mesoporous Materials

The synthesis of mesoporous materials has been investigated for over twenty years, but initially the structures produced had pores which were irregularly spaced and very broadly distributed in size.[11] The traditional methods used to synthesise zeotype materials are not easily extended to create structures with much larger pores, as this would involve the formation of 30-40 member rings. The standard synthetic procedures do not have sufficient control over the eventual structure, and so a new methodology has been developed. In 1992 Beck *et al* used the property of micelle formation in aqueous solution displayed by surfactant molecules to introduce a novel method of templating mesoporous materials.[12,13] A regular silicate or aluminosilicate structure is obtained as the inorganic framework is formed around the organic species in solution, and the size of the channels in the product can therefore be controlled by the choice of a templating molecule with an appropriate physical magnitude. By variation of the surfactant to silicon ratio, it was possible to obtain hexagonal (MCM-41), cubic (MCM-48), and lamellar (MCM-L) phases of the material, each displaying a very intense low angle X-ray powder diffraction reflection relating to large repeat distances of 20-100Å as well as secondary reflections by which the phase may be assigned. Removal of the organic template was achieved by calcination, and this resulted in materials with surface areas of $\sim$1000m^{2}g^{-1}, and very narrow pore size distributions. The templates used were cationic surfactants [$C_nH_{2n+1}(CH_3)_3N^+$] (n = 8-16) at 25 wt%. This amount of amphiphile is above the critical micellar concentration, but below that at which the surfactant will form a liquid crystal phase in aqueous solution. This will be discussed in greater depth below.

Since this method was proposed, a large number of related synthetic strategies have been used in the formation of analogous materials, and these may be subdivided into five

categories. The first four apply to the charge-matching, electrostatic templating approach, and these have been achieved, and summarised, by Huo *et al.*[14]

Pathway one involves the direct co-condensation of a cationic surfactant (S^+) with anionic inorganic species (I^-) to produce assembled ion pairs (S^+I^-). This is the approach used by the Mobil group.[12] In the second pathway, known as the charge-reverse synthesis, an anionic template (S^-) is used to direct the self-assembly of cationic inorganic species (I^+) through S^-I^+ ion pairs. Pathways three and four involved counterion mediated assemblies of surfactants and inorganic species of similar charge. These counterion mediated pathways produced assembled solution species of the type $S^+X^-I^+$ (where $X^- = Cl^-$ or Br^-) or $S^-M^+I^-$ (where $M^+ = Na^+$ or K^+), respectively. The viability of pathway three was demonstrated by the synthesis of a hexagonal MCM-41 silica with quaternary ammonium cations under strongly acidic conditions (5 to 10M HCl or HBr) to generate and assemble positively charged framework precursors.[14] These four synthetic pathways are all based on strong electrostatic interactions between the surfactant and the charged framework, and this makes template recovery problematic. It has been found that ionic template recovery is possible, without high temperature calcination, providing that the exchange ions or ion pairs are present in the extraction process.[15,16] However, this has a detrimental effect on both pore structure and surface area.[17]

Pinnavaia *et al* have proposed a fifth synthetic route to ordered mesoporous materials via a neutral templating method.[18,] This procedure involves the use of neutral primary amines as the templating surfactant ($S°$), and a nominally neutral inorganic precursor ($I°$). This methodology yields mesostructures with larger wall thickness and greater textural mesoporosity, but a lower degree of long range order, and smaller scattering domain sizes than the electrostatic routes. The neutral templating pathway allows for a greater ease of recovery of the surfactant by simple solvent extraction. This method has more recently been adapted with (poly)ethylene oxides as the templating materials and the introduction of metal ions into the synthesis mixture.[19] This does result in a subsequent increase in long range order, but this is essentially a duplication of the electrostatic methods described above.

All of the five methods detailed above utilise surfactants at concentrations above the critical micellar concentration but below that at which a liquid crystal phase may be formed, and many of the examples of these routes involve hydrothermal synthesis. In 1995 Attard *et al* made use of surfactants with well-defined lyotropic liquid crystal phase

diagrams to synthesise a purely siliceous mesoporous material.[20] The concentration of the surfactant could then be chosen to produce the desired organic mesophase, and the silica framework produced is simply a cast of that phase. The surfactants used were octaethylene glycol monododecyl ether ($C_{12}EO_8$), and octaethylene glycol monohexadecyl ether ($C_{16}EO_8$), and the silica source was tetramethyl orthosilicate (TMOS). Aside from the greater control of silica mesostructure produced, this synthetic method has a number of advantages of those detailed above, including the fact that the procedure may be carried out at room temperature and pressure. Also, the particle size derived from this route is much larger than that of the low wt% surfactant methods, with monoliths rather than fine powders being produced. This makes handling of these substances much less problematic, and affords them great potential with regard to membrane applications. Due to the fact that this method provides long range order in solution without the participation of the inorganic material, it has also been shown to be applicable to the synthesis of mesoporous metals, such as platinum and tin.[21,22,23]

The mechanism associated with the synthesis of mesoporous materials by the surfactant templating route has not, as yet, been comprehensively explained, but that proposed by Beck *et al*[12] will be used to introduce the more important principles. A typical surfactant molecule has a polar, hydrophilic, head group, and a non-polar hydrocarbon, hydrophobic, tail. At very low surfactant concentrations, the amphiphile is present as monomer, with the individual molecule headgroup solvated, typically with water in this type of synthesis. As the amount of surfactant in solution is increased, eventually this concentration of monomer reaches a constant, maximum value. Above this value, known as the critical micelle concentration, a proportion of the surfactant molecules form aggregates in solution. The concentration at which this occurs depends on the magnitude of the enthalpic and entropic terms associated with solvation, which, in turn, depend on the chemical structure of the surfactant. These micelles may have different shapes, once again depending on the shape and chemical nature of the amphiphile molecule. Further increases in concentration may cause an alteration in the shape of the aggregate, as the surface curvature is forced to change to minimise the free energy, and this may result in the formation of a liquid crystal phase if these micelles agglomerate to give a structure with some long range order. The micelle shape dependence on surfactant concentration is illustrated in figure 1.2.
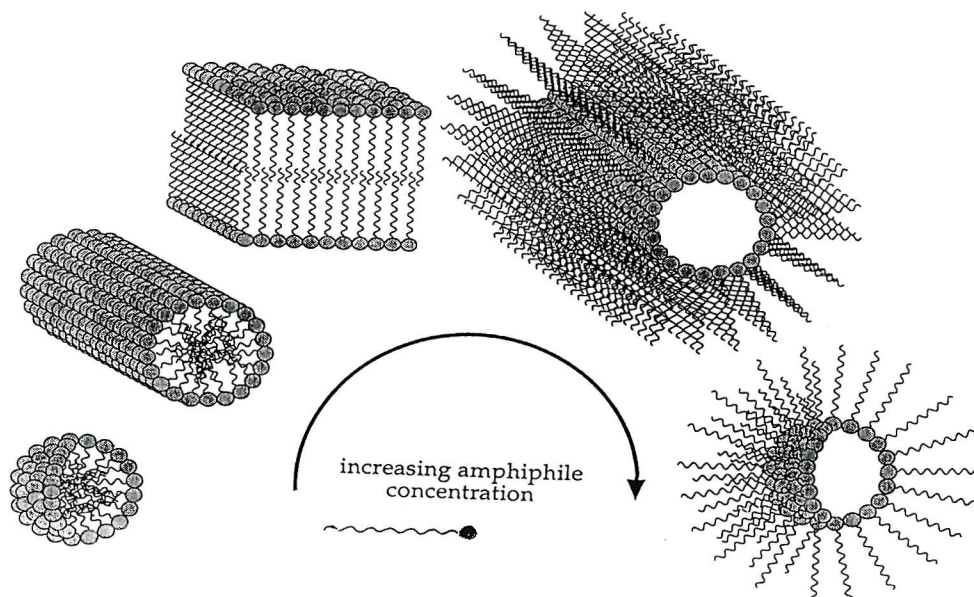
Figure 1.2 The aggregate shape dependence on surfactant concentration.

It has been proposed by Klinowski *et al*[24] that at low concentrations of the surfactant, such as that in the synthesis described by Beck et al,[12] the solution silicate species begin to condense on the surface of individual micelles, before these agglomerate to give the mesostructure. Once these groups of silicate covered micelles reach critical dimensions, then they precipitate out of the reaction solution, and this explains why the average particle size of silicas synthesised under these conditions is so small.

In contrast, the synthetic route associated with the Attard method[20] follows a mechanism whereby the long range order is established in the organic phase, and the inorganic framework is simply a cast of this phase. The presence of the liquid crystal phase may be confirmed by polarised light microscopy prior to addition of the silicate precursor, and it is shown to reform after the removal of the silicate hydrolysis products. The resultant material is formed as a glass, and the template may then be removed by calcination, or solvent extraction. This mechanism is illustrated in figure 1.3.

i) Formation of inorganic network
ii) Removal of surfactant

Surfactant + water +
inorganic precursor

H_I mesoporous
material
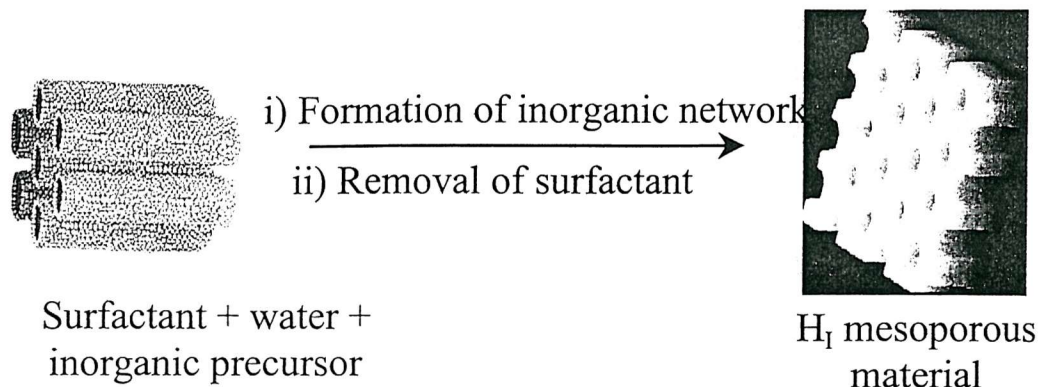
Figure 1.3 The formation of mesoporous silica from a liquid crystal template.

In common to both mechanisms is the mesostructure dependence on the physical size of the surfactant molecule. Control of these dimensions is routinely achieved by variation of the amphiphile hydrocarbon chain length, but this may also be obtained by the inclusion of a compound soluble in the non-polar domain of the micelles formed. This results in a swelling of the surfactant aggregates, which in turn increases the dimensions of the pores in the inorganic material formed. Commonly used for this purpose are n-alkanes, and this is illustrated in figure 1.4.[25]

(a)   (b)   (c)
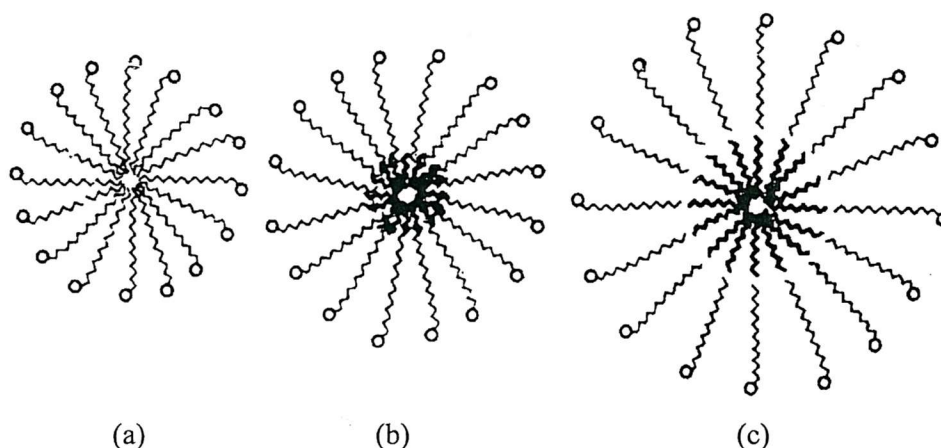
Figure 1.4 The effect of n-alkane inclusion on micelle dimensions, (a) in the absence of alkane, (b) in the presence of n-hexane, (c) in the presence of n-decane.

1.1.3   Modification of Mesoporous Materials

Since 1992, the amount of research into ordered mesoporous materials has grown exponentially. A brief review of this work will introduce the methods used in their modification, and the potential applications to which they may be applied. The mesoporous materials may either be modified from a purely siliceous system by inclusion of other species, such as metals, in the synthesis mixture, or, alternatively, the chemical

variation may be introduced by adsorption of other material after template removal. Although only the second method has been employed in this work, both approaches will be briefly discussed.

1.1.3.1 Modification of Mesoporous Materials by Isomorphous Substitution

The aim of modification of mesoporous materials by variation of the initial reaction mixture is to achieve the isomorphous substitution of a desired metal for silicon within the framework. The majority of reports found within the literature relating to this subject are concerned with the inclusion of titanium and vanadium. Vanadium containing mesoporous materials have been synthesised using both the electrostatic,[26,27] and the neutral templating methods[28] and have been found to be good catalysts for the selective oxidation of large organic molecules such as cyclododecane and 1-naphthol using diluted hydrogen peroxide. Titanium materials have also been synthesised via the electrostatic[29,30,31,32] and neutral assembly[29,33] processes at low wt% surfactant, as well as a method modified from that proposed by Attard *et al*[20] using a true liquid crystal phase as a template.[34] The titanium mesoporous materials demonstrate catalytic activity comparable to that of titanium silicate for many processes, but have been shown to be far superior for the liquid phase peroxide oxidations of methyl methacrylate, styrene and 2,6-di-tert-butyl phenol.[29]

Interest in metal incorporated mesoporous materials is not limited to titanium and vanadium, and there are reports of examples where silicon has been substituted for aluminium(III),[35] boron(III),[36] chromium(III),[37,38] iron(III),[36, 39] cobalt(II),[40] copper(II),[41,42] zinc(II),[43] gallium(III),[36,44] zirconium(IV),[45] niobium(V),[46] molybdenum(VI),[39] tin (IV)[47] and tungsten(VI).[48] Mesoporous manganosilicates such as Mn-MCM-41 (hexagonal), Mn-MCM-48 (cubic) and Mn-MCM-L (lamellar) are also known,[49] and the synthetic route to these materials is typical of this type of procedure. A known percentage of the metal (2%mol compared with the silicon) in the correct oxidation state is added to the synthetic mixture, which usually contains a source of silicate, a templating agent, and a solvent (often water). In the manganosilicate synthesis, the metal is introduced as $MnCl_2$, the silica source is sodium silicate and the surfactant used is cetyltrimethylammonium chloride or bromide.

1.1.3.2 Modification of Mesoporous Materials by Surface Adsorption

The type of material that has been adsorbed into the pores, and onto the surface of the mesostructure is quite varied, with an entire class of materials resulting from failed attempts to incorporate metals into the framework. The result is adsorbed metal, or metal oxide such as titanium,[50] vanadium,[51] chromium,[52] cobalt,[53] copper,[41] molybdenum, rhenium, tungsten,[54] rhodium[55], or platinum.[56]

A second approach is that of grafting transition metal complexes directly to the silicate framework. There are many examples of this type of metal modification of mesoporous materials which include the reaction of metal alkoxides,[57,58] the attachment of rhodium carbonyl complexes,[59] trimethylstannyl molybdenum materials $(Me_3SnMo(CO)_3(\eta\text{-}C_5H_5))$,[60] rare-earth bis(dimethylsilyl)amides,[61, 62] vanadyl triisopropoxide $(O=V(O^iPr)_3)$, [63] chiral alkene polymerisation catalysts, and dicyclopentadienyltitanium dichloride $(TiCp_2Cl_2)$.[64, 65] Maschmeyer *et al* directly grafted a titanocene-derived catalyst precursor to the pore walls of MCM-41, to yield a very promising catalyst for the epoxidation of cyclohexene and more bulky cyclic alkenes.[66]

An alternative to this route is the prior functionalisation of the silica surface with species such as amino-,[67,68,69,70] thiol-,[67] alkyl,[68] and phosphinate-[71] organosilanes. The transition metal complex may then be bound to these sites. Copper and manganese phenanthroline complexes,[72] cobalt (II) species,[73] ruthenium porphyrins,[74] and chromium binaphthyl Schiff base complexes[75] have been supported in this way.

An alternative to the modification of mesoporous silicate or aluminosilicate materials is the synthesis of mesoporous metal oxides and phosphates. Mesostructured titania has been synthesised by Antonelli and Ying,[76] and Stucky *et al,* have synthesised mesoporous oxides of lead, tungsten, iron, molybdenum, tantalum, hafnium, zirconium, niobium and tin.[77,78,79] Mesoporous phosphates of aluminium[80,81] and zinc[82] have also been made.

Many of the materials and processes described above concern the potential of these systems as heterogeneous catalysts, which is the most relevant application with regard to this work, but it has been demonstrated that mesoporous materials may have a large number of uses. They have been applied as chromatographic materials for chiral HPLC,[83] toxic metal adsorbents,[84] high surface area electrodes,[85] supports for dyestuffs,[86] deodorants,[87] and ion exchange media.[88]

1.2 The Chemistry of Uranium

The atomic spectra of the f elements are very complex, and it is often difficult to identify levels in terms of quantum numbers and configurations. In terms of chemical behaviour, the lowest energy configuration is of the most interest, and therefore, for the actinides, competition between $5f^n 7s^2$ and $5f^{n-1} 6d 7s^2$ configurations is of great importance in determining the reactivity of these elements. For elements in the first half of the f shell, of which uranium is one, it appears that less energy is required for the promotion $5f \rightarrow 6d$ than for the comparable $4f \rightarrow 5d$ promotion in the lanthanides. This results in a tendency to provide more bonding electrons, with a consequence of relatively higher valences in the early actinides. The chemistry of the second half of the actinide series more closely resembles that of the lanthanides.

The $5f$ orbitals have a greater spatial extension relative to the $7s$ and $7p$ orbitals than $4f$ to $6s$ and $6p$, which may be observed to result in some f covalent contribution to the bonding of some actinide compounds, whereas the bonding in lanthanide materials may be considered as purely ionic with no contribution from the inner $4f$ orbital. In the actinide series, therefore, and especially for uranium, the energies of the $5f$, $6d$, $7s$, and $7p$ are comparable. Since the orbitals may also overlap spatially, bonding may involve any or all of them, and this is indicated in the chemistry of these elements by the fact that the actinides are much more prone to form complexes than the lanthanides. The oxidation states of uranium are 3+, 4+, 5+, and 6+, with uranium (IV) and (VI) being the most common.

1.2.1 Uranium Oxides

The uranium-oxygen system is not only the most complex actinide oxide system, but it is also one of the most complex oxide systems known. Due to this complexity, and the importance of uranium dioxide as a nuclear reactor fuel, many studies of the uranium-oxygen system over a wide range of temperatures have been made.[89,90] Despite this effort, a full explanation and understanding of this binary system is far from complete. The oxides (in order of increasing O/U ratio) that have been reported at one time or another are: UO, UO_2, U_5O_{11}, U_4O_9, $U_{16}O_{37}$, U_3O_7, U_8O_{19}, U_2O_5, U_5O_{13}, $U_{13}O_{34}$, U_8O_{21}, $U_{11}O_{29}$, U_3O_8, $U_{12}O_{35}$, and UO_3. In addition, several polymorphs of many of these have been suggested.[91] Different workers have assigned different stoichiometries to what undoubtedly constitute the same crystalline phases, and older work often refers to phases that are now generally

considered to have more complex stoichiometries. The result of these conflicting reports makes a definitive discussion of the uranium-oxygen system very difficult, but some general comments may be made.

UO_2 has a face centred cubic structure, and the oxides of uranium may be best understood if it is considered that addition of oxygen to UO_2 produces incrementally increased distortion of the original fluorite lattice. The added oxygen can be distributed at random to produce a single phase of constant space group but of variable stoichiometry, lattice parameters, and density, such as UO_{2+x}, or it can be distributed in an ordered fashion, forming cubic, tetragonal, or monoclinic superlattices still based on the fluorite structure. The stoichiometric range of a phase at a particular temperature is a measure of its ability to resist a change in long range order with the addition of randomly distributed oxygen atoms. Once this limit is reached, at least some of the added oxygen atoms must become ordered in a superlattice structure, with the production of a new phase, possibly also of variable composition. This behaviour continues from UO_2 to approximately $UO_{2.4}$, producing a series of phases with very similar densities (10.9-11.5 gcm^{-3}). As further oxygen is added, an abrupt change to lower density ($\sim$9 gcm^{-3}) occurs. The phases in this region contain uranyl-type bonding, where there are two short collinear uranium-oxygen bonds, with 4-6 weaker U-O bonds in a plane approximately perpendicular to these shorter bonds. In this instance, the $[UO_2]$ uranyl-type unit is not necessarily a discrete uranyl group, as is often observed for uranium (VI) systems, but more likely bridging between uranium atoms.

The trioxide, UO_3, is best prepared by the thermal decomposition of uranyl nitrate, and UO_2 or U_3O_8 may be obtained from this by the reactions:

$$3UO_3 \xrightarrow{700°C} U_3O_8 + {}^1/_2O_2$$

$$UO_3 + CO \xrightarrow{350°C} UO_2 + CO_2$$
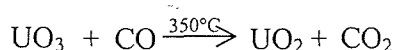
1.2.1.1 Uranium Oxides as Heterogeneous Catalysts

Uranium compounds have been reported as catalysts for a variety of applications. For instance, uranium intermetallics such as UNi_5 have been used in Fischer-Tropsch processes and for hydrogen storage.[92,93,94] Mixed oxides of uranium and a second metal have also found a wide range of catalytic activity. Uranium-molybdenum oxides have been

reported as active for the selective oxidation of isobutene to methacrolein.[95,96,97]   This is illustrated in figure 1.5

$$O_2 \quad + \quad \diagup\!\!\!\diagdown \quad \longrightarrow \quad \diagup\!\!\!\diagdown\!\!=\!\!O \quad + \quad H_2O$$
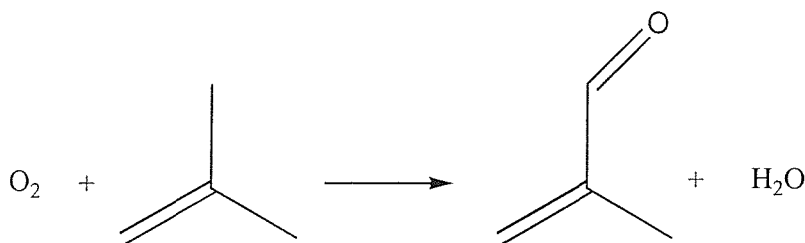
Figure 1.5 Conversion of isobutene to methacrolein

One of the best known catalytic systems for the controlled oxidation of alkenes consists of a uranium-antimony mixed oxide, which has been used industrially to produce acrolein and acrylonitrile from propene.[98,99]

$$O_2 \quad + \quad \diagup\!\!\!\diagdown \quad \longrightarrow \quad \diagup\!\!\!\diagup\!\!=\!\!O \quad + \quad H_2O$$

a)

$${}^{3}/_{2}\,O_2 + NH_3 \quad \diagup\!\!\!\diagdown \quad \longrightarrow \quad N \quad + \quad 3H_2O$$

b)
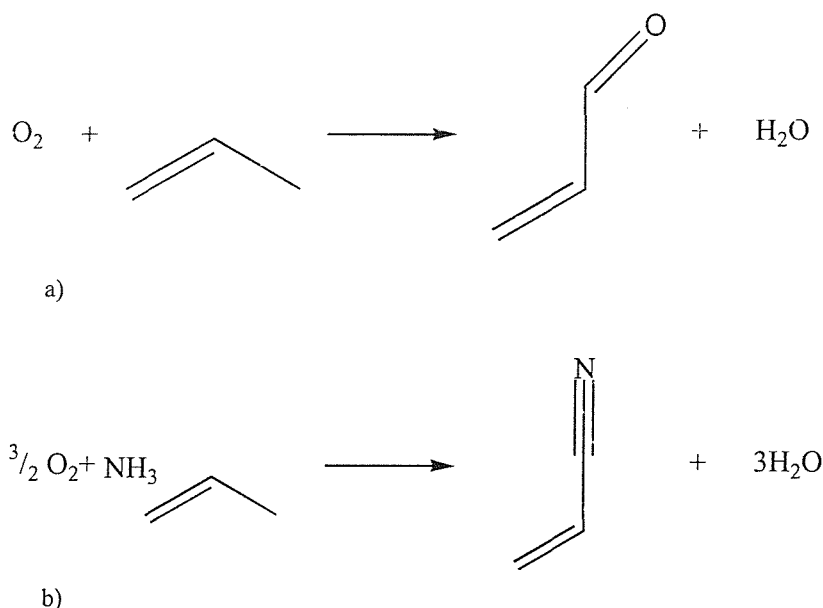
Figure 1.6 Conversion of propene to a) acrolein and b) acrylonitrile over USb_3O_{10}

It has been proposed that this material has U(V) sites present in the structure, which is a very difficult oxidation state to stabilise in binary oxides.[100]   By relating data from surface-sensitive techniques to catalytic testing, a stepwise oxidation-reduction mechanism was proposed for this by Graselli _et al_ for the oxidation of propene.[101]   Such a mechanism involves the direct incorporation of lattice oxygen from the catalyst. Since oxygen is lost, oxygen vacancies are produced, resulting in a change of co-ordination of the uranium cations. The catalyst may then be re-oxidised by molecular oxygen. Oxygen transfer via the lattice is an important aspect of this reaction, as it shows that the lattice oxygen of

reducible oxides should serve as a more functional oxidising agent than O_2. This was emphasised by the use of a mixed bismuth-uranium oxide for the oxidative demethylation of toluene, where the absence of gaseous oxygen is required to achieve good selectivity.[102,103] Bi_2UO_6 was found to be able to lose 50% of its lattice oxygen without substantial structural modification.[104] A further system of interest is nickel-uranium oxide which has been known for many years to be catalytically active for reforming hydrocarbons with steam to produce a fuel gas comprised of hydrogen, methane and carbon oxides,[105,106,107] and some interest has been shown in their ability to form methane from carbon monoxide and hydrogen.[108]

It is the properties of the binary oxides of uranium that are of particular relevance to this work, and in the 1970's binary uranium oxides were shown by Nozaki and Inami to be active for the dehydrogenation and dehydration of ethanol[109], propan-2-ol, and butan-2-ol[110], and the dehydrogenation of ethylbenzene.[111] More recently, uranium oxide, in the form of U_3O_8, has been shown to be a very active catalyst for the total oxidation of volatile organic compounds (VOCs).[112] Chlorobenzene and chlorobutane were selected to demonstrate the effectiveness of this catalyst, as these compounds are difficult to totally oxidise, particularly chlorobenzene, and chlorine containing VOCs rapidly deactivate industrial catalysts based on precious metals. The uranium oxide materials convert these VOCs at 100% to carbon oxides, water and HCl at industrially relevant flow rates and feed gas concentrations, and at a relatively low temperature of 350°C. Interestingly, supporting of the uranium oxide phase on silica actually reduced the activity of these materials for some substrates, whilst the addition of 1mol% of chromium greatly enhanced the total oxidation of butane.[113,114] The use of isotopically labelled oxygen in the gas feed confirmed that it is the lattice oxygen, rather than gas phase O_2 that is incorporated into oxidation products.[115]

Also reported is the catalytic oxidation of carbon monoxide with oxygen using a binary uranium oxide. Studies were initially carried out by Nozaki _et al_ with bulk, unsupported, uranium oxide (nominally U_3O_8),[116] and the same research group found that supporting the oxide on alumina greatly enhanced activity, whereas using silica as a carrier suppressed catalytic performance.[117] This work was extended to include other support materials, such as TiO_2 and MgO, and suggested that the support destabilised the uranium precursor, uranyl nitrate, in favour of U_3O_8 in the order $TiO_2 > SiO_2 > Al_2O_3$.[118]

Uranium oxides have also been studied previously with respect to the catalytic reduction of NO to N_2 with CO as the reductant. Nozaki *et al* performed catalytic testing on bulk, unsupported U_3O_8, and demonstrated that the addition of alkali metal oxides enhances the activity of this material.[119] The ease of reduction of these systems decreased in the order U-Cs>U-K>U-Na, and this was also the noted activity trend. The suggestion is that this ease of reducibility is of great importance in determining the catalyst activity. The active phase identified for all systems except U-Cs was U_3O_8, whereas a reduced form of this oxide, U_3O_7, was found for the caesium containing material. More recently, Wells *et al* investigated the effect of supporting the uranium oxide phase at 30wt% U on alumina.[120] Catalysts were prepared from the calcination of supported uranyl nitrate prior to reaction. They found that supporting the uranium phase on a high surface area support gave a decrease in light-off temperature, and activity comparable with that of a 5wt% Pt/γ-Al_2O_3 catalyst. They also suggested that the selectivity of the supported uranium material towards N_2 was markedly better than that of the supported platinum material. The active phase was identified as UO_2, and it was shown that materials calcined at 800°C prior to reaction performed better than those at 450°C.

1.2.2 Organouranium chemistry

This area of chemistry has been quite extensively studied, and this section is not intended to be a complete review of the subject, but more a brief outline of the areas of research which are of interest with respect to this project. Much of the work that has been done previously has centred on complexes of cyclopentadienyl species of differing degrees of co-ordinative saturation. Variation in the auxiliary ligands, including halides,[121] amides,[122] alkyls,[123] borohydrides,[124] alkoxides[125] and even carbonyl[126] species has allowed an expansion in the understanding of organouranium chemistry. The significance of this class of materials with respect to catalytic applications will be expanded upon in a later section.

1.2.2.1 Uranium triamidoamine complexes

Many of the organometallic compounds that have been employed up to this point in the project are based on triamidoamine complexes of uranium. For this reason it is necessary to give a brief account of the nature of this ligand type, and the complexes it forms, in order to demonstrate the rationale behind choosing this particular primary

coordination set. Triamidoamine ligands $[(RNCH_2CH_2)_3N]^{3-}$ in which R is a bulky substituent, bind to a variety of transition metals and are able to stabilise oxidation states of III or higher. The early work on the synthesis of these ligands was done by Verkade _et al_[127] and Schrock and co-workers[128] and knowledge of their coordination chemistry has steadily grown over recent years. The usual mode of coordination is in a tetradentate manner, which creates a sterically protected 3-fold symmetric pocket.
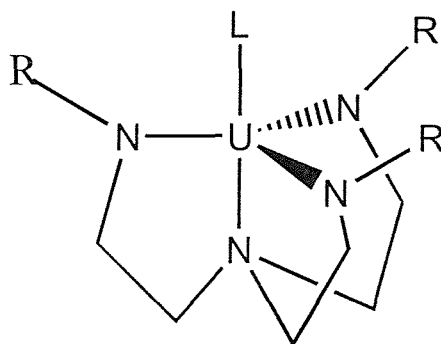
Figure 1.7 Representation of a (triamidoamine)uranium complex

The ligand may be considered to occupy the three equatorial and one of the two axial sites of a geometry that approximates to a trigonal bipyramid. The second axial site may then be occupied by a wide variety of species (for uranium X= halide[129], OR^{130}, Cp, BH_4[131] R, NR_2[132], $OP(NMe_2)_3$[133]). The syntheses of $(Me_3SiNHCH_2CH_2)_3N$[127] and its pentane soluble trilithium salt[128] from the inexpensive tris(2-aminoethyl)amine (tren) made the rapid development of triamidoamine co-ordination chemistry possible, and the presence of the bulky silyl groups has shown itself to be of great importance in dictating the ease of complexation and subsequent stability of the organometallic compounds. For example, the use of $L^3 = [(Me_2Bu^tSiNCH_2CH_2)_3N]^{3-}$, facilitates the formation of L^3UX complexes where X is a halide[129], whereas if the apical ligand is rather more sterically demanding, such as $C_5Me_5^-$ or, then the silyl group that is to be used must be proportionally less spatially significant, e.g $SiMe_3$, if a stable compound is to form.[131] Using this tetradentate ligand as a basis it is possible to synthesise uranium complexes where the oxidation state of the metal centre may be formally assigned as III, $(L^3UOP(NMe_2)_3)$, IV (L^3UCl), (L^3UNEt_2), V $(L^3U=N-SiMe_3)$, $(L^3U=O)^{134}$, or even as a mixed valence (III/IV) species $[(L^3U)_2-\mu-Cl]$.

It has been shown that these complexes demonstrate novel properties and reactivity in the area of organoactinide chemistry. The alkoxido derivatives are catalysts for the

polymerisation of polar olefins such as methyl methacrylate[135], the tetravalent complexes of the type L^3UR undergo intramolecular C-H activation[136], and the trivalent complexes accomplish the property previously unknown in actinide chemistry of reversibly co-ordinating dinitrogen.[137] This project has been inspired by a desire to investigate and develop these compounds as surface species by heterogenising the exciting behaviour that they display as isolated molecules. The volatile nature of these compounds has allowed the possibility of subliming the organometallic directly onto the inorganic oxide to accomplish the chemisorption process by vapour deposition.

1.2.2.2 Supported Organoactinides as Heterogeneous Catalysts

This area of chemistry has benefited from only a relatively small amount of investigation, but that which has been done has yielded some interesting results. Marks and co-workers reported that compounds of the type $Cp_2'Th(CH_3)_2/DA$ and $Cp'Th(CH_2C_6H_5)_3/DA$ ($Cp'= \eta^5-Me_5C_5$; DA= dehydroxylated γ-alumina) are highly active catalysts for ethylene polymerisation[138] and, per active site, rival the activities of the most active platinum metal heterogeneous catalysts for the hydrogenation of simple olefins.[139] The order of activity found for the latter transformation is $Cp'Th(CH_2C_6H_5)_3/DA$ > $Cp_2'Th(CH_3)_2/DA$ > $Cp_3Th(CH_3)/DA$, which suggests the importance of precursor coordinative unsaturation in influencing ultimate adsorbate catalytic activity. They showed from ^{13}C CPMAS NMR experiments that chemisorption involves methide anion transfer from the actinide centre to a Lewis acid site on the surface.[140] Cationic hydrocarbyl species may be expected to be highly electrophilic, and have been demonstrated as kinetically suitable for olefin hydrogenation and polymerisation.

The thorium complex $Th(\eta^3-allyl)_4/DA$ has also been employed by the same group for the heterogeneous hydrogenation of arenes.[141] The rate ordering follows the trend benzene>toluene>>p-xylene>>naphthalene. This trend is also found for conventional heterogeneous catalysts[142], but in contrast, for this actinide system, partially hydrogenated products are not detected in incompletely converted reaction mixtures when the substrate is benzene, toluene, or p-xylene. The same complex has been shown to promote the highly demanding process of C-H activation in alkanes[141], demonstrating rapid C-H/C-D exchange with turnover frequencies comparable to or exceeding those of conventional group 9 heterogeneous activation catalysts.

1.3 The Selective Catalytic Reduction of NO

The reduction of nitrogen oxide emissions has become one of the most important challenges in environment protection over recent years. NO and NO_2 are major atmospheric pollutants, and play an important role in the photochemistry of the troposphere and stratosphere. In the troposphere, NO_2 may be photolysed to yield NO and O, with resultant ozone formation. The nitrogen oxides also react with other species present in this level of the atmosphere such as formaldehyde, and organic hydroperoxides to create a photochemical smog containing ozone, CO, peroxyacetyl nitrates, alkyl nitrates and ketones. The dissolution of NO_2 in atmospheric water contributes significantly to the environmental problems associated with acidified rain. In the stratosphere, NO derived species are responsible for further environmental impact in their role in the depletion of ozone. As well as these effects, the presence of a high concentration of atmospheric NO has the potential to contribute substantially to the phenomenon of global warming, as it has a very high greenhouse coefficient. As a reaction to the perturbation of local and global environment caused by the presence of NO_x species, and the associated introduction of stringent governmental legislation regarding their abatement, there has been an increasing quantity of research conducted to develop systems capable of removing nitrogen oxides from both stationary and mobile source exhaust gas emissions.

1.3.1 The Catalytic Reduction of NO in the presence of ammonia

The catalytic reduction of nitrogen oxides in effluent residual gases from various industries, but particularly nitric acid plants, is often carried out with the use of ammonia or urea and a carefully chosen heterogeneous catalyst. More than one thousand systems of varying composition have been investigated with respect to this purpose.[143] Base metal oxides have been extensively studied, and all of the following materials show some activity towards this reaction: V_2O_5, Fe_2O_5, CuO, Cr_2O_3, Co_3O_4, NiO, CeO_2, La_2O_3, Pr_6O_{11}, Nd_2O_3, Gd_2O_3, Yb_2O_3. Of these, vanadia has demonstrated the most favourable combination of activity and selectivity. Deposition of the base oxide on a support has been shown to enhance catalytic performance, and the exact nature of this support material has also been shown as an important factor in determining the efficacy of the catalyst. Bauerle *et al* reported very good activity for V_2O_5 supported on TiO_2 and Al_2O_3[144], and Shikada *et al* extended this investigation to systematically determine the promotional effect of titania.[145] They reported that the order of activity for supported vanadia is TiO_2-SiO_2>γ-Al_2O_3>SiO_2,

and Pearson *et al* reported that the use of the anatase rather than rutile phase of titania further enhances activity.[146]

Supported chromia catalysts have also been extensively investigated with respect to the SCR of NO. Niyama *et al* studied the behaviour of chromia-alumina catalysts,[147,148] and reported good activity for lower chromia concentrations, and for pure Cr_2O_3. Interestingly, conversions were insignificant for intermediate loadings of chromium, which suggests a complex relationship between support interaction/interference and active phase dispersion. More recently, Baiker *et al* demonstrated that the initial activity of titania-supported chromia catalysts depends strongly on the catalyst pre-treatment conditions.[149] Reductive pre-treatment at temperatures below 720K yielded materials with improved selectivity towards N_2 formation at reaction temperatures below 420K. At higher temperatures a decrease in activity was observed, and this was attributed to the partial crystallisation and particle growth of the chromia phase. The improved selectivity was considered to be due to the partial reduction of Cr(VI) and Cr(V) surface species to hydroxylated Cr(III), which is more active for ammonia chemisorption. However, a totally reduced surface is inactive, and maintenance of a partially oxidised state with the use of oxygen in the gas feed is essential for good activity. The notion of a partially oxidised, or partially reduced, surface as important in determining the activity of the catalyst is particularly relevant to this project.

1.3.2 The Catalytic Reduction of NO in the presence of CO and H_2

The investigation of the use of CO and H_2 in the catalytic reduction of NO was prompted by the need to eliminate nitrogen oxides from automotive exhaust emissions. The reaction of NO with CO is one of the most important occurring in a catalytic converter, as both reactants are undesirable pollutants:

$$NO + CO \longrightarrow CO_2 + \tfrac{1}{2} N_2$$
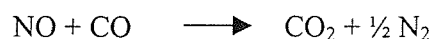
An amount of hydrogen, from water-gas shift and hydrocarbon cracking, is also present in the exhaust stream, and this allows the possibility of a second route to NO reduction:

$$NO + H_2 \longrightarrow N_2 \text{ (or } NH_3, N_2O) + H_2O$$
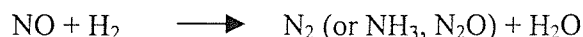
With the presence of oxygen in the exhaust gas, neither of the above processes may be considered selective towards N_2, as both N_2O and NH_3 (in the case of hydrogen reduction) are formed in substantial amounts. The oxygen excess prevents the total reduction of NO, and causes the concomitant oxidation of CO and H_2. This is not necessarily the case in systems where oxygen may be excluded, and in these conditions the reduction of NO may be

achieved with greater selectivity towards N_2 formation. For this reason, the use of CO, H_2 and hydrocarbons as NO_x reductants for use in stationary, as well as mobile, emission sources has been extensively investigated in recent times.

Several categories of catalysts have been investigated for their activity towards this reaction, both in the presence and absence of oxygen and water. These include some base metal oxides, mixed metal oxide compounds, such as perovskites,[150] supported metal catalysts,[151] zeolites,[152] and alloys.[153] The study of base metal oxides (supported on 95% alumina, 5% silica), completed by Shelef and Kummer,[154] gave the following order of reactivity for the reduction by CO: $Fe_2O_3 > CuCr_2O_4 > Cu_2O > Cr_2O_3 > NiO > Pt > Co_3O_4 > Al_2O_3(5\% \ SiO_2) > MnO > V_2O_5$. Good selectivity towards N_2 and CO_2 was shown for the supported iron and chromium oxide catalysts, particularly at higher temperatures (>575K), but a dependence on the inlet NO-to-CO ratio was very evident. For the other oxide materials tested, the oxidation of CO to CO_2 by O_2 is a much faster reaction than that between CO and NO, leading to a non-selective reduction. Stegenga *et al* demonstrated the effectiveness, and N_2 selectivity, of an alumina-supported mixed copper-chromium oxide material towards this reaction, and suggested the importance of determining the optimum base metal to support ratio.[155] The dispersion of the active species, as well as the nature of the support, is also an important factor in determining the catalyst stability, particularly with regard to H_2O deactivation and SO_2 poisoning.[156]

In summary, the type, structure and stability of the support material, the dispersion of the active phase and the interaction it has with the support, the pre-treatment of the catalyst, and the extent of active surface oxidation/reduction may all be expected to be key factors in determining catalyst activity, selectivity, and stability.

1.4 Project Aims

This chapter has introduced three areas of chemistry; mesoporous materials; the chemistry of uranium and its oxides, and the selective catalytic reduction of nitric oxide. Currently, there exist no reports within the literature regarding uranium species in mesoporous materials, few investigations relating to the use of uranium oxides in NO reduction catalysis,[119,120] and limited work on the use of mesoporous materials for NO_x abatement.[157,158,159] The aim of this project is then to attempt to combine the properties of mesoporous materials and uranium oxides, in order to design a new class of heterogeneous catalysts for the selective reduction of NO. The basis of this approach may be summarised in three sections:

1) The synthesis and characterisation of mesoporous silica materials, and the investigation of the effect of thermal treatment on stability and surface structure. This work is described in chapter 3.

2) The synthesis and characterisation of supported uranium materials. The characterisation and effect of thermal treatment on mesoporous silica, amorphous silica, and γ-alumina supported uranyl nitrate and uranium tetrachloride is described in chapter 4. The characterisation of mesoporous silica supported organouranium compounds is dealt with in chapter 7.

3) The catalytic testing of mesoporous silica, amorphous silica, and γ-alumina supported uranyl nitrate and uranium tetrachloride, with regard to the oxidation of CO with oxygen to CO_2, and the selective reduction of NO with CO, is described in chapters 5 and 6 respectively. The dependence of the activity, and selectivity in the case of the NO reduction reaction, of these materials on the pre-treatment conditions employed is also investigated. A comparison with an alumina supported platinum catalyst is also conducted for the NO reaction with CO.

1.5 References

1)   W. Keim, *Angew. Chem. Int. Ed. Engl. Transl.*, 235, **29**, 1990.

2)   J. Klinowski, *Chem. Rev.*, 1459, **91**, 1991.

3)   A.M. Healey, Southampton University. Thesis, 1999.

4)   D.W. Breck, W.G. Eversole, R.M. Milton, T.B. Reed, T.L. Thomas, *J. Am. Chem. Soc.*, 5963, **78**, 1956.

5)   P.B. Weisz, V.J. Frilette, R.W. Maatman, E.B.J. Mower, *J. Catal.*, 307, **1**, 1962.

6)   C.D. Chang, C.T.W. Chu, *J. Catal.* 203, **74**, 1982.

7)   S.T. Wilson, B.M. Lok, C.A. Messina, T.R. Cannon, E.M. Flanigen, *J.Am.Chem.Soc.*, 1146, **104**, 1982.

8)   B.M. Lok, C.A. Messina, R.L Patton, R.T. Gajek, T.R. Cannon, E.M. Flanigen, *J.Am.Chem.Soc.*, 6092, **106**, 1984.

9)   M. Esterman, L.B. McCusker, C. Baerlocher, A. Merrouche, H. Kessler, *Nature*, 320, **352**, 1991.

10)   D.W. Sindorf, G.E. Maciel, *J.Am.Chem.Soc.*, 1487, **105**, 1983.

11)   R.K. Iler, The Chemistry of Silica, Wiley, New York, 1979.

12)   J.S. Beck, J.C. Vartuli, W.J. Roth, M.E. Leonowicz, C.T. Kresge, K.D. Schmitt, C.T-W. Chu, D.H. Olson, E.W. Sheppard, S.B. McCullen, J.B. Higgins, J.L. Schlenker, *J.Am.Chem.Soc.*, 10834, **114**, 1992.

13)   C.T. Kresge, M.E. Leonowicz, W.J. Roth, J.C. Vartuli, J.S. Beck, *Nature*, 710, **359**, 1992.

14)   Q. Huo, D. I Margolese, U. Ciesla, P. Feng, T.E. Gler, P. Sieger, R. Leon, P.M. Petroff, P. Schuth, G.D. Stucky, *Nature*, 317, **368**, 1994.

15)   R. Mokaya, W. Jones, *J.Mat. Chem.*, 2819, **8**, 1998.

16)   V. Antochshuk, M. Jaroniec, *Chem. Commun.*, 2373, 1999.

17)   Z.R. Zhang, J.S. Suo, X.M. Zhang, S.B. Li, *Acta Phys.-Chim. Sin.*,333, **13**, 1999.

18)   S.A. Bagshaw, E. Prouzet, T.J. Pinnavaia, *Science*, 1242, **249**, 1995.

19)   W. Zhang, B. Blomski, T.R. Pauly, T.J. Pinnavaia, *Chem. Commun.*, 1803, 1999.

20)   G.S. Attard, J.C. Glyde, C.G. Göltner, *Nature*, 366, **378**, 1995

21)   G.S. Attard, P.N. Bartlett, N.R.B. Coleman, J.M. Elliott, J.R. Owen, J.H. Wang, *Science*, 838, **278**, 1997.

22)   G.S. Attard, N.R.B. Coleman, J.M. Elliott, *Stud. Surf. Sci. Catal.*, 89, **117**, 1998.

23)   A. H. Whitehead, J.M. Elliott, J.R. Owen, G.S. Attard, *Chem. Commun.*, 331, 1999.

24)   C.F. Cheung, Z.H. Luan, J. Klinowski, *Langmuir*, 2815, **11**, 1995.

25)   N. Ulagappan, C.N. R Rao, *Chem Commun.*, 2759, 1996.

26)   K.M. Reddy, I. Moudrakovski, A. Sayari, *Chem. Commun.*, 1059, 1994.

27)   D.H. Park, C.F. Cheung, H. He, J. Klinowski, *J. Mater. Chem.*, 159, **7**, 1997.

28)   J.S. Reddy, A. Sayari, *Chem. Commun.*,2231, 1995.

29)   W. Zhang, M. Fröba, J. Wang, P.T. Tanev, J. Wong, T.J. Pinnavaia, *J. Am. Chem. Soc.*, 9164, **118**, 1996.

30)   A. Corma, M.T. Navarro, T.J. Perez-Pariente, *Chem. Commun.*, 147, 1994.

31)   S. Gontier, A. Tuel, *J. Catal.*, 124, **157**, 1995.

32)   G.S. Sankar, F. Rey, J.M. Thomas, G.N. Greaves, A. Corma, B.R. Dobson, A.J. Dent, *Chem. Commun.*, 2279, 1994.

33)   P.T. Tanev, M. Chibwe, T.J. Pinnavaia, *Nature,* 321, **368**, 1994.

34)   M.R. Raimondi, L. Marchese, E. Gianotti, T. Maschmeyer, J.M. Seddon, S. Coluccia, *Chem. Commun.*, 87, 1999.

35)   (a) R. Schmidt, D. Akropriaye, M. Stöcker, O.H. Ellestad, *Chem. Commun.*, 1493, 1994. (b) G.S. Attard, M. Edgar, C.G. Göltner, *Acta. Mater.*, 751, **46** 1998.

36)   (a) S. Gontier, A. Tuel, *Chem. Mater.*, 114, **8**, 1996. (b) A. Sayari, C. Danumah, I.L. Moudrakovski, *Chem. Mater.*, 813, **7**, 1995. (c) D.T. On, P.N. Joshi, S. Kaliaguine, *J. Phys. Chem.*, 6743, **100**, 1996.

37)   (a) N. Ulaggapan, C.N.R. Rao, *Chem. Commun.*,1047, 1996. (b) D. Wei, N.S. Yao, G.L. Haller, *Stud. Surf. Sci. Catal.*, 239, **121**, 1999. (c) H. Yamashita, M. Ariyuki, S. Higashimoto, S.G. Zhang, J.S. Chang, S.E. Park, J.M. Lee, Y. Matsumura, M. Anpo, *J. Synch. Rad.*, 453, **6**, 1999.

38)   S.G. Fiddy, J.M. Corker, *Stud. Surf. Sci. Catal.* 365, **117**, 1998.

39)   Z.Y. Huan, S. Q. Liu, T.H. Chen, J.Z. Wang, H.X. Li, *Chem. Commun.*,973, 1995.

40)   S. Ayappan, N. Ulagappan, *Proc. Indian Acad. Sci., Chem. Sci.*, 505, **108**, 1996.

41)   M. Hartmann, S. Racouchot, C. Bischof, *Chem. Commun.*,2367, 1997.

42)   M.A. Karassides, K.G. Fournaris, A. Travlos, D. Petridis, *Adv. Mater.*, 483, **10**, 1998.

43)   M. Hartmann, S. Racouchot, C. Bischof, *Micro. Meso. Mater.*, 309, **27**, 1999.

44)   (a) C.F. Cheung, H.Y. He, W.Z. ZHou, J. Klinowski, J.A.S. Goncalves, L.F. Gladden, *J. Phys. Chem.*, 390, **100**, 1996. (b) C.F. Cheung, J. Klinowski, *J. Chem. Soc., Faraday Trans.*, 289, **92**, 1996.

45)   M.S. Morey, G.D. Stucky, S. Schwarz, M. Froba, *J. Phys. Chem. B*, 2037, **103**, 1999.

46)   (a) M. Ziolek, I. Nowak, Zeolites, 356, **18**, 1997. (b) L. Zhang, J.Y. Ying, *Aiche Journal*, 2793, **43**, 1997.

47)   (a) T.K. Das, K. Chaudhari, A.J. Chandwadker, S. Sivasanker, *Chem. Commun.*,2495, 1995. (b) T.M. Abdel-Fattah, T.J. Pinnavaia, *Chem. Commun.*,665, 1996.

48)   Z.R. Zhang, J.S. Sue, X.M. Zhang, S.B. Li, *Appl. Catal. A, General*, 11, **179**, 1999.

49)   D. Zhao, D. Goldfarb, *Chem. Commun.* 875, 1995.

50)   (a) H. Yamashita, Y. Fujii, Y. Ichihashi, S.G. Yhang, K. Ikeue, D.R. Park, K. Koyano, T. Tatsumi, M. Anpo, *Catal. Today,* 221, **45**, 1998. (b) M. Anpo, H. Yamashita, K. Ikeue, Y. Fujii, S.G. Yhang, Y. Ichihashi, D.R. Park, Y. Suzuki, K. Koyano, T. Tatsumi, *Catal. Today,* 327, **44**, 1998.

51)   G. Grubert, J. Rathousky, G. Schulz-Ekloff, M. Wark, A. Zukal, *Micro. Meso. Mater.*, 225, **22**, 1998.

52)   Z.D. Zhu, M. Hartmann, E.M. Maes, R.S. Czernuszewicz, L. Kevan, *J. Phys. Chem. B*, 4690, **104**, 2000.

53)   A. Jentys, N.H. Pham, H. Vinek, M. Englisch, J.A. Lercher, *Micro. Mater.*, 13, **6**, 1996.

54)   J-Y. Piquemal, E. Briot, M. Vennat, J-M. Bregeault, G. Chottard, J-M. Manoli, *Chem. Commun.*, 1195, 1999.

55)   (a) R.S. Mulukutla, K. Asakura, S. Namba, Y. Iwasawa, *Chem. Commun.*, 1425, 1998. (b) R.S. Mulukutla, K. Asakura, T. Kogure, S. Namba, Y. Iwasawa, *PCCP-Phys. Chemistry.Chem. Physics*, 2027, **1**, 1999.

56)   M.A. Aramendia, V. Borau, C. Jimenez, J.M. Marinas, F.J. Romero, *Chem. Commun.*, 873, 1999.

57)   M.S. Morey, G.D. Stucky, S. Schwarz, M. Froba, *J. Phys. Chem. B*, 2037, **103**, 1999.

58)   R. Mokaya, W. Jones, *PCCP-Phys. Chemistry Chem. Physics*, 207, **1**, 1999.

59)   A. Janssen, J.P.M. Niederer, W.F. Holderich, *Catal. Lett.,* 165, **48**, 1997.

60) C. Huber, K. Moller, T. Bein, _Chem. Commun._, 2619, 1994.

61) R. Anwander, R. Roesky, _J. Chem. Soc. Dalton Trans.,_ 137, **2**, 1997

62) R. Anwander, O. Runte, J. Eppinger, G. Gerstberger, E. Herdtweck, M. Spiegler, _J. Chem. Soc. Dalton Trans.,_ 847, **5**, 1998.

63) M. Morey, A. Davidson, H. Eckert, G.D. Stucky, _Chem. Mater._, 486, **8**, 1996.

64) R.D. Oldroyd, J.M. Thomas, G, Sankar, D. Özkaya, _J. Phys. Chem. B_, 1849, **102**, 1998.

65) R.D. Oldroyd, J.M. Thomas, G, Sankar, _Chem. Commun._, 2025, 1997.

66) T. Maschmeyer, F. Rey, G. Sankar, J.M. Thomas, _Nature_, 159, **378**, 1995.

67) A.M. Liu, K. Hidajat, S. Kawi, D.Y. Zhao, _Chem. Commun._, 1145, 2000.

68) C.P. Jaroniec, M. Kruk, M. Jaroniec, A. Sayari, _J. Phys. Chem. B._ 5503, **102**, 1998.

69) J. Evans, A.B. Zaki, M.Y. El-Sheikh, S.A. El Safty, _J. Phys. Chem. B_, 10271, **104**, 2000.

70) X. Feng, G.E. Frywell, L-Q. Wang, A.Y. Kim, J. Liu, K.M. Kemner, _Science_, 923, **276**, 1997.

71) S-G. Shyu, S-W. Cheng, D-L. Tzou, _Chem. Commun._, 2337, 1999.

72) S. Zheng, L. Gao, J.K Guo, _J. Solid State Chem._, 447, **152**, 2000.

73) J. F. Diaz, K.J. Balkus, F. Bedioui, V. Kurshev, L. Kevan, _Chem. Mater._, 61, **9**, 1997.

74) C.J. Liu, S.H. Li, W.Q. Pang, C.M. Che, _Chem. Commun._, 65, 1997.

75) I.C. Chisem, J. Rafelt, M. Tantoh Shieh, J. Chisem, J.H. Clark, R. Jachuk, D. Macquarrie, C. Ramshaw, K. Scott, _Chem. Commun._, 1949, 1998

76) D.M. Antonelli, J.Y Ying, _Angew. Chem. Int. Ed.,_ 2014, **34**, 1995.

77) P.D. Yang, D.Y Yao, D.J. Margolese, B.F. Schmelka, G.D. Stucky, _Chem. Mater.,_ 2811, **11**, 1999.

78) Q. Huo, D.J. Margolese, U. Ciesla, D.G. Demuth, P. Feng, T.E. Gier, P. Sieger, A. Firouzi, B.F. Schmelka, F. Schuth, G.D. Stucky, _Nature_, 316, **368**, 1994.

79) U. Ciesla, D.G. Demuth, R. Leon, P. Petroff, G.D. Stucky, K. Unger, F. Schuth, _Chem. Commun._, 1387, 1994.

80) A. Sayari, V.R. Karra, J.S. Reddy, I. Moudrakovski, _Chem. Commun._ 411, 1996.

81) A. Chenite, Y. LePage, V.R. Karra, A. Sayari, _Chem. Commun._, 413, 1996.

82) Q. Huo, D.J. Margolese, U. Ciesla, D.G. Demuth, P. Feng, T.E. Gier, P. Sieger, A. Firouzi, B.F. Schmelka, F. Schuth, G.D. Stucky, _Chem. Mater._, 1176, **6**, 1994.

83)   C.C. Landry, A.G. Eklund, S.T Jull,

84)   J. Brown, R. Richer, L. Mercier, *Micro. Meso. Mater.* 41, **37**, 2000.

85)   S. Kambe, K. Murakoshi, T. Kitamura, *Sol. Energ. Mat. Sol. C,* 427, **61**, 2000.

86)   M. Shibata, H. Hotta, T. Suzuki, *Chem. Lett.,* 1291, **12**, 1999.

87)   M. Ziolek, I. Sobczak, P. Decyk, *Stud. Surf. Sci. Catal.,* 691, **125**, 1999.

88)   D.A. Kron, B.T. Holland, R. Wipson, *Langmuir,* 8300, **15**, 1999.

89)   (a) S. Aronson, R.B. Roof, J. Belle, *J.Chem.Phys.,* 137, **27**, 1957. (b) M.J.
       Bannister, *J.Nucl. Mater.,* 174, **26**, 1968. (c) P.E. Blackburn, J. Weissbart, E.A.
       Gulbransen, *J. Phys. Chem.,* 902, **62**, 1958. (d) K.T. Harrison, C. Padgett, K.T.
       Scott, *J.Nucl. Mater.,* 121, **23**, 1967. (e) H.R. Hoekstra, A. Santoro, S. Siegel, *J.
       Inorg. Nucl. Chem.,* 166, **18**, 1961.

90)   R.J. McEachern, P. Taylor, *J.Nucl. Mater.,* 87, **254**, 1998.

91)   K.W. Bagnall, K.W. Bagnall Ed., Lanthanides and Actinides, Butterworths
       Baltimore, London, 1972.

92)   A. Elattar, T. Takeshita, W.E. Wallace, R.S. Craig, *Science,* 1093, **196**, 1977.

93)   R.L. Chin, A. Elattar, W.E. Wallace, D.M. Hercules, *J. Phys. Chem.,* 2895, **84**,
       1980.

94)   L.S. Schiappback, *Europhys. News,* 7, **14**, 1983.

95)   V. Corberan, A. Corma, G. Kremenic, *Ind. Eng. Chem. Prod. Res. Dev.,* 546, **23**,
       1984.

96)   V. Corberan, A. Corma, G. Kremenic, *Ind. Eng. Chem. Prod. Res. Dev.,* 62, **24**,
       1985.

97)   J.L.G. Fierro, E. Salazar, J.A. Legarreta, *Surf. Inter. Anal.,* 97, **7**, 1985.

98)   J.L Callahan, B. Gertisser, *U.S. Patent,* 3, 308, 151 (1967).

99)   J.L Callahan, B. Gertisser, *U.S. Patent,* 3, 198, 750 (1965).

100)   R. Delobel, H. Baussart, J.M. Leroy, J. Grimblot, L. Gengembre, *J. Chem. Soc.,
       Faraday Trans. 1,* 879, **79**, 1983.

101)   R.K. Graselli, D.D. Suresh, *J. Catal.,* 273, **23**, 1972

102)   J.C. Steenhof de Jong, C.H.E Guffens, H.S. van der Baan, *J. Catal.,* 401, **26**, 1972.

103)   J.C. Steenhof de Jong, C.H.E Guffens, H.S. van der Baan, *J. Catal.,* 127, **31**, 1973.

104)   H. Collette, V. Deremince-Mathieu, Z. Gabelica, J.B. Nagy, E.G. Derouane, J.J.
       Verbist, *J. Chem. Soc., Faraday Trans. 2,* 1263, **83**, 1987.

105)   T. Nicklin, K.H. Burgess, J. Clack, *Br Patent,* 1196411, 1967

106)   T. Nicklin, J. Clack, R. Whittaker, B.M. Holland, *Br Patent,* 1196412, 1967

107)   T. Nicklin, K.H. Burgess, *Br Patent,* 1196413, 1967

108)   R.G. Duranleu, W.C. Gates, *U.S. Patent,* 4341531, 1982.

109)   F. Nozaki, I. Inami, *Nippon Kagaku Kaishi,* 2202, 1972

110)   F. Nozaki, I. Inami, *Nippon Kagaku Kaishi,* 1855, 1974

111)   F. Nozaki, I. Inami, *Nippon Kagaku Kaishi,* 254, 1973

112)   G.J. Hutchings, C.S. Heneghan, I.D. Hudson, S.H. Taylor, *Nature,* 341, **384**, 1996.

113)   G.J. Hutchings, C.S. Heneghan, I.D. Hudson, S.H. Taylor, *ACS Symp. Ser. 638,* 58, 1996.

114)   S.H. Taylor, S.R. O'Leary, *Appl. Catal. B Environ.,* 137, **25**, 2000.

115)   C.S. Heneghan, G.J. Hutchings, S.R. O'Leary, S.H. Taylor, V.J. Boyd, I.D. Hudson, *Catal. Today,* 3, **54**, 1999.

116)   F. Nozaki, K. Ohki, *Bull. Chem. Soc. Jpn.,* 3473, **45**, 1972.

117)   F. Nozaki, M. Kobayashi, S. Yoshida, *Nippon Kagaku Kaishi,* 26, 1972.

118)   H. Collette, S. Maroie, J. Riga, J.J. Verbist, Z. Gabelica, J.B. Nagy, E.G. Derouane, *J. Catal.,* 326, **98**, 1986.

119)   F. Nozaki, F. Matsukawa, Y. Mano, Bull. *Chem. Soc. Jpn.,* 2674, **48**, 1975.

120)   S.D. Pollington, A.F. Lee, T.L. Overton, P.J. Sears, P.B. Wells, S.E Hawley, I.D. Hudson, D.F. Lee, V. Ruddick, *Chem. Commun.* 725, 1999.

121)   B.E. Bursten, A. Fang, *J.Am.Chem.Soc.* 6495, **105**, 1983.

122)   C. Boisson, J-C. Berthet, M. Lance, M. Nierlich, J. Vigner, M. Ephritikhine, *Chem.Comm.,* 543, 1995.

123)   M.Y. He, R.L. Burwell, T.J. Marks, *Organometallics,* 566, **2**, 1983.

124)   D. Baudry, A. Dormond, O. Lesprit, *Bull.Soc.Chim.Fr,* 183, **132**, 1995.

125)   M.S. Gill, V.S. Sagoria, Indian *J.Chem.,Sect A,Inorg., Bio-inorg., Phys., Theor., Anal. Chem,* 997, **34**, 1995.

126)   J. Parry, E. Carmona, S. Coles, M. Hursthouse, *J.Am.Chem.Soc.* 2649,**117**, 1995.

127)   D. Gudat, J.G. Verkade, *Organometallics,* 2772, **8**, 1989.

128)   C.C. Cummins, R.R. Schrock, W.M. Davis, *Organometallics,* 1452, **11**, 1992

129)   P. Scott, P.B. Hitchcock, *Polyhedron,* 1651, **13**, 1994.

130)   P. Roussel, P. B. Hitchcock, N.D. Tinker, P. Scott, *Inorg. Chem.,* 5716, **36**, 1997

131)   P.Scott, P.B. Hitchcock, *J.Chem.Soc.Dalton Trans.,* 603, 1995.

132) P. Roussel, N.W. Alcock, R.Boaretto, A.J. Kingsley, I.J. Munslow, C.J. Sanders, P. Scott, *Inorg. Chem.*, 3651, **38**, 1999.

133) P.Scott, P.B. Hitchcock, *J.Chem.Soc.Dalton Trans.,* 603, 1995.

134) P. Scott, A. Kingsley, University of Warwick, unpublished results

135) N.D. Tinker, P. Scott, P. Roussel, *UK Patent Application* 9623685.6.

136) P. Roussel, BNFL quarterly CASE report.

137) P. Roussel, P. Scott, *J. Am. Chem. Soc.,*1070, **120**, 1998.

138) R.L Burwell, T.J. Marks, *R.L. Augustine Ed., Catalysis of organic reactions, Marcel Dekker, New York,* 207, 1985.

139) M-Y. He, G. Xiong, P.J. Toscano, R.L Burwell, T.J. Marks, *J.Am.Chem.Soc.* 641, **107**, 1985

140) K.H. Dahmen, D. Hedden, R.L. Burwell, T.J. Marks, *Langmuir*, 1212, **4**, 1988.

141) M. Eisen, T.J. Marks, *J.Mol.Catal.,* 23, **86**, 1994.

142) J.S. Yu, B.C. Ankioniec, M.F. Nguyen, I.P. Rothwell, *J.Am.Chem.Soc.* 1927, **114**, 1992.

143) H. Bosch, F. Janssen, *Catal. Today,* 369, **2**, 1988.

144) G.L. Bauerle, S.C. Wu, K. Nobe, *Ind. Eng. Prod. Res. Dev.,* 117, **17**, 1978.

145) T. Shikada, K. Fujimoto, T. Kunugi, H. Tominaga, S. Kaneko, Y. Kubo, *Ind. Eng. Prod. Res. Dev.,* 91, **20**, 1981.

146) I.M. Pearson, H. Ryu, W.C. Wong, K. Nobe, *Ind. Eng. Prod. Res. Dev.,* 91, **20**, 1981.

147) H. Niyama, K. Murata, A. Ebitani, E. Echigoya, *J. Catal.* 194, **48**, 1977.

148) H. Niyama, K. Murata, E. Echigoya, *J. Catal.* 201, **48**, 1977.

149) a) H.E. Curry-Hyde, A. Baiker, *Ind. Eng.Chem.Res.,*1985, **29**, 1990; b) H.E. Curry-Hyde, M. Musch, A. Baiker, *Appl.Catal.,* 211, **65**, 1990; c) H.E. Curry-Hyde, M. Musch, M. Schrame-Marth, A. Wokaun, A. Baiker, *J.Catal.,* 397, **133**, 1992; d) M. Schrame-Marth, A. Wokaun, H.E. Curry-Hyde, A. Baiker, *J.Catal.,* 415, **133**, 1992; e) M. Schrame-Marth, A. Wokaun, H.E. Curry-Hyde, A. Baiker, *J.Catal.,* 431, **133**, 1992; f) M. Schrame-Marth, A. Wokaun, A. Baiker, *J.Catal.,* 306, **138**, 1992; g) J. Engweiler, J. Nickl, A. Baiker, K. Kohler, C.W. Schlapfer, A. von Zelewsky, *J.Catal.,* 141, **145**, 1994; h) J. Engweiler, J. Nickl, A. Baiker, K. Kohler, C.W. Schlapfer, A. von Zelewsky, *J.Catal.,* 201, **143**, 1993; i) U. Scharf, H. Schneider,

A. Baiker, A. Wokaun, *J.Catal.*, 464, **145**, 1994; j) U. Scharf, H. Schneider, A. Baiker, A. Wokaun, *J.Catal.*, 145, **147**, 1994.

150) B. Viswanathan, *Catal. Rev. Sci. Eng.*, 337, **34**, 1992.

151) R.T Rewick, H. Wise, *J. Catal.*, 301, **40**, 1975.

152) M.S. Tzou, K. Asakura, Y. Yamazaki, H. Kuroda, *Catal. Lett.*, 33, **11**, 1991.

153) R.F. van Slooten, B.E. Nieuwenhuys, *J. Catal.*, 429, **122**, 1990.

154) M. Shelef, J.T. Kummer, *Chem. Eng. Prog., Symp. Ser.*, 115, **67**, 1972.

155) S. Stegenga, N. Dekker, J. Bijsterbosch, F. Kapteijn, J. Moujin, G. Belot, R. Roche, *A. Crucq Ed., Catalysis and Automotive Pollution Control II, Stud. Surf. Sci. Catal.,Elsevier, Amsterdam*, 353, **71**, 1991.

156) F. Kapteijn, S. Stegenga, N. Dekker, J. Bijsterbosch, J. Moujin, *Catal. Today*, 273, **16**, 1993.

157) G. Moretti, C. Dossi, A. Fusi, S. Recchia, R. Psaro, *Appl. Catal. B, Environ.* 67, **20**, 1999.

158) R.Q. Long, R.T. Yang, *Cat. Lett.*, 91, **52**, 1998.

159) R.T. Yang, T.J. Pinnavaia, W.B. Li, W.Z. Zhang, *J. Catal.*,488, **172**, 1997.

Chapter 2. Experimental Methods

2.1 EXAFS

2.1.1 EXAFS Theory

When an X-ray of a particular wavelength impinges upon an atom it may be absorbed, which in turn causes the ejection of a core electron with an energy equal to the incident X-ray energy less its binding energy. This results in an outgoing photoelectron wave from the absorbing atom, which is modulated by backscattering from surrounding atoms. EXAFS, Extended X-ray Absorption Fine Structure, is the phenomenon of observed oscillations in the absorption coefficient as the outgoing and backscattered waves constructively, or destructively, interfere on the variation of the impinging X-ray beam wavelength. This occurs because the wavelength of the ejected photoelectron is dependent on its energy, and thus, the phase of the backscattered wave at the central atom will change with the energy of the incoming photon. $\mu(E)_x$ is the absorbance and may be represented as the following:

$$\mu(E)_x = [\mu(E)_s + \mu(E)_m + \mu(E)_0 + \mu(E)_{EXAFS}]_x \qquad \text{Eq. 2.1}$$

where $\mu(E)_s$ is the sloping spectrometer baseline, $\mu(E)_m$ is the absorption due to the matrix in which the absorbing atom is imbedded, $\mu(E)_0$ is the absorption that would be observed for a free atom, and $\mu(E)_{EXAFS}$ is the modulation in the absorption about $\mu(E)_0$. The EXAFS intensity, denoted $\chi(E)$, is isolated by subtraction of the background components and normalisation with respect to the free atom absorption:

$$\chi(E) = \mu(E)_{EXAFS}/\mu(E)_0 = [\mu'(E)/ \mu(E)_0] -1 \qquad \text{Eq. 2.2}$$
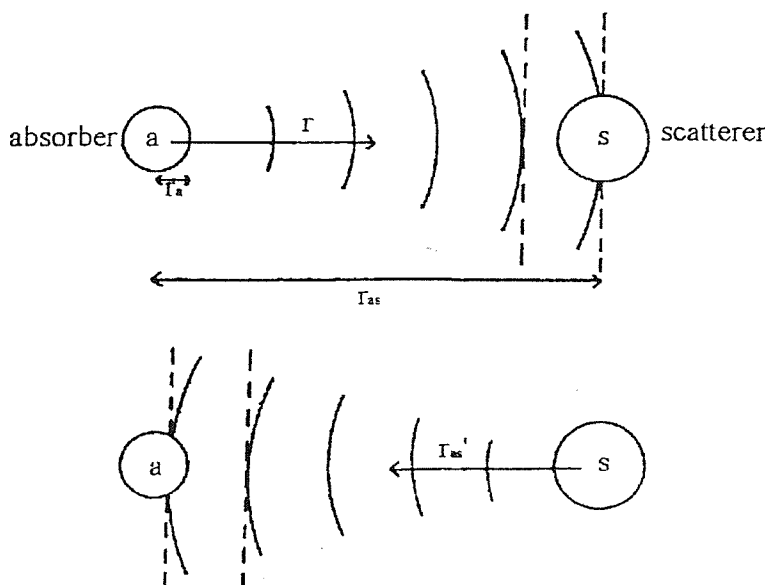

Figure 2.1 A schematic representation of the outgoing and backscattered photoelectron wave

X-ray absorption spectroscopy is a powerful technique in the determination of local structure in a variety of different materials. EXAFS has advantages over other techniques of being element specific, and independent of the physical state of the material under study. This allows the extraction of chemical information from materials that are traditionally difficult to characterise, such as systems in the gas phase, in solution, or present as amorphous solids. The disadvantages include the fact that the oscillation of absorption coefficient is an inherently weak effect, requiring high X-ray flux to obtain a reasonable signal to noise ratio,

2.1.2 Data Acquisition

Electromagnetic radiation is generated when any charged particle is accelerated through a magnetic field. At very high energies, relativistic phenomena result in increasing mass and shrunken space, and an effect of this is to fold the radiation output into a narrow cone emitted tangentially from the particle beam. The result is highly intense, and highly collimated, electromagnetic radiation over a broad wavelength range. This is known as synchrotron radiation. EXAFS spectra were recorded at the Synchrotron Radiation Source at the Daresbury Laboratory on experimental station 9.2. The intensity of the radiation is *ca.* 10^5 that of a conventional laboratory X-ray source, allowing realistically short acquisition times, and the study of more dilute samples. Station 9.2 employs a double crystal silicon (220) monochromator, which allows the required energy of the X-rays to be selected, and the desired energy range to be scanned. Two modes of data acquisition, transmission and fluorescence, may be used in recording EXAFS spectra.

2.1.2.1 Transmission Mode

Two ionisation chambers are used; I_0 is placed in front of the sample and I_t behind it in a linear arrangement. A mixture of noble gases with different X-ray absorption coefficients are used to fill these chambers such that I_0 absorbs ~20%, and I_t ~80%, of the radiation. As the wavelength of the X-rays used is varied over the region of interest, relative absorbance is measured as log I_t/I_0,

$$I_t = I_0 \exp(-\mu t) \qquad\qquad \text{Eq. 2.3}$$

where μ is the absorption coefficient, and t is the thickness of the sample. Also

$$\mu \text{ total}(E) = \mu_b(E) + \mu_{a'}(E) \qquad\qquad \text{Eq. 2.4}$$

where $\mu_b(E)$ is the absorption of the matrix, and $\mu_{a'}(E)$ is the absorption of the absorbing atom

In transmission mode solid samples are usually prepared by grinding the material to a fine homogeneous powder, and, if the sample is too concentrated with respect to the element of study, diluting with boron nitride to approximately 10wt% of the absorbing atom. This dilution may be required to prevent absorbance from being too high; ideally I_t should be such that $\Delta\mu \approx 1$, whilst maintaining that the contribution of noise to the signal in this rear ion chamber is kept to a minimum in order to obtain a good spectrum

2.1.2.2 Fluorescence Mode

Data is collected in fluorescence mode for one of two reasons. Firstly, when the sample is too absorbing, and cannot be diluted without destroying its integrity. Secondly, when there is a low concentration of absorbing atom in the sample, and $\mu_b(E) > \mu_{a'}(E)$; to remove the contribution from $\mu_b(E)$. The fluorescence intensity is a direct measure of the absorption probability for thin or dilute samples. Thus, an excitation spectrum of a ratio of I_f/I_0 versus photon energy is equivalent to an absorption spectrum of μ versus photon energy. In order to maximise the fluorescence yield, the sample is placed at 45° to the X-ray beam, and the detector is positioned perpendicular to the beam. A 13-element solid state germanium detector was used to measure total photon yield within a certain energy range. This range is selected to coincide with the sample fluorescence energy, but to exclude X-ray scatter, and is designed to maximise signal to noise ratio.

2.1.3 Data Analysis

Analysis of the EXAFS data is carried out in three stages. The first stage involves the calibration of the absorption spectra, and this is performed in a software program called EXCALIB[1], which is part of a suite of software available to Daresbury Laboratory users. The experimental data is recorded in the form of an ion chamber reading versus monochromator angle, and this must be converted to a spectrum of absorption against photon energy. The data from several different scans of the same sample may be averaged at this stage to enhance signal to noise ratio. Once this has been achieved, the background subtraction to separate the EXAFS from the remainder of the absorption spectrum is carried out in a PC program named PAXAS[2]. The program EXCURV98[3] is then used to fit a theoretical model to the experimental data.

PAXAS[2]

The programme removes the absorption due to the spectrometer by means of a subtraction of the pre-edge background, which is defined by three points. The first two points are found at the beginning and end of the pre-edge region, whilst the third point is chosen at the end of the post-edge region. This third point is usually weighted, and its Y-coordinate is adjusted to achieve an approximately horizontal background subtracted absorption (BSA) once the 2nd or 3rd order polynomial based on these three points has been subtracted from the absorption spectrum. The absorption due to other elements, such as the sample matrix, is then removed by means of a post-edge background subtraction; typically involving coupled polynomials of order 6,7 or 8. Any systematic glitches due to monochromator flaws may be removed at this point, to avoid such features dominating the EXAFS. A poor post-edge background subtraction results in the distortion of the amplitude of the EXAFS oscillations, which leads to unwanted features at R values below 1Å in the Fourier transform. An important function of the background subtraction procedure is thus to minimise these peaks or features at low R values. In order to achieve this, a window limit in R space in the Fourier transform is selected to include only real coordination shells. The EXAFS contribution from these shells is calculated by a back transform process, and this may then be compared to the original EXAFS to ascertain which peaks in the Fourier transform are responsible for the shape of the EXAFS. The variables in the polynomial expression fitted to the post-edge region are then iterated to try and minimise the difference between the experimental and theoretical EXAFS. Once this has been achieved to a satisfactory level, the EXAFS spectrum is then ready for the next stage in analysis. Figure 2.2 illustrates the procedures performed in PAXAS
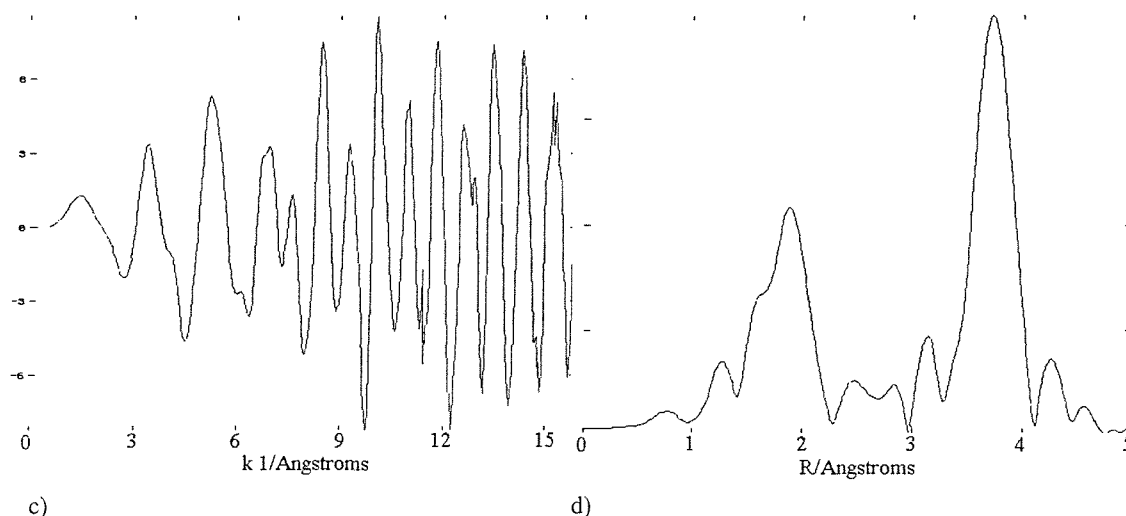

a)   b)
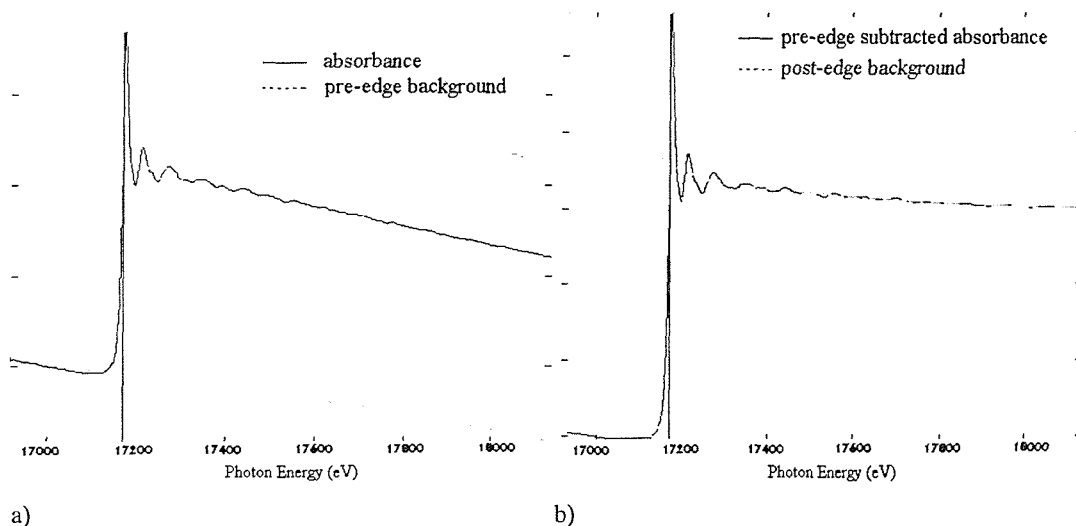
Figure 2.2 U_{LIII} edge EXAFS of UO_2, diluted to 10wt% U in a boron nitride matrix a)pre-edge background subtraction, b)post-edge background subtraction, c)k^3-weighted EXAFS, d)radial distribution curve from Fourier transform of EXAFS

EXCURV98[3]

The curve fitting programme EXCURVE version 98 uses curved wave theory, and computationally fast algorithms to theoretically model the oscillations in the EXAFS, and to determine structural information. The phaseshifts associated with the photoelectron wave passing through the potential of surrounding atoms are calculated by *ab initio* methods, using X_α potentials and muffin tin radii potentials in the calculations. The nearest neighbour atom type is chosen for this calculation, to resemble the local chemical environment of the central atom. In EXCURV98 a theoretical spectrum is generated using a number of structure dependent parameters. These parameters are then refined using least squares iteration to optimise the fit between the theoretical, and the experimental spectrum.

structural parameters :

NS   – The number of shells for which the model is calculated

N_n – The number of atoms in shell n

T_n – The type of atom in shell n

A_n – The Debye-Waller factor for shell n, given as $2\sigma^2$, where σ is the mean square variation in interatomic distances

E_f - The difference between the calculated Fermi level energy and the known values for the element, typically –15 to 5eV

AFAC-The energy independent amplitude factor which accounts for the reduction in amplitude to multiple excitations occurring at the central atom. It is different for each absorbing element, and is obtained from the analysis of model compounds

VPI - The constant imaginary potential which describes the lifetime of the core hole, and accounts for inelastic scattering due to the neighbouring environment

L_{max} –The maximum angular momentum used in theory calculations

E_{min} -The minimum energy used to calculate the theoretical spectrum

E_{max} -The maximum energy used to calculate the theoretical spectrum

The goodness of fit between the experimental and theoretical curve is measured in two ways:

1) When refining a set of parameters EXCURVE seeks a minimum in the function known as the fit index, FI.[4] For k^3 weighted data FI is described as:

$$FI(EXAFS) = \Sigma_I [(k_i)^3 (\chi_i^T - \chi_i^E)^2] \qquad \text{Eq. 2.5}$$

The fit index is thereby calculated as the sum of the square of the differences between the theoretical and experimental data points. A good fit has an FI value of below 5 x 10^{-4}, although FIs of less than 8 x 10^{-4} are acceptable.

2) The R-factor is calculated as the total sum of all the errors between all the data points, and gives the result as a percentage against the experimental curve.[5] R is described as:

$$R(EXAFS) = \Sigma_I [|\chi_i^E(k) - \chi_i^T(k)|/\sigma_i] \times 100\% \qquad \text{Eq. 2.6}$$

The R-factor should not normally exceed 30%, although for dilute samples, where signal to noise is high, a value of approximately 45% is acceptable. Debye-Waller factors are acceptable if they lie between 0.003 and 0.03, though an estimate of best values is obtained from a spectrum of a model compound. Parameters that are highly correlated, such as Debye-Waller factors and co-ordination numbers, should not be refined simultaneously. EXAFS analysis can provide information on first co-ordination sphere distances, with an accuracy of ±0.01Å, and co-ordination numbers, to approximately ±10%.[4,5]

2.2 Powder X-ray Diffraction

When a metal is bombarded with electrons of a sufficiently high energy, the generated radiation is a continuous range of wavelengths called Bremstrahlung, with a few high intensity, sharp peaks superimposed on this continuum. These peaks arise from the

collision of incident electrons with core shell electrons of the metal atoms. The collision may result in the expulsion of this inner shell electron, and an electron of higher energy drops into the vacancy, emitting the excess energy as an X-ray photon. If one of these peaks may be selected in isolation, then the result is a monochromatic X-ray beam of a wavelength that is of the same order of magnitude as the separation of lattice planes within a material. These X-rays may then be diffracted when passing through a crystal:
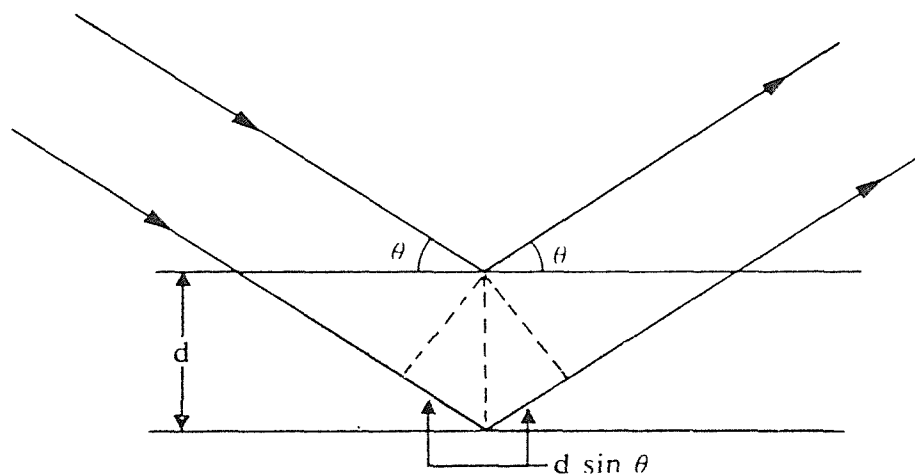

figure 2.3 The dependence of X-ray path length difference on incident angle and d-spacing

The path length difference of the two X-rays shown above is given as $2d\sin\theta$, where d is the interplanar spacing, and θ is the incident angle. The wavelength of the X-ray for $K\alpha$ radiation from a copper source is 1.54Å, λ. For many incident angles the path length difference is not an integral number of wavelengths, and the result is destructive interference. However, when the path length difference is an integral number of wavelengths, i.e. $n\lambda$, then the reflected waves are in phase, and interfere constructively. This applies when the Bragg law is satisfied:

$$n\lambda = 2d\sin\theta \qquad\qquad \text{Eq. 2.7}$$

When the sample is a powder, at least some of the crystallites will be oriented so as to satisfy the Bragg condition for each set of planes. The crystallites with this incident angle will lie at all possible orientations to the incoming X-ray beam, so the diffracted beams lie on a cone at an angle 2θ to the direction of this incident beam. Using the Bragg equation, the 2θ value of a particular reflection may be related to a d-spacing for the associated lattice plane. If the lattice plane indices from which this reflection originates are known, or

more often deduced, then information regarding the unit cell of the diffracting material can be obtained.

Powder X-ray diffraction is a technique of use in the characterisation of any material with inherent long range order. It is routinely used for the identification of unknown powders, with the use of a diffraction peak database. It is also widely used for ascertaining the purity of a compound with respect to any other diffracting phase. The room temperature powder X-ray diffraction patterns were recorded on a Siemens θ-2θ D5000 diffractometer fitted with a Cu Kα X-ray source. The diffracted beam is detected with a standard scintillation counter. The *in situ* calcination experiments were performed using a Philips Xpert MPD diffractometer with Cu Kα radiation, in conjunction with an Anton Paar XRK cell.

2.3 Isothermal Nitrogen Adsorption Analysis

The adsorption of nitrogen on an oxide surface, which is the subject of interest here, may be considered to occur in two stages. The initial stage, at low pressures of adsorbate, is the formation of a monolayer on the surface. If this overlayer may act as a substrate for further adsorption, then the formation of multilayers at higher pressures will occur. The most widely used isotherm that is applicable to these phenomena is known as the BET isotherm, constructed by Brunauer, Emmett and Teller in 1938[6]:

$$\frac{V}{V_{mon}} = \frac{cz}{(1-z)\{1-(1-c)z\}} \qquad \text{where } z = \frac{p}{p^*} \qquad \text{Eq. 2.8}$$

In this expression, p^* is the vapour pressure above a layer of adsorbate that is more than one molecule thick, and which resembles a pure bulk liquid. V_{mon} is the volume corresponding to monolayer coverage, and c is a constant which is large when the enthalpy of desorption, $\Delta_{des}H°$, from a monolayer is large compared with the enthalpy of vaporisation, $\Delta_{vap}H°$ of the liquid adsorbate:

$$c \approx e^{(\Delta_{des}H°-\Delta_{vap}H°)/RT} \qquad \text{Eq. 2.9}$$

when the coefficient c is large ($c \gg 1$), the BET isotherm takes on the simpler form

$$\frac{V}{V_{mon}} = \frac{1}{1-z} \qquad \text{Eq. 2.10}$$

This expression is true for unreactive gases on polar surfaces, such as nitrogen on a silica surface, for which $c \approx 10^2$ because $\Delta_{des}H°$ is then significantly greater than $\Delta_{vap}H°$. At sub-monolayer relative pressures this expression can be used to find V_{mon}, as the total adsorbed

volume and relative pressure are measured. The volume can then be related to the number of moles of gas adsorbed, and if the area that each adsorbate molecule occupies on the surface can be determined, then this can be used to obtain a value for the surface area in m^2. If the mass of the sample is known, then the specific surface area in m^2g^{-1} can be found. The BET isotherm fits experimental observation well over a restricted pressure range, but it should be noted that it tends to underestimate the extent of adsorption at low pressures, and overestimate at high pressures.

The surface area of a heterogeneous catalyst is an important property of the material to be able to measure, as it is likely to have ramifications in terms of activity per mass unit. In porous materials it is also desirable to gain an estimate of pore size distribution, and one way in which this may be successfully achieved is by the manipulation of isothermal adsorption/desorption data. Several methods of manipulation have been reported in the literature[7,8,9,10,11], but the strategy chosen for this work was proposed by Dollimore and Heal[12]. A brief description of this is given below.

If the amount of adsorbed material, at any point on the isotherm, is converted to liquid volume, and the amount lost in a desorption step is ΔV, then ΔV is the sum of capillary desorption ΔV_c, and multilayer desorption ΔV_m.

$$\Delta V = \Delta V_m + \Delta V_c \qquad\qquad\qquad \text{Eq. 2.11}$$

The number of molecules in the multilayer varies over the surface, but for any relative pressure p/p_0, the average thickness t may be determined, and also the decrease in multilayer thickness Δt for the desorption step. If it is assumed that ΔV_m may be calculated, then ΔV_c for the desorption step is obtained. This volume, ΔV_c, is the capillary liquid lost between the beginning and end of a step between two relative pressures p_1/p_0 and p_2/p_0. When capillary liquid is lost, multilayers are left on the pore walls, and thus the radius of the capillary condensate is less than the actual radius of the pores by the amount t. The capillary condensate radii, r_{k1} and r_{k2} are related to p_1/p_0 and p_2/p_0 by the Kelvin equation:

$$\ln \frac{p}{p_0} = \frac{-2V\gamma}{r_K RT} \cdot \cos\theta \qquad\qquad\qquad \text{Eq. 2.12}$$

where γ is the surface tension of the adsorbate

V is the molar volume of the adsorbate

θ is the angle of contact of adsorbate and adsorbent (taken to be 0°)

Note that a correction must be made to allow for the curvature of the pore walls, as the Kelvin equation assumes a flat surface, and overestimates the extent of multilayer desorption at a given relative pressure. The details will not be discussed here, but by developing these principles it is possible to obtain a value for the change in pore volume, ΔV_p for each radius, or, rather for each range of radii from the beginning to the end of each desorption step, Δr. A plot of $\Delta V_p/\Delta r$ versus pore radius gives a pore size distribution.

Nitrogen adsorption measurements were collected at 77K, using a Micrometrics GEMINI III 2375 surface area analyser. Typically, 30mg of previously dried sample was used for the analysis.

2.4 Temperature Programmed Plug Flow Microreactor Studies

The large number of experiments performed using this equipment necessitates a brief description of its specification, characteristics, and capabilities. The microreactor is specifically designed to be suitable for the study of *in situ* reactions by the novel characterisation technique, Energy Dispersive EXAFS[13]. This requires that the material to be studied be held in a configuration that allows the transmission of X-rays, which is achieved with the use of a quartz tube as a sample holder. This in turn demands a novel approach to the efficient introduction of gas into the sample bed. The remainder of the apparatus is similar to that which may be found in many conventional microreactors. A schematic diagram of the basic configuration is given below:
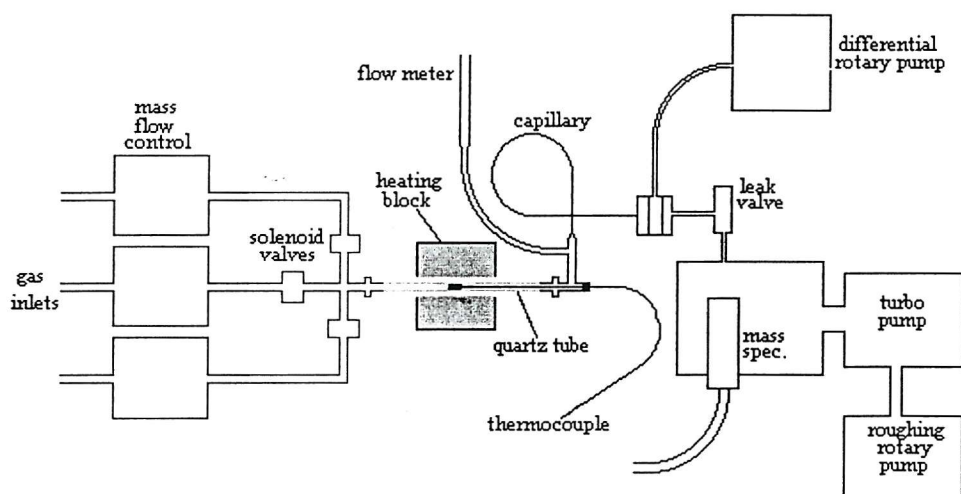

Figure 2.4 A schematic diagram of the plug flow microreactor system

The passage of gas through the catalyst bed is indicated above. The current arrangement allows up to three different gases, or gas mixtures, to be used at any one time. The flow rate of each is set individually, with the use of UNIT UFC-1100GI mass flow controllers. Solenoid valves are used to select or mix gases prior to entering the catalyst bed.

The catalyst charge, typically ~20mg, is loaded into the centre of a 200mm long quartz tube with an internal diameter of 3mm. The powdered sample is held in place with two plugs of quartz wool, to give a catalyst bed length of 8-10mm. On each end of the quartz tube is glued a $\frac{1}{8}$" push on fitting. This allows the tube to be attached to the gas line without the need for screw threads, which would result in frequent breakage of the brittle quartz. One end is attached to the outlet from the solenoid valves, and through the other a type K thermocouple is simultaneously introduced to the centre of the catalyst bed as the seal with the second push on fitting is made.

The vast majority of the gas exiting from the reactor bed passes out through the flow meter, and the total gas flow may be determined in this way. However, a proportion of the gas effluent may be allowed to enter the uhv chamber via the stainless steel capillary and the leak valve, where its composition can be analysed with the use of the mass spectrometer.

All couplings and tubing throughout the system are of minimum volume. For example, $\frac{1}{16}$"fittings are used wherever possible; the stainless steel capillary is of 0.25mm internal diameter and is coupled to the reactor bed exit via a zero volume t-piece. This is done in order to minimise the dead volume of the microreactor, and thus reduce the extent to which a short pulse of gas entering the catalyst bed will lose time resolution as it travels through the system and into the mass spectrometer analyser. The capillary is differentially pumped, to prevent poor conductance through it increasing the response time of the mass spectrometer. The result is that a two-second pulse, at a total gas flow of 20ml/min, has a peak width at half peak height of approximately 20 seconds at the mass spectrometer.

The mass spectrometer used is a Fisons Quartz 200AMU VG quadrupole instrument. There are two different methods available for the detection of ions. The simplest of the detectors is the Faraday plate. Ions exit the mass analyser, pass through a collimating slit, and strike a metallic plate. The current caused by this ionic bombardment is converted to a potential, amplified electronically, and transmitted to the readout device. The Faraday plate has the advantages of being very simple and dependable. The second

detector available is an electron multiplier. This is based on a dynodic strip, where a potential difference is maintained across the strip by a regulated power supply. The potential drop across the strip is typically about 2kV. Ions from the analyser bombard the cathode at one end of the strip, inducing the emission of electrons. A magnetic field is used to direct the emitted electrons in a cycloidal path back towards the dynodic strip. Upon striking the strip, the current is further amplified by the emission of several electrons for each impinging electron. The process is repeated many times along the length of the strip toward the anode, where the resulting current flow is monitored on an external circuit. The electron multiplier is the more sensitive of the two detectors, and has routinely been the detector of choice throughout this work.

The heating system for this microreactor is a simple arrangement of twelve ¼",75W cartridge heaters inserted into a brass block. The brass block is actually in two pieces that are screwed together, with a groove cut in each half to accommodate the quartz tube. A ceramic insulating hood is then placed over the block to reduce temperature fluctuation on heating, and allow higher temperatures to be achieved. An Eurotherm 902 series temperature controller is used to control the power output to these heaters, in order to achieve the desired heating rate. A maximum catalyst bed temperature of approximately 700°C is obtainable.

2.5 Thermogravimetric Analysis and Differential Thermal Analysis

Any process that involves a change in mass of a solid may be studied by thermogravimetric analysis,(TGA). While performing a thermogravimetric study, the mass of the sample is measured as a function of temperature. The plot of the mass, or the percentage of the initial mass, as a function of temperature is a thermal curve. An example of this is given below:
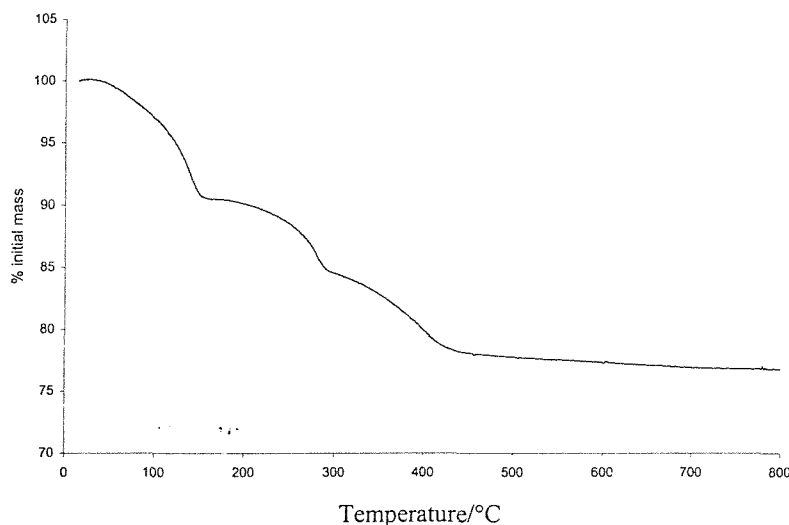

Figure 2.5 An example of a thermal curve obtained by thermogravimetric analysis

The change in mass can be used for quantitative analysis, and the temperature at which the change takes place is useful for obtaining qualitative information on the processes involved. The apparatus that simultaneously heats the sample and monitors its mass is known as a thermobalance. The sample is placed in a small combustion boat on one pan of the balance, with counterweights on the second pan. An insulated wire wound furnace is used to heat the sample at the desired rate.

Differential Thermal Analysis, (DTA), is the analytical technique in which the temperature differential between the sample and an unreactive reference material is monitored while the two substances are subjected to identical heating conditions. In this instance, the initial plot is of the temperature difference between sample and reference versus temperature. Unlike TGA, DTA does not require a change in mass of the sample in order to obtain meaningful information. DTA can be used to study any event in which heat is absorbed or evolved. Thermal curves obtained with DTA show peaks corresponding to processes where the temperature of the sample is increased or decreased relative to that of the reference material. Upward deflections designate an exothermic process, and

downward deflections indicate an endothermic event. In practice, the same apparatus is often used for both TGA and DTA, and they are, in this work, recorded simultaneously. The instrument is a Polymer Laboratories Simultaneous Thermal Analyser STA 1500, and the reference material used for DTA measurements was alumina. The sample was heated to 900°C at a linear ramp rate of 20Kmin^{-1}. This heating rate was chosen as a compromise, in order to maximise the resolution of both techniques. A slower ramp rate would afford greater TGA resolution, but features in the DTA trace would tend to be smeared out, as the sample temperature has more time to equilibrate.

2.6 Diffuse Reflectance Infrared Spectroscopy (DRIFTS)

Obtaining the infrared spectrum of a solid by transmission of the beam through the sample requires that the material is diluted and pressed into a disc, or ground with a hydrocarbon oil into a mull and then held between two non-absorbing discs. However, this type of pre-treatment is not always acceptable as the material is not recoverable, and it may affect the nature of the sample being characterised. Diffuse Reflectance Infrared Spectroscopy, (DRIFTS), is an experimental technique that allows spectra of solid materials to be obtained without the need for the type of sample preparation described above. A schematic diagram depicting the path of the incident beam is given below:
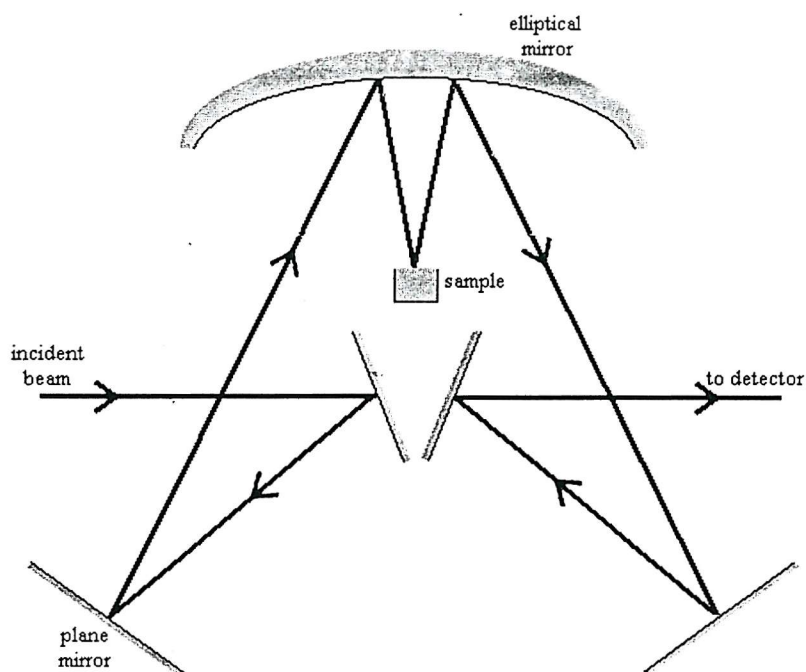

Figure 2.6 A schematic diagram of the mirror arrangement used in the DRIFTS cell

The solid sample is loaded as a powder into a stainless steel crucible, and the arrangement of mirrors is adjusted to focus the incident beam onto the sample, and the reflected beam into the detector. The incident beam interacts with the particles in one of several ways. Firstly, the radiation can undergo mirror-like reflection from the top surface of the particles. This surface reflection is true specular reflection and is a function of the refractive index and the absorptivity of the sample. Secondly, the beam can undergo multiple reflections off many particle surfaces, still without penetrating the particles. After these multiple reflections, the resulting beam emerges from the sample at random angles relative to the incident beam. This reflection mode, called diffuse specular reflectance, is once again a function of the refractive index of the sample. The third mode of interaction, true diffuse reflectance, results from the penetration of the incident radiation into one or more sample particles and subsequent scatter from the sample matrix. The resulting radiation may emerge at any angle relative to the incident radiation and since it has travelled through the particles it now contains information about the absorption characteristics of the material. It is this interaction that provides the infrared spectrum of the sample. However, this diffuse reflection is optically indistinguishable from diffuse specular reflection, and it is worth noting that the mixing of these different reflection types can lead to distortions in the final data. This is not a significant problem for many simple experiments, and will not be dealt with in detail here. Spectra were recorded using a Perkin Elmer 1710 FTIR spectrometer.

2.7 Electron Microscopy

In an electron microscope, a narrow beam of high energy electrons is directed at a specimen. Images may be formed either by electrons passing through a thin sample (transmission electron microscopy, TEM), or by secondary emissions from the surface of a thick sample (scanning electron microscopy, SEM). The obtainable resolution, which is the closest spacing of two points that can be distinguished through the microscope, is proportional to the wavelength of the light impinging on the sample. A beam of electrons at 100keV has a wavelength of 0.0037nm, compared to ~400nm for a conventional light microscope. The table overleaf shows a comparison between light and electron microscopy.

Type of microscopy	Resolution (nm)	Magnification	Depth of Field (μm)
Light (λ = 400nm)	150	10^3	<1
Electron (for a 100keV electron beam)	0.2	10^6	10

Table 2.1 A Comparison of the capabilities of electron microscopy vs. light microscopy

Transmission electron microscopy provides microstructural and ultrastructural information. The electron beam used in TEM is typically generated at 100-200keV, affording a resolution of 0.2nm and a magnification of 1×10^6. On passing through a specimen, the primary electrons may be either be transmitted without being deflected, elastically scattered (e.g. diffracted), or inelastically scattered. The image formed in brightfield mode using the TEM is the result of variable transmittance across the sample area. Parts of the sample where the electron beam has passed through unperturbed will appear white. The image is darker where the inelastic scattering increases, which occurs when the mean atomic number and thickness of the sample increases (mass-thickness contrast). A darkfield image may be produced by the selection of a diffracted beam, and is achieved by moving the detector off the axis of the impinging electron beam. The image produced is magnified by electromagnetic projector lenses and viewed on a scintillation screen. The specimen must, however, be very thin (<100nm)

The collection of TEM images was carried out on a JEOL FX 2000 transmission electron microscope. The samples were prepared as follows. 10^{-4}g of sample was crushed with a pestle and mortar for ca. 5-10mins. Distilled water is then added slowly into the mortar and the sample ground for ca. 5mins, until a fine suspension of the material is observed. The fine suspension is then transferred to a specimen container, which is then placed in an ultrasonic bath and left for ca. 5mins. A small drop of the fine suspension is dropped onto a copper disc with a fine carbon grid. The copper discs are then placed in a vacuum desiccator for a minimum of 24h. All TEM images were obtained in brightfield mode.

SEM images were obtained with the use of a JEOL JSM 6400 analytical scanning electron microscope. Powdered samples were coated with a thin layer of carbon by a spattering process prior to introduction into the microscope. This was done to avoid the accumulation of charge on the sample, which would cause distortion in the viewed image.

2.8 Magic Angle Spinning Nuclear Magnetic Resonance (MAS NMR)

The collection of NMR spectra of species in solution is a routine characterisation technique for many chemists. The extent to which a nucleus is interacts with an applied magnetic field, termed B_0, will depend on its relative orientation. In solution, molecules tumble very rapidly with respect to the NMR timescale, such that any orientation dependent parameters of these nuclei are averaged to their isotropic values. The intrinsic anisotropic nature of solids, where molecular motion is very restricted, results in an added level of complexity in their spectra. The very broad lines that are often evident in the NMR spectra of powders are derived from three orientation dependent interactions.

- Dipolar coupling:- This is the result of dipole-dipole interactions between the nuclei in the solid. Consider two nuclei a distance r apart, where, in the strong magnetic field B_0 of an NMR spectrometer, both nuclear spins are quantized along the field direction (the z axis). The resonance frequency of one nucleus is determined by the net field in the z direction, i.e. $B_0 \mp b$, where b is the z component of the dipolar field of the other nucleus. This doublet splitting is dependent on the distance between nuclei, r, and the angle between this internuclear vector and the applied magnetic field, θ. In a single crystal this angle is fixed for any identical nuclear pair, but it in a powder the situation is more complex. Each pair of nuclei has a unique value of θ, but different molecules have different values. The result of a random distribution of orientations is very broad spectral lines.

- Chemical shift anisotropy :- This is caused by an induced magnetic dipole in one part of a molecule shielding, or deshielding a nearby nucleus from the applied magnetic field. In solution, the rapid tumbling of molecules results in a single averaged chemical shift. This effect has the same distance and angle dependence as that of dipolar coupling, and again causes line broadening in anisotropic systems.

- Quadrupolar interactions :- This occurs in nuclei with a nuclear spin quantum number (I) greater than ½. Nuclei with $I > ½$ possess a nuclear electric quadrupole moment, which interacts with an electric field gradient at the nucleus. This electric field gradient

is dependent on the orientation of the molecule with respect to the applied magnetic field, and this leads to line broadening in the same way as above.

All three of the above phenomena contain a $(3\cos^2\theta - 1)$, angular dependence where θ is the angle between the internuclear vector and the applied field. If θ is set to an angle of $54°44`$, β, then the expression $(3\cos^2\theta - 1)$ reduces to zero and these broadening effects may be removed, producing the equivalent of a solution NMR spectra. The angle is known as the magic angle, and this particular technique is known as magic angle spinning (MAS). This procedure narrows linewidths considerably for a number of nuclei.
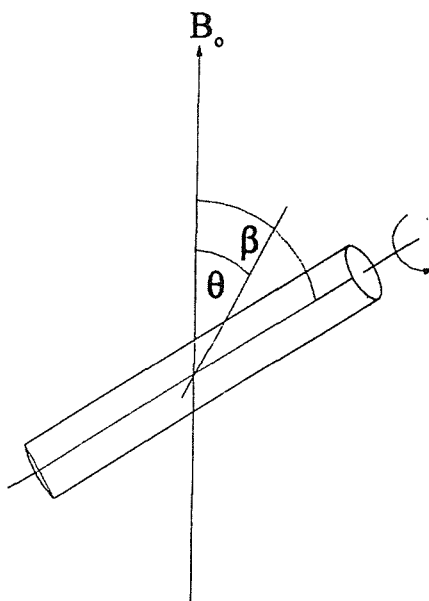
Figure 2.4 The magic angle, β, at $54°44'$ to the applied magnetic field, B_0

A technique known as cross polarisation (CP) has also been used, where the magnetisation of one nucleus, in this case ^{29}Si, is enhanced from the magnetisation of nearby proton nuclei. The effect is actually twofold, as not only does the pulse sequence used enhance the signal to noise ratio of the ^{29}Si NMR spectrum for each acquisition, but the silicon nuclei adjacent to protons are afforded a faster relaxation process, so the wait time between pulse sequences may be reduced. On a solid oxide sample, where the majority of protons are on the external surface of the particles, this actually has the effect of making CP MAS a surface sensitive technique. ^{29}Si MAS NMR was performed on a Bruker AM300 NMR spectrometer. The samples were finely ground and loaded into ZrO_2 or SiN rotors and spun at 4.5 kHz. The ^{29}Si chemical shifts are reported relative to tetramethyl silane $Si(CH_3)_4$. The spectrometer frequency for ^{29}Si MAS NMR is 59.628MHz.

2.9 References

1) *EXCALIB*, SERC Daresbury Laboratory Program, 1990.

2) N.Binsted, *PAXAS, Program for the Analysis of X-ray Absorption Spectra,* University of Southampton, 1988

3) N.Binsted, S.Gurman, J.W.Campbell, *EXCURV98,* SERC Daresbury Laboratory Program, 1998.

4) R.W. Joyner, K.J. Martin, P. Meeham, *J. Phys. C:Solid State Phys.,* 4005, **20**, 1987.

5) N. Binsted, S.L. Cook, J. Evans, G.N. Greaves, R.J. Price, *J. Am. Chem. Soc.,*3669, **109**, 1987.

6) S.Brunauer, P.H.Emmett, E.J. Teller, *J.Am.Chem.Soc.* 309, **60**, 1938

7) C.Pierce, *J.Phys.Chem.,* 149, **57**, 1953.

8) E.P.Barrett, L.G.Joyner, P.P.Halenda, *J.Am.Chem.Soc.* 373, **73**, 1951

9) M.M.Dubinin, *Zh.Fiz.Khim.,* 1652, **30**, 1956.

10) C.G.Shull, *J.Am.Chem.Soc.* 1405, **70**, 1948

11) M.Kruk, M.Jaroniec, *Langmuir,* 6267, **13**, 1997.

12) D.Dollimore, G.R.Heal, *J.Appl.Chem.,*109, 1964

13) S.Fiddy, M.A.Newton, A.J.Dent, G.Salvini, J.M.Corker, S.Turin T.Campbell, J.Evans, *Chem. Comm.* 851, 1999.

Chapter 3. Synthesis and Characterisation of Mesoporous Silica

3.1 Synthesis of Mesoporous Silica

The general synthetic route used to form a mesoporous silica was as follows. One mass equivalent of the chosen surfactant was dissolved in two mass equivalents of tetramethylorthosilicate, $((CH_3O)_4Si)$. To this was added one mass equivalent of dilute hydrochloric acid, pH1.3. The methanol that was produced by the hydrolysis of the tetramethylorthosilicate was removed *in vacuo* at 30°C over a period of thirty minutes. The resultant gel was then left to condense to form a clear, colourless, glassy solid over a period of 1-2 days. The exact time taken for this to occur, and the temperature at which the condensation was allowed to proceed, varied with the surfactant chosen. The glass formed was then heated to 470°C under a constant 20ml/min flow of nitrogen, and held at this temperature for a period of 4h. Without cooling, the gas flow was changed to 20ml/min of oxygen, and the sample was held at the same temperature for a further 8h. This is the synthetic method first proposed by Attard *et al.*[1] A schematic diagram of this route is shown below:

i) removal of hydrolysis and condensation of silica

ii) removal of surfactant by calcination in N_2/O_2

H_1 surfactant phase in dil. HCl + $(CH_3O)_4Si$
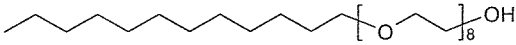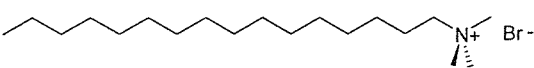
H_1 mesoporous silica
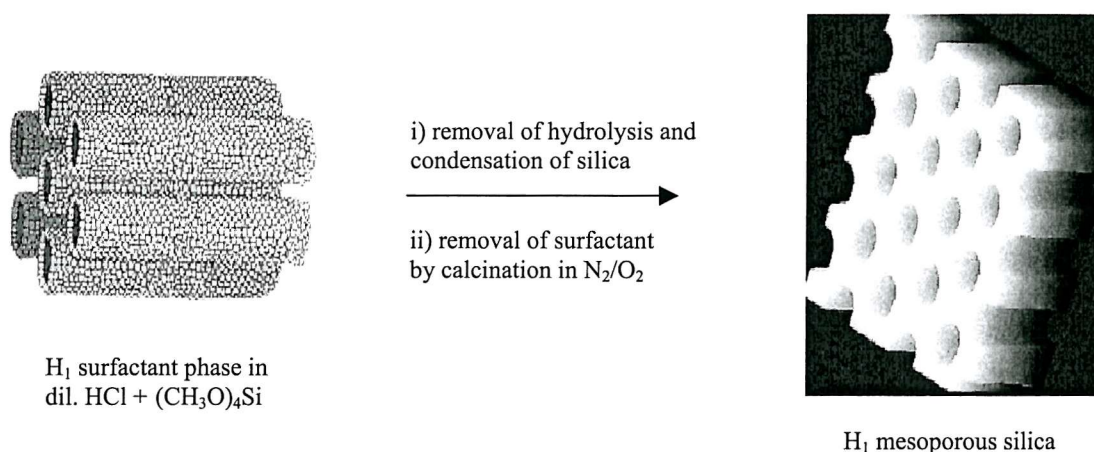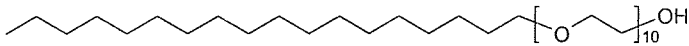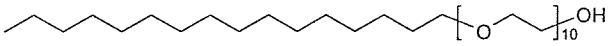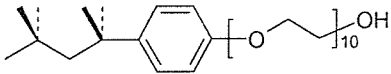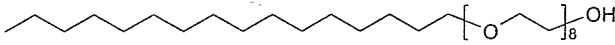
Figure 3.1 Schematic diagram of mesoporous silica synthesis procedure

A brief discussion of the strategy behind this synthetic route, and of the considerations to be taken, is appropriate. The basic principle is that the silica precursor, tetramethylorthosilicate, is hydrolysed in the presence of the surfactant. The hydrolysis product, in this case methanol, must be removed, as its presence in the reaction mixture will prevent the formation of the surfactant liquid crystal phase. Once this is achieved, then the polycondensation of the hydrolysed silicate species in solution proceeds around the surfactant micelles, yielding an inorganic cast of the organic phase. The pH at which the hydrolysis of the silica precursor is allowed to occur is carefully chosen. At a pH of 1.3,

the hydrolysis reaction is very fast, and is complete within approximately ten minutes. The polycondensation process to form the solid silica phase occurs over a period of several hours, so these two reactions are essentially decoupled. This is important, because if the hydrolysis is not complete as the condensation proceeds, then the methanol produced will disrupt the liquid crystal phase and the silica formed will not have the desired long range order. The integrity of the liquid crystal phase on removal of the methanol may be verified by observation of the gel under a light microscope. The microscope is fitted with a polariser and analyser, and one is rotated with respect to the other. A liquid crystal phase has a capacity to rotate the plane of polarised light that an isotropic phase does not have. Using this method it is also possible to identify liquid crystal mesophase present.[2] It is also possible to observe that once condensation is complete, the monoliths produced are birefringent materials. This birefringence is not removed on calcination.

The choice of surfactant is influenced by a number of factors. Most importantly, the chosen surfactant must form the desired liquid crystal phase at an attainable temperature and percentage composition. All the surfactants used form a hexagonal liquid crystal phase at 50 wt% in water.[3,4,5] The temperature chosen for the condensation reaction, at which this phase is stable for each surfactant, as well as the name and structure, is given below:

Brij76		40°C
Brij56		40°C
Triton X100		20°C
$C_{16}EO_8$		20°C
$C_{12}EO_8$		20°C
cetyltrimethylammonium bromide (CTMABr)		20°C

Brij76, Brij56, Triton X100 and CTMABr were purchased from Aldrich. $C_{12}EO_8$, $C_{16}EO_8$, and the tetramethylorthosilicate were purchased from Fluka.

The nature of the templating process implies that the physical size of the surfactant chosen will have a direct effect on the dimensions of the pores within the final calcined structure.[6] This does indeed allow some control of pore size by the choice of liquid crystal template. With the exception of cetyltrimethylammonium bromide, all the surfactants used are based on a non-polar hydrocarbon tail with a polar polyethylene glycol head. The use of non-ionic amphiphiles, as opposed to charged surfactants, should reduce the electrostatic interaction between template and silica matrix. This might imply less disruption to the long range order on calcination, as a result of easier removal of the surfactant.[7]

3.2 Characterisation of Mesoporous Silica

Several techniques have been employed in order to attempt to characterise these materials. The long range order in these silicas may be readily investigated by X-ray powder diffraction, as the ordered pore structure results in low angle reflections due to the very large repeat distances. The sample is ground for at least five minutes using a pestle and mortar before the diffraction pattern is collected. An example of this type of diffraction pattern is given below:
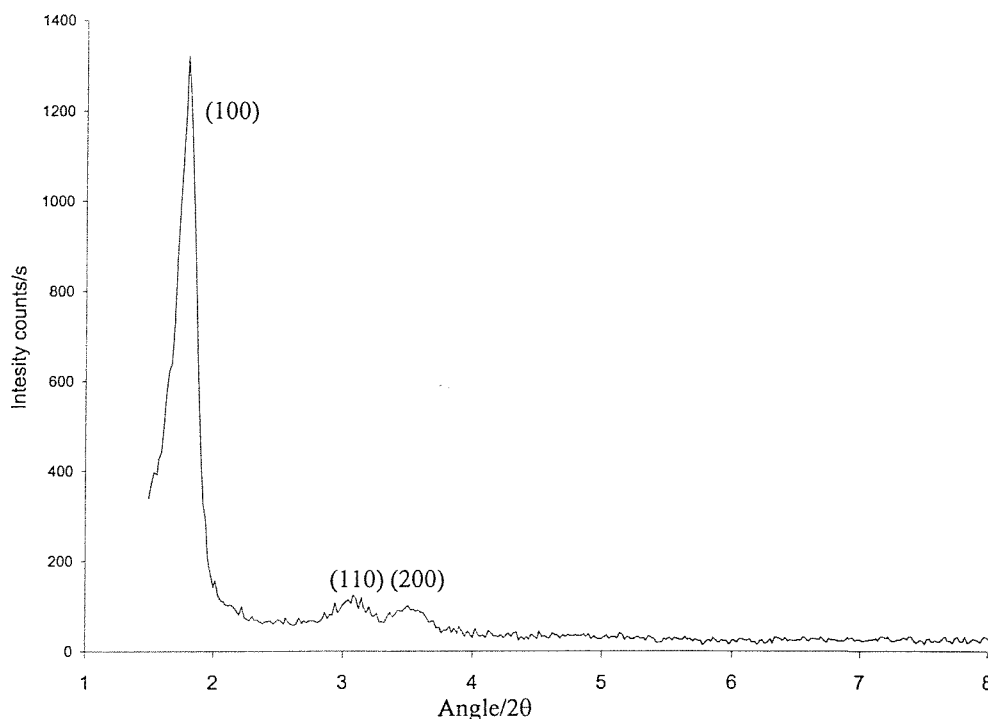

Figure 3.2 An X-ray powder diffraction pattern of calcined Brij76 templated silica

In the diffraction pattern above, it is possible to observe not only the primary diffraction peak, centred at about 1.7°2θ, which corresponds to the (100) reflection, but also secondary peaks at higher angle. The primary peak alone does not allow the mesophase from which the silica is formed to be determined, and in the absence of the secondary peaks an assignment of a lamelllar, or even a cubic phase is equally valid to that of a hexagonal array of pores. However, the positions of these peaks may be indexed for the (110) and (200) reflections, and are shown to be consistent with a hexagonal unit cell.
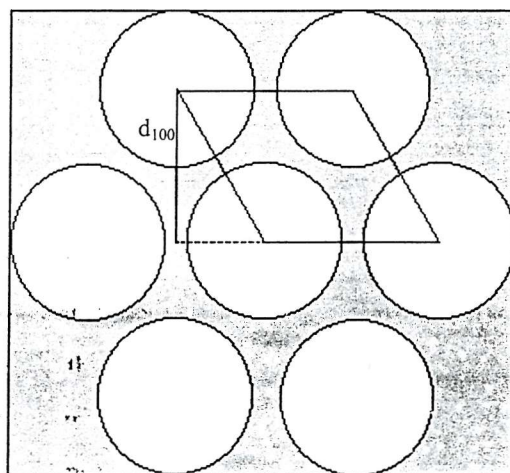
Figure 3.3 A representation of the unit cell in an H_1 mesoporous silica

From the diagram above, it is possible to observe the relationship between the value obtained for the d_{100} spacing, and the pore to pore distance. The d-spacing is obtained from the Bragg Law:

assuming n = 1 $\lambda = 2d\sin\theta$ Eq. 3.1

rearranged gives $d = \lambda/2\sin\theta$ Eq. 3.2

The distance, r, from the centre of one pore to that of its nearest neighbour is then:

$$r = d_{100}/\cos30°$$ Eq. 3.3

It was observed that, independent of the surfactant used, the (100) reflection was of greater intensity, and at higher 2θ value (smaller d-spacing) for the calcined material, than for that of the silica with surfactant still within the pores. This is characteristic of mesoporous materials synthesised in this way, and has been previously observed in the literature.[8] One explanation given for this effect on peak intensity with template removal is that calcination promotes siloxane bond formation at the surface, increasing order within the oxide structure.[9] This theory does not seem totally satisfactory, as it does not explain the shift in d-spacing observed. A more reasonable explanation is that these observations

are the result of water removal, not only from the pore wall surface, but also from micropores within the oxide structure. This would indeed encourage siloxane bond formation, which may lead to greater local order, and it might also explain the structural contraction observed if the water originally within the superstructure is thought of as a swelling agent. This effect on powder diffraction pattern is illustrated in Figure 3.4:
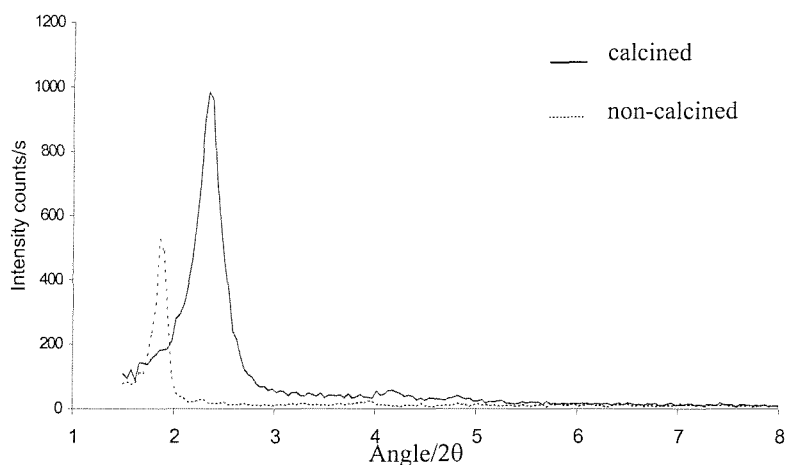

Figure 3.4 X-ray powder diffraction patterns of a $C_{12}EO_8$ templated silica

^{29}Si Cross Polarisation Magic Angle Spinning (CPMAS) NMR was also used to investigate this change in the local environment of the silicon on calcination. The nature of the cross polarisation experiment makes this a surface sensitive technique, or, more accurately, the technique is sensitive to silicon nuclei in close proximity to hydrogen atoms. These silicon nuclei also have a fast relaxation mechanism due to their hydrogenous environment, and so by using short relaxation times between pulses the signal from the bulk silicon nuclei, which take much longer to relax back to the ground state, is negligible. This is important to note, as it means that the spectra obtained cannot be used to estimate the average silicon environment within the bulk. NMR spectra of silica consist typically of a number of broad resonances, which are assigned with respect to a well-established nomenclature. Silicon environments in these types of systems may be readily divided into five groups, denoted Q branches. A Q^4 environment pertains to a silicon in the centre of an SiO_4 tetrahedron that is linked to four other silicons. In a Q^3 environment the SiO_4 tetrahedron is directly bonded to three other silicon atoms plus one other, often a hydrogen atom. The spectra of a Brij76 templated mesoporous silica before and after calcination are shown in Figure 3.5:
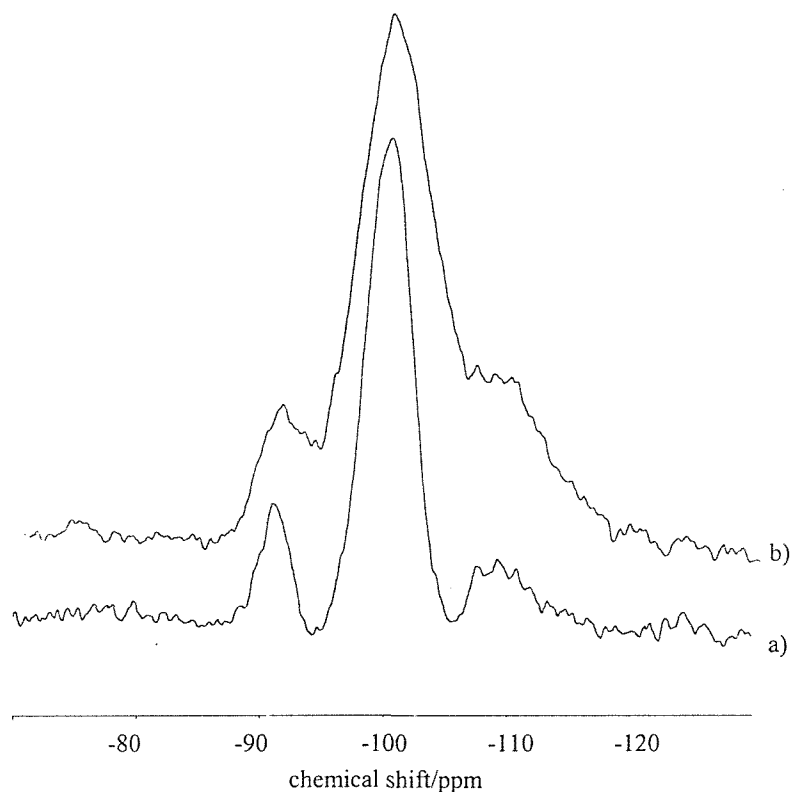
-80   -90   -100   -110   -120
chemical shift/ppm

Figure 3.5 ^{29}Si CPMAS NMR spectra of Brij76 templated mesoporous silica; a)as synthesised, b) calcined at 470°C in nitrogen, 4h, and oxygen, 8h.

Both spectra show Q^4, Q^3, and Q^2 resonances centred at –109, -100, and –91ppm respectively. The first observation is that the peaks in the spectra are broad and closely resemble those of amorphous silica, which is a strong indication that the pore walls are actually amorphous, with a wide range of O-Si-O angles.[9] The Q^3 branch may be conveniently thought of as a silanol group, and the Q^2 branch as a geminal disilanol. It is possible to observe the reduction in Q^2 intensity, and simultaneous increase in Q^4 intensity on calcination. This may be attributed to the loss of adsorbed water, or a result of dehydroxylation and further siloxane bond formation, or perhaps due to the removal of surface-surfactant interactions. It is reasonable to associate these changes in silicon environment with the unit cell contraction observed by X-ray powder diffraction. The intensity of the Q^2 peak in the spectrum of the material calcined at 450°C is perhaps a little surprising, as it is generally observed only as a shoulder of the Q^3 peak in those of similarly treated non-mesoporous amorphous silicas, even with the use of the cross polarisation technique.[10] One explanation of this phenomenon is that there is simply a much greater

area of silica surface per unit mass for the mesoporous materials, and it is at the surface that these disilanol species are most likely to exist. It is still unexpected for these Q^2 environments to persist in a material pre-treated to such a high temperature, so it may be that the pore morphology stabilises these species in some way.

Another technique that is very amenable to the characterisation of these materials is isothermal nitrogen adsorption, and this has been extensively employed to obtain a measure of surface area and pore size distribution. An example of a typical isotherm showing both adsorption and desorption branches is given below:
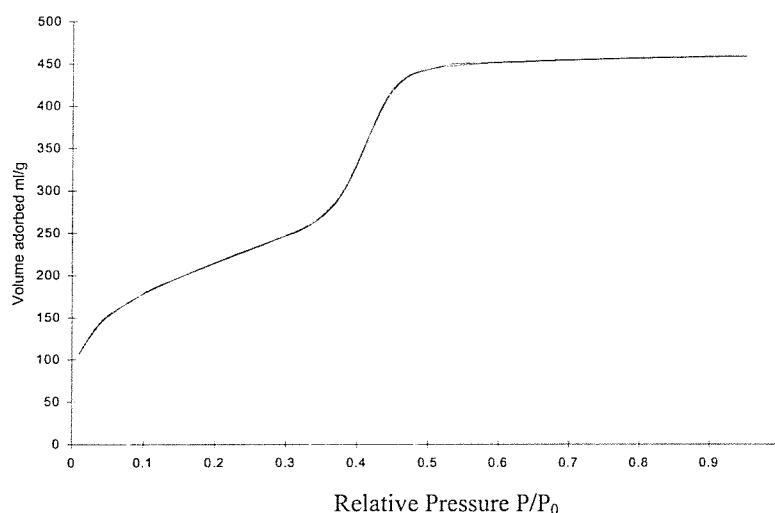
Figure 3.6 N_2 adsorption/desorption isotherm of Brij76 templated calcined H_1 silica

The volume of N_2 adsorbed is expressed at standard temperature and pressure, and P/P_0 is the partial pressure of N_2 in equilibrium at 77K. Samples were kept in a vacuum dessicator after calcination, to avoid water adsorption. Above is a type IV isotherm with no observable hysteresis. A well-defined step occurs in the adsorption curve between partial pressures P/P_0 0.4 and 0.5, which is indicative of multilayer adsorption and capillary condensation within the framework defined mesopores. The absence of adsorption-desorption hysteresis due to interparticle capillary condensation, showing a lack of textural mesoporosity, indicates that the elementary particle size of these silicas is orders of magnitude larger than the framework-confined mesopores. This, in turn, suggests that the broad lines observed in the X-ray powder diffraction patterns of these materials arise from the intrinsic disorder in the assembly of the surfactant templated channels, rather than from the effects of finite particle size. Interestingly, the only template that yielded a silica with a

different type of nitrogen adsorption isotherm was the only non-neutral surfactant, cetyltrimethylammonium bromide. This is shown below:
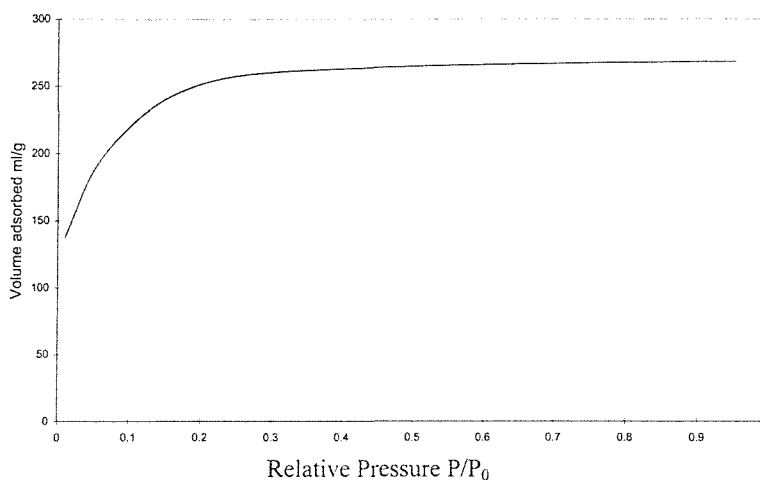

Figure 3.7 N_2 adsorption/desorption isotherm of CTMABr templated calcined H_1 silica

It is possible to observe the absence of a well-defined step in the isotherm for this system, which is indicative of the lesser degree of long range order for this material. This is confirmed by the presence of only weak reflections in the X-ray powder diffraction pattern. It is reasonable to suggest that the use of a non-neutral surfactant in this instance may have resulted in a greater disruption of the silica matrix on template removal.

The nitrogen adsorption data was fitted to the BET isotherm in order to obtain a value for the surface area, and the Dollimore Heal method,[11] described previously, was used to estimate a pore size distribution. Such a distribution, calculated from the desorption branch of the isotherm for the Brij76 templated silica is shown in Figure 3.8:
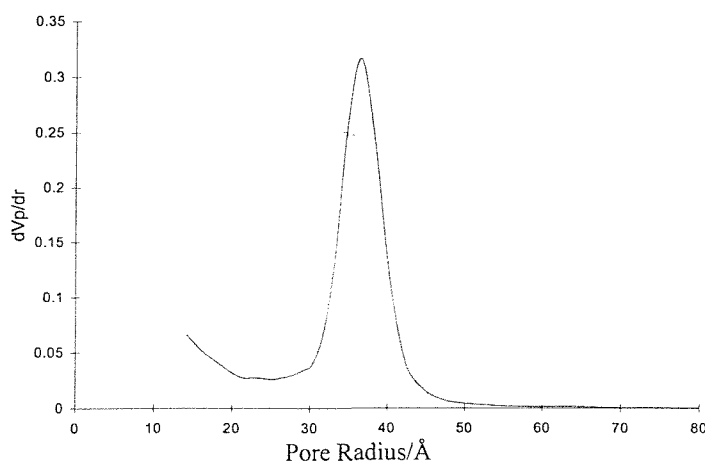

Figure 3.8 Pore size distribution for a Brij76 templated calcined silica

The plot above shows a narrow distribution of mesopores centred around 37Å. This also suggests a long range ordered material with a high degree of structural directionality derived from the templating surfactant.

The effect of surfactant on the structure of the mesoporous silica formed is summarised in the table below:

surfactant	surface area/m^2g^{-1}	d_{100} value/Å	XRD, r/Å	P.S.D. maximum/Å	wall thickness/Å
Brij76	870	49	57	37	20
Brij56	930	42	49	34	15
$C_{16}EO_8$	1200	42	49	34	15
$C_{12}EO_8$	1260	37	43	27	16
Triton X100	1100	36	42	23	19
CTMABr	760	29	34	<18	>16

Table 3.1 The effect of liquid crystal template on the mesoporous silica structure.

Surface area measurements are reproducible to within $10m^2g^{-1}$, d_{100} values are accurate to ± 1Å, and the pore wall thickness is calculated from the pore to pore distance, r, less the maximum in the pore size distribution (P.S.D.). The measured surface area is significantly higher for silicas templated by the $C_{16}EO_8$ and $C_{12}EO_8$ surfactants than for those made using the Brij amphiphiles. This may be attributable to the fact that the C_xEO_8 materials are pure compounds, whereas the Brij surfactants are mixtures of compounds with slight variation in the polyethyleneglycol chain lengths. It is reasonable to suggest that the micellar aggregations in the liquid crystal phase of a pure compound may have a higher degree of order than that of a mixture, but this would not necessarily lead to a higher surface area. Indeed, the intensity and width of reflections in the resulting silica X-ray powder diffraction patterns of both types of surfactant are approximately equivalent, suggesting that the scattering domains are of a comparable degree of order. It is therefore more likely that this difference in surface area is due to the presence of more amorphous, or more accurately non-templated, material in the Brij-templated silicas. As well as a slight variation in polar head group size, these surfactants also contain a small amount of other substances such as antioxidants, and it is feasible that silica condensation occurs simultaneously at these sites in solution.

A comparison of the structural parameters determined for the C_xEO_8 templated silicas reveals the effect of variation of surfactant hydrocarbon tail length. The C_{12} templated material has a hole to hole distance from X-ray powder diffraction of 43Å, compared to 49Å for the C_{16} analogue. The maxima in pore size distribution for the C_{12} and C_{16} silicas occur at 27 and 34Å respectively. These values are in reasonable agreement with those found from transmission electron microscopy (for $C_{12}EO_8$[1], r = 42Å, pore size = 27Å; for $C_{16}EO_8$[12] r = 50Å, pore size = 32Å). This suggests that the pore size is proportional to hydrocarbon tail length, but that there is no significant effect on the pore wall thickness for these surfactants. The surface area is found to be larger for the shorter hydrocarbon tail length template. This feature is also observed in the structural data obtained for the two Brij templated silicas with the Brij56 (C_{16} tail) material having a greater surface area than Brij76 (C_{18} tail). However, the increase in hole to hole spacing with increasing tail length is manifested in an increase in pore wall thickness rather than pore diameter. From C_{16} to C_{18} the maximum in pore size distribution is shifted from 34 to 37Å, whereas the shift in pore wall thickness is from 15 to 20Å. A greater pore wall thickness is often associated with a greater thermal stability, which is useful if the support is to be used in reactions at elevated temperatures. An explanation for this difference between classes of surfactant is not obvious.

It is interesting to note that, aside from the measured surface area, the structural data from silicas templated by $C_{16}EO_8$ and Brij56 are the same within experimental error. Both of these surfactants have C_{16} hydrocarbon tails, and the difference between them is in the size of the head group. $C_{16}EO_8$ has an octaethylene glycol head group, whereas Brij56 has, on average, a decaethylene glycol group. This suggests that the head group size is of less importance than surfactant molecule tail length in the dictation of the mesoporous silica structural repeat distance.

The Diffuse Reflectance Infra Red (DRIFTS) spectra of the as-synthesised and calcined mesoporous silicas were recorded, and a comparison of these is shown below:
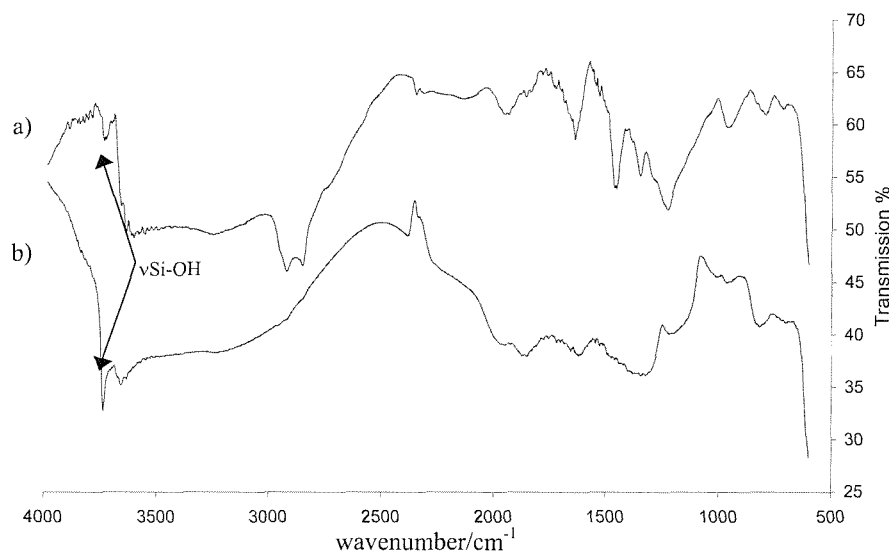

Figure 3.9 DRIFTS spectra of $C_{12}EO_8$ templated mesoporous silica; a) as-synthesised,
b) calcined at 470°C in nitrogen, 4h, and oxygen, 8h.

There are several differences between the two above spectra that are worth noting. Many of these changes are simply a function of the template removal, with the obvious disappearance of bands due to the hydrocarbon backbone of the surfactant. The bands in the spectrum of the as-synthesised material between 2800 and 3000cm^{-1} may be assigned to C-H stretching frequencies. The sharp bands apparent in the fingerprint region below 1500cm^{-1} are due to C-H bending modes, as well as some contribution from C-C and C-O stretching modes. The broader bands in this region in both spectra may be assigned to Si-O stretching modes, but little information can be gleaned from their position and intensity. More interesting in terms of structural information are the absorption bands in the Si-OH stretching region from 3800 to 3000cm^{-1}. It is possible to observe a very significant increase in the intensity of the band at 3740cm^{-1} on calcination. This is assigned as the absorption due to isolated terminal silanol groups on the silica surface.[13,14] The enhanced strength of the absorption, and the reduction in width of this band is probably due to a decrease in the extent of hydrogen bonding to these species on surfactant removal. In the spectrum of the calcined silica there is also a band at 3660cm^{-1}, which seems too narrow to be due to an extensively hydrogen bonded species. This may be tentatively assigned as non-hydrogen bonded bridging hydroxyl species, though there is no obvious precedent for this band in the literature. There is also a very broad band between 3000 and 3600cm^{-1} in

both spectra which is due hydrogen bonded hydroxyl groups and adsorbed water.[13] This suggests that, despite calcination at 450°C, the dehydroxylation of the surface is not complete.

A minor point to note is that the DRIFTS spectrum of the Brij76/Brij56 templated mesoporous silica calcined at 470°C does not show the band at 3660cm^{-1} that is observed in the spectrum of a $C_{12}EO_8$ templated silica prepared under identical conditions. An explanation for this is not obvious.

3.3 An Investigation of the Thermal Stability of Mesoporous Silica

It has been shown in the previous section that these mesoporous silicas are stable to surfactant removal at 470°C. Chen *et al* reported that the MCM-41 mesoporous silica is stable to 900°C in air,[15,16,17] though it should be noted that these materials do not have the same extent of long range order as those reported here. It is important to establish the limits of the thermal stability of liquid crystal templated, and to obtain information on the effect of increasing the calcination temperature on the surface structure. This is necessary to determine both the temperature range over which these materials are suitable heterogeneous catalyst supports, and the pre-treatment conditions required to obtain a desired surface composition. For this purpose, an investigation of the effect of a systematic increase in calcination temperature on a Brij76 templated mesoporous silica has been performed.

The mesoporous silica was prepared as previously described, and calcined at 470°C for 4h in a flow of nitrogen, then 8h in a flow of oxygen to remove the surfactant. The material was then further calcined at a temperature of 470, 600, 700, 800, 850, 900, or 950°C in oxygen at a flow of 20ml/min for a period of 16h. The resultant samples were held in a vacuum desiccator prior to use. Attempts were then made to characterise these silicas with a variety of techniques.

3.31 X-ray Powder Diffraction

The X-ray powder diffraction patterns of these calcined mesoporous silicas are shown in Figure 3.10:
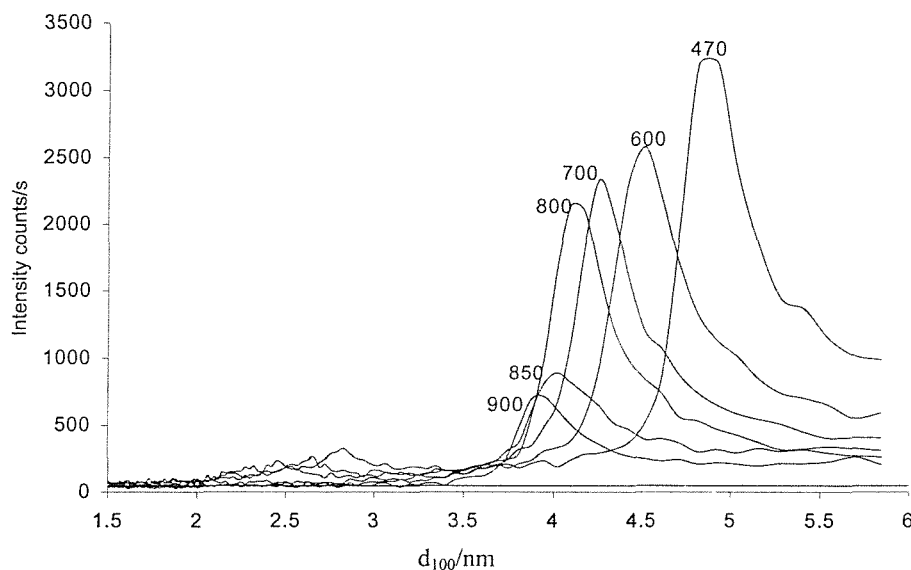

Figure 3.10 d_{100} dependence on calcination temperature of Bri76 templated mesoporous silica

The information that may be obtained from the plot above can be divided into two parts. Firstly, there is a gradual coincident decrease in lattice spacing and reflection intensity with increasing calcination temperature up to 800°C. The d_{100} shift from 49Å for material calcined at 470°C to 42Å at 800°C suggests that there is a continuous process that probably relates to dehydroxylation and water loss, causing a contraction of the unit cell. The reduction in reflection intensity with increasing temperature indicates that whatever process is responsible for the unit cell contraction, is also resulting in either some small degree of structural collapse, or some increase in the disorder of the pore walls. As has been stated previously, a process such as dehydroxylation would lead to the formation of new siloxane bonds that should, in theory, increase the extent of long range order, so it seems more likely that there is some limited structural collapse. Between pre-treatment temperatures of 800 and 850°C there appears to be the onset of a process with more drastic structural consequences. The decrease in lattice spacing is accelerated to some extent over this temperature range, but the much more obvious effect is the decrease in intensity of the reflection. It should be noted that the intensity, measured simply in counts per second, is not a quantitative measurement of long range order in isolation. It is, however, a good qualitative indicator of the extent of order in analogous systems prepared under the same

conditions. This decrease in diffracted intensity continues as the calcination temperature is increased, and indeed, at a pre-treatment temperature of 950°C, there is no observable (100) reflection.

3.32 Isothermal Nitrogen Adsorption Analysis

The adsorption-desorption isotherms and derived pore size distributions for these silica samples are shown below:
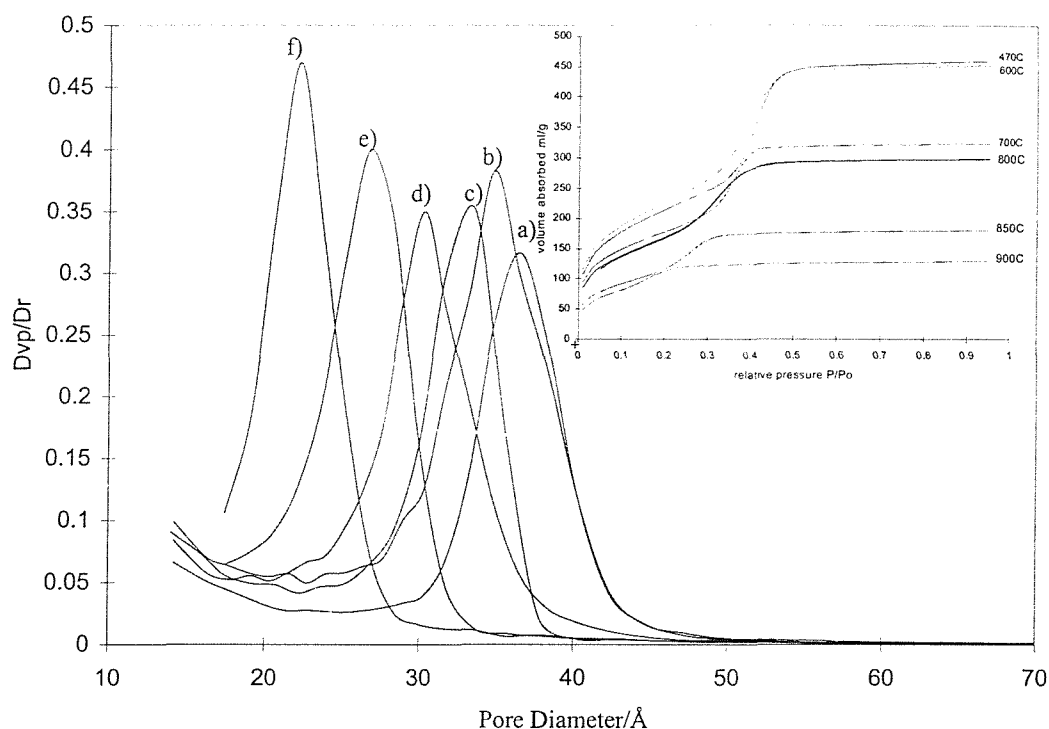

Figure 3.11 Dollimore-Heal pore size distribution dependence on calcination temperature; a)470°C, b)600°C, c)700°C, d)800°C, e)850°C, f)900°C (inset: nitrogen adsorption isotherms)

The figure above shows the decrease of pore diameter with increasing calcination temperature. This appears in agreement with the X-ray powder diffraction data, as this pore size decrease occurs gradually between pre-treatment temperatures of 470 and 800°C, from 37 to 30Å, before dropping more sharply at calcination temperatures above 800°C. Interestingly, the pore size distribution does not seem to broaden with increasing temperature, as might be intuitively expected with structural collapse. It is possible that this lack of broadening is an artefact of the method of distribution calculation, but a more likely chemical explanation for this can be found. It may be that the parts of the structure

that do remain intact at these elevated temperatures genuinely do have a narrow distribution of pore sizes, whereas those parts of the silica that do collapse have an amorphous structure with no mesoporosity. There is evidence of the extent of structural disintegration within the changing shape of the adsorption isotherms on increasing pre-treatment temperature. The well-defined step in this adsorption is absent in the isotherm of the sample calcined at 900°C, and the measured surface areas support this evidence:
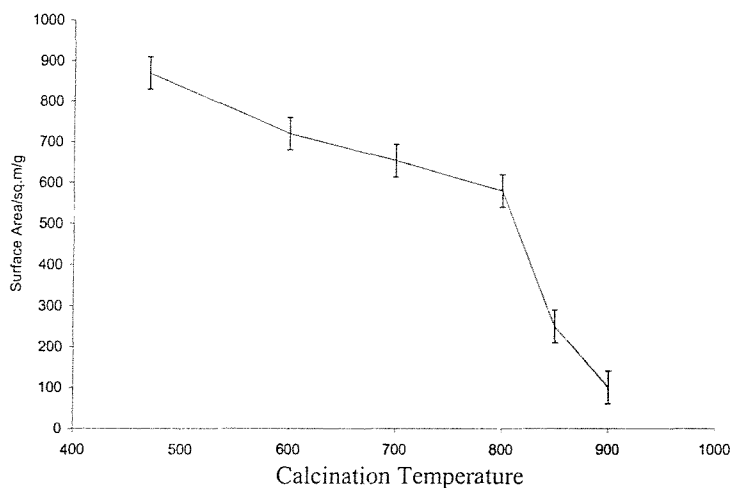
Figure 3.12 surface area dependence of calcination temperature

Again, the same dependence on pre-treatment temperature is observed, and the low surface area of the sample calcined at 900°C certainly suggests that much of this material is non-mesoporous and amorphous.

3.33 DRIFTS Spectroscopy

The DRIFTS spectra of the calcined silica samples are shown below:
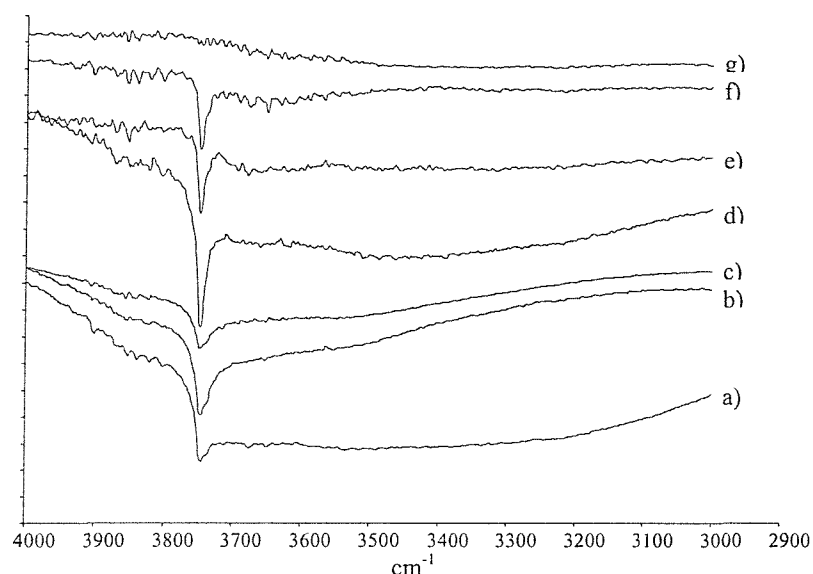
Figure 3.13 DRIFTS spectra of Brij76 templated mesoporous silica calcined at a)470°C, b)600°C, c)700°C, d)800°C, e)850°C, f)900°C, g)950°C

From the spectra above it is possible to observe dehydration and dehydroxylation occurring in two stages as the pre-treatment temperature increases. The first event is the disappearance of the very broad band centred at approximately 3300cm^{-1} that is probably due to a small amount of adsorbed water within the framework, as well as hydrogen bonded silanols at the surface. As these hydroxyl groups are removed it is possible to observe the narrowing and increasing intensity of the absorption band at 3740cm^{-1} due to isolated terminal silanols. This narrowing is a result of the removal of minor hydrogen bonding effects, and as dehydroxylation proceeds the number of these isolated sites will actually increase.[13] This process continues as the pre-treatment temperature rises to 800°C, at which point it appears that the only hydroxyl groups remaining are the isolated terminal silanols. As the calcination temperature is increased further, then these hydroxyl groups are also slowly lost, until, at 950°C, the silica is totally dehydroxylated.

It is important to note that this dehydroxylation occurs first at sites where there are other hydroxyl groups in close proximity, evidenced by the broadness of the absorption band. This is not surprising if dehydroxylation is considered to occur via the loss of water and formation of a siloxane bond.[18]

A schematic diagram for this process is given below:
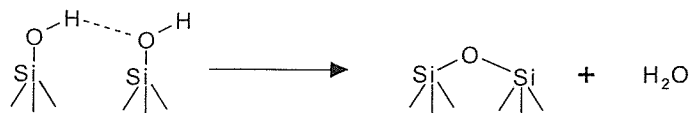
Dehydroxylation at isolated sites would then be expected to be more difficult, and this is indeed apparent.

3.34 ^{29}Si MAS NMR Spectroscopy

Two types of NMR experiment were used. The first is the cross-polarisation MASNMR experiment previously described where the proton spin reservoir is utilised to enhance the signal from silicon atoms in close proximity to protons. The CP MASNMR spectra of the mesoporous silica samples are dominated by the Q^3 peak at around -100ppm in all cases, but at lower pre-treatment temperatures this is accompanied by a shoulder at around -91ppm which may be assigned as Q^2 silicon. As the temperature of calcination is increased up to 800°C the disappearance of this Q^2 shoulder is observed, along with the appearance of a shoulder at approximately -110ppm which can readily be attributed to Q^4 silicon.

Once the pre-treatment temperature is increased to 850°C there are no longer sufficient protons in the sample to achieve a reasonable signal by the use of a cross polarisation experiment, as one might expect from the marked decrease in hydroxyl band intensity in the DRIFTS spectrum between these temperatures. So, a second MAS NMR experiment is required to study the silicas calcined at temperatures above 800°C. A high power decoupling (HPDEC) experiment with a long relaxation time between pulses (900s), and a ^{1}H decoupling end stage was employed. Unfortunately the signal obtained is no longer attributable solely to surface silicons, but it is very indicative of the nature of the bulk. In practice, both CP and HPDEC experiments were performed on all samples, and the HPDEC MAS NMR spectra of silicas with high pre-treatment temperatures, i.e. above 800°C, revealed, as expected, a solely Q^4 environment for silicon.

3.35 The Gas Titration of Hydroxyl Groups

The relationship between silanol concentration on the silica surface and the pre-treatment calcination temperature has been determined by titration of these hydroxyl groups with methylmagnesium bromide. The titration proceeds by reaction of methylmagnesium bromide with the surface hydroxyls, which generates one mole of methane per mole of hydroxyl groups. The pressure of the evolved methane is measured, and this value can be used to determine the number of moles of hydroxyl groups in a given mass of silica. If the surface area of the silica is known, then this may be used to generate a value for the number of hydroxyl groups per square nanometre. The procedure involves taking an accurately known mass of previously calcined mesoporous silica, and placing it in an evacuable flask fitted with a pressure gauge and two taps. This is then evacuated, and flushed with nitrogen before 5ml of butyl ether is added to the flask to act as the solvent (chosen due to the fact that the Grignard reagent is obtained as a 1.0M solution in butyl ether). This is then degassed by repeatedly cooling in liquid nitrogen, evacuating, and allowing to warm to room temperature under static vacuum. Once the system has been checked for leaks, and the initial temperature and pressure noted, then 5ml Grignard reagent (an excess) is injected through a suba seal placed in one of the necks of the flask. An exothermic reaction occurs, with the evolution of methane. The reaction is left stirring for two hours, by which time the temperature has returned to the initial value, and the final pressure noted.

This procedure was initially performed on a known quantity of methanol in order to calibrate the system, and then on three occasions each for silicas calcined at 470°C, 600°C, 700°C, 800°C, 850°C and 900°C. A control experiment was also performed, where the Grignard reagent was added to the butyl ether alone. The method of calculation is given below

From the reaction $n_{OH} = n_{CH4}$ Eq. 3.4

$$C_{OH} = n_{OH} / m_{silica}$$ Eq. 3.5

Ideal gas equation, $n = PV / RT$ Eq. 3.6

so $C_{OH} = n_{CH4} / m_{silica} = P_{CH4}V / RTm_{silica}$ Eq. 3.7

Where $P_{CH4} = P_e - P_o - P_b$ and $V = V_{tot} - V_{gri} - V_{solv} - V_{silica}$ Eq. 3.8

i.e. $C_{OH} = (P_e - P_o)*(V_{tot} - V_{gri} - V_{solv} - V_{silica})/(m_{silica} * RT)$ Eq. 3.9

and $V_{silica} = m_{silica} / \rho$ Eq. 3.10

Therefore $C_{OH} = (P_e - P_o) * (V_{tot} - V_{gri} - V_{solv} - m_{silica} / \rho) / (m_{silica} * RT)$ Eq. 3.11

Where

- C_{OH}, in $mol.kg^{-1}$
- P_o, the pressure before the injection of Grignard reagent (in bar)
- P_e, the pressure when equilibrium is reached (after one hour) in bar
- P_b, the pressure increase noted from the blank experiment, 0.01 bar
- V_{tot} of the apparatus is 330 ml = 330×10^{-6} m^3 (where 160 ml is the internal volume of the manometer and 170 ml is the glassware volume measured)
- V_{gri}, volume of Grignard reagent injected (5 ml of CH_3MgBr in butyl ether, 5mmol)
- V_{solv}, volume of solvent injected (5 ml of butyl ether)
- m_{silica}, the mass of silica (in kg)
- ρ, the density of the mesoporous silica (2000 $kg.m^{-3}$)
- $R = 8.10047385 \times 10^{-5}$ $bar.m^3.mol^{-1}.K^{-1}$
- T, the starting, and equilibrium temperature

To obtain this concentration in $mol.nm^{-2}$, the surface area of the mesoporous silica will have to be taken into consideration

With consideration to the final equation above, the standard error in the measurement of hydroxyl concentration is given by the following equation:[19]

$$\delta n_{OH}/n_{OH} = \sqrt{((\sqrt{\delta P_e^2 + \delta P_o^2})/(P_e - P_o))^2 + (\sqrt{\delta V_{tot}^2 + \delta V_{solv}^2 + \delta V_{gri}^2} + (\delta m_{silica}/\rho)^2)}$$
$$\overline{(V_{tot} - V_{solv} - V_{gri} - m_{silica}/\rho) + (\delta T/T)^2 + (\delta m_{silica}/m_{silica})^2)}$$ Eq. 3.12

Where

- $\delta P_e = \delta P_o$, the standard error for the measurement of the manometer pressure
- δV_{tot}, the standard error for the measurement of the total volume of the apparatus
- $\delta V_{solv} = \delta V_{gri}$, the standard error for the measurement of the syringe volume

- δm_{silica}, the standard error for the measurement of the mass of the silica

- δT, the standard error for the temperature measurement

The results of these titrations are tabulated below:

Calcination Temp./°C	$C_{OH}/molkg^{-1}$	$n_{OH}/OHnm^{-2}$
470	1.67(2)	1.21(4)
600	1.30(2)	1.03(4)
700	1.20(2)	1.02(4)
800	0.27(2)	0.24(4)
850	0.11(1)	0.12(2)
900	0.041(4)	0.060(8)

Table 3.2 calcination temperature dependence of surface hydroxyl concentration (statistical errors in parentheses)

Below is a graphical representation of these results:
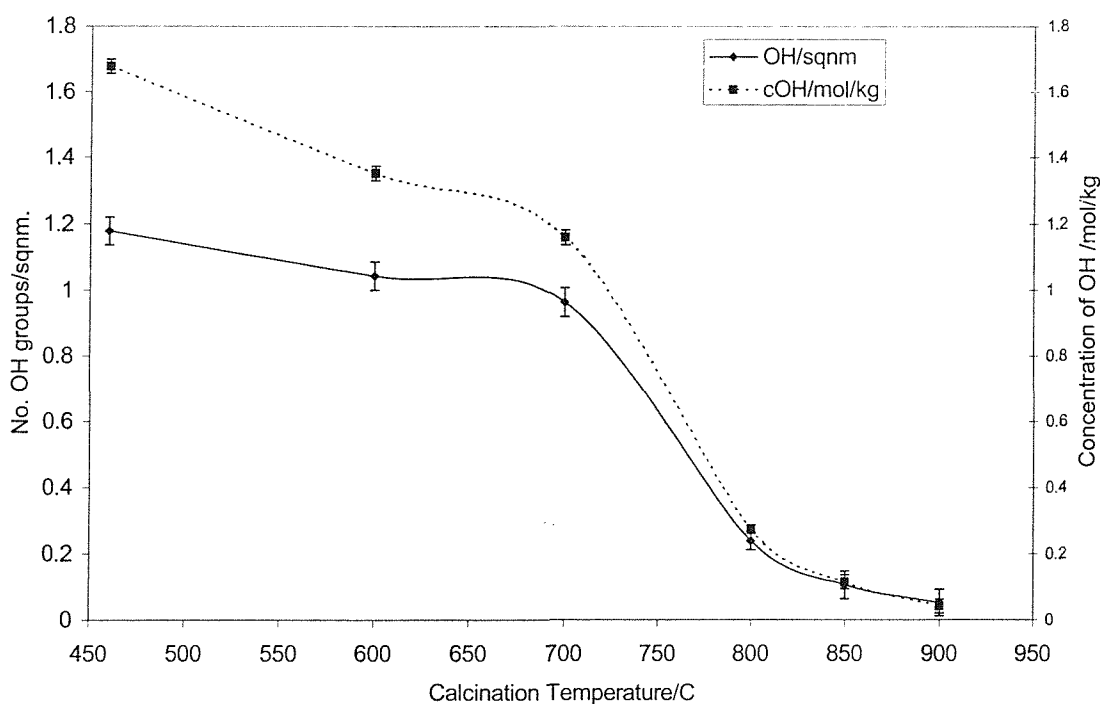
Figure 3.14 A graph of hydroxyl concentration in mol/kg^{-1}(dotted line) and OHnm^{-2} (solid line) versus calcination temperature

The trend observed, with a slow steady decline in hydroxyl group concentration from 1.7 to 1.2 molOH/kg^{-1} between calcination temperatures of 470 and 700°C, followed by a dramatic decrease at 800°C and subsequent steady decline is similar to that observed from the previous experiments. However, significant structural collapse was observed to occur between 800 and 850°C by X-ray powder diffraction and isothermal nitrogen absorption, so it would appear the extensive dehydroxylation may occur before the loss of mesoporosity. The reaction with the Grignard reagent appears to take longer for a mesoporous silica than for a non-porous analogue, and great care was taken to try and ensure that the reaction proceeded to completion. This is presumably due to a rate limiting factor originating from slow diffusion of reagent in the solution phase through the mesopores. The concentration of hydroxyl groups within the mesoporous silica after calcination at 800°C is 0.25 OHnm^{-2}, which is markedly less than that found for a non-mesoporous silica by similar methods;[20] 0.9 OHnm^{-2}. This difference is rather less, though still notable, for materials calcined at lower temperatures (at 700°C the concentration is 0.95 OHnm^{-2} for the mesoporous system compared with 1.1 OHnm^{-2} for the amorphous silica), and suggests that dehydroxylation is actually enhanced by the mesoporous structure at temperatures greater than 700°C. Possibly this is a result of the intrinsic pore curvature in mesoporous silica, which may result in closer proximity of nominally isolated hydroxyl groups, facilitating dehydroxylation. It is worth noting that this method for the measurement of hydroxyl group concentration may not accurately reflect the total number of OH groups present in the whole sample, but it will give a very good measure of the number of hydroxyl groups that are accessible to the Grignard reagent. It is this information that is the most useful in determining the density of sites available for adsorption/reaction.

In summary, all of the above techniques provide complementary information on the effect of calcination temperature on surface composition and structural integrity. Rapid structural collapse occurs at between 800and 850°C, and rapid dehydroxylation between 700 and 800°C.

3.4 References

1) G.S. Attard, J.C. Glyde, C.G. Göltner, *Nature*, 366, **378**, 1995.

2) C.G. Göltner, M. Antonietti, *Adv. Mater.*, 431, **9**, 1997.

3) S.N. Guha, P.N. Moorty, K. Kishore, D.B. Naik, K.N. Rao, *Proc. Indian Acad. Sci.*, 99, **261**, 1987.

4) D.J. Mitchell, G.J.T. Tiddy, L. Waring, T. Bostock, M.P. McDonald, *J. Chem. Soc. Faraday Trans.* 975, **79**, 1983.

5) N.R.B. Coleman, PhD thesis, University of Southampton, 1999.

6) J.S. Beck, J.C. Vartuli, W.J. Roth, M.E. Leonowicz, C.T. Kresge, K.D. Schmitt, C.T-W. Chu, D.H. Olson, E.W. Sheppard, S.B. McCullen, J.B. Higgins, J.L. Schlenker, *J.Am.Chem.Soc.*, 10834, **114**, 1992.

7) S.A. Bagshaw, E. Prouzet, T.J. Pinnavaia, *Science*, 1242, **269**, 1995.

8) G.S. Attard, M. Edgar, C.G. Göltner, *Acta Mater.* 751, **46**, 1998.

9) A. Sayari, *Stud. Surf. Sci. Catal.*, 1, **102**, 1996.

10) D.W. Sindorf, G.E. Maciel, *J. Am. Chem. Soc.*, 1487, **105**, 1983.

11) D.Dollimore, G.R.Heal, *J.Appl.Chem.*, 109, 1964.

12) S.G. Fiddy, University of Southampton, unpublished results.

13) H. Landmesser, H. Kosslick, W. Storek, R. Fricke, *Solid State Ionics,* 271, **101-103**, 1997.

14) J. Weglarski, J. Datka, H. He, J. Klinowski, *J. Chem. Soc. Faraday Trans.* 5161, **92**, 1996.

15) C.-Y. Chen, H.-X. Li, M.E. Davis, *Microporous Mater.* 17, **2**, 1993.

16) C.-Y. Chen, S.L. Burkett, H.-X. Li, M.E. Davis, *Microporous Mater.* 27, **2**, 1993.

17) C.-Y. Chen, S.-Q. Xiao, M.E. Davis, *Microporous Mater.* 1, **4**, 1995.

18) H. Naono, M. Hakuman, T. Tanaka, N. Tamura, K. Nakai, *J. Colloid. Interf. Sci.*, 411, **225**, 2000.

19) J.C. Miller, J.N. Miller, Statistics for Analytical Chemistry, Ellis Horwood Limited, Chichester, 1988.

20) S.Turin, University of Southampton, unpublished results.

Chapter 4. Characterisation of Supported Uranium Oxide Materials

This chapter describes the preparation and characterisation of supported uranium oxide species. This includes the synthesis, where appropriate, of the uranium oxide precursors; the deposition of these precursors on inorganic supports and the characterisation of supported species; the calcination of these supported species and characterisation of the resulting uranium oxide phase. Two precursors, uranium tetrachloride, UCl_4, and uranyl nitrate, $UO_2(NO_3)_2$, were supported on three different inorganic oxide supports, mesoporous silica, amorphous silica, and amorphous alumina. The result is a total of six different supported uranium systems.

4.1 Synthesis and Characterisation of Uranium Oxide Precursors

Uranyl nitrate was purchased from STREM as the hexahydrate, $UO_2(NO_3)_2.6H_2O$. Uranium tetrachloride was synthesised by a method first proposed by Herman *et al* in 1957.[1] Uranium (VI) oxide (UO_3 10g, 0.035mol) and hexachloropropene (25ml, 0.21mol) were placed in a three-necked round-bottomed flask fitted with a condenser and a nitrogen bubbler. The flask was then slowly heated to 60°C over a period of one hour, at which temperature a highly exothermic reaction occurred. The flask was cooled in ice water at this time to prevent the temperature exceeding 100°C. After this initial reaction had subsided the mixture was allowed to reflux at 158°C for a further 6 hours. A green solid precipitated from the dark red solution over this period of time. The mixture was then filtered using Schlenk apparatus, and the green uranium tetrachloride was washed with dry dichloromethane (3 x 50ml). The contents were then dried under vacuum, transferred to a Schlenk tube in a dry box, and dried for a further 24 hours at 200°C under vacuum yielding olive green uranium tetrachloride (12g, 90.1%yield). The synthetic procedure utilises hexachloropropene as a chlorinating agent, and the initial exothermic reaction is the formation of uranium pentachloride, UCl_5. As the mixture is further heated in the refluxing trichloroacryloyl chloride produced, the uranium pentachloride is thermally decomposed to form the tetrachloride. This material was characterised by diffuse reflectance UV-vis/NIR spectroscopy and X-ray powder diffraction, with reference to the literature,[2,3] and by U L(III) EXAFS. A fit obtained for this EXAFS data, along with the parameters used to define it, is given in figure 4.1:
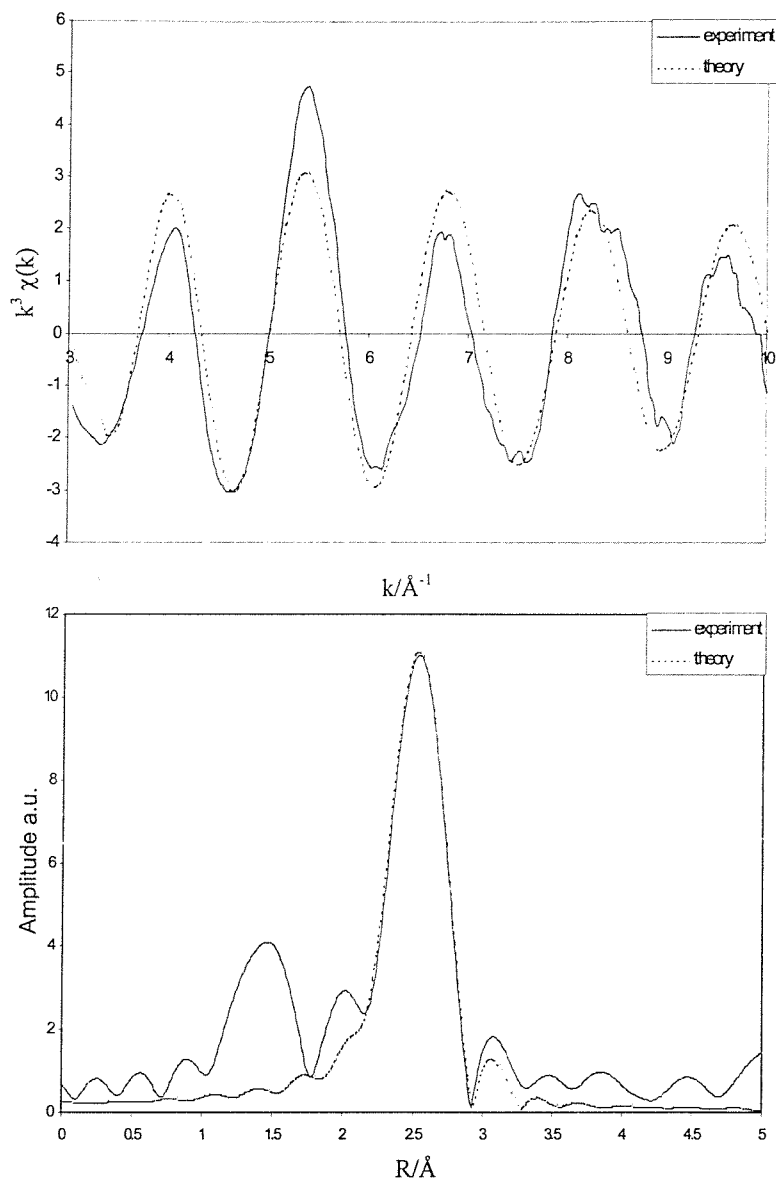
Figure 4.1 The U L (III)-edge k^3 weighted EXAFS spectrum and phase shift corrected Fourier transform of uranium tetrachloride, diluted to 10wt% U in a boron nitride matrix

$$EF= -7.6 \qquad R= 36.14 \qquad F.I= 11.4 \times 10^{-4}$$

Shell(n)	Tn	Cn	Rn(Å)$_{EXAFS}$	Rn(Å)$_{Neutron}$[4]	a $(2\sigma^2/Å^2)_{EXAFS}$
1	Cl	4	2.63(1)	2.638(4)	0.013(2)
2	Cl	4	2.82(2)	2.866(1)	0.028(2)

Table 4.1 EXAFS derived structural parameters for uranium tetrachloride, diluted to 10wt% U in a boron nitride matrix. Statistical errors are given in brackets

The uranium-chlorine distances found are in reasonable agreement with those derived from a neutron diffraction study by Taylor *et al* in 1973[4] also given in table 4.1. UCl_4 has a body-centred tetragonal unit cell with the uranium surrounded by eight chlorine atoms, all of which are bridging between two uranium centres. These eight may be divided into two orthogonal coincident tetrahedra. As such, the chlorines are fitted as two shells of four atoms. The large feature in the Fourier transform of the experimental data centred at 1.4 Å is thought to be the result of multiple excitations at the absorbing atom making background subtraction problematic. This can become significant for the heavier elements with large numbers of core electrons.

4.2 Precursor Deposition and Characterisation of Supported Materials

The mesoporous silica support used was synthesised using Brij76 as the liquid crystal templating surfactant, as previously described. This was calcined in nitrogen at 470°C for 4h, and at the same temperature in oxygen for 8h to remove the organic material. It was then further calcined at 800°C for 8h in oxygen. The non-mesoporous silica used was ES70 silica obtained from BP, which has a disordered structure with some microporosity. The γ-alumina used was obtained from Degussa, and both this and the ES70 silica were also pre-treated at 800°C in oxygen for 8h. All support materials were kept in a vacuum desiccator prior to use.

Both precursors were evaporation deposited at 30wt% uranium maximum theoretical loading on to the support. This is equivalent to approximately 10mol% uranium. Uranyl nitrate was deposited from aqueous solution, and a typical preparation was as follows. 2.52g $UO_2(NO_3)_2.6H_2O$ was dissolved in 4.56g of distilled water. This was added dropwise to 1.48g of support, and allowed to mix to homogeneity for 2h. The water is then removed *in vacuo*, and the material is then further dried at 100°C under vacuum for 12h. Uranium tetrachloride was deposited in exactly the same way, except that the solvent used was tetrahydrofuran. Several methods have been used in an attempt to determine the structure of these supported materials.

4.2.1 Characterisation of Supported Uranium Species
4.2.1.1 X-ray Powder Diffraction

Characterisation of the supported uranyl nitrate species is facile with the use of X-ray powder diffraction. The diffraction pattern of the material is shown to be independent

of the support used, and may be identified as uranyl nitrate dihydrate using the JCPDS peak index database.[5] The hexahydrate was originally used in the preparation, and this indicates that the deposition and drying process has resulted in incompletely hydrated uranyl nitrate crystallites on the surface.

The structures of the supported uranium tetrachloride materials have proved more difficult to identify. No diffracted X-ray intensity was observed for the amorphous silica and alumina supported samples. However, the mesoporous silica supported material did afford a complex powder diffraction pattern, and this is compared with that of unsupported uranium tetrachloride below:
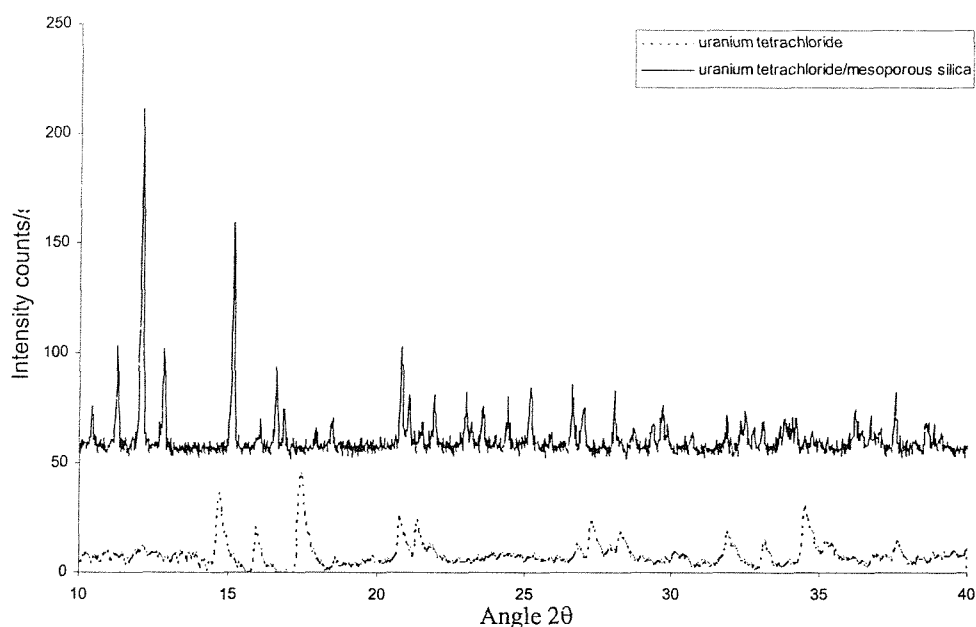
Figure 4.2 X-ray powder diffraction patterns of uranium tetrachloride and uranium tetrachloride/mesoporous silica

It is possible to observe a very clear difference between these two diffraction patterns. The unsupported material diffracts only weakly, but it is possible to identify the phase as uranium tetrachloride by comparison with the literature.[2] The supported sample diffracts more strongly, but it has not been possible to identify with any certainty the phase produced. This diffraction pattern does not agree well with any of the literature examples of patterns from uranium chloride, or oxychloride materials, but there does appear to be some level of similarity between the general appearance of the pattern above, and that calculated from the neutron diffraction pattern for the orthorhombic uranium oxide dichloride $(UOCl_2)$[6]. However, it should be noted that the pattern shown above is far more complicated than the literature example, and the reflections that do appear common to both

are shifted with respect to each other. These shifts in d-spacing are not consistently to either higher or lower values, and there are a large number of reflections in the pattern of uranium tetrachloride/mesoporous silica that are not present in that of $UOCl_2$, and vice versa.

There are three reasonable explanations for this observed chemical change on deposition. One is that the tetrachloride undergoes a chemisorption reaction with the silica surface to produce an adsorbed species, but it is not clear how this would result in a material with sufficient long range order to constructively diffract X-rays. A second explanation is that this change in structure is a result of the formation of a tetrahydrofuran adduct in solution, which persists on the removal of bulk solvent. Uranium tetrachloride is known to undergo adduct formation in a number of co-ordinating solvents, including nitriles,[7] isonitriles,[8,9] ethers,[10,11,12,13], and phosphines,[14] although the structures of very few of these compounds are known. Adduct formation with tetrahyrofuran to form $[UCl_4(thf)_3]$ has also previously been observed, and for this material a crystal structure has been determined[15]. Within the rhombohedral unit cell, the structure is one of discrete molecular units, where the geometry of each unit is based on a pentagonal bipyramid (see opposite). However, dissolution of UCl_4 in tetrahydrofuran, followed by solvent removal *in vacuo* did not yield a diffracting material in the absence of the mesoporous silica. It is possible that the structure of the mesopores in the templated silica have an influence on the

formation of particles, with some directional ordering effect. The absence of a long range ordered uranium material on amorphous silica and alumina analogues is limited supporting evidence for this proposal. The third, and most likely, explanation for this chemical change, noted by comparison of the X-ray powder diffraction patterns, is some support mediated reaction of the uranium tetrachloride, or its tetrahydrofuran adduct, to form a $UOCl_2$-type phase. Note that the existence of the uranium species on the surface as a mixture of all three possibilities cannot be discounted at this stage.
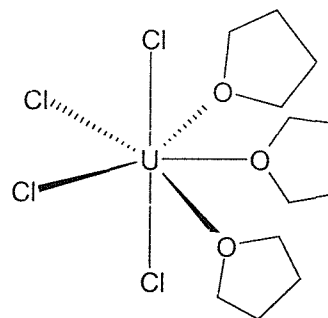
The X-ray diffraction patterns of the mesoporous materials displayed a single peak at low angle corresponding to the (100) reflection. The intensity of this peak was reduced with respect to the pure silica, and, taken with the lack of other low angle peaks, this suggests that there is a decrease in long range order. This is due to the fact that the mol% of material adsorbed is large, and this has the effect of decreasing the local order of the

pore walls. This will result in a broadening of the diffraction peak, but does not necessarily indicate any support structure collapse.

4.2.1.2 Isothermal Nitrogen Adsorption

This technique has been used to measure the effect of uranium precursor deposition on the surface area and pore size distribution of materials. The table below demonstrates this dependence:

Sample	Surface Area/m^2g^{-1}	Surface Area/ m^2/gram of support
mesoporous silica/H_1SiO_2	700	
UCl_4/H_1SiO_2	430	826(725)
$UO_2(NO_3)_2.6H_2O/H_1SiO_2$	313	845(789)
amorphous silica/SiO_2	219	
UCl_4/SiO_2	65	115(143)
$UO_2(NO_3)_2.6H_2O/SiO_2$	61	164(154)
amorphous alumina/γ-Al_2O_3	90	
UCl_4/γ-Al_2O_3	18	32(40)
$UO_2(NO_3)_2.6H_2O/\gamma$-$Al_2O_3$	15	40(38)

Table 4.2 Surface area dependence on uranium precursor and inorganic oxide support. The numbers in brackets correspond to the adsorption of the tetrahydrofuran adduct [$UOCl_2$] for tetrachloride materials, and the dihydrate [$UO_2(NO_3)_2.2H_2O$] for uranyl nitrate materials.

The second column of table 4.2 gives the surface area in m^2g^{-1}, and this absolute value is very useful in many respects. However, the data presented in this form can be misleading, as it suggests some support structural collapse unless the mass of the supported material is taken into account. This contribution is important if, as in this case, the mass of supported material is large compared to the mass of support. For this reason, a third column has been included to give surface area per mass unit of support. In addition, for the uranium tetrachloride materials, a value corrected for the adsorption of the $UOCl_2$-type species has also been included in brackets in this third column, and for the uranyl nitrate materials a value corrected for the dihydrate [$UO_2(NO_3)_2.2H_2O$].

With these corrections it is possible to note a number of trends. Firstly, the alumina supported materials show the greatest relative reduction in surface area on precursor deposition. The amorphous silica systems show a reduction of approximately 25%, and the mesoporous samples actually appear to show very small increase in surface area if the

bracketed, corrected values are taken. These observations may be giving information about the ability of the support to adsorb solvent, rather than the extent of support structural change. All the supports have been pre-treated at 800°C in oxygen, which will result in extensive surface dehydroxylation. From results discussed earlier, it is clear that this temperature regime will lead to greater dehydroxylation for the mesoporous silica, than for the amorphous silica. It has been suggested that alumina requires higher temperatures for equivalent dehydroxylation compared to silica,[16] and that it rehydrates more readily. So, if the mesoporous silica has the most hydrophobic surface after calcination, then it is reasonable to suggest that it will adsorb the least water in the uranyl nitrate deposition, with amorphous silica slightly more, and alumina more again. Indeed this is confirmed in the DRIFTS spectra of these materials This adsorbed water will contribute to the mass of the sample in the surface area analysis, and this is not accounted for either in the mass of support originally used, or in the corrected value. The result will be that the greater the ability of a support to adsorb water, the greater the observed reduction in surface area will be, and this is in agreement with the table above. These same sites may be expected to enhance the adsorption of tetrahydrofuran in the deposition of the tetrachloride, leading to similar results for both precursor systems. This probably indicates that the deposition has little effect on support structure.

The pore size distributions of the mesoporous silica supported uranium materials were calculated,[17] and these are given below:
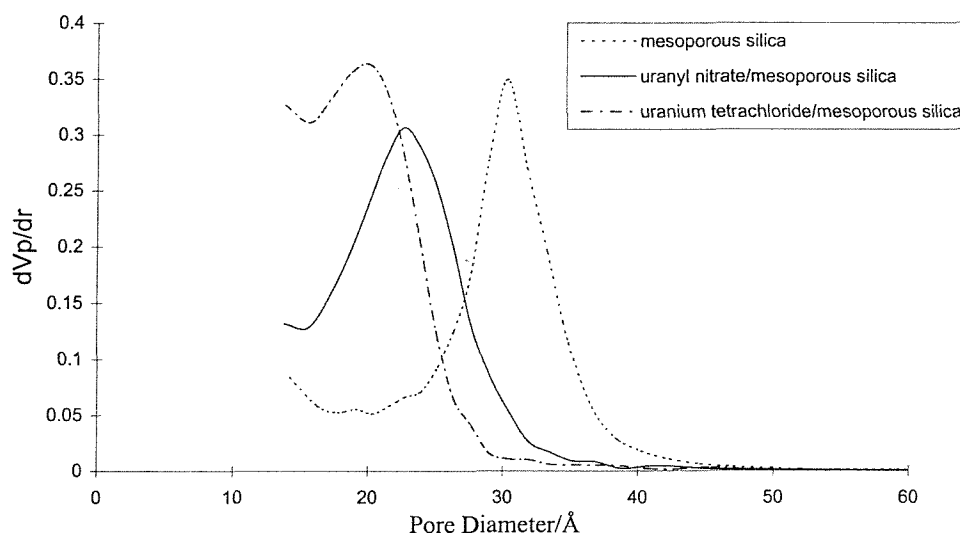
Figure 4.3 Dollimore-Heal pore size distributions for mesoporous silica supported uranium materials

It is possible to observe that the maxima in the pore size distributions of uranium impregnated materials is reduced with respect to the pure support. The maximum decreases from 30Å to 22Å for the uranyl nitrate material, and to 20Å for the uranium tetrachloride derivative. This is as expected if the pore walls are considered to be covered with uranium material. There also appears to be a slight broadening of distribution, relating to greater disorder in the pore channels. This is also apparent in the nitrogen adsorption isotherms of these materials with the absence of the well-defined step apparent in that of the pure silica. The maximum in pore diameter in the distribution of the tetrachloride material is approximately 2Å less than that of the nitrate analogue, and it is proposed that this is a result of the physical size of the adsorbate.

4.2.1.3 EXAFS Analysis

U_{LIII} edge EXAFS spectra of these supported materials have been recorded. The spectra of the supported uranyl nitrate species were indistinguishable from that of the pure compound by this technique, and the details will not be presented here. A fit obtained for the EXAFS spectrum of uranium tetrachloride supported on mesoporous silica, along with the parameters used to define it, is given below:
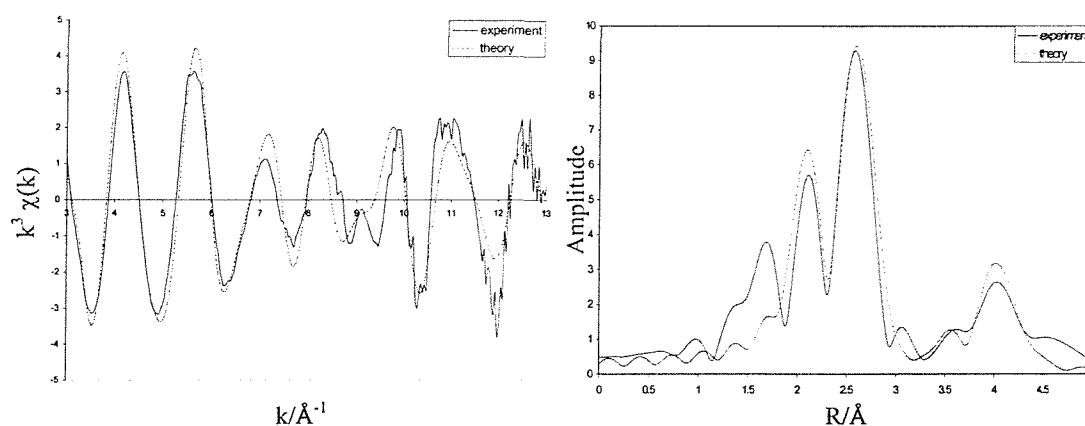
Figure 4.4 The U L (III)-edge k^3 weighted EXAFS spectrum and phase shift corrected Fourier transform of uranium tetrachloride/H_1SiO_2, diluted to 10wt% U in a boron nitride matrix

$$EF= -2.3 \qquad R= 32.14 \qquad F.I= 6.5 \times 10^{-4}$$

Shell(n)	Tn	Cn	Rn(Å)$_{EXAFS}$	a $(2\sigma^2/\text{Å}^2)_{EXAFS}$
1	O	2.0(2)	2.22(1)	0.007(1)
2	Cl	3.9(2)	2.61(1)	0.018(1)
3	U	2.0(4)	3.68(1)	0.013(3)
4	U	2.0(5)	4.31(3)	0.018(4)

Table 4.3 EXAFS derived structural parameters for uranium tetrachloride/H_1SiO_2, diluted to 10wt% U in a boron nitride matrix. Statistical errors are given in brackets

This data did not fit to the same parameters used for pure uranium tetrachloride, which is further evidence for some structural change on dissolution or deposition. The theoretical model to which the data was fitted consists of four shells of atoms. The first shell is of two oxygens at 2.22Å. In a U^{6+} uranyl type system, the axial U=O double bond is typically ~1.75Å, and this value is almost independent of the number of equatorial ligands.[18] These uranyl systems, based on the ion UO_2^{2+} are by far the most prevalent for U^{6+}. It was not possible to fit oxygen at such a short distance for this data, so it is reasonable to suggest that uranium tetrachloride supported on mesoporous silica is not a U(VI) system. A U-O distance of 2.22Å is more typical of a U-O single bond,[18] but this distance is obviously quite sensitive to the type of oxygen donor. For a neutral oxygen ligand such as isopropanol,[19] or tetrahydrofuran,[15] this distance is approximately 2.4 to 2.5Å. A distance of 2.22Å is in closer agreement with that found for the co-ordination of charged oxygen species such as alkoxides,[20] or neutral donors with some double bond character such as ureas[21] i.e. C=O-U. The second shell to be fitted is for four chlorines at 2.61Å, which is similar to the distance found for the first chlorine shell in pure uranium tetrachloride (2.63Å). The length of the uranium chlorine bond in the systems discussed above varies very little with the type of oxygen donor for neutral molecues. As such, using the length of this U-Cl bond as evidence for the overall structure, only the formation of a salt, where U-Cl distances are significantly different,[22] may be discounted. Attempts to fit a second shell of chlorine at ~2.8Å, as for the pure system, resulted in an extreme increase in the fit index. It was, however, possible to fit two shells of two uraniums at 3.68Å and 4.31Å, and the presence of these uranium shells is another clear difference between this system and that of the pure tetrachloride. It should also be noted that the minimum U-U distance in the tetrahydrofuran adduct is greater than 5Å. These uranium-uranium

distances should be related to either the uranium-oxygen, or uranium-chlorine distance, as they suggest the presence of a bridging species. One possible explanation is shown below:

$$2 \times (2.61\cos45°) = 3.68$$

The trigonometric relationship is only limited evidence for the bridging chlorine species, as it assumes a U-Cl-U bond angle of 90°, and the distance found for the second uranium shell (4.31Å) is slightly shorter than might be expected for a linear U-O-U linkage (4.44Å assuming U-O-U angle of 180°). However, it does allow a structural model for the supported species to be proposed:
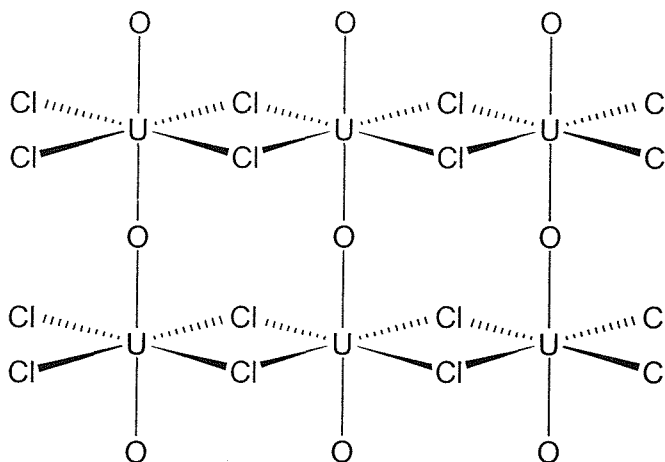
The mechanism of formation of this structure from the tetrahydrofuran adduct, or the pure tetrachloride, is not obvious. It should also be noted that the inclusion of a second oxygen shell at 2.48Å, possibly due to co-ordinated tetrahydrofuran, did result in some reduction of the fit index, but this decrease was not sufficient to satisfy statistical tests of the relevance of this shell.[23]. The structure proposed above would have the same stoichiometry as the previously discussed $UOCl_2$, and as such, a description of the structure of this material is appropriate. Within the structure, there are three different uranium environments.[6] The arrangement around U(1) is dodecahedral (C.N. = 8, 3O and 5Cl),

around U(2) trigonal prismatic (C.N. = 9, 4O and 5Cl), and around U(3) is approximately dodecahedral (C.N. = 7, 3O and 4Cl). The three types of polyhedra occur in $U_3O_3Cl_6$ chains running parallel to the c-axis. The chains form a pseudohexagonal array, and are linked by chlorine bridges. The uranium chlorine distances found for this structure range between 2.66 and 3.15Å, and the uranium oxygen distances between 2.17 and 2.40Å. It was not possible to fit this range of values to the EXAFS data obtained, and it may be that the EXAFS fit given is an average structure of the three types of uranium described. Interestingly, there is good agreement between the U-U distances found by the two methods. The formation of a chain structure might provide some explanation for the appearance of a structure of sufficient order to produce an X-ray diffraction pattern when the support used is mesoporous silica, especially if the unidirectional pore structure has a directional ordering effect.

EXAFS spectra of the analogous amorphous alumina and amorphous silica materials provide similar models to that given above. This suggests that supporting the uranium compound on mesoporous silica affords it a greater degree of order, without altering the local structure with respect to that formed on the non-mesoporous supports.

4.2.1.4 Diffuse Reflectance UV-vis/NIR Spectroscopy

As has been previously stated, the UV-vis absorption spectra of actinide compounds are very complex, and no attempt has been made to try and assign the features in the spectra obtained to particular electronic transitions. Instead, these spectra are used as a fingerprint for a particular system. The spectra obtained for pure uranium tetrachloride, and the mesoporous silica supported material are given below:
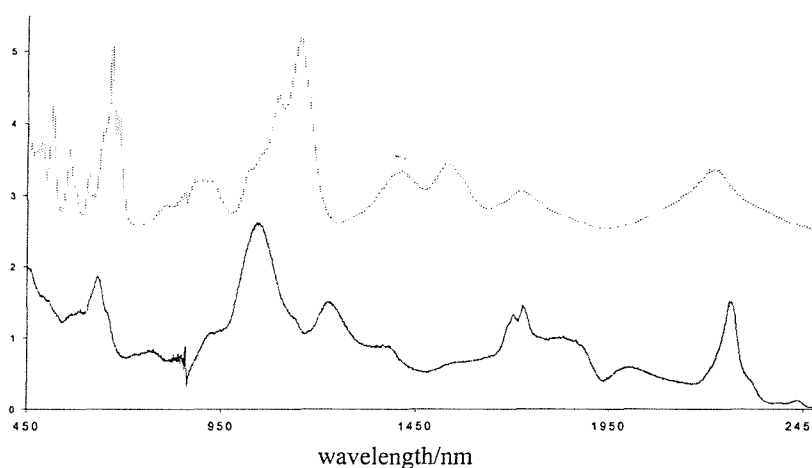
Figure 4.5 Diffuse Reflectance UV-vis/NIR spectra of UCl_4 (dashed line) and UCl_4/H_1SiO_2 (solid line)

A comparison of the two spectra above demonstrates a clear difference between the pure and adsorbed species, and also indicates that this is not a result of oxidation to U^{6+} as transitions involving f electrons are observed in the spectra of both. Comparison with a literature spectrum of the tetrahydrofuran adduct demonstrates that the supported material is different again. It is difficult to gain any further information without very extensive calculations.

4.2.1.5 Simultaneous Thermal Analysis

This technique is simply a combination of thermogravimetric analysis (TGA) and differential thermal analysis (DTA). Samples were heated in static air to 800°C at a constant ramp rate of 20K/min. The TGA thermal curves for uranyl nitrate, and supported materials are given below:
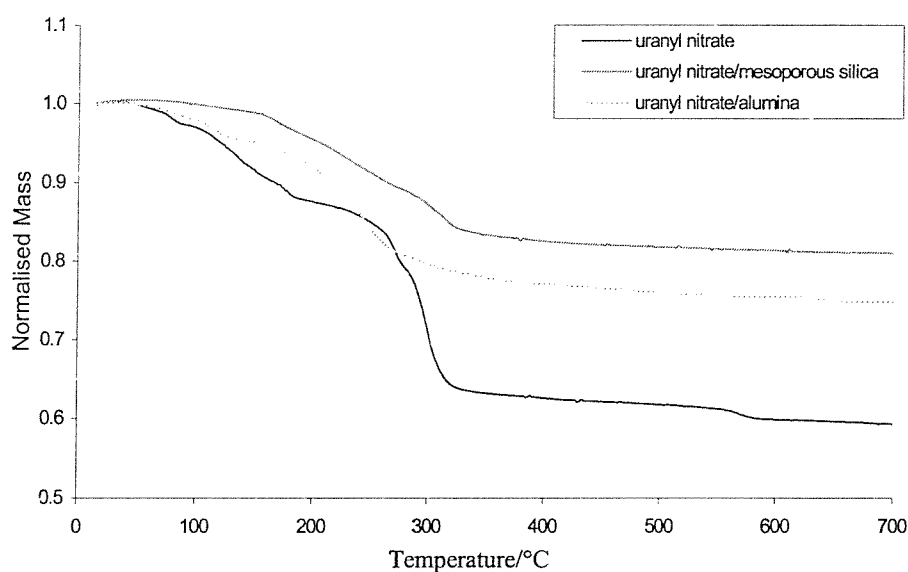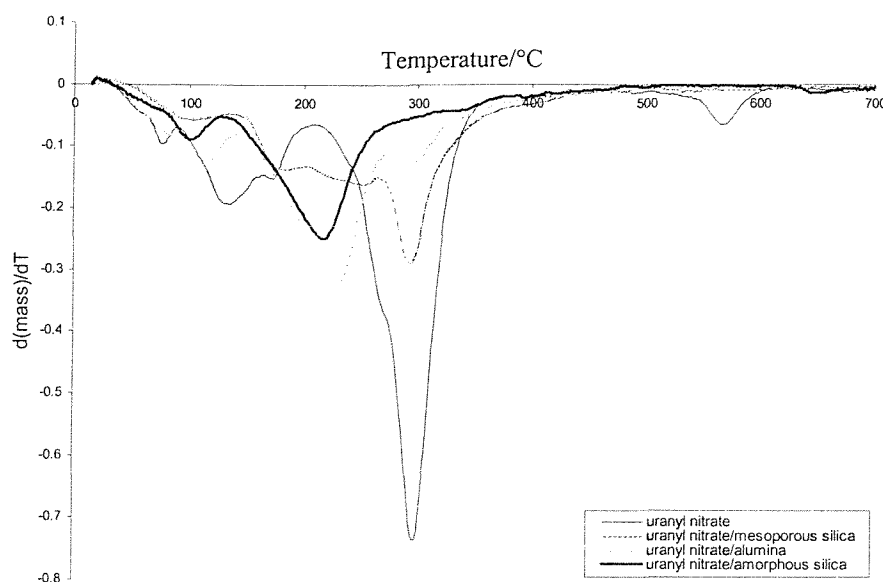

Figure 4.6 Thermal curves of normalised mass loss against temperature for uranyl nitrate hexahydrate, uranyl nitrate/mesoporous silica and uranyl nitrate/alumina

As would be expected, the pure uranyl nitrate sample is subject to greater %weight loss over the temperature range to 700°C shown above than either of the supported samples. This final normalised mass of 58% for this system may be equated with the transition from $UO_2(NO_3)_2.6H_2O$ to uranium oxide U_3O_8 (calculated as 57%). The mass loss for the mesoporous silica supported system may be equated with the transition of 30wt% uranium present as $UO_2(NO_3)_2.2H_2O$ to U_3O_8. The mass loss for the alumina , and to a lesser extent the amorphous silica (not shown) systems is slightly greater than expected. This can be related to the greater capability of these supports to adsorb water

after calcination at 800°C. This may also explain the slightly less well defined shape of the thermal curve for the alumina system, as loss of this adsorbed water would be expected to be a gradual process over a large temperature range. The thermal decomposition of uranyl nitrate hydrates has been extensively investigated,[24,25,26,27,28] and a reaction sequence depicting the evolution of various intermediates has been established for the pure compound $[UO_2(NO_3)_2.2H_2O].4H_2O$.[29] The process involves four sequential dehydration steps:

$$[UO_2(NO_3)_2.2H_2O].4H_2O$$

$$\downarrow$$

$$[UO_2(NO_3)_2.2H_2O].2H_2O$$

$$\downarrow$$

$$[UO_2(NO_3)_2.2H_2O].H_2O$$

$$\downarrow$$

$$[UO_2(NO_3)_2.2H_2O]$$

$$\downarrow$$

$$[UO_2(NO_3)_2.xH_2O].$$
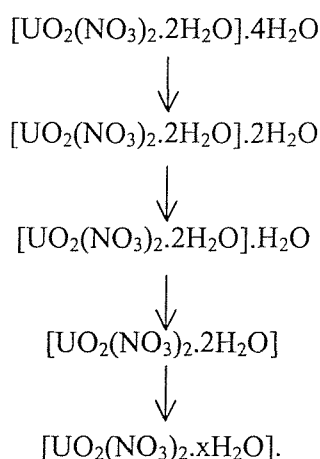
The first two of these steps occur at ~60-90 and 90-100°C respectively. The third stage occurs at 110-130°C and the last is believed to happen concurrently with the first of two NO_x loss events at ~190°C. The second NO_x loss event occurs at ~280-300°C and results in the conversion of $[UO_2(NO_3)_y.xH_2O]$ to $[UO_2(OH)_x]$. The final stages of decomposition occur over rather larger temperature ranges, and involve the transition of $[UO_2(OH)_x]$ to U_3O_8 via UO_3H_x.

The weight loss events that are apparent in the thermal curve of the pure compound at ~170 and 290°C are also observed in that of the mesoporous silica supported material, and suggest that the support is having little influence in the temperature at which these stages of decomposition occur. It is difficult to obtain exact temperatures from the thermal curves as they are given as above, particularly for the alumina supported material. For this reason, these curves are differentiated with respect to temperature. The result is a much more accessible plot from which temperatures may be more accurately determined. This is shown overleaf:

Figure 4.7 Differentiated thermal curves of mass loss against temperature for uranyl nitrate hexahydrate, uranyl nitrate/mesoporous silica, uranyl nitrate/alumina and uranyl nitrate/amorphous silica

From this plot it is possible to observe that the major weight loss event for the decomposition of uranyl nitrate has a support dependence, with this process occurring at lower temperature for amorphous silica and alumina supported than for the mesoporous silica analogue. Possibly this initial decomposition stage is accelerated in the presence of water.

The differential thermal analysis experiments allow these weight loss events to be related to the thermodynamics of phase change or decomposition. From the raw data, it is possible to determine whether heat flow is occurring to or from the sample, but the temperature at which this occurs is difficult to determine. For this reason, the data presented overleaf is shown with the result of differentiation with temperature; essentially a second derivative plot.
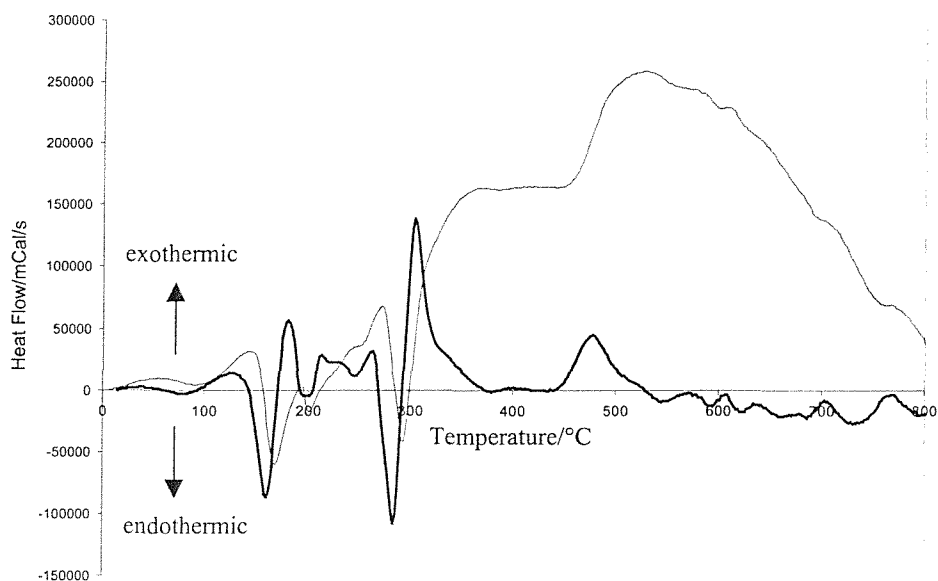
Figure 4.8 Differential thermal analysis curve (thin line) and derivative plot (thick line)for uranyl nitrate/mesoporous silica

The plot above is for the uranyl nitrate system supported on mesoporous silica. It is possible to observe that there are at least two endothermic processes that occur as the sample is heated, and a plot showing derivative curves from both TGA and DTA for this system demonstrates the link between these endotherms and weight loss events:
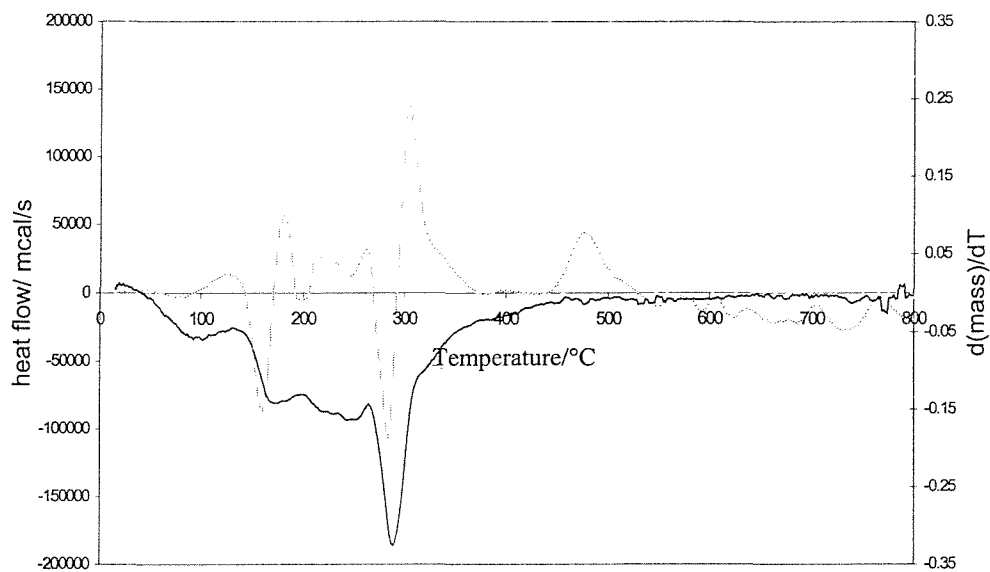
Figure 4.9 Derivative plots of the TGA curve (solid line) and DTA curve (dashed line) for uranyl nitrate/mesoporous silica

It is now possible to directly relate the weight loss events to thermodynamic processes. The most likely explanation is that these features are due to the thermal desorption of water and nitrogen oxide species as the uranyl nitrate decomposes to form a uranium oxide phase, as has been demonstrated for the pure compound,[29] but another technique is required in order to confirm this. To this end, the thermal decomposition has also been followed with the use of mass spectrometry. The microreactor configuration is described in chapter 2. Experiments were performed on 20mg of sample in an oxygen flow of 10ml/min, and the sample was heated to 600°C at a linear ramp rate of 10K/min. A plot of selected masses from such an experiment on the uranyl nitrate on mesoporous silica system, along with the associated derivatised TGA curve (inverted for an easier comparison) is shown below:
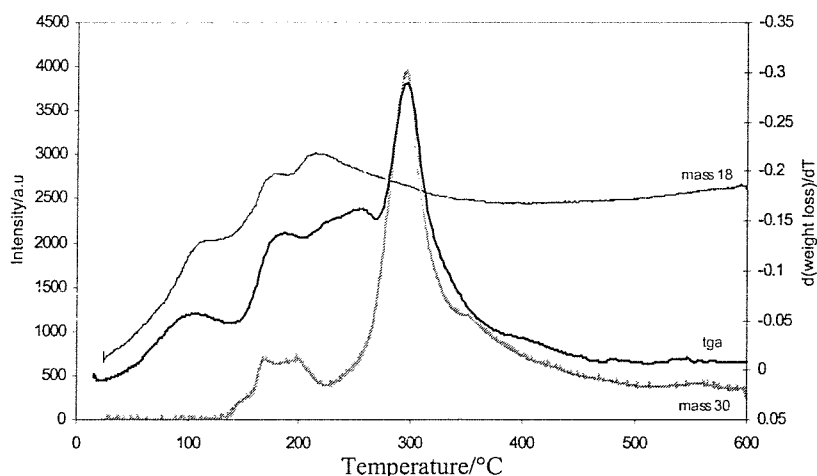
figure 4.10 Mass spectrometry trend curves with the inverted derivatised TGA of uranyl nitrate on mesoporous silica

The graph above allows the mass loss events observed in the TGA to be directly attributed to the desorption products. The intensity of the mass 18 curve may, in this case, be reasonably assigned as solely due to the desorption of water. This curve follows that of the TGA trace very well at lower temperatures, and water loss events may be observed at ~100, 170, and 210°C. These events are consistent with features in the TGA, and the fact that there is some structure to this desorption curve suggests that this is not simply due to the loss of randomly adsorbed water. It is worth noting that the second and third of these events occur at higher temperatures than that previously reported,[29] and that found in this work, for the pure uranyl nitrate material. Mass 30 is assigned as the NO species, and the

shape of this curve is also observed for that of mass 46, assigned as NO_2 (not shown). The conclusion is that the intensity in the mass 30 trend graph is attributable to decomposition of the nitrate species. This appears to occur in two stages, the first at ~170-200°C, and the second at 300°C. These values agree well with those found for the pure material. The second of these involves much greater NO_x desorption than the first for the mesoporous system, reflected in both the mass 30 intensity, and the TGA mass loss curve. If this was a sequential loss of nitrate species from $UO_2(NO_3)_2$, then it would be expected that both mass loss peaks would be of equal intensity, and this is not the case. A possible explanation is that this process occurs by firstly a decomposition of uranyl nitrate, which results in a small amount of NO_x desorption and significant NO_x adsorption on the silica surface, and secondly the desorption of this adsorbed material. Another explanation is that initial water and NO_x loss is the result of a phase change to a material with nitrate groups bridging between an increased number of uranium atoms, and the second mass loss peak is a result of decomposition of this intermediate phase. This second mechanism is that previously reported in the literature for the pure material.[29] If these two NO_x loss processes are termed NO(I) and NO(II), with NO(I) referring to the lower temperature event, then the temperatures at which these occur may be a sensible method by which to summarise the effect of support variation on uranyl nitrate decomposition. This is shown in Figure 5.11
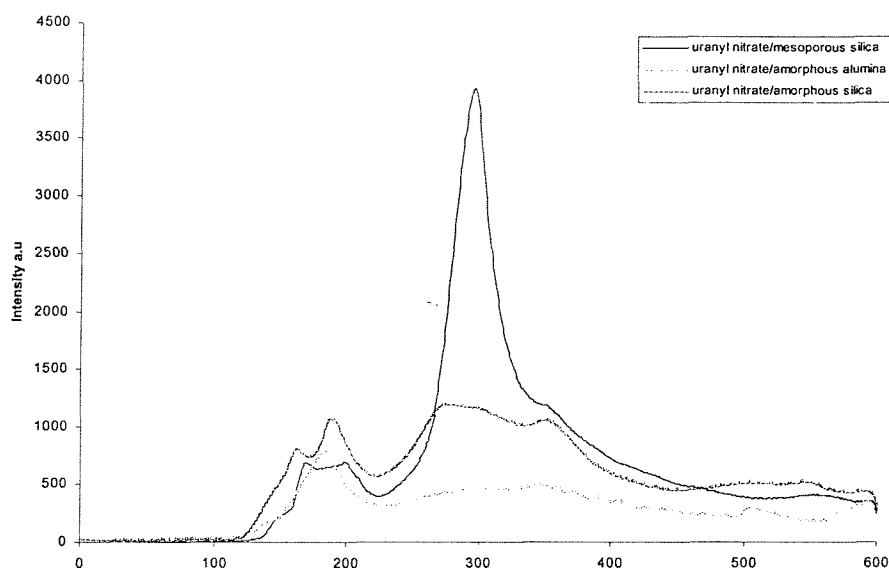
Figure 4.11 Mass 30 desorption trend graphs for uranyl nitrate supported on mesoporous silica, amorphous silica, and amorphous alumina

It is very interesting to note the different shapes of these trend graphs, and the variation in relative intensity of the two NO_x evolution peaks discussed earlier. It appears that there is a different mechanism of decomposition, or at least of NO desorption for the mesoporous material. The temperatures at which the events occur are similar from one support to another, but, as was noted by TGA, much of the mass loss occurs at the lower temperature event NO(1) for the amorphous materials. This may again be possibly due to the water content of the support being greater for these systems. This may enhance desorption over decomposition and adsorption, or prevent the formation of an intermediate phase. The pore structure of the mesoporous material may also have an effect, promoting the retention of NO_x on the surface, or preventing intermediate phase formation.

The supported uranium tetrachloride materials have been subjected to identical analysis techniques. The TGA thermal curves differentiated with respect to temperature for these systems are given below:
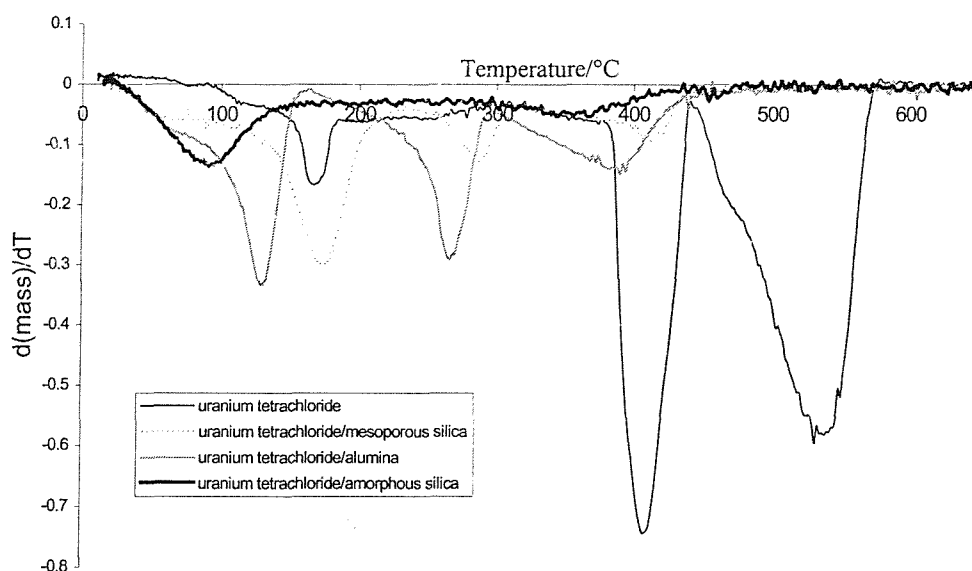
Figure 4.12 Differentiated thermal curves of mass loss against temperature for uranium tetrachloride, uranium tetrachloride /mesoporous silica uranium tetrachloride /alumina and uranium tetrachloride /amorphous silica

The total mass loss for pure uranium tetrachloride equates with a transition from UCl_4 to U_3O_8, which is as expected. There are mass loss events at 170, 400 and 530°C. The first of these is quite possibly the loss of water that is adsorbed in the short time that the sample is exposed to air before the experiment begins. The higher temperature features are almost certainly due to the loss of chlorine containing species. It is interesting to note

that this appears to occur in two stages. The first stage is very likely to be the result of the following reaction:[30]

$$UCl_4 + O_2 \xrightarrow{\;350°C/2h\;} UO_2Cl_2 + Cl_2$$
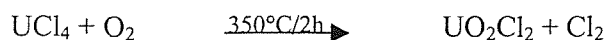
The theoretical mass loss for this process is calculated as equal to that observed from the TGA feature centred at 400°C. The fact that this reaction is known to occur at 350°C, but mass loss does not begin until 390°C according to the TGA curve is an important point to note. The ramp rate used for these experiments is 20K/min, which is slightly higher than would be ideal to gain maximum resolution by TGA but is required to avoid the smearing out of thermodynamic events in the DTA curve. The result is obviously some degree of apparent temperature lag, and this should be considered when assigning exact temperatures to processes. The mass loss event centred at 530°C is proposed as the transition from UO_2Cl_2 to a uranium oxide phase, with the loss of further chlorine, and again the calculated mass loss agrees with that observed.

The most obvious point to note from the plot on the previous page is that the major mass loss events occur at much lower temperatures for the supported samples, with the apparent order amorphous silica ● alumina < mesoporous silica. The combination of results from mass spectrometry and TGA for the UCl_4/γ-Al_2O_3 system are plotted below
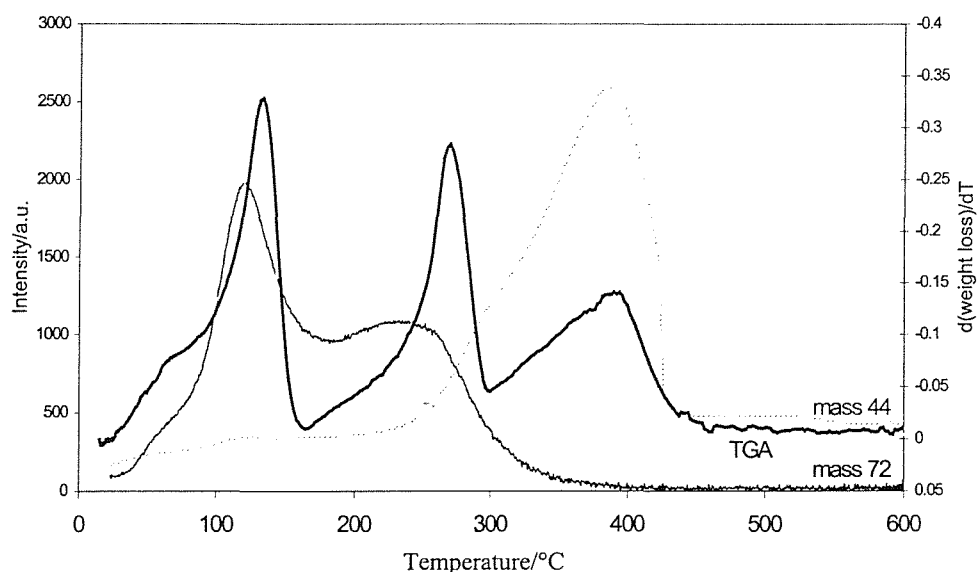
Figure 4.13 Mass spectrometry trend curves with the inverted derivatised TGA of uranium tetrachloride on amorphous alumina

There are three distinct mass loss events in the TGA of the alumina supported material, and these are all coincident with endotherms in the DTA. They occur at 130, 265

and 390°C, and the mass spectrometry trend graphs allow the origins of these features to be proposed. The mass 72 signal is expected to have contributions from both tetrahydrofuran and chlorine. These may be separated out from the coincident signal due to chlorine at mass 70 and 74. The low temperature mass loss event is due to the loss of tetrahydrofuran. This will probably be the loss of tetrahydrofuran adsorbed on the support surface, though the presence of a small amount of tetrahydrofuran adduct on the surface cannot be discounted. The second mass loss peak also has a contribution from mass 72, as well as mass 44 that may be assigned as CO_2 formation. At this temperature there is also evidence of species in the mass spectrometer that are likely to signify the formation of HCl at masses 36 and 38, so it appears that chlorine loss is occurring at this point in the decomposition. The possible origin of this is conversion of the $UOCl_2$-type phase to a more highly oxidised uranium species such as a UO_3-type material. The origin of CO_2 evolution, which also seems to account for the mass loss peak at 390°C, must be the total oxidation of tetrahydrofuran decomposed on the surface. Presumably, when the tetrahydrofuran is lost from the uranium tetrachloride adduct, some of this desorbs immediately but some adsorbs on the surface and decomposes. This decomposed material then persists until the temperature is high enough to enable full oxidation to CO_2 and water (mass 18 not shown).

The reasons why the uranium tetrachloride decomposition occurs at lower temperature for the supported materials compared to the pure material may be complex. The increased dispersion of the uranium species on deposition may have an effect, as, obviously, will the fact that the starting material appears to be a $UOCl_2$-type phase in the supported materials. The support dependence of this temperature variation might be related to the number of surface hydroxyl groups available as sites for adsorption, which may also have a direct effect on the dispersion of uranium phase. Uranium tetrachloride and its oxychlorides, like most uranium halides, is very moisture sensitive, and though the surface hydroxyls are not expected to be very reactive,[31,32] it is possible that a hydrolysis process accelerating decomposition may occur at higher temperatures. Note also that the amorphous silica and alumina supported materials did not have sufficient long range order to yield an X-ray diffraction pattern, in contrast with the mesoporous silica analogue. The apparent long range ordering for this system could point to a less well-dispersed uranium system on the mesoporous silica, hindering the decomposition process.

The next logical step is to attempt to characterise the uranium oxide phase that is formed on the calcination of the supported materials.

4.2.2 Characterisation of Calcined Supported Uranium Species

The supported uranium materials described in the previous section were then calcined, in order to produce a supported uranium oxide. Initially, two calcination temperatures were chosen, at 450 and 800°C, to allow a direct comparison with systems reported in the literature.[33] The sample was placed in a porcelain combustion boat, which in turn was placed in the centre of a tube furnace under a flow of air at 20ml/min. Samples were heated to the target temperature at a linear ramp rate of 10K/min, and held at this temperature for 3h, before being allowed to cool. Samples were kept in an evacuated dessicator prior to further analysis. The result of this treatment is 12 different systems, and for convenience and brevity these are designated precursor/calcination temperature/support e.g.Cl/800/H_1SiO_2, Nit/450/γ-Al_2O_3 etc.

4.2.2.1 X-ray Powder Diffraction and Electron Microscopy

These two techniques are to be dealt with simultaneously, as the characterisation information provided by them is complementary. The X-ray powder diffraction patterns of uranium tetrachloride supported on mesoporous silica, calcined at 450 and 800°C are given below:
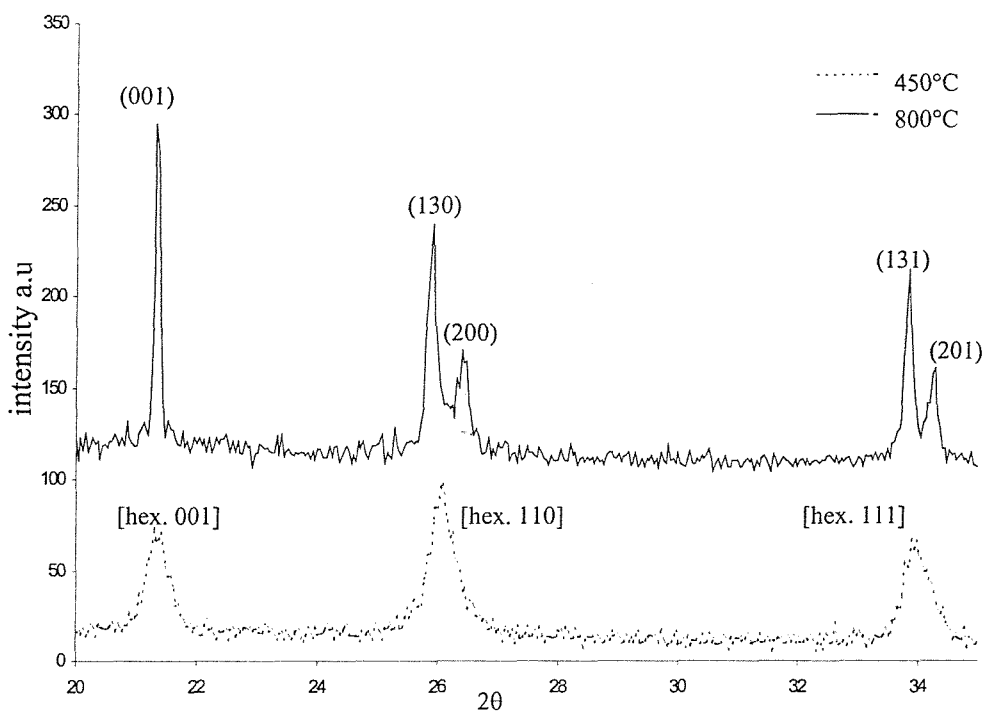
Figure 4.14 X-ray powder diffraction patterns of uranium tetrachloride supported on mesoporous silica, calcined at 450 and 800°C

The powder diffraction pattern for $Cl/800/H_lSiO_2$ may be identified as that of the orthorhombic phase of α-U_3O_8,[34] with the reflections indexed as shown in the figure. The dark green/black coloured U_3O_8 is the most thermodynamically stable of the uranium oxides in oxidising conditions at elevated temperatures,[35] and at an atmospheric pressure of oxygen it is formed from UO_3 at 650-700°C.[36] It is therefore not remarkable that, after calcination at 800°C, U_3O_8 is the product identified. All of the supported materials calcined at 800°C are dark green in colour, and indeed, for all of the six precursor/support systems, α-U_3O_8 is the only identifiable product by X-ray powder diffraction. The $Cl/450/H_lSiO_2$ system is green/yellow in appearance, and the peaks in the diffraction pattern corresponding to the formation of U_3O_8 are of lower intensity, and are broader than for the analogous material calcined at 800°C. This broadening occurs to such an extent, that it is no longer possible to resolve the pairs of reflections around 26 and 34° 2θ. This lack of resolution makes it impossible to unequivocally characterise the supported uranium oxide as the orthorhombic phase, and the presence of the hexagonal phase of U_3O_8 cannot be discounted.[37] The orthorhombic phase has been shown to be the most stable below 375°C, but above this temperature, for the pure material, the hexagonal phase is favoured.[38] This phase transition is totally reversible in conditions where heating and cooling rates are very slow, but the possibility that the hexagonal phase may be effectively frozen out by rapid cooling in the above example cannot be excluded. It is also known that U_3O_8 can undergo oxygen loss processes to become substoichiometric at temperatures in excess of 570°C to become U_3O_{8-z}, and although it is likely that this will also be reversible on cooling, the presence of such material in the final sample is possible. To distinguish between this oxygen deficient product, and the stoichiometric phase is not possible with the techniques discussed here, and so the material will be assigned as simply U_3O_8 for convenience.

It is important to note that the many yellow/orange polymorphs of UO_3, the other likely products of extensively heating uranium compounds in oxidising conditions, are often formed as an amorphous material,[39] and even the crystalline forms of most polymorphs are only weakly diffracting.[40] It is therefore quite likely that the uranium oxide present in the $Cl/450/H_lSiO_2$ material is actually a mixture of U_3O_8 and UO_3.

Interestingly, there is only evidence of U_3O_8 formation for two systems calcined at 450°C, the previously mentioned $Cl/450/H_lSiO_2$, and $Cl/450/\gamma$-Al_2O_3. Both of these materials are green/yellow, and, as suggested above, it is quite probable that the formation of U_3O_8 from the UO_3 type phase is not complete for both these materials. In contrast, for

the amorphous silica supported analogue and all the nitrate derivative samples, no observable peaks are present in the recorded diffraction patterns of materials calcined at 450°C. All these materials are a bright yellow/orange colour, which suggests the presence of UO_3. It would then appear that both the nature of the uranium precursor, and the support material, are factors affecting U_3O_8 formation.

In order for sharp diffraction maxima to be observable in the powder patterns of X-ray diffracting materials, the crystallites must be of sufficient size to ensure that, slightly away from the 2θ maximum, destructive interference occurs. In materials with very small crystallites and few diffracting planes, the diffracted X-ray intensity at a small increment removed from the Bragg angle does not totally destructively interfere, and this leads to a broadening of the reflections. As such, the peak widths of the reflections in the diffraction patterns of these calcined materials may be used to gain an estimate of the average U_3O_8 particle size, with the use of the Scherrer formula. This formula relates the thickness of the crystallites to the breadth of peaks in the diffraction pattern:[41]

$$t = \frac{0.9\lambda}{\cos\theta\sqrt{B_M^2 - B_S^2}}$$ Eq. 4.1

where t is the crystallite thickness, λ the X-ray wavelength, θ the Bragg angle and B_M and B_S are the full width in radians of diffraction peaks of the sample and a standard at half height. The standard peak width was obtained from a highly crystalline sample of U_3O_8, and this represents the instrumental broadening. It is assumed when using the Scherrer equation, that the lattice is not strained. The peak chosen for this analysis is the (001) reflection centred at ~21° 2θ, as it is not split into two peaks by the reduction in symmetry from hexagonal to orthorhombic phase, and therefore no assumptions regarding which phase is present are necessary. The statistical, and systematic errors present in this form of data analysis will be discussed later in this section. The results of the analysis are presented in table 5.4:

Supported Material	Crystallite Thickness/nm
$Cl/450/H_ISiO_2$	41
$Cl/800/H_ISiO_2$	156
$Cl/450/SiO_2$	N/A
$Cl/800/SiO_2$	36
$Cl/450/\gamma\text{-}Al_2O_3$	23
$Cl/800/\gamma\text{-}Al_2O_3$	65
$Nit/450/H_ISiO_2$	N/A
$Nit/800/H_ISiO_2$	130
$Nit/450/SiO_2$	N/A
$Nit/800/SiO_2$	33
$Nit/450/\gamma\text{-}Al_2O_3$	N/A
$Nit/800/\gamma\text{-}Al_2O_3$	71

Table 4.4 Calcination temperature and support dependence of U_3O_8 crystallite thickness.

The table above reveals a complex relationship between U_3O_8 particle size and precursor/support. The first point to note is that, where there is evidence of U_3O_8 at 450°C, the particle size has increased with the calcination temperature, so that the U_3O_8 crystallite size is larger for materials calcined at 800°C. This suggests that some sintering process is occurring beyond the initial U_3O_8 formation. This is an important phenomenon to consider, as any sintering will obviously reduce the specific surface area of the uranium oxide phase, and this could be expected to be a factor in determining the activity of these materials as heterogeneous catalysts.

A second very important point is that the U_3O_8 particles formed from the mesoporous silica supported materials appear, on average, to actually be much larger than the pore dimensions. The maximum in the pore size distribution of the Brij76 templated mesoporous silica calcined at 800°C was at 3.0nm, whereas the average crystallite thickness for U_3O_8 particles in the $Cl/800/H_ISiO_2$ and $Nit/800/H_ISiO_2$ systems are calculated as 156 and 130nm respectively. These dimensions are more than an order of magnitude larger than the pore diameter, and strongly suggest that the diffracting U_3O_8 material is actually on the external surface of the mesoporous silica. This is confirmed with the use of electron microscopy, and scanning electron micrographs of uranium tetrachloride supported on mesoporous silica, both before and after calcination, are given overleaf:
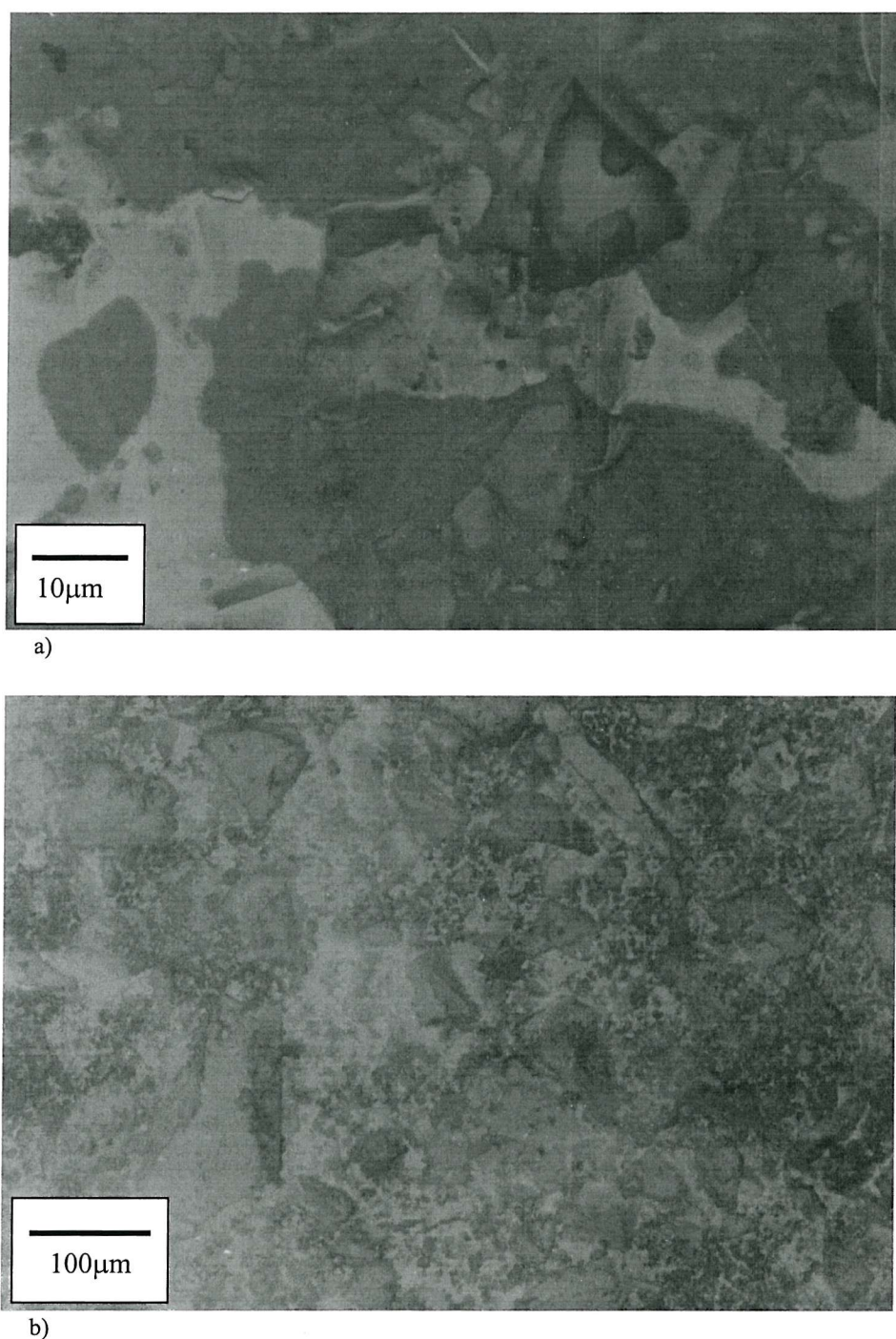
a)

b)

Figure 4.15 Scanning electron micrographs of UCl_4/H_1SiO_2 a) as prepared, b) after calcination at 800°C for 3h in air.

It is possible to observe the effect of calcination, with U_3O_8 particles evident as very dark spots on the micrograph of the material treated at 800°C. This contrasts with that of the unheated supported sample, where the uranium tetrachloride, or oxychloride appears to be evenly dispersed on the large, glassy silica particles. This extrusion of the uranium

material from the mesopores may be an important observation, as it may have ramifications not only for the catalytic activity of the systems studied here, but also for the production of other metal oxide phases supported on mesoporous materials.

Transmission electron microscopy performed on the calcined material has provided an opportunity to obtain a second estimate of the U_3O_8 particle size, which may be compared with that found from manipulation of the X-ray diffraction data. Several transmission electron micrographs from different areas of the sample have been used in this process, in order to gain a statistically significant sample size, and to negate the effects of any sample inhomogeneity. Particles were observed to be spherical or ellipsoidal in shape. Particle sizes were measured manually from enlarged images, with reference to the scale bar. The results of this analysis are shown in the histogram below:
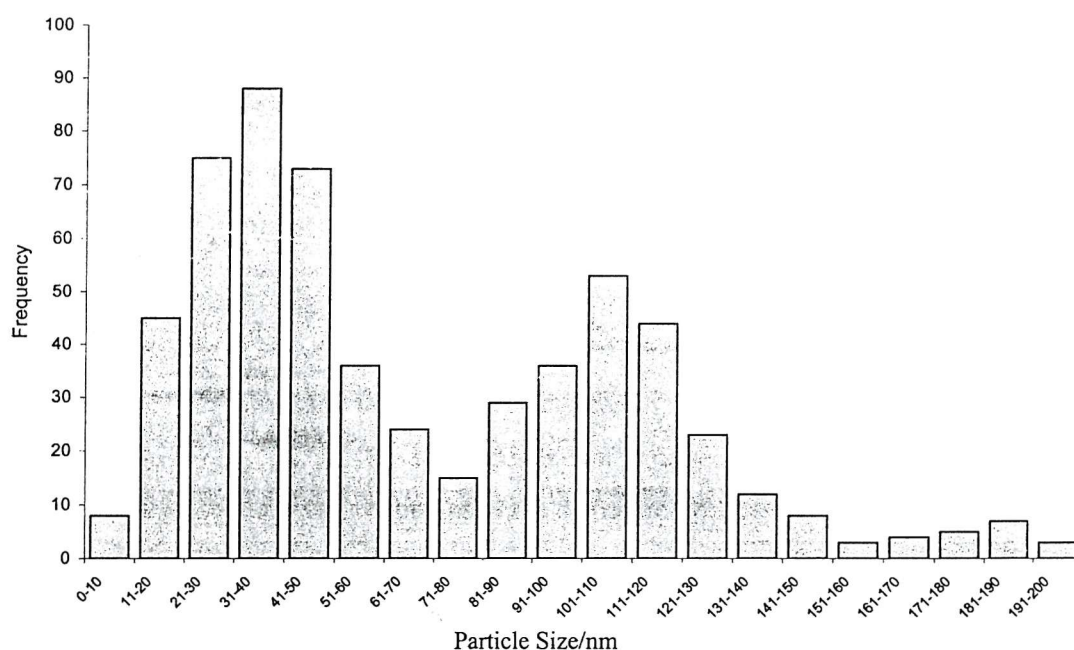
Figure 4.16 U_3O_8 particle size frequency distribution for $Cl/800/H_1SiO_2$

It is possible to observe two broad maxima in the distribution above, centred at 31-40nm and 101-110nm. It should be noted that the electron microscopy determination is a direct technique, and the results shown above can be assumed to be correct for the sample area studied. The major source of possible error in this method, omitting small inaccuracies in the values measured, is derived from the extrapolation of the above measurements to the sample as a whole. Although the total number of particles measured

was 591, it is not possible to state irrefutably that this is representative of the entire sample. However, the number of measurements taken is probably sufficiently large to give a result of reasonable precision. An explanation for the bimodal nature of the above distribution is not immediately obvious, but it may be suggested that the origin of this phenomenon is probably related to the observed temperature dependence of U_3O_8 formation for this system. It should be recalled that calcination of the UCl_4/H_1SiO_2 material at 450°C for 3h in air yielded a yellow/green material, where conversion from UO_3 to U_3O_8 was incomplete. However, the size of U_3O_8 particles formed after this treatment was clearly of sufficient magnitude to constructively diffract X-rays. The suggestion is then that there are two U_3O_8 nucleation processes, one at low temperature, ● 450°C, and one that occurs at > 450°C. A reasonable supposition is that the low temperature process involves an interaction with the support material that promotes this conversion, whereas the higher temperature event is akin to that which would occur in the bulk, unsupported uranium material. The result is the bimodal distribution observed, with the lower temperature process leading to the larger particles as calcination temperature is increased. Confirmation of this theory would require a much greater level of investigation into these nucleation processes and support interactions.

The arithmetic mean value for particle size, $\bar{x}$, determined by electron microscopy is calculated as 67nm. This value compares with an average crystallite thickness of 156nm found by Scherrer analysis of the X-ray diffraction pattern of this system. The large difference between the results achieved by these two methods requires an explanation. The sample dependent parameter used to perform the Scherrer analysis is the full width at half-height of the diffraction peak. This is a difficult value to accurately measure when signal to background ratio is low, as is the case for the diffraction patterns of a number of these samples, and this source of error will obviously have an effect on the calculated particle size. However, this type of error is shown, by repeated analysis of the same sample, to be small ($\approx \pm 2nm$), and to give an approximately normal distribution of values around a central figure. This does not account for the much larger value obtained by X-ray diffraction analysis compared to that found by electron microscopy, and further explanation of exactly what average particle size refers to needed. The average particle size, found by electron microscopy, is the arithmetic mean diameter of all the particles measured:

$$\bar{x} = \frac{\sum_i^n x}{n} \qquad\qquad Eq.4.2$$

where n is the total number of particles, and x is the diameter of particle i. In contrast, the Scherrer formula may be thought of as a calculation to determine the particle size in which an atom is most likely to be found. This is most easily related to particle volume, and, assuming spherical particles, this results in the application of a $(x/2)^3$ weighting factor. When this is introduced to the data obtained by electron microscopy analysis, then a histogram plot of the contribution of each particle diameter range as a percentage of total volume may be obtained. This is shown below:
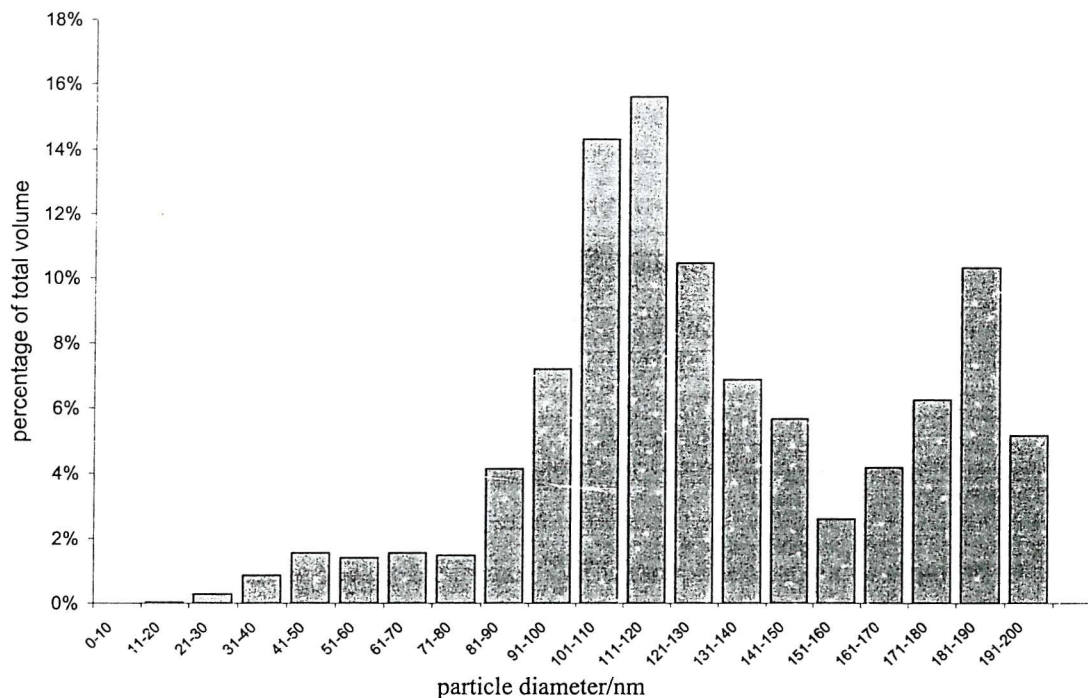
Figure 4.17 U_3O_8 particle size contribution to total volume for $Cl/800/H_1SiO_2$

From the plot above, it is now possible to reconcile the average value of 156nm obtained from the Scherrer analysis for this system, although the average particle diameter obtained from the analysis of the above plot is still lower, at 129nm.

It should be carefully noted that the procedure that has been used, in order to gain a direct comparison between these two methods of particle size determination, does involve some approximations. Firstly, a spherical particle shape has been assumed, and a study of the TEM images suggests that this is a reasonable approximation. Secondly, an assumption regarding the crystallinity of the particles must be made. If, for example, the smaller particles are amorphous, then this would reduce their contribution to the diffraction pattern and their importance may be underestimated by this method. Indeed, this may account for

the residual difference between results from each method. Thirdly, it must be remembered that the Scherrer formula is itself an approximation of the relationship between crystallite thickness and peak broadening.[41]

For the reasons stated above, values obtained from the Scherrer analysis of X-ray diffraction data must be treated with caution, and not taken as an average of particle diameter. The arithmetic mean diameter of particles, as would be determined by the electron microscopy method, will be considerably lower than the value found by the Scherrer analysis. Also, the value obtained is only an average of the whole system, and a distribution of particle sizes cannot be gained by the use of this method. However, this analysis is still very useful in terms of qualitative information, and it does allow a reasonable comparison of different systems to be achieved.

From the diameters of the particles measured from the electron micrographs, it is also possible to obtain an estimate of the specific surface area of the uranium oxide particles. Assuming that the uranium oxide material is present as pure U_3O_8, then the density of this may be taken as $8.395 gcm^{-3}$.[42] The total volume and the total area of the particles studied are calculated from the diameters measured. The result is an average value of $6.2 m^2 g^{-1}$ for the uranium oxide present in the $Cl/800/H_1SiO_2$ system.

There are some other general observations that should be mentioned with relation to the uranium precursor and support dependence on the temperature at which U_3O_8 is formed. The supported uranium chloride materials appear to form U_3O_8 at a lower temperature than the analogous uranyl nitrate samples. This effect, as well as the observed differences from one support to another, has been investigated with the use of in situ X-ray powder diffraction. The collection of a diffraction pattern every 10°C, during the calcination of supported materials in static air, allows a more accurate determination of the temperature at which U_3O_8 formation occurs. A stack plot of the X-ray diffraction patterns obtained in the calcination of the $UCl_4/\gamma-Al_2O_3$ system is given overleaf:
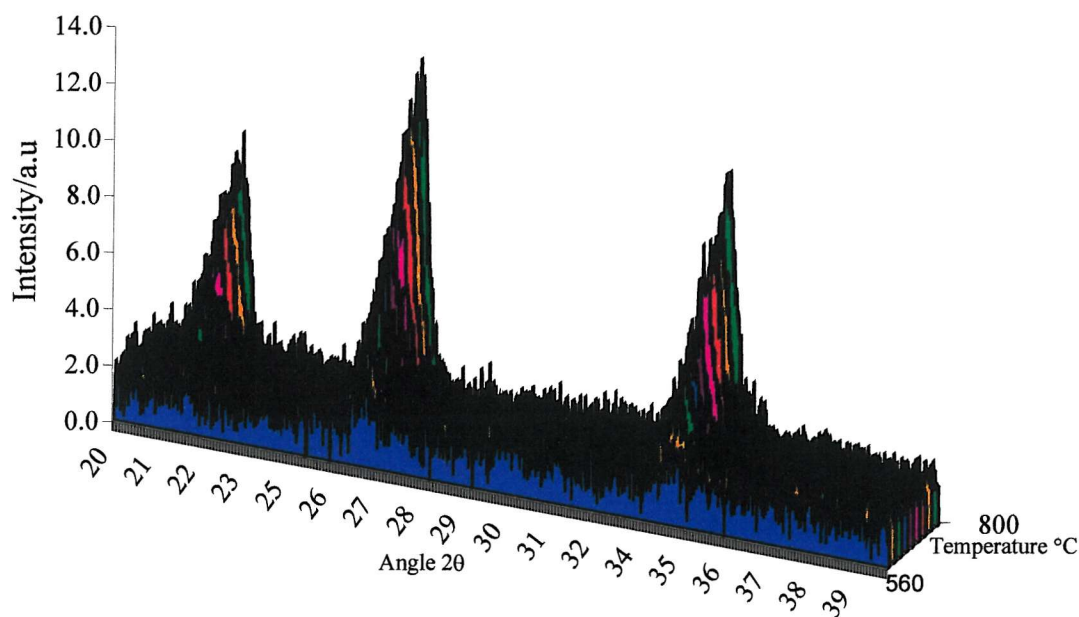
Figure 4.17 A plot of the change in X-ray diffraction pattern with temperature for the calcination of UCl_4/γ-Al_2O_3 in static air

Samples were heated at a linear ramp rate of 10K/min between scans. The sample was held at the designated temperature for 10min, and then the diffraction pattern collected over a period of 15min. Note that this introduces a complex time dependence to the diffraction patterns if U_3O_8 formation is slow, but that conditions are consistent between samples. A table summarising the results of these experiments is given below:

Supported Material	U_3O_8 Formation Temp./°C
UCl_4/H_ISiO_2	460
UCl_4/SiO_2	620
UCl_4/γ-Al_2O_3	560
$UO_2(NO_3)_2.6H_2O/H_ISiO_2$	490
$UO_2(NO_3)_2.6H_2O/SiO_2$	600
$UO_2(NO_3)_2.6H_2O/\gamma$-$Al_2O_3$	590

Table 4.5 U_3O_8 formation temperature dependence on uranium precursor material and support type.

From the above table, it is possible to make several observations. Firstly, the mesoporous silica support promotes U_3O_8 formation at a substantially lower temperature with respect to the other support materials. This occurs at 460°C for the uranium chloride material, and at 30°C higher for the supported uranyl nitrate system. It is worthy of note that the temperature of 490°C for the $UO_2(NO_3)_2.6H_2O/H_ISiO_2$ corresponds to an endothermic feature in the DTA curve that is not associated with a resolvable mass loss

formation of U_3O_8 from a UO_3 type phase. The temperatures at which this feature appears in the DTA curves of the other five precursor/support systems is also in agreement with those values in the above table.

The same 30°C difference is also apparent for the alumina supported samples, which would suggest that the uranium chloride is converted to U_3O_8 at lower temperatures than the uranyl nitrate. However, this is not reflected in the results obtained for the amorphous silica samples, and this is difficult to explain in terms of precursor-support interactions. It is possible that at these slightly higher temperatures, the formation of U_3O_8 is dominated by a different mechanism compared to that occurring below 600°C, and that the promoting effect of the tetrachloride precursor is no longer important. The simultaneous thermal analysis results indicated that precursor decomposition occurred in the temperature order amorphous silica • amorphous alumina < mesoporous silica. This is the opposite order to that at which U_3O_8 is first observed. This may suggest that the promoting effect of the mesoporous silica on the formation of U_3O_8, is in fact the result of the inability of this support to stabilise the intermediate phase formed on decomposition of the precursor. If this intermediate phase persists over a greater temperature range on amorphous silica than the other supports, then, possibly, the effect of the choice of precursor loses its significance.

4.2.2.2 EXAFS Analysis

Uranium L_{III} EXAFS spectra were collected for all the calcined samples described above, as well as for the unsupported uranium oxides U_3O_8 and UO_3. Samples were diluted prior to the experiment to approximately 10wt% U in dry boron nitride. Given that the oxide phase formed is likely to be one of the two mentioned above, it is clearly important to determine whether or not they may be distinguished by this technique. Overleaf are the fits obtained for the EXAFS spectra of U_3O_8 and UO_3, along with the parameters used to define them:
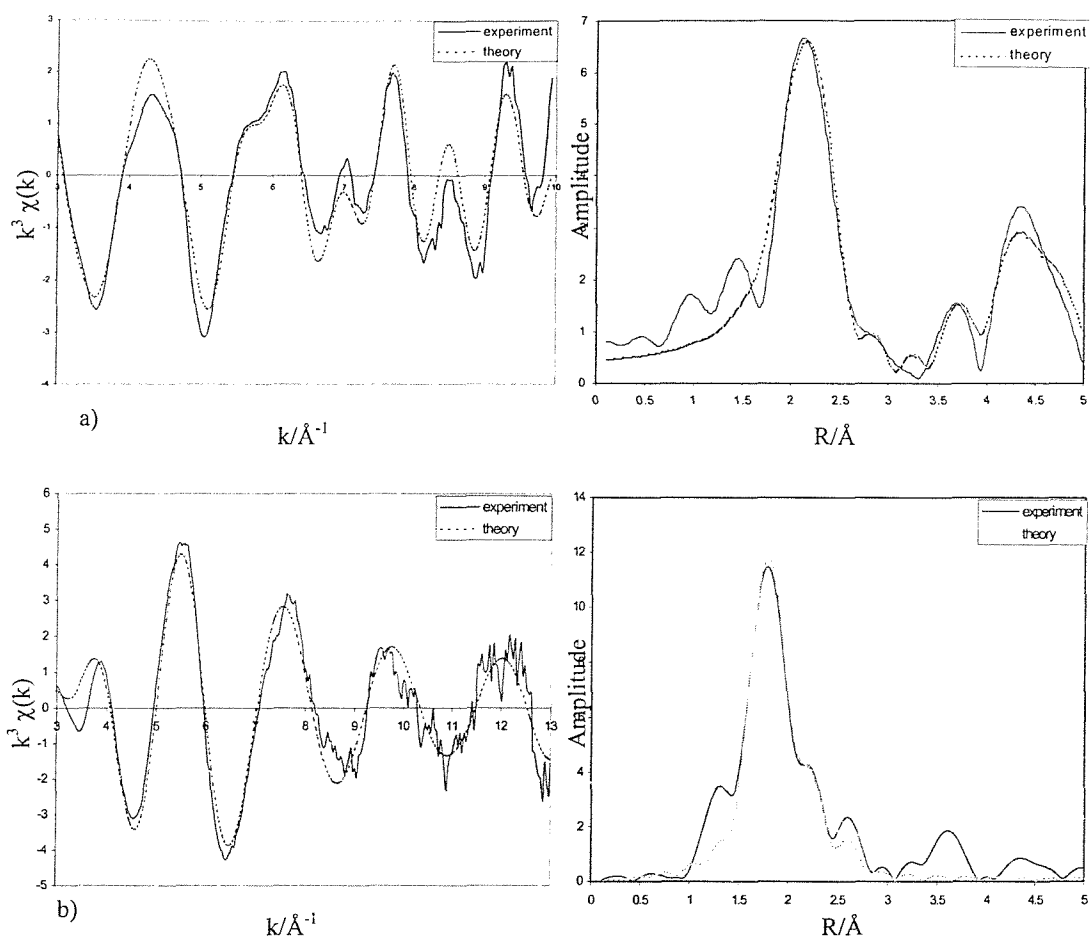
Figure 4.18 The U L (III)-edge k^3 weighted EXAFS spectrum and phase shift corrected Fourier transform of a) U_3O_8 and b) UO_3, diluted to 10wt% U in a boron nitride matrix

EF= -9.8   R= 33.14   F.I= 9.5×10^{-4} EF= -10.6   R= 32.31   F.I.= 5.5×10^{-4}

Shell(n)	Tn	Cn	Rn(Å)	a $(2\sigma^2/Å^2)$
1	O	4	2.22(1)	0.020(3)
2	U	3	3.85(2)	0.022(5)
3	U	4	4.26(2)	0.015(3)

a)

Shell(n)	Tn	Cn	Rn(Å)	a $(2\sigma^2/Å^2)$
1	O	2	1.81(1)	0.007(1)
2	O	2	2.27(1)	0.010(2)
3	O	2	2.45(2)	0.013(4)

b)

Table 4.5 EXAFS derived structural parameters for a) U_3O_8, b) UO_3 diluted to 10wt% U in a boron nitride matrix. Statistical errors are given in brackets.

The UO_3 sample was obtained from BNFL, and the U_3O_8 was prepared by the calcination of UO_3 in a flow of oxygen for 8h at 800°C. The EXAFS spectrum of the U_3O_8 sample was fitted to a theoretical model of three shells of atoms, as given above. The uranium co-ordination sphere in α-U_3O_8 has been previously determined by X-ray and neutron diffraction,[38,43,44] and, though there is some small variation between accounts, it is shown to include a range of uranium-oxygen bond distances. In the structure determined

105

by Loopstra, there were found to be seven oxygen atoms in the first co-ordination sphere, at distances ranging from 2.07 to 2.71Å (2 at 2.07Å, 4 at 2.12-2.25Å, 0.33 at 2.45Å, and 0.67 at 2.71Å).[44] Previously, attempts have been made by Berry *et al* to fit the EXAFS data obtained from a U_3O_8 sample to a total of nine shells of atoms, with five shells of oxygen (totalling nine atoms), and four shells of uranium (seven atoms).[45] Aside from the fact that it is unlikely to be statistically valid to fit such a large number of shells to the data, the distances and co-ordination numbers used are not in agreement with those found by X-ray diffraction. The model to which EXAFS data obtained in this work is fitted is different again. The co-ordination numbers and distances found for the two uranium shells in the table above, at 3.85 and 4.27Å, are in good agreement with the X-ray data.[44] However, only four oxygen atoms were actually included in the model as, although it was possible to fit a total of seven, fitting an additional three as a separate shell did not result in a statistically significant decrease in the fit index. This type of problem is common when modelling a system where a number of distances may need to be averaged to a single shell. It should be noted that the X-ray diffraction structure referred to was determined in 1977, and it is quite possible that there is also some uncertainty in the uranium-oxygen distances from this technique, as the diffracted intensity will be dominated by the contribution from the uranium atoms. This is a problem that has been repeatedly observed for materials where the uranium is surrounded by light atoms.[46,47] The important point to note is that there is an obvious difficulty in fitting a chemically sensible oxygen co-ordination shell to EXAFS data obtained from this system. This highlights both the deficiencies of this technique, and the advantage of collecting EXAFS data from a model system which may compared to that from a supported material. So, the fit shown above for the U_3O_8 system, and the parameters used to define it, may be best used as a fingerprint for comparison with a supported uranium oxide system.

Importantly, there are very clear differences between the EXAFS of U_3O_8 and UO_3, and this is most clearly demonstrated by direct comparison of the two Fourier transforms shown in the figure above. The most obvious contrast is in the magnitude of features at R>3Å, as these are greatly reduced in that of UO_3 with respect to U_3O_8. These peaks correspond almost exclusively to uranium-uranium distances, and it is interesting to note that there is such a large difference in the intensity of these features between two systems with similar structures. The crystal structure reports of α-UO_3 show great inconsistencies, with considerable variations in the described radial distributions.[43,48,49] This implies some

uncertainty in the validity of the model used to fit the EXAFS data for this system, but the three oxygen shells that have been included in the above fit agree well with the distances and co-ordination numbers found by Siegel *et al.*[49] The uranium-uranium co-ordination described in the same report comprised of four shells of two atoms at 3.69, 3.99, 4.03 and 4.18Å. It was possible to fit these shells to the EXAFS data, but the observed decrease in the fit index was not sufficiently large to justify their inclusion in the final model. Once again, the fit obtained for the UO_3 system is probably best employed as a fingerprint with which supported oxide materials may be compared.

In summary, it would appear that it is possible to differentiate between the two oxide systems discussed above using EXAFS as a technique, but a full description of the structure is probably not obtainable.

The uranium L(III) edge EXAFS spectrum and phase shift corrected Fourier transform of the $Cl/800/H_1SiO_2$ system is compared in the plot below with that obtained for the pure U_3O_8 sample:
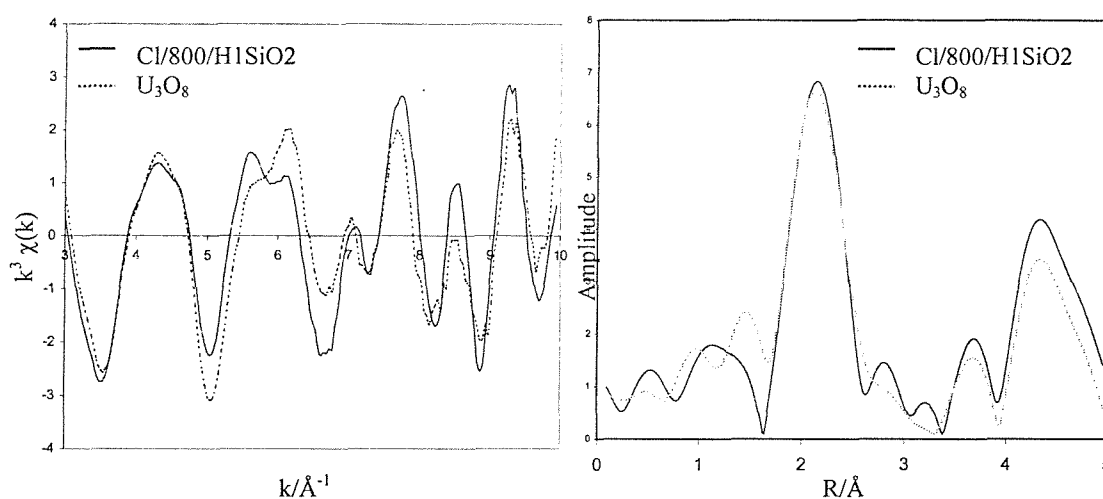
Figure 4.19 The U L(III)-edge k^3 weighted EXAFS spectrum and phase shift corrected Fourier transform of $UCl_4/800/H_1SiO_2$, diluted to 10wt% U in a boron nitride matrix compared with that for U_3O_8

It is possible to observe close agreement between these two spectra, which suggest that the supported uranium oxide material is a U_3O_8 phase. This is in accord with the X-ray powder diffraction data discussed in the previous section.[44] In fact, all of the materials calcined at 800°C have an EXAFS spectrum similar to that of U_3O_8, but there are also some subtle differences between samples that seem to suggest the formation of this phase has a support and precursor dependence. This is demonstrated in the plot overleaf, where the Fourier transforms of all three uranium tetrachloride derivatives are shown
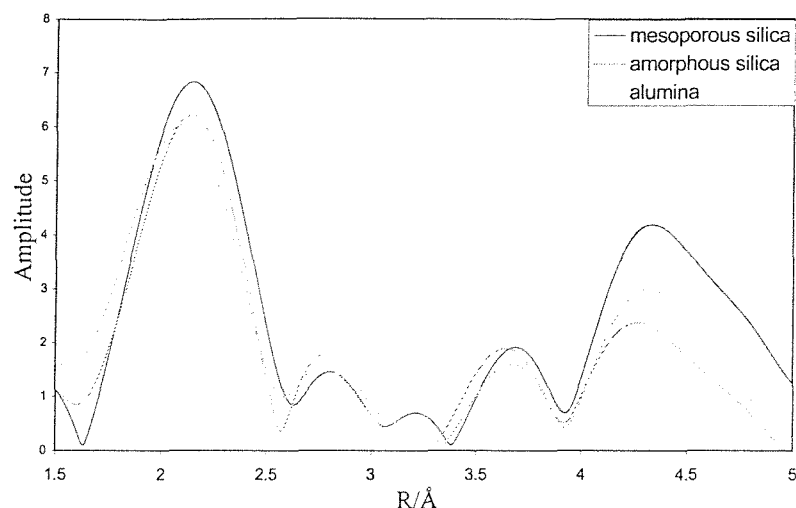
Figure 4.20 U L(III) edge phase shift corrected EXAFS Fourier transforms of Cl/800/H₁SiO₂,
Cl/800/SiO₂, Cl/800/γ-Al₂O₃

The interesting feature of the plot above is the variation in intensity of the peak in the Fourier transform at ~4.3Å. The magnitude of this peak decreases in the order H_1SiO_2 > γ-Al₂O₃ > SiO₂. This is the same order that was found for the effect of the support on the size of the U_3O_8 particles formed on calcination. The origin of this feature is a uranium-uranium distance, and the reduction in intensity suggests a lowering of co-ordination number. Qualitatively this would make sense, as if the particles were becoming smaller, the proportion of uranium atoms on or near the surface would increase. As EXAFS provides information on the average environment, then the greater the proportion of surface atoms, with lower uranium co-ordination than those in the bulk, the lower the average co-ordination will appear.

The EXAFS spectra of materials calcined at 450°C were fitted to the theoretical model used for the UO₃ sample, and this gave good agreement in most cases. The Cl/450/H₁SiO₂ and Cl/450/γ-Al₂O₃ systems, for which evidence was found for the presence of U_3O_8 by X-ray diffraction, fitted less well to the UO₃ model. For these systems, attempts were made to fit two separate uranium environments simultaneously; one based on the UO₃ model, and the second on the U_3O_8 parameters. The ratio of one type of central atom to another was allowed to vary, and the refined model suggested that the extent of U_3O_8 formation is less than 10% in both cases. This highlights the fact that X-ray powder diffraction can only provide information about the diffracting material within the sample, and the presence of a coincidental amorphous phase cannot be discounted.

4.2.2.3 Isothermal Nitrogen Adsorption

Nitrogen adsorption/desorption isotherms have been recorded for all of the calcined systems, and the surface area and pore size distribution determined from this data. For the materials based on amorphous supports, this yielded little useful information beyond a measure of the change in surface area on calcination. Indeed, for these samples the specific surface area is increased on calcination, and this is typified by the $UO_2(NO_3)_2.6H_2O/\gamma$-$Al_2O_3$ system, where the surface area increases from 15 to $33m^2g^{-1}$ on treatment at 800°C. This may reasonably be attributed to the mass per uranium difference between $UO_2(NO_3)_2.6H_2O$ and UO_3/U_3O_8, as well as the loss of adsorbed water, both of which would result in an increase in the proportion of total sample mass due to the alumina.

For the mesoporous silica supported samples the observed behaviour is rather different. The value obtained for the specific surface area is significantly reduced on calcination. The fact that the amount of adsorbed solvent included in the pre-calcined samples is less for this support than the amorphous alternatives has been discussed previously, and this may account for this difference in part. However, there does appear to be some degree of support structural change on calcination. Below is a summary of these results:

Sample	Surface Area/m^2g^{-1}	
	as made	800°C/3h/air
UCl_4/H_1SiO_2	330	205
$UO_2(NO_3)_2/H_1SiO_2$	313	195
UCl_4/SiO_2	65	80
$UO_2(NO_3)_2/SiO_2$	61	82
UCl_4/γ-Al_2O_3	18	31
$UO_2(NO_3)_2/\gamma$-Al_2O_3	15	33

Table 4.6 The effect of calcination at 800°C in air on sample surface area

The pore size distributions of the mesoporous silica supported samples were calculated,[17] and the results for the uranium tetrachloride derivative materials are plotted below:
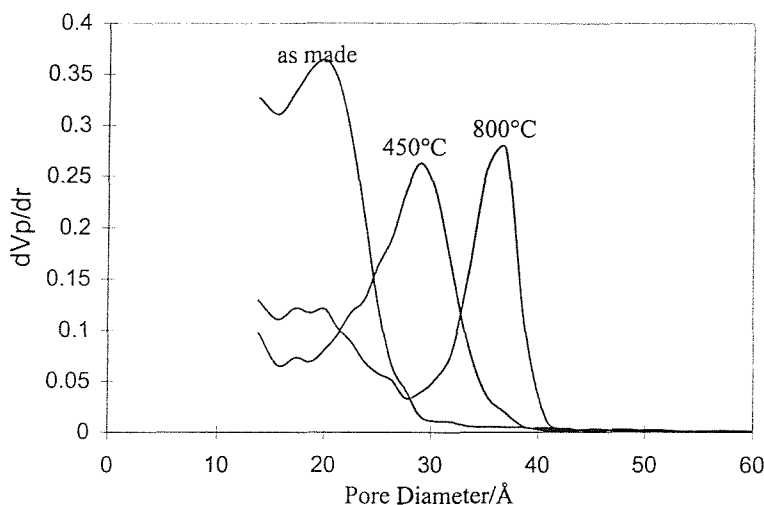

Figure 4.21 The Dollimore-Heal pore size distribution as a function of calcination temperature for the UCl_4/H_1SiO_2 system

The maxima in these distributions lie at approximately 20Å for the material prior to calcination, 29Å for the sample treated at 450°C, and 37Å for that calcined at 800°C. It has been observed with the use of electron microscopy that the uranium material migrates out of the pores on calcination, so the trend observed is not remarkable. More interesting is the fact that the material calcined at 800°C would appear to have larger pores than the original mesoporous silica; 37Å compared with 30Å. This difference is large, and the same effect is observed for the uranyl nitrate derivative materials. Previously, it has been shown that structural collapse as a result of thermal treatment causes a decrease in pore diameter, so this simple process would not appear to explain this result satisfactorily. A possible explanation for this phenomenon is that the calcination process causes some damage to the pore walls, with the extrusion of the growing uranium oxide phase effectively causing the coincidental uniform stripping of a layer from the support walls.

4.2.3 Characterisation of Reduced Supported Uranium Oxide Materials

The materials calcined at 800°C for 3h in air, described in the previous section, were further heated to 523°C at a linear ramp rate of 10K/min, and held at that temperature for 10h in a flow of 20ml/min of 10%H_2 in N_2. Samples were kept in an evacuated desiccator prior to further use. The temperature at which this treatment is performed was chosen with reference to the work of Madharavam et al[50], in order to reduce the U_3O_8 phase to UO_2. UO_2 is considered to be the active phase in the catalytic selective reduction of NO using uranium oxide materials.[33] As such, characterisation of this reduced phase is of obvious importance in any investigation of precursor and support effects on the activity of these materials as catalysts. The mesoporous and amorphous silica supported samples appeared dark brown after this treatment, whilst the alumina supported materials had a slate grey colour. For convenience, these samples are denoted precursor/support/H_2 e.g. Cl/H_1SiO$_2$/H_2

4.2.3.1 X-ray Powder Diffraction

The X-ray powder diffraction patterns of all samples displayed two reflections in the range studied at 28.2 and 32.3 °2θ, and these have been indexed as the (111) and (200) reflections of the UO_2 phase[51], which has a face centred cubic fluorite structure. Figure 4.22 gives a representation of the support dependence of this structure for the uranyl nitrate derivative materials:
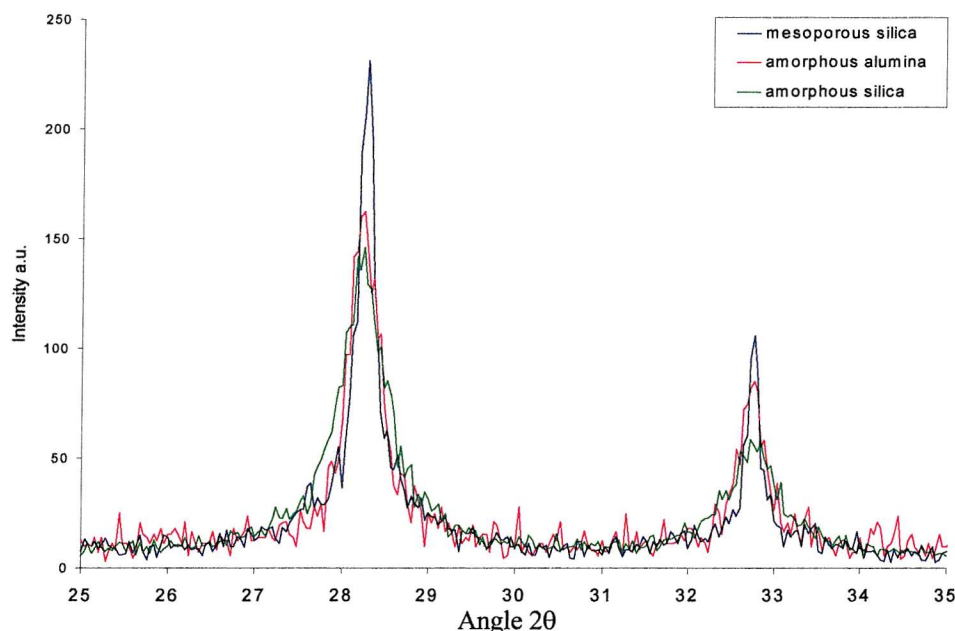
Figure 4.22 X-ray powder diffraction pattern dependence on support for calcined and reduced $UO_2(NO_3)_2.6H_2O$ derivative materials

The diffraction peak intensity follows the trend $H_1SiO_2 > \gamma\text{-}Al_2O_3 > SiO_2$, and, as expected, this is the same trend observed for the peaks indexed as due to the presence of U_3O_8 in the materials prior to reduction. The Scherrer formula has again been used to gain an estimate of particle size from the peak broadening effects, and these results are tabulated below:

Sample	Crystallite Thickness/nm
$Cl/H_1SiO_2/H_2$	71
$Cl/SiO_2/H_2$	18
$Cl/\gamma\text{-}Al_2O_3/H_2$	39
$Nit/H_1SiO_2/H_2$	56
$Nit/SiO_2/H_2$	16
$Nit/\gamma\text{-}Al_2O_3/H_2$	35

Table 4.7 The UO_2 crystallite size dependence on support and uranium precursor.

Again, the values above follow the same trend as for the U_3O_8 crystallite size, but interestingly the values appear to be of approximately half the magnitude. This may be due to particle degradation on reduction, which has been previously observed on conversion of U_3O_8 to UO_2. The limitations of the Scherrer formula, discussed earlier, must again be considered as a source of error.

4.2.3.2 EXAFS Analysis

The uranium L(III) edge EXAFS spectra were recorded for all reduced supported materials, as well as a bulk UO_2 sample. The fit obtained for the bulk UO_2 EXAFS spectrum and phase shift corrected Fourier transform, the parameters used to define it, and an illustration of the structural model, are given below:
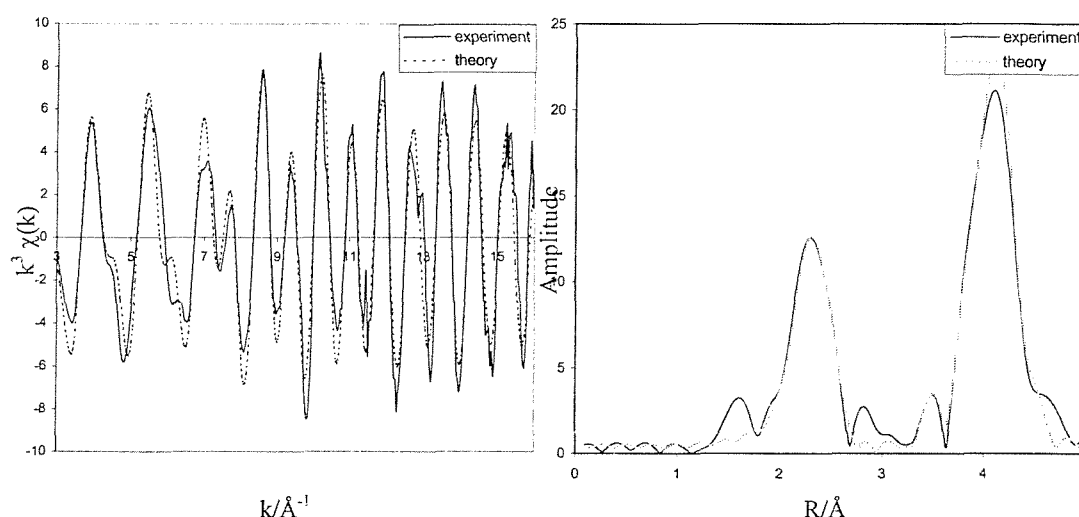

Figure 4.23 The U L(III)-edge k^3 weighted EXAFS spectrum and phase shift corrected Fourier transform of UO_2, diluted to 10wt% U in a boron nitride matrix.

EF= -9.54   R= 31.78   F.I= 4.7×10^{-4}

Shell(n)	Tn	Cn	Rn(Å)$_{EXAFS}$	a $(2\sigma^2/\text{Å}^2)_{EXAFS}$
1	O	8	2.369(0.007)	0.015(0.002)
2	U	12	3.872(0.003)	0.010(0.001)

Table 4.7 EXAFS derived structural parameters for UO_2 diluted to 10wt% U in a boron nitride matrix. Statistical errors are given in brackets.
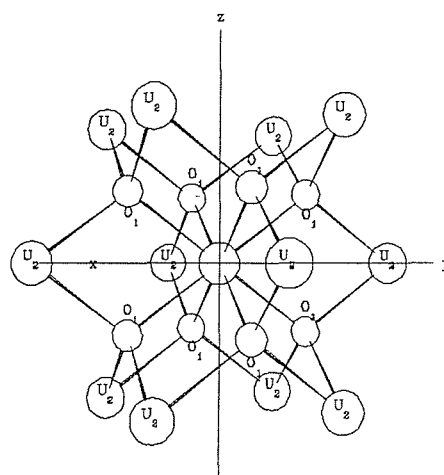

Figure 4.24 An illustration of the fluorite type structural model used in order to fit the bulk UO_2 EXAFS data

The EXAFS spectrum of this material fitted well to the fluorite structural model, and the distances found are in agreement with the literature values.[48] The supported materials were fitted to a model using the same atom types and bond distances. The Debye-Waller factors were also held constant, and only the co-ordination numbers were allowed to vary. The results of this analysis are presented in the table below:

Sample	Oxygen Co-ordination	Uranium Co-ordination
UO_2	8	12
$Cl/H_1SiO_2/H_2$	5.6(4)	3.7(3)
$Cl/SiO_2/H_2$	4.8(3)	2.8(3)
$Cl/\gamma\text{-}Al_2O_3/H_2$	4.1(3)	1.0(4)
$Nit/H_1SiO_2/H_2$	5.5(4)	3.4(3)
$Nit/SiO_2/H_2$	4.7(4)	2.5(3)
$Nit/\gamma\text{-}Al_2O_3/H_2$	4.4(4)	1.1(5)

Table 4.8 1st and 2nd shell co-ordination dependence on support and uranium precursor. Statistical errors are given in brackets

This is illustrated by the plot below, which shows the variation in Fourier transform with support for the uranyl nitrate derivative materials:
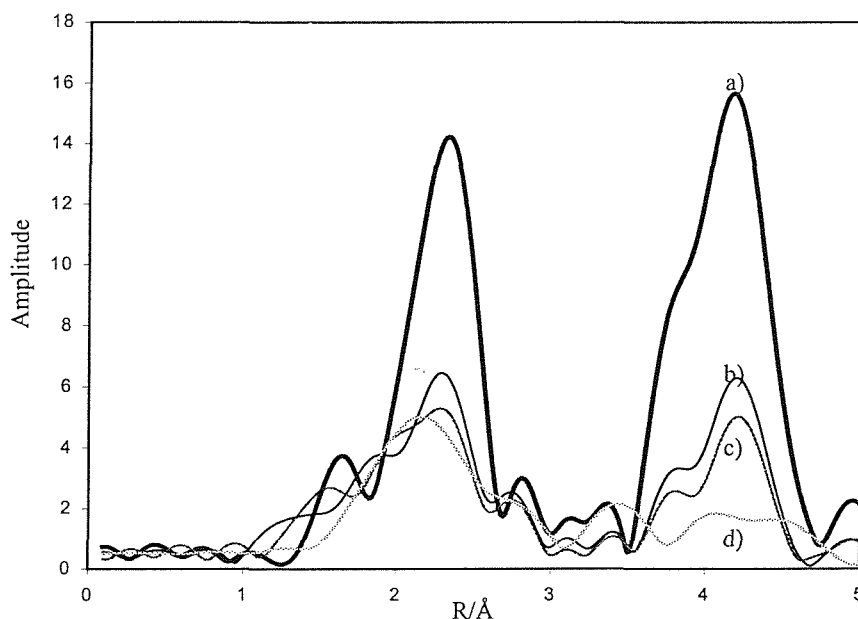

Figure 4.25 The phase shift corrected Fourier transforms for a) bulk UO_2, b) $Nit/H_1SiO_2/H_2$, c)$Nit/\gamma\text{-}Al_2O_3/H_2$, d) $Nit/SiO_2/H_2$

The first thing to note is that co-ordination numbers for all the supported materials are significantly lower than for the bulk oxide. This is due to the fact that uranium oxide particle sizes for these materials are small relative to those found in the unsupported sample. As has been discussed previously, this implies a greater proportion of uranium atoms at or near the surface of these particles, leading to a reduced average co-ordination, as is observed by EXAFS. As would be expected, the support dependence of the co-ordination numbers follows the same trend as that found for diffraction peak intensity and estimated particle size. A second observation, with the same explanation, is that the uranium co-ordination number is affected to a greater extent than the oxygen shell by this reduction in particle size, to the point where fitting a uranium shell for the amorphous silica supported materials is possibly statistically invalid.

4.2.3.3 Isothermal Nitrogen Adsorption

Nitrogen adsorption/desorption isotherms were recorded for all reduced samples. The calculated surface areas and pore size distributions for these materials were the same, within experimental error, to the values obtained for the calcined materials prior to reduction. This simply suggests that the support structure is not adversely affected by the act of heating in a reducing atmosphere. Although this degree of structural integrity is not unexpected, its demonstration may be important when considering the suitability of these materials for a range of heterogeneous reactions.

4.3 Summary

The supported uranyl nitrate hexahydrate derivative materials have been identified, prior to calcination, as [$UO_2(NO_3)_2.2H_2O$]/support material. The analogous uranium tetrachloride derivatives have been characterised as predominantly a $UOCl_2$-type phase on deposition, although only the mesoporous silica provides a material with sufficiently long-range order to give an X-ray diffraction pattern. The decomposition of these supported materials occurs at lower temperatures compared to the pure, unsupported materials. This phenomenon has a support dependence which is the same for both precursors, where the temperature of initial decomposition increases in the order amorphous silica $\leq$ amorphous alumina $<$ mesoporous silica $<$ unsupported bulk material. For the nitrate materials, this decomposition proceeds via dehydration and deNO$_x$ steps, whereas for the chloride materials, chlorine loss in the form of HCl is observed. These decomposition processes for

both precursors result in the formation of an oxygen rich uranium material, such as aUO_3-type phase, which converts to U_3O_8 at higher temperatures. The temperature at which this U_3O_8 formation process occurs also has a support dependence, and this is opposite to that given above for the initial decomposition, i.e. mesoporous silica < amorphous alumina $\leq$ amorphous silica < unsupported bulk material. This occurs at lower temperatures for the tetrachloride derivative materials compared to the nitrate analogues. It has been shown that the U_3O_8 particle size formed at a given temperature is larger for materials that promote U_3O_8 formation at lower temperatures, i.e. a sintering process occurs. The U_3O_8 particles formed on the mesoporous silica support at elevated temperatures are much larger than the dimensions of the pores, and the majority of the uranium oxide is present on the external surface of the silica.

4.4 References

1) J. A. Herman, J. F. Suttle, *Inorg. Synth.,* 143, **5**, 1957.

2) T. Schleid, G. Meyer, L.R. Morss, *J. Less Common Met.,* 132, **69**, 1987.

3) J.C. Krupa, *Inorg. Chim. Acta,* 223, **139**, 1987.

4) J.C. Taylor, P.W.Wilson, *Acta Cryst.,*1942, **29**, 1973.

5) N.K. Dalley, M.H. Mueller, S.H. Simonsen, *Inorg. Chem.* 323, **10**, 1971.

6) J.C. Taylor, P.W. Wilson, *Acta Cryst.B,* 175, **30**, 1974.

7) F.A. Cotton, D.O. Marler, W. Schotzer, *Acta Cryst. C,*1186, **40**, 1984.

8) F.Lux, U.B. Bufe, *Angew. Chem. Int. Ed. Engl.,* 274, **10**, 1971.

9) G. Bombieri, D.Brown, R. Graziani, *J. Chem. Soc. Dalton Trans.,* 1873, 1975.

10) D.C. Moody, R.A. Penneman, K.V. Salazar, *Inorg.Chem.,* 208, **18**, 1979.

11) G.B. Deacon, T.D. Tuong, *Polyhedron,* 249, **7**, 1988

12) M.Caiva, L.R. Nassimbeni, *J.Inorg. Nucl. Chem.,* 455, **39**, 1977.

13) J.G.H. du Preeze, *J. Chem. Soc. Dalton Trans.,* 1062, 1977.

14) P.G. Edwards, R.A. Andersen, A. Zalkin, *J.Am.Chem.Soc.,* 7792, **103**, 1981.

15) W.G. Van Der Sluys, J.M. Berg, D. Barnhardt, N.N. Sauer, *Inorg.Chim. Acta,* 251, **204**, 1992.

16) M-Y. He, R.L. Burwell Jr., T.J. Marks, *Organometallics,* 566, **2** 1983.

17) D.Dollimore, G.R.Heal, *J.Appl.Chem.,*109, 1964.

18) P.C. Burns, R.C. Ewing, F.C. Hawthorne, *Can. Mineral.,* 1551, **35**, 1997.

19) P.L. Gordon, J.A. Thompson, J.G. Watkin, C.J. Burns, N.N. Sauer, B.L. Scott, *Acta Cryst. C,* 1275, **55**, 1999.

20) P.Roussel, P.B. Hitchcock, N.D. Tinker, P. Scott, *Inorg.Chem.,* 5716, **36**, 1997.

21) J.G.H. du Preeze, B. Zeelie, U. Casellato, R. Graziani *,Inorg.Chim. Acta,* 122, **119**, 1986.

22) M. Nottmeyer, J.W. Gilje, H.W. Roesky, *Acta Cryst. C,* 1665, **48**, 1992.

23) R.W. Joyner, K.J. Martin, P. Meeham, *J.Phys.Chem.C:Solid State Phys.* 4005, **20**, 1987.

24) J.E. Fleming, H. Lynton, *Chem. Ind.,* 1416, **19**, 1960.

25) J.C. Taylor, M.H. Muller, *Acta Cryst.,* 536, **19**, 1965.

26) B.M. Gatehouse, A.E. Comyns, *J.Chem.Soc.,* 3965, 1958.

27) J.L. Woodhead, A.M. Deane, A.C. Fox, J.M. Fletcher, *J. Inorg. Nucl. Chem.,* 2175, **28**, 1966.

28) R.S. Ondrejcin, T.P. Garrett Jr, *J.Phys.Chem.*, 470, **65**, 1961.

29) S. Dash, M. Kamruddin, S. Bera, P.K. Ajikumar, A.K. Tyagi, S.V. Narasimhan, B. Raj, *J. Inorg. Nucl. Chem.*, 271, **264**, 1999.

30) E.H.P. Cordfunke, *J. Inorg. Nucl. Chem.*, 2189, **39**, 1977.

31) H. Landmesser, H.Kosslick, W. Storek, R. Fricke, *Solid State Ionics,* 271, **101**, 1997.

32) J. Weglarski, J.Datka, H. He, J. Klinowski, *J.Chem.Soc.Faraday Trans.*, 5164, **92**, 1996.

33) S.D. Pollington, A.F.Lee, T.L. Overton, P.J. Sears, P.B. Wells, S.E. Hawley, I.D.Hudson, D.F. Lee, V. Ruddick, *Chem. Commun.*, 725, 1999.

34) B. Loopstra, *J. Appl. Crystallogr.*, 94, **3**, 1970.

35) A.F. Andresen, *Acta Cryst.,* 612, **11**, 1958

36) B. Loopstra, *Acta Cryst.,* 651, **17**, 1964

37) W.H. Zachariasen, *Acta Cryst.,* 268, **1**, 1948

38) R.J Ackerman, A.T. Chang, C.A. Sorrell, *J. Inorg. Nucl. Chem.*, 75, **39**, 1977.

39) M. El-Mamoon Yahia, S.A. El-Fekey, A.M. El-Razek, *Radiochimica Acta*, 205, **72**, 1996.

40) H.R.Hoekstra, S. Siegel, F.X. Gallagher, *J. Inorg. Nucl. Chem.*, 3237, **32**, 1970.

41) P.Scherrer, *Nachr. Göttinger Gesell.*, 98, 1918.

42) H. Collette, S. Maroie, J. Riga, J.J. Verbist, Z. Gabelica, J.B. Nagy, E.G. Derouane, *J. Catal.*, 326, **98**, 1986.

43) L.M. Kovba, N.L. Komarevtseva, E.U. Kuzmitcheva, *Radiokhimiya*, 754, **21**, 1979.

44) B. Loopstra, *J. Inorg. Nucl. Chem.*, 1713, **39**, 1977.

45) F.J. Berry, A. Murray, A.T. Steel, *J.Chem.Soc. Faraday Trans.* 2783, **84**, 1988.

46) R.C.L. Mooney, *Acta Cryst.,* 189, **2**, 1949.

47) C-H. Wong, T-M. Yen, T-Y. Lee, *Acta Cryst.,* 340, **18**, 1965.

48) S. Siegel, H.R. Hoekstra, E. Sherry, *Acta Cryst.,* 292, **20**, 1966.

49) S. Siegel, H.R. Hoekstra, *Inorg Nucl. Chem. Lett.*, 497, **7**, 1971.

50) H. Madhavaram, P. Buchanan, H. Idriss, *J.Vac.Sci.Technol.A,* 1685, **15**, 1997.

51) S.A. Barrett, *Acta Cryst. B,* 2775, **38**, 1982.

Chapter 5. Catalytic Oxidation of Carbon Monoxide

This chapter is concerned with a brief investigation of supported uranium materials as catalysts for the oxidation of carbon monoxide with oxygen. Results describing the activity of bulk U_3O_8[1] for this reaction, and some limited work on supported uranium oxide systems[2], have been previously published, and these will be used for direct comparison with the findings obtained from this work. As described in the previous chapter, two precursors; uranium tetrachloride, UCl_4, and uranyl nitrate hexahydrate, $UO_2(NO_3)_2.6H_2O$, were supported on three different inorganic oxide supports; mesoporous silica, amorphous silica, and amorphous alumina. This provides a total of six different supported uranium systems, deposited at 30wt% U, and allows the activity dependence of precursor and support to be investigated. Systems will be denoted in an abbreviated form for convenience, e.g. $Nit/600/H_1SiO_2$ for uranyl nitrate supported on mesoporous silica pre-treated at 600°C, or $Cl/nc/\gamma-Al_2O_3$ for uranium tetrachloride supported on alumina and not calcined prior to reaction.

Little attempt will be made in this section to compare the activity of the supported uranium oxide materials with that of supported platinum group metals, which are used industrially to achieve the catalytic oxidation of carbon monoxide. There exist many good articles on, and reviews of, the CO oxidation mechanism and associated activity of these materials.[3,4,5,6,7] However, some discussion of the more closely analogous transition metal oxide systems, particularly Cr_2O_3 [8,9,10,11] and $Co_3O_4/\gamma-Al_2O_3$,[12,13,14] will be appropriate.

5.1 Experimental

The choice, synthesis where appropriate, and pre-treatment of oxide supports has been discussed in previous chapters, as well as the methodology used in the deposition of the uranium material. Although the general microreactor configuration has also been previously documented, (Chapter 2), a more detailed description of reaction parameters is required. Two distinct types of experimental conditions have been employed; a continuous flow arrangement with linear temperature ramp rate, and a pulsed gas experiment under isothermal conditions. The apparatus configuration for each will be dealt with separately, but the experimental features common to both should firstly be detailed. Samples were ground to a particle size of 5-50μm using a pestle and mortar. 20mg of sample was packed into a quartz capillary, and held in place by plugs of quartz wool. The capillary was then mounted in the reactor, and thoroughly purged with a helium flow of 40ml/min.

5.1.1 Continuous Flow Experiments

For each of the six precursor/support systems, the effect of catalyst pre-treatment on the CO oxidation reaction has been investigated, and two sets of experiments have been performed for this purpose. In one set, the supported uranium material was not subjected to any pre-treatment prior to its reaction with CO and oxygen. The sample was subjected to a continuous flow of 10ml/min 5%CO in He, 5ml/min O_2, and 5ml/min He, giving a total flow of 20ml/min (20°C). A total pressure of 2bar (20°C) was used throughout. It is important to note that this results in net oxidising conditions, with a $pCO:pO_2$ ratio of 1:10. The sample was then heated to 600°C at a linear ramp rate of 10K/min, with the exhaust gases constantly monitored by mass spectrometry. The second set of experiments was performed under identical flow conditions and heating rate, but samples had previously been calcined *in situ*. In this calcination, the sample was subjected to a continuous flow of 5ml/min O_2 and 15ml/min He, giving a total flow of 20ml/min. The sample was heated to 600°C at 10K/min, and held at this temperature for a period of two hours, before being allowed to cool to room temperature under an equivalent flow of pure He.

5.1.2 Pulsed Gas Experiments

Samples were calcined *in situ*, and then heated under a $CO/O_2/He$ mixture in continuous flow conditions, as described above. The sample was then held at 600°C, and flow conditions altered to a pulse configuration. A total flow of 40ml/min was maintained throughout, and only the composition of this flow was varied during the CO pulse sequence. This sequence of a 2-second CO pulse in every 300 seconds is detailed below:

between pulses:-35ml/min He, 5ml/min O_2, 0ml/min 5%CO/He   duration 298s

during pulse:-0ml/min He, 5ml/min O_2, 35ml/min 5%CO/He   duration 2s

This pulse sequence was carried out under isothermal conditions at selected temperatures for each sample.

5.2 Results and Discussion

5.2.1 Continuous Flow Experiments

A brief description of the normalisation process applied to the mass spectrometry data for the CO oxidation experiment is appropriate. Firstly, the $m/z = 4$ intensity, reasonably attributed solely to helium, was used in order to account for any variations in total pressure within the uhv chamber during the experiment. Secondly, throughout this set of experiments, the $m/z = 44$ signal was assumed to be due only to the evolution of CO_2, with the contribution due to CO oxidation within the mass spectrometer shown to be negligible. This assumption, along with a separate experiment to determine the cracking pattern of CO_2 under identical conditions, was used to remove the contribution of CO_2 production to the $m/z = 28$ intensity. This normalised $m/z = 28$ intensity is then assumed to be due solely to detected CO, as the background of residual N_2 is shown to be negligible, and the trend graphs of this signal with temperature may then be converted to a percentage CO uptake. This allows direct comparison between systems.

5.2.1.1 Materials Calcined *in situ* at 600°C

The table below gives the temperature at which 50% CO conversion is achieved for each system, along with surface areas calculated with the use of the BET adsorption isotherm and the temperature at which U_3O_8 has been observed to form:

System	T 50%/°C	Surface Area /m^2g^{-1}	T U_3O_8 formation/°C
Nit/600/H_1SiO_2	>600	215	490
Nit/600/SiO_2	567	80	560
Nit/600/γ-Al_2O_3	576	25	590
Cl/600/H_1SiO_2	>600	218	460
Cl/600/SiO_2	570	76	620
Cl/600/γ-Al_2O_3	350	23	600
U_3O_8	>600	16	-

Table 5.1 50% CO conversion temperature dependence on uranium precursor and support.

The first thing to note from the values above is the poor performance of the mesoporous silica supported samples. This is illustrated in the figure overleaf:
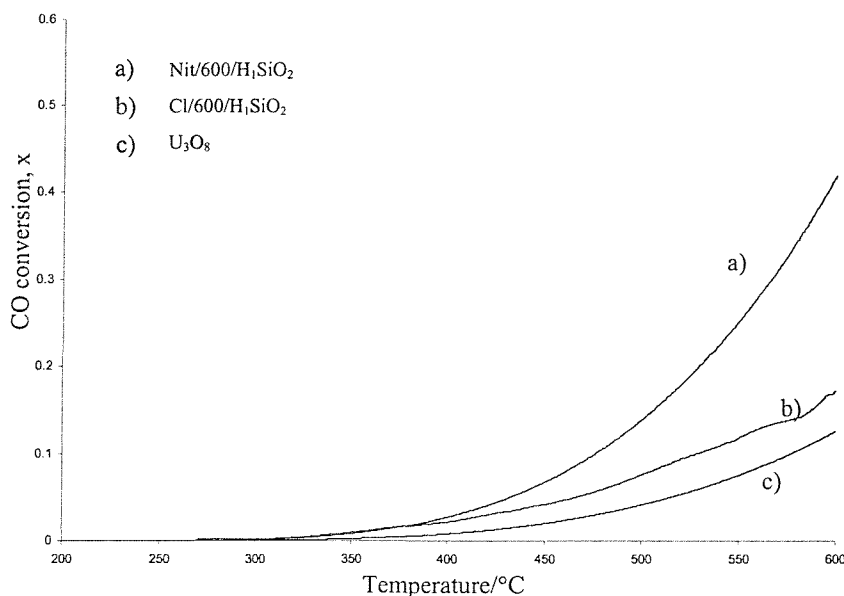
Figure 5.1 A plot of CO conversion versus temperature for the systems Nit/600/H$_1$SiO$_2$, Cl/600/H$_1$SiO$_2$ and unsupported U$_3$O$_8$.

On first inspection, the low activity of these systems is slightly surprising, considering the enhanced surface area of these materials compared to the amorphous support analogues. Indeed, the extent of CO conversion observed is comparable with that found for the bulk oxide U$_3$O$_8$. However, it is very important to note that the surface area determined by isothermal nitrogen adsorption does not necessarily relate directly to the surface area of the supported material. It is a measure of the area of any exposed surface, and this will include that of the support as well as that of the supported uranium material. This factor will become very important when dispersion of supported material is low and particle size is large, as in this case the majority of the measured surface area is attributable to the exposed support which is not expected to be active for this reaction. In Chapter 5, the temperature at which U$_3$O$_8$ formation is observed for these systems was discussed, and the results of this analysis are also given in the above table. Note that U$_3$O$_8$ is shown to form at considerably lower temperatures for the mesoporous silica supported materials compared to amorphous analogues, and it is reasonable to suggest that this will have an effect on the size of supported U$_3$O$_8$ particles present after treatment at 600°C for two hours. Indeed, this has been shown in Chapter 5 to be true for samples calcined at 800°C for three hours in air, where, for mesoporous silica supported materials, U$_3$O$_8$ particles of an average diameter, determined by electron microscopy, of ~70nm are formed. These

particles are larger than dimensions of the pores, and are found on the external surface of mesoporous silica particles. It would be expected for a similar phenomenon to occur in the course of the *in situ* calcination described here. The result of this sintering process is a very low uranium oxide surface area per unit mass, and this is demonstrated by the low activity of the mesoporous silica materials. Essentially, the systems are little more active than bulk U_3O_8, which was sieved to a particle size of 5-50μm, simply because the uranium oxide present is only a little more dispersed than in the bulk. In a comparison of the two H_1SiO_2 systems, the uranium tetrachloride derivative shows even less activity than the uranyl nitrate analogue. This may be solely due to the fact that the U_3O_8 formation temperature is 30°C less for the former, but a subtler precursor effect should not be discounted.

To illustrate further the precursor and support dependence of the CO oxidation activity, the results achieved from all six supported samples are shown below and overleaf in Figures 5.2 and 5.3:
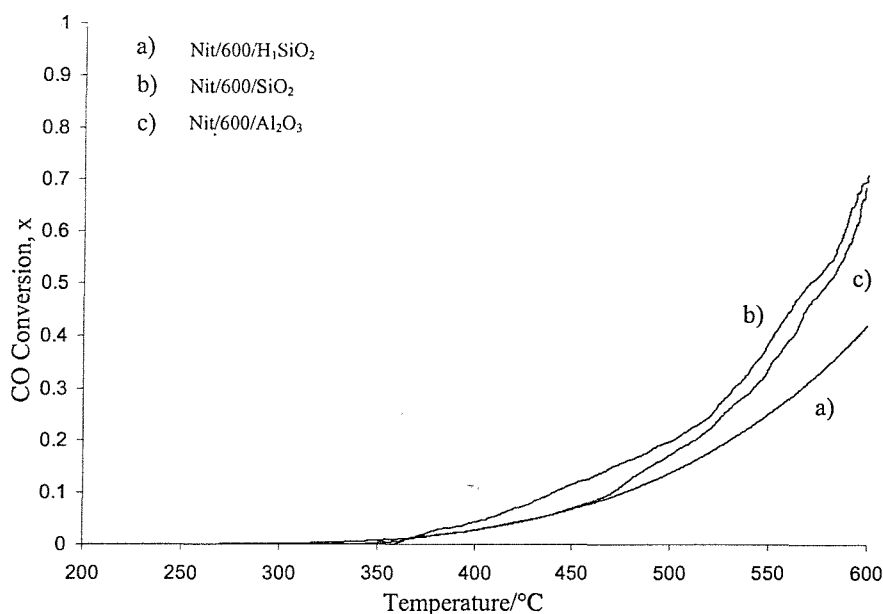
Figure 5.2 A plot of CO conversion versus temperature for the supported uranyl nitrate derivative materials
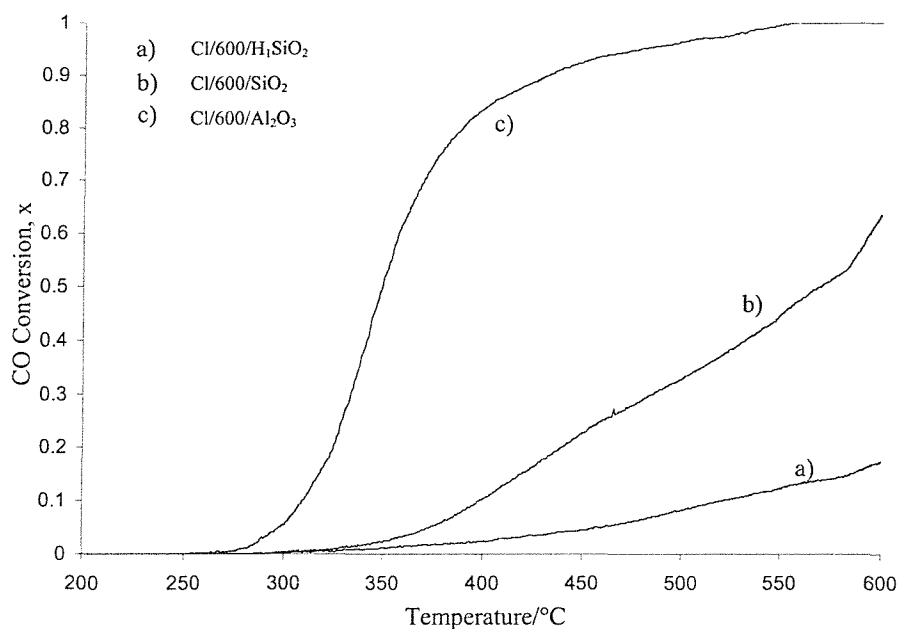
Figure 5.3 A plot of CO conversion versus temperature for the supported uranium tetrachloride derivative materials

The alumina and amorphous silica supported uranyl nitrate derivative samples show very similar activity, and their 50% conversion temperatures are within 10°C of each other. The Cl/600/SiO$_2$ system also affords similar activity, whereas the Cl/600/Al$_2$O$_3$ material demonstrates a remarkable 50% conversion temperature of 350°C, which is >200°C lower than the other three amorphous support-based materials. This suggests that the observed increased activity for this system is neither an effect solely due to support, as it would be expected that the Nit/600/Al$_2$O$_3$ material would give the same result, nor entirely due to precursor choice, as the Cl/600/SiO$_2$ should then be analogous. The indication is then for a more complex relationship between precursor and support.

A consideration of the differences between alumina and silica with respect to their use as supports for heterogeneous catalysis is required. After treatment at high temperature, alumina has a much higher Lewis acidity as a support than silica[15], and this property has been exploited in the preparation of a range of heterogeneous catalysts for reactions where the presence of surface acid sites is important. One example is supported platinum as a hydrocarbon reforming catalyst, where Pt/SiO$_2$ demonstrates poor activity compared to Pt/Al$_2$O$_3$.[16] In this reaction, the support itself has a role in the catalysis, and the activity of the Pt/Al$_2$O$_3$ may be increased further by the inclusion of chloride in the alumina synthesis. This is believed to increase the acidity of surface sites by the inductive effect of the chloride. This would provide a convenient explanation for the behaviour

observed above. However, the acidity of support surface sites is not expected to be an important factor in determining the activity of a catalyst towards the CO oxidation reaction[17]. Also, chemical analysis by X-ray fluorescence spectroscopy indicates that chlorine is not retained in supported uranium tetrachloride samples calcined in oxygen at temperatures of 600°C (see figure 6.10 in subsequent chapter). This suggests that the higher activity of the $Cl/600/Al_2O_3$ system, compared to the other materials, is not a direct result of the nature of the alumina surface. Instead, the combination of the tetrachloride precursor and the alumina support must influence the formation of the uranium oxide phase in such a way as to make it more active for this reaction. The mechanism by which this may occur is not obvious, and the supported uranium oxide phase is difficult to characterise in sufficient detail to distinguish the more and less active phases, but further analysis of the data may at least provide some information on how the reaction proceeds. This information may then be used to propose a sensible explanation for the differences observed between systems.

The mechanism of CO oxidation on uranium oxide has not been previously investigated in any detail, but this reaction on the surfaces of both platinum group metals[3,4], and selected transitional metal oxides,[10,14] has been extensively studied. A brief discussion of the steps involved in these systems may provide some insight into the processes that are likely to be important on the uranium oxide surface. The mechanism below is that proposed for CO oxidation on a palladium surface, and S represents indeterminate surface sites:

$$O_2 + 2S \longrightarrow 2O_{ads}$$
$$CO + S \longrightarrow CO_{ads}$$
$$CO_{ads} + O_{ads} \longrightarrow CO_2 + 2S$$
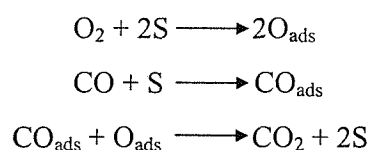
Some plausible steps have been omitted. For example, in the Langmuir-Hinshelwood type mechanism proposed above, the formation of CO_2 via two adsorbed species ignores the possibility of the reaction of gas phase oxygen with adsorbed CO, or indeed the reverse. At low partial pressures, and low coverages, with randomly distributed surface species, the rate determining step is apparently the dissociative adsorption of oxygen. The mechanisms that are proposed for the reaction on Cr_2O_3[10] and Co_3O_4/γ-Al_2O_3[14] are essentially identical for both systems:

$$O_2 + 2S \longrightarrow 2O_{ads}$$

$$CO_{(g)} + O_{ads} \longrightarrow CO_{2ads}$$

$$CO_{2ads} \longrightarrow CO_2 + S$$
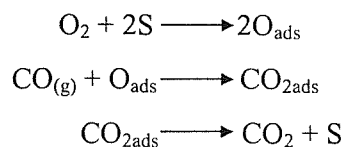
This mechanism is of the Eley-Rideal type, with CO_2 formed from adsorbed oxygen and gas phase CO, followed by rapid desorption of the carbon dioxide. The choice of adsorbed oxygen resulting from the dissociative adsorption of O_2, rather than lattice oxygen, as the source of O in CO_2 formation is an important distinction. Boreskov[18] investigated the relative rates of metal oxide surface reduction and CO oxidation, and concluded that for cobalt oxide the rate of surface reduction is orders of magnitude slower than CO oxidation below 600K. The suggestion is then that the lattice oxygen is unlikely to participate at lower temperatures for these systems. This is in contrast with that observed for uranium oxide catalysts in the total oxidation of hydrocarbons.[19,20,21] In experiments using isotopically labelled oxygen, it has been shown that the origin of the oxygen in the product stream is exclusively from the lattice of U_3O_8. Although the temperatures used for these studies are 100K higher than the figure quoted above, they are of a similar range to that which are used in this work, and may therefore offer a useful comparison. Also, it has been shown that the ease with which U_3O_8 may be reduced is greater than for many 3d transition metal oxides.[22] Qualitatively, it may be expected that, for a system where the oxygen incorporated in the product originates from the dissociative adsorption of O_2, then this may be the most important step in the determination of the rate. Whereas, for a system where lattice oxygen is readily available, then the concentration of CO will be rate determining. This will obviously not apply over a full range of conditions, but may be a useful starting point. The experiments described in this work are performed under a net oxidising reactant mixture. These conditions may not alter the nature of the key steps in the reaction, but will probably alter their relative significance, and they should be considered when making any assumptions to simplify the analysis.

In order to obtain thermodynamic and kinetic parameters for these reactions, an understanding of how a plug flow reactor operates is required[23].

kc^n dV dt disappear
by reaction in time dt

direction of flow

uc dt moles of reactant   dV $u(c+dc)$ dt moles of
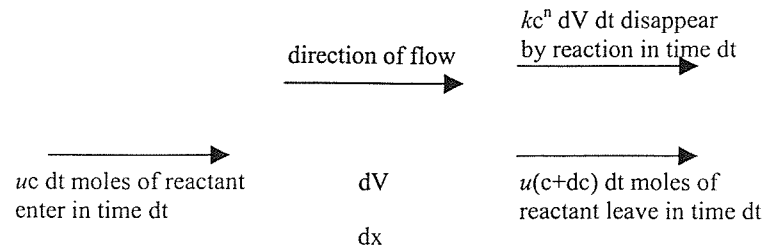enter in time dt   reactant leave in time dt

dx

Figure 5.4 A schematic illustration of plug flow

The reaction mixture is passed through the reactor at a volume rate of flow, equal to u. Consider an element of volume dV in the reactor, and, for simplicity, suppose that the reaction rate depends on the concentration c of a single reactant. For a reaction of the nth order the rate of disappearance of the substance is given by:

$$r = -\frac{dc}{dt} = kc^n$$

Eq. 5.1

The rate of disappearance of reactant in a volume dV is therefore kc^n dV. After the system has been operating for a sufficient period of time, a steady state is established. This means that there is no change, with time, in the concentration of reactant in the volume element. Three processes contribute to this concentration:

1. Molecules of reactant enter the volume element through the left face, with the number of moles entering in time dt being uc dt.

2. Molecules leave the volume element by the right face, with the number of moles leaving in time dt being $u(c+dc)$ dt.

3. Molecules disappear by chemical reaction. For a reaction of nth order the number of moles (-dn) disappearing in time dt is kc^n dV dt.

The steady-state equation is obtained by equating the rate of entry of reactant into the volume element (by process 1) to the sum of the rates of removal (by processes 2 and 3).

$$uc.dt = u(c+dc)dt + kc^n dVdt$$

Eq. 5.2

or

$$-\frac{dc}{c^n} = \frac{k}{u}dV$$

Eq. 5.3

This equation must be integrated over the volume V_o of the reactor; at the entrance to the reactor V=0 and $c=c_I$ (the initial concentration), while at the exit $V=V_o$ and $c=c_f$ (the final concentration of reactant). Therefore

$$-\int_{c_i}^{c_f} \frac{dc}{c^n} = \frac{k}{u} \int_0^{V_o} dV \qquad\qquad \text{Eq. 5.4}$$

For the particular case in which $n=1$, integration gives

$$-\ln\frac{c_f}{c_i} = \frac{kV_o}{u} \qquad\qquad \text{Eq. 5.5}$$

or

$$c_f = c_i e^{-kV_o/u} \qquad\qquad \text{Eq. 5.6}$$

The quantity V_o/u is known as the contact time for the reaction; it is the average time that a molecule takes to pass through the reactor. This type of flow system is suitable for fast reactions, where the contact time may be reduced by the use of high flow rates and small volume.

One of the assumptions stated above is that the rate of reaction depends only on the concentration of a single reactant. In a large excess of oxygen, as used here, this assumption should be valid, and the rate should depend solely on the concentration of CO. A second requirement in the derivation given is the existence of a steady state. Under isothermal conditions this could be assumed with a high level of confidence. However, with the use of a linear temperature ramp rate configuration, this is less certain. In order for this to be a good approximation, the reaction must be fast, and the product and unreacted starting material must be removed rapidly from the reactor to the mass spectrometer. The CO oxidation reaction is indeed expected to be very fast[24], but the character of the reactor must be confirmed.

The following equation has been used to calculate the rate of reaction from the experimental data:

$$r = \frac{y_o x}{\left(m/F\right)} \qquad\qquad \text{Eq. 5.7}$$

where: r is the reaction rate in moles of gas per mass of uranium per hour ($molg^{-1}h^{-1}$)

y_0 is the CO mole fraction at the inlet of the catalyst bed (0.025)

x is the normalised conversion of carbon monoxide

m is the mass of uranium in the catalyst sample (0.006g)

F is the total flow of feed gas ($0.05molh^{-1}$)

From an initial assumption that the reaction is first order with respect to CO, and zeroth order with respect to O_2 (at least at high O_2 partial pressure), k may be calculated using a rearranged form of Eq. 5.5. In order to avoid possible complication from mass transport

limitations at high CO conversions, data points where CO conversion is between 10 and 20% $(0.1 < x < 0.2)$ have been used to calculate the variation in k with temperature. As

$$k = Ae^{-E_a/RT} \qquad \qquad \text{Eq. 5.8}$$

an Arrhenius plot of $\ln k$ against $1/T$ should yield the activation energy and a value for the frequency factor. This is illustrated in the plot below for the systems $Cl/600/Al_2O_3$ and $Nit/600/Al_2O_3$, where the best linear fit has a gradient of $-E_a/R$ and an extrapolated intercept of $\ln A$. The $1/T$ axis is unmarked, as one set of data has been shifted in the x-direction to allow comparison of the gradients:
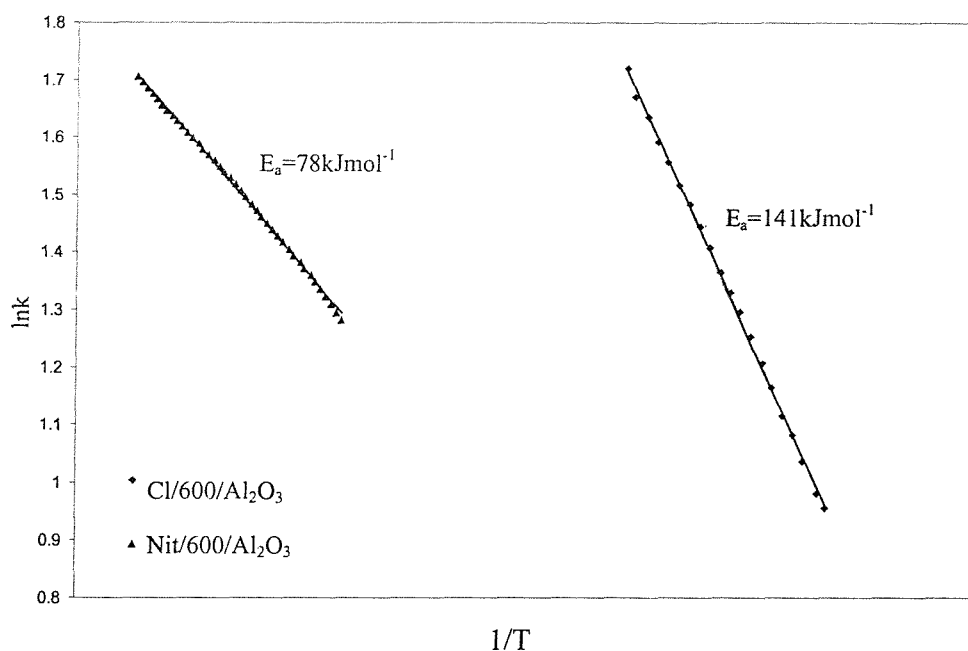
Figure 5.5 A plot of $\ln k$ vs. $1/T$ for the systems $Cl/600/Al_2O_3$ and $Nit/600/Al_2O_3$

Several assumptions must be made calculating these kinetic parameters. It is reasonably assumed that the temperature dependence of the pre-exponential term over this limited range is negligible. Also, in order to compare the rates of reaction, and rate constants from one system to another, it is necessary to choose a single temperature, that for the most active system is substantially outside the range $0.1 < x < 0.2$. At this level of conversion, it is possible that the reaction is no longer exhibits first order behaviour, and the numbers generated should be considered with caution.

Table 5.2 gives the calculated Arrhenius parameters for all six systems, as well as the calculated rates and rate constants at 450°C:

System	$E_a/kJmol^{-1}$	A/s^{-1}	$r_{450}/$ $molg_U^{-1}h^{-1}$	k_{450}/s^{-1}
Nit/600/H$_1$SiO$_2$	70	1.9×10^6	0.014	1.7
Nit/600/SiO$_2$	55	3.2×10^5	0.025	3.2
Nit/600/γ-Al$_2$O$_3$	78	6.2×10^6	0.012	1.6
Cl/600/H$_1$SiO$_2$	39	3.0×10^4	0.0092	1.1
Cl/600/SiO$_2$	67	1.2×10^6	0.047	6.2
Cl/600/γ-Al$_2$O$_3$	141	1.3×10^{13}	0.19	64
U$_3$O$_8$	62	8.2×10^4	0.0081	1.0

Table 5.2 Calculated activation energy and frequency factor dependence on precursor and support

The statistical errors associated with the values above are not simple to estimate. The plotted data fitted very well to a linear function, but some correlation between points derived from the normalisation process cannot be discounted. Therefore, although the residual fit to a linear function describing the variation of lnk with 1/T is typically less than 1% for this analysis, a statistical error calculated from this value may not accurately represent the level of experimental exactitude. In order to try and remove contributions from normalisation processes, activation energies have also been calculated from the m/z = 44 signal, and values obtained using this CO_2 evolution curve are within ∓ 10% of those quoted above. This probably provides a reasonable estimate of the error associated with these values, and it also affords some confirmation regarding the differential character of the reactor. The fact that both the calculated rates of CO disappearance, and that of CO_2 formation, are within experimental error of each other is good evidence for the suitability of the reactor configuration for the study of this reaction. Considering the above arguments, the errors associated with the calculated frequency factors are even more difficult to estimate, but the fact that the value is dependent on an extrapolation of the linear regression means that the potential error is larger than for the activation energy. A value of ∓ 8% is achieved from this extrapolation, but comparison with the figure obtained from the CO_2 formation data suggests that ∓ 20% is a more realistic error.

The value of activation energy obtained for the unsupported U$_3$O$_8$ sample is in agreement with that given in the literature for this reaction[1]. There is only limited variation between the systems Nit/600/Al$_2$O$_3$, Nit/600/SiO$_2$, and Cl/600/SiO$_2$, and indeed the mesoporous system Nit/600/H$_1$SiO$_2$, with activation energies found to be similar to that for the bulk uranium oxide. The previously quoted figure for uranium oxide supported on alumina[2], derived from calcination of uranyl nitrate at 800°C, i.e. analogous to the

Nit/600/Al$_2$O$_3$ system, is ~104kJmol^{-1}. This compares with a value of 78kJmol^{-1} found in this work. In the same article, it was claimed that the silica supported material displayed no activity for the reaction below 600°C.

The much higher value of 141kJmol^{-1} obtained for the Cl/600/Al$_2$O$_3$ material, the most active system for this reaction, is counterintuitive. It might reasonably be expected that the material with the lowest T 50% value would have a coincidentally lower barrier to activation, and in order to find an explanation for this phenomenon it is necessary to consider the associated frequency factor. A value of ~10^{13} is observed for this system, compared to 10^{5}-10^{6} for many of the other materials. In qualitative, and simplified, terms this means that, although the energy required for the reaction to occur is much greater, the likelihood that a collision of sufficient energy with the surface will result in reaction is also much increased. This may suggest that for materials displaying low activation energies, low frequency factors, and low activity there are a small number of very active surface sites, whereas for the Cl/600/Al$_2$O$_3$ system, although the surface sites are less active, there are many more sites capable of supporting the reaction. This may be an illustration of the compensation effect[25], which may be observed when the same reaction is studied using several different catalysts. This term applies when an increase in activation energy is compensated by a coincident increase in frequency factor. The origin of this effect is not agreed, but it has been proposed that, for many reactions, the measured activation energy is not the true activation energy. This is due to the fact that at higher temperatures the surface coverage of reactant may decline, and in this case, the apparent activation energy has a contribution from the enthalpy of adsorption of the reactant, ΔH_a. The quantity ΔH_a is always negative, so the lower the magnitude of ΔH_a, the higher the apparent activation energy, i.e $E_{true} = E_{apparent} - \Delta H_a$. The suggestion is that the true activation energy is a constant value. This is, in fact, in agreement with the qualitative argument given above, where the most active system has a large number of less active sites. In this case, although the enthalpy of adsorption is low, the likelihood of adsorption is still high due to the large number of sites. Indeed, this principle of a compensation effect appears to apply to the less active systems to some extent. A plot of lnA against activation energy fits well to a linear function for these materials, but there remains great variation in the measured rate.

An obvious, but important point, is the confirmation that the reaction is catalytic, and not simply a bulk reduction of the uranium oxide phase with carbon monoxide. This is demonstrated by the fact that the number of moles of CO that is oxidised may be shown to

be far in excess of the amount that would be required to reduce U_3O_8 to UO_2, although a partial reduction of the oxide in the initial stage of the reaction cannot be discounted. Indeed, an observation that the reaction may continue at the same rate for a short time in the absence of oxygen flow suggests that this bulk reduction is possible. A likely explanation for the observed activity is then simultaneous, but not site interdependent, reduction of the oxide by CO and reoxidation by O_2, i.e. continuous partial bulk reduction/oxidation.

5.2.1.2 Materials not Calcined Prior to Reaction

The table below gives the temperature at which 50% CO conversion is achieved for each system, along with surface areas calculated with the use of the BET adsorption isotherm.

System	T 50%/°C	Surface Area /m^2g^{-1}
Nit/nc/H_1SiO_2	363	313
Nit/nc/SiO_2	450	61
Nit/nc/γ-Al_2O_3	570	15
Cl/nc/H_1SiO_2	>600	430
Cl/nc/SiO_2	450	65
Cl/nc/γ-Al_2O_3	554	18
U_3O_8	>600	16

Table 5.3 50% CO conversion temperature dependence on uranium precursor and support.

The first observation to make is that the T 50% values are, with the exception of the uranium tetrachloride on alumina system, generally lower than for the analogous pre-treated materials. The most notable feature of the table above regards the mesoporous silica supported systems, where there is a very apparent precursor dependence on activity. This is shown in Figure 5.6:
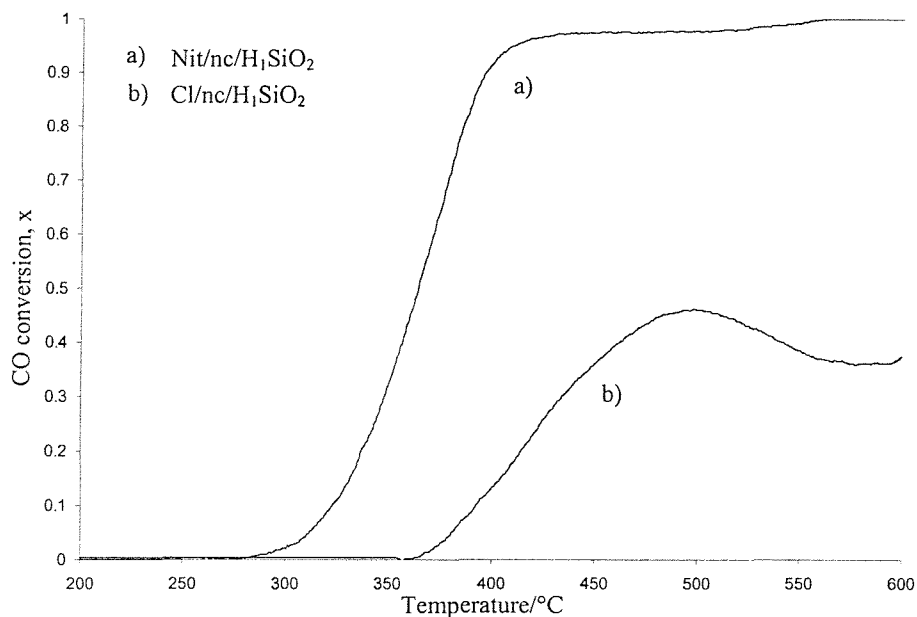
Figure 5.6 A plot of CO conversion versus temperature for the systems Nit/nc/H_1SiO_2 and Cl/nc/H_1SiO_2

For the analogous materials calcined *in situ*, the difference between systems was much less obvious, and indeed both precursors resulted in materials of poor catalytic activity. The pre-treatment, with its resulting formation of a uranium oxide, might be expected to remove some of the importance of the nature of the precursor, whereas formation of the catalytically active phase within the reaction mixture itself may allow this factor to dominate in the determination of activity. However, as was observed in the previous section, the tetrachloride on alumina system was much more active than the nitrate analogue even after pre-treatment. Also, for the Nit/nc/SiO_2 and Cl/nc/SiO_2 systems T 50% values are identical, and for the analogous alumina supported materials precursor choice appears to have a very limited effect. A reasonable explanation for these phenomena must again involve consideration of all the factors simultaneously. It has been previously stated that U_3O_8 formation occurs at a much lower temperature for the mesoporous silica supported systems, and that calcination of these materials at higher temperatures results in the sintering of this U_3O_8 phase leading to a low active surface area. Formation of the active phase under reaction conditions may be expected to prevent this sintering process, or at least to retard it over the period of study. If this should result in a highly dispersed active uranium phase on a high surface area support, then the greatly

increased activity observed for the Nit/nc/H$_1$SiO$_2$ over its pre-treated analogue is explicable. The fact that the same relative increase in activity is not observed for the Cl/nc/H$_1$SiO$_2$ system, and indeed the CO oxidation reaction appears to be slightly inhibited at elevated temperatures, suggests that chloride retained in the system under these reaction conditions is having a negative effect on activity. This chlorine retention is measured at a level of approximately 0.3wt% by X-ray fluorescence spectroscopy, and it is worthy of note that this level was also found for the amorphous silica, and alumina systems. This behaviour may be the basis of an explanation for the shapes of the CO conversion against temperature curves shown overleaf in Figure 5.7. These show a clear disparity in behaviour between the two silica and the alumina systems that must be a reflection of the surface chemistry. A similar plot for the nitrate systems is also shown in Figure 5.8:
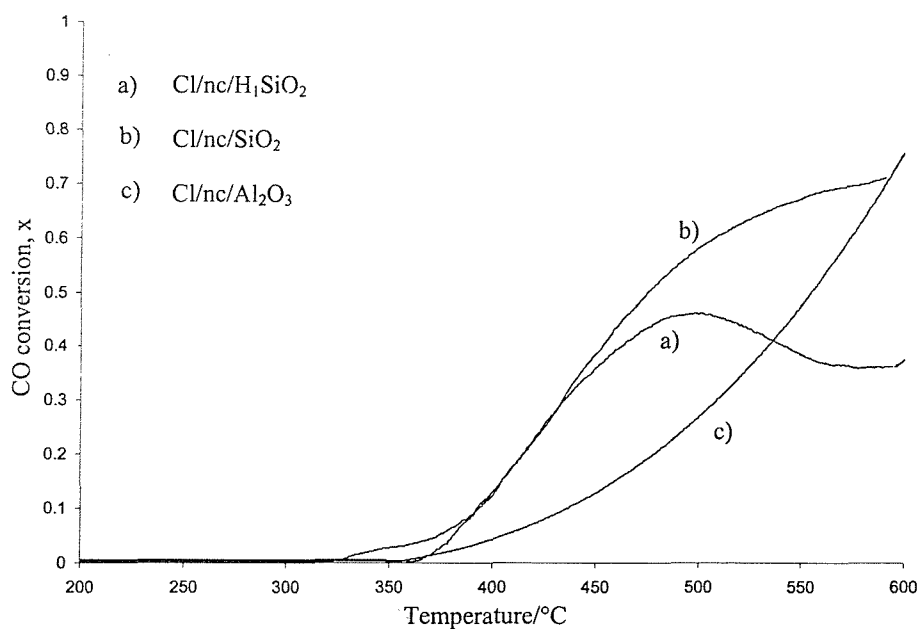
Figure 5.7 A plot of CO conversion versus temperature for the supported uranium tetrachloride derivative materials
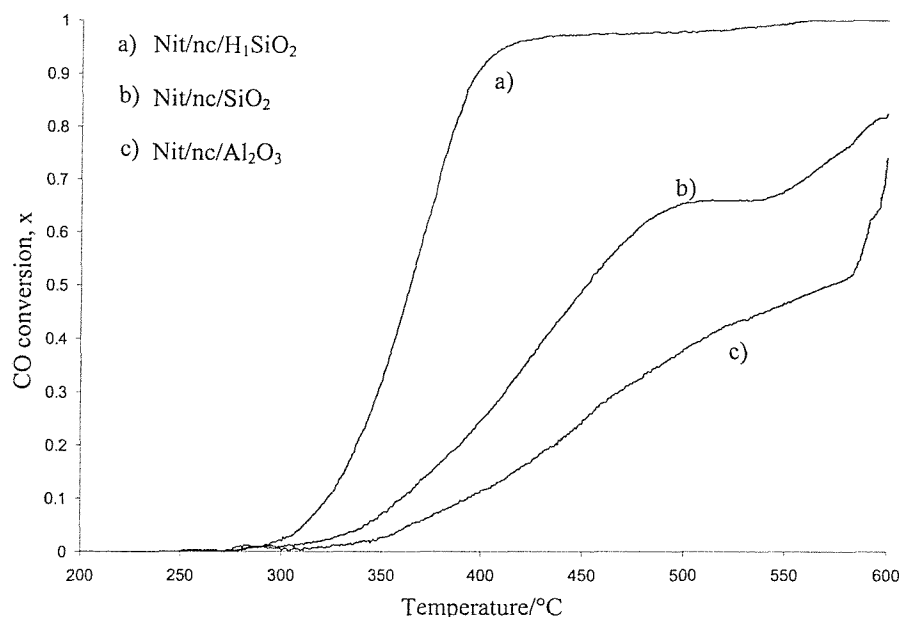
Figure 5.8 A plot of CO conversion versus temperature for the supported uranyl nitrate derivative materials

The shapes of many of the trend graphs in the above figures show a greater complexity of behaviour than that observed for the pre-treated samples. This is reasonable if the processes controlling the decomposition of the precursor, and the formation of the active phase are not totally decoupled under reaction conditions. This complexity is reflected in the Arrhenius parameters determined for these systems, and these are tabulated below along with the calculated rates and rate constants:

System	$E_a/kJmol^{-1}$	A/s^{-1}	$r_{450}/ molg_U^{-1}h^{-1}$	k_{450}/s^{-1}
$Nit/nc/H_1SiO_2$	157	1.7×10^{14}	0.20	89
$Nit/nc/SiO_2$	89	7.0×10^7	0.10	16
$Nit/nc/\gamma-Al_2O_3$	65	7.9×10^5	0.050	6.8
$Cl/nc/H_1SiO_2$	113	8.1×10^9	0.059	8.2
$Cl/nc/SiO_2$	138	1.8×10^{11}	0.081	12
$Cl/nc/\gamma-Al_2O_3$	79	1.6×10^6	0.027	3.4
U_3O_8	62	8.2×10^4	0.0081	1.0

Table 5.4 Calculated activation energy and frequency factor dependence on precursor and support

As for the pre-treated materials, the most active system, $Nit/nc/H_1SiO_2$, has the highest activation energy and the highest frequency factor. This is presumably due to the factors already discussed. Figure 5.9 illustrates the possible compensation effect, although

it must again be noted that any compensation is not complete, as the observed rate varies considerably from one system to another:
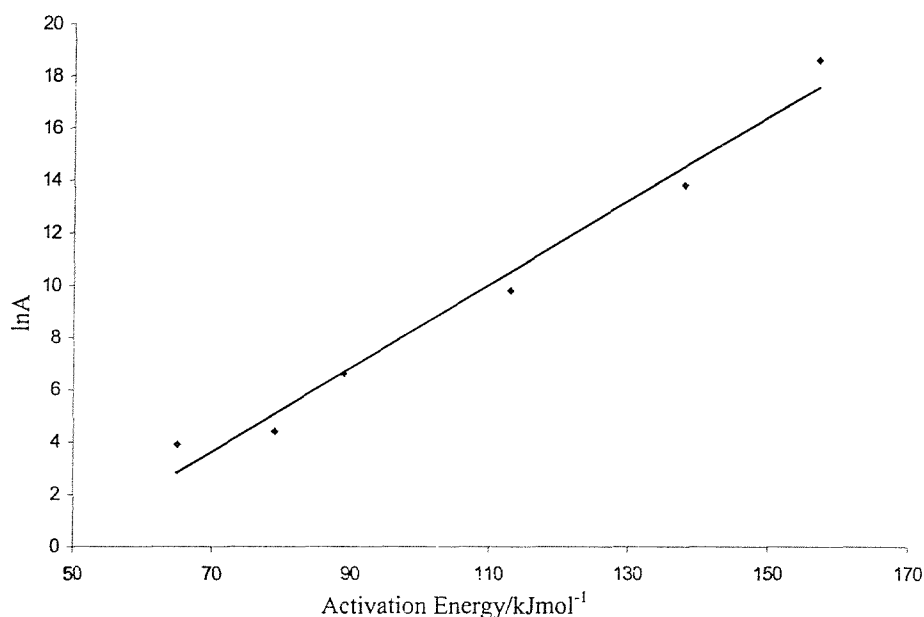

Figure 5.9 A plot of activation energy against lnA for materials not calcined prior to reaction showing a possible compensation effect.

Interestingly, the two silica supported tetrachloride systems, $Cl/nc/H_1SiO_2$ and $Cl/nc/SiO_2$, afford high activation energies and large frequency factors, but do not display the implied activity at higher temperatures. By comparison of the trend graphs, it is reasonable to suggest that this contradiction is due to the choice of points taken for the log plot. The values that have been used satisfy the condition $0.1<x<0.2$, and in Figure 5.7 it may be observed that for these two systems the initial light-off is quite rapid with temperature, before the gradient of these curves begin to reduce at higher conversions. An explanation for this behaviour is not immediately obvious, but one suggestion is that these materials are in some way self-poisoning, and active surface sites are consumed as the reaction proceeds. This might reasonably be associated with the observed chlorine retention, although the exact mechanism of this interaction is not known. The unexpected relative inactivity of the $Cl/nc/\gamma-Al_2O_3$ system compared to the $Cl/600/\gamma-Al_2O_3$ material is probably also due to the effect of chlorine retention on the nature of surface sites. The support dependence of the effect that the persistence of chlorine has on catalytic activity highlights fundamental differences between a silica and an alumina surface.

5.22 Pulse Flow Experiments

These experiments afford an alternative method of comparing the activity the supported materials, using the slightly different conditions of higher space velocity and lower contact times. The normalisation process applied to this data requires further explanation. As for the continuous flow experiments, the $m/z = 4$ signal was used in order to account for any variation in leak rate to the mass spectrometer during the isothermal experiment. This was also used to facilitate normalisation between experiments on the same system at different temperatures. Once each temperature has been normalised with respect to another for a given sample, and with the blank response recorded at room temperature, then a plot such as that given below may be achieved:
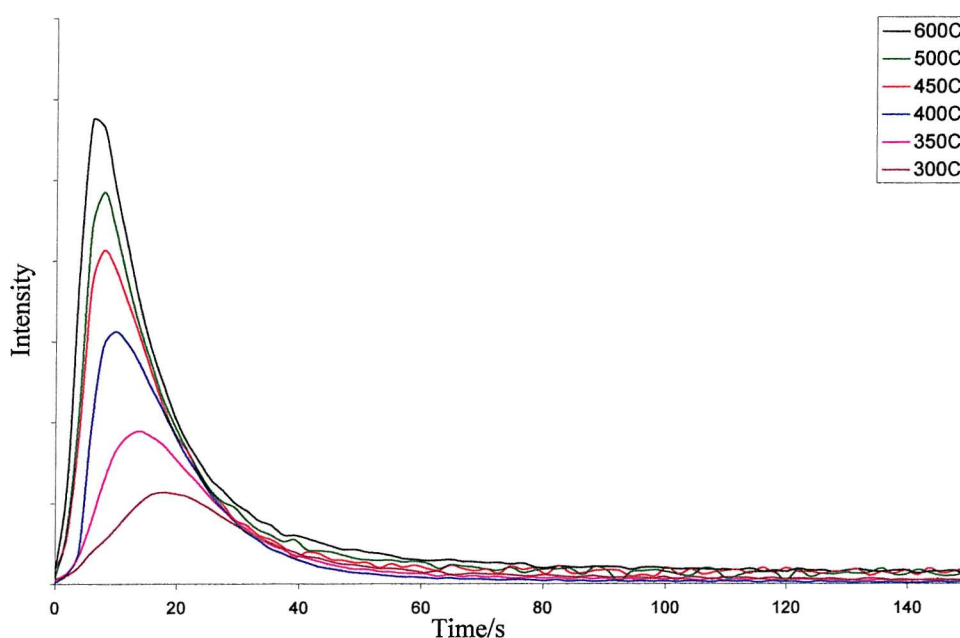
Figure 5.10 Temperature dependence of CO_2 evolution versus time curves for $Cl/600/SiO_2$

The graph above is useful with respect to a qualitative determination of the variation of reactivity with temperature for a single system, and as an assessment of the reactor character, where it shows that the peak width at half height of a two-second pulse is typically less than 20s. However, the plot in isolation provides no quantitative information regarding the relative activity of the materials. In order to achieve this, further normalisation between systems is required. This has been achieved by comparison of the integrated blank response CO pulse at room temperature. Once this is completed, it is possible to represent the relative performance of different materials. The figure overleaf depicts the CO_2 evolution curves for the uranium tetrachloride derivative systems:
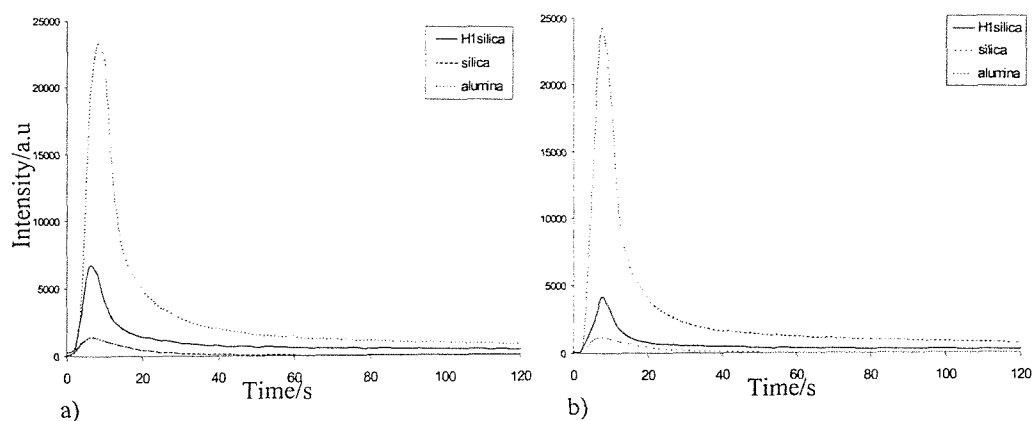
Figure 5.11 CO_2 evolution curves for the systems $Cl/600/H_1SiO_2$, $Cl/600/SiO_2$, and $Cl/600/Al_2O_3$ at a) 600°C, and b) 500°C

The graphs above allow direct comparison between analogous systems. It is possible to observe that, for the uranium tetrachloride derivative materials, not only is the alumina supported sample much more active than the amorphous and mesoporous silica samples at 600°C, but also the fall off in reactivity as the temperature decreases to 500°C is much reduced for this material under these conditions. This statement is in agreement with the information obtained from the continuous flow experiments, but there are notable differences in the trends observed under pulse conditions. The amorphous silica system was found to be markedly less active than the mesoporous silica analogue under the pulsed flow conditions, which is the opposite of that demonstrated under a total of 20ml/min continuous flow. An explanation for this observation is not immediately obvious, but it may help to consider the differences between the two experiments. Although both configurations are operating under a net oxidising atmosphere, there is a constant amount of reductant, i.e. CO, present under continuous flow, whereas the occurrence of this situation is only transient under pulse conditions. From the kinetic analysis performed previously, it was suggested that for the less active systems there were a small number of very active sites, and hence low activation energies and frequency factors. The $Cl/600/H_1SiO_2$ system has the lowest activation energy at 39kJmol^{-1}, which is considerably less than for $Cl/600/SiO_2$, 67kJmol^{-1}. This suggests that the sites at which the reaction is occurring are different, and it may be that the availability of sites for reaction in each system has a different dependence on the oxidant/reductant composition of the reactant mixture. There is no convincing evidence or applicable precedent for this suggestion, but the possibility that some surface defect sites may be annealed or unavailable under an almost constant oxidising atmosphere at high temperature should not be ignored. There is

some limited evidence for this process, in the reduction of CO_2 evolution with increasing time at constant temperature for the $Cl/600/SiO_2$ system. This phenomenon, which does not occur for the other tetrachloride derivative materials, is illustrated below:
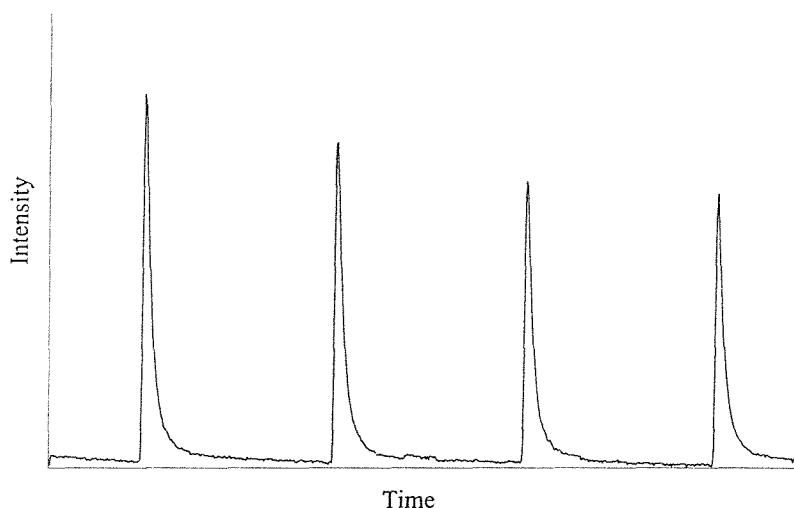

Figure 5.12 CO_2 evolution curves for the $Cl/600/SiO_2$ system at 600°C.

Figure 5.11 allowed a comparison of systems, but did not afford any quantitative information. This may be achieved by again integrating the area of the blank response CO pulse for each system, and assuming that this is the maximum theoretical amount of CO that is released through the reactor bed in a single pulse. From this figure, the CO consumption at each temperature may be calculated by integrating the area of the normalised m/z = 28 curve. Alternatively, the same information may be obtained by integrating the normalised m/z = 44 curves once the relative sensitivities of CO and CO_2 in the mass spectrometer have been determined by calibration. Indeed, it can be demonstrated that both methods provide the same results. Once this has been achieved, there is no requirement to normalise between systems, as the results obtained are absolute conversions. The results of this analysis for the uranium tetrachloride derivative materials are plotted overleaf:
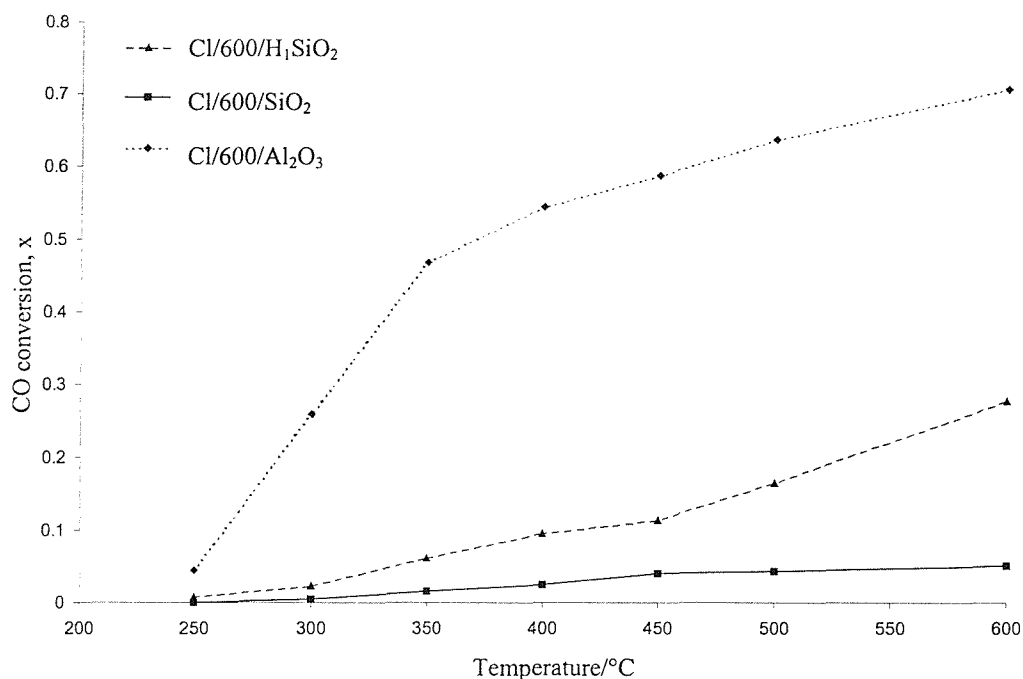
Figure 5.13 CO conversion vs. temperature under pulse flow conditions for the systems Cl/600/H$_1$SiO$_2$, Cl/600/SiO$_2$, and Cl/600/Al$_2$O$_3$.

The above curve for the Cl/600/Al$_2$O$_3$ system is, unsurprisingly, very similar to that obtained from the continuous flow experiment. The only differences are that 100% CO conversion is not achieved in the pulse flow experiment, presumably due to the increased space velocity, and that the material performs slightly better in pulse flow at temperatures between 250 and 300°C. This may be due to the fact that the plotted continuous flow data is collected with increasing temperature, whereas the pulse flow data is obtained at isothermal points decreasing from 600°C to 250°C.

A similar analysis of the data collected for the uranyl nitrate derivative materials yielded information consistent with that found by continuous flow experiments. Unlike the tetrachloride derivatives, no inversion of activity for the amorphous/mesoporous silica supported systems was observed.

5.2.3 Characterisation of Materials Post-Reaction

X-ray powder diffraction was used in order to characterise the uranium oxide phase present in the sample on removal from the microreactor. Analysis of the collected diffraction patterns enabled the phase to be tentatively identified as U_3O_8 in each case.[26] This is probably as would be expected, because even if the catalytically active phase were a partially reduced form of this oxide, a similar diffraction pattern would be predicted. The broadness of the peaks in many of the diffraction patterns disallows the opportunity measure the positions of peaks with sufficient accuracy to be able to assign a mixed phase, or to observe a shift in lattice parameters possibly consistent with a non-stoichiometric material.[27] Anyway, given the net oxidising conditions under which the reactions occurred, it is probable that any reduced active phase would be re-oxidised within the reactor before removal. As described in Chapter 4, the full diffraction peak width at half height was used to gain an estimate of the uranium oxide crystallite thickness with the Scherrer formula. Isothermal nitrogen adsorption has also been performed on these samples, and the BET isotherm used to obtain a measure of the surface area. These results are summarised in the table below:

Supported Material	Crystallite Thickness/nm	Surface Area/m^2g^{-1}
Cl/600/H_1SiO_2	65	251
Cl/600/SiO_2	12	76
Cl/600/γ-Al_2O_3	17	32
Nit/600/H_1SiO_2	62	225
Nit/600/SiO_2	14	72
Nit/600/γ-Al_2O_3	20	33
Cl/nc/H_1SiO_2	4	320
Cl/nc/SiO_2	2	65
Cl/nc/γ-Al_2O_3	2	22
Nit/nc/H_1SiO_2	2	301
Nit/nc/SiO_2	1	61
Nit/nc/γ-Al_2O_3	2	26

Table 5.5 Uranium oxide crystallite size dependence on precursor, support, and pre-treatment conditions

The systematic errors that may be associated with these methods of characterisation have been discussed previously (chapter 4), and will not all be repeated. However, it should be noted that the percentage error is considerably larger for very small particles due to excessive broadening,[28] and for the materials not calcined prior to reaction a value of $\mp$ 50% is not unrealistic. From the values of crystallite thickness given above, it is possible to observe a very marked difference in uranium oxide dispersion between the pre-treated

and non-calcined materials. This is most notable for the mesoporous silica supported systems where, for example, the $Nit/600/H_1SiO_2$ material has an average U_3O_8 crystallite thickness of 62nm compared with 2nm for $Nit/nc/H_1SiO_2$. The figure of 62nm compares with a larger value of 130nm for the same material calcined at 800°C for 3h, but it demonstrates that, even at 600°C, there is a sintering process and extrusion of oxide material from the pore structure. 62nm is an order of magnitude larger than the pore diameter, and suggests that this material, and its tetrachloride analogue, will behave similarly to bulk uranium oxide. This is indeed observed in the activity studies detailed in the previous sections. Conversely, the materials that were not subjected to the pre-calcination demonstrate much smaller supported uranium oxide particles. A figure of 2nm, found for the $Nit/nc/H_1SiO_2$ system, is very close to the measured dimensions of the pores of an H_1 silica templated by Brij76. The possibility of pore blocking certainly exists, but the errors associated with particle size determination do not allow any definitive statement to be made. Indeed, the adsorption/desorption isotherms associated with this material display no evidence of pore-necking or blocking which might be indicated by some hysteresis in the desorption branch. A more likely representation is the existence of some larger particles on the external surface, with smaller particles supported on the pore walls. This proposal is given some credence by the calculated pore size distributions, and this is illustrated below:
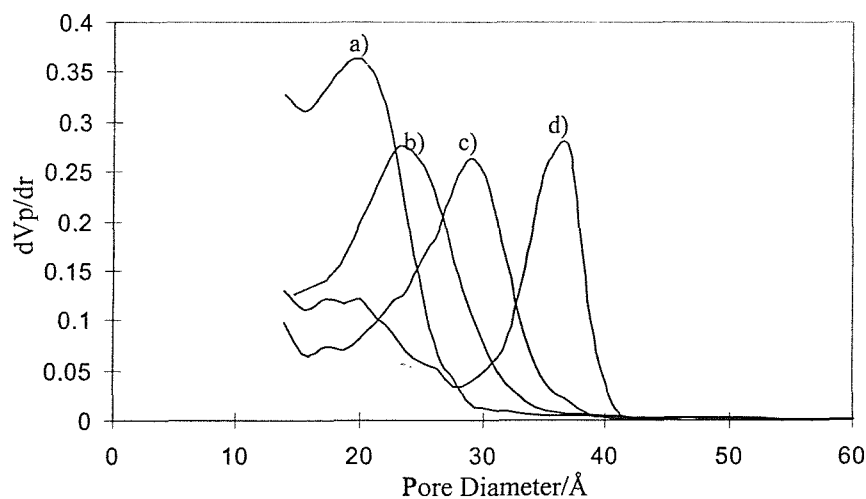

Figure 5.14 Pore size distribution for $UO_2(NO_3)_2.6H_2O/H_1SiO_2$ a) as made, b)post reaction, no pre-treatment, c)post-reaction, pre-treated 600°C/2h/*in situ*, d)pre-treated 800°C/3h/*ex situ*

The maxima in these distributions lie at approximately 2.0nm for the as made material, 2.3nm for the sample that had not been pre-treated prior to reaction, 3.0nm for the sample calcined at 600°C *in situ* prior to reaction, and 3.7nm for the material that had been

calcined *ex situ* at 800°C. These values compare with a value of 3.0nm for the mesoporous silica prior to deposition. This suggests that, without pre-calcination, much of the uranium material remains within the pores throughout the course of the reaction. This compares with the Nit/600/H$_1$SiO$_2$ system, where pore size after reaction is approximately equal to that of the pure mesoporous silica, suggesting that much of the supported uranium oxide has indeed been extruded from the pores.

5.3 Summary

The most active system after pre-treatment at 600°C for two hours *in situ* is the uranium tetrachloride on alumina system. This material achieves 90% CO conversion to CO$_2$ at 400°C under continuous flow conditions, which is significantly more active than the other five systems. Under these conditions, the mesoporous silica supported materials display low activity, and fail to achieve 50% CO conversion at 600°C. This is probably mainly due to the fact that during the pre-treatment, the uranium oxide particles formed are extruded from the pore structure and sinter to form very large particles analogous to bulk uranium oxide. The uranyl nitrate on mesoporous silica system is the most active material when samples are not subjected to calcination prior to reaction, with conversions similar to that found for Cl/600/Al$_2$O$_3$. The lack of pre-treatment increases the activity of most systems with respect to the CO oxidation reaction. The exception is the Cl/nc/Al$_2$O$_3$ system, where pre-calcination enhances activity. The most active systems display the highest activation energies for the process (~150kJmol^{-1}), with coincidentally high frequency factors.

Pulse flow experiments yielded similar information regarding the activity of the supported materials. An exception was made for the Cl/600/H$_1$SiO$_2$ and Cl/600/SiO$_2$ systems, where the relative activity was shown to be the reverse of that displayed under continuous flow conditions. The pulse flow experiments also confirmed the character of the reactor as suitable for following this type of reaction.

Characterisation of materials post-reaction suggested that the active phase is U$_3$O$_8$, and confirmed that pre-treatment at 600°C serves to sinter this phase to form large particles, especially with regard to the mesoporous silica supported materials where this oxide material is extruded from the pore structure. Where pre-treatment is avoided, analysis of isothermal nitrogen adsorption data suggests that material is retained within the pore structure throughout the course of the reaction.

5.4 References

1) F. Nozaki, K. Ohki, _Bull. Chem. Soc. Japan,_ 3473, **45**, 1972.

2) F. Nozaki, M. Kobayashi, S. Yoshida, _Nippon Kagaku Kaishi,_ p26, 1972.

3) T. Engel, G. Ertl, _Adv. Catal._ 1, **28**, 1979.

4) R. Imbihl, G. Ertl, _Chem. Rev._ p697, 1995.

5) S.N. Pavlova, V.A. Sadykov, N.N. Bulgakov, M.N. Bredikin, _J. Catal.,_ 517, **161**, 1996

6) T. Bunluesin, H. Cordatos, R.J. Gorte, _J. Catal.,_ 222, **157**, 1995

7) S.H. OH, C.C. Eickel, _J. Catal.,_ 543, **112**, 1988.

8) M. Kobayashi, H. Kobayashi, _Bull. Chem. Soc. Japan,_ 3009, **49**, 1976

9) M. Kobayashi, T. Date, H. Kobayashi, _Bull. Chem. Soc. Japan,_ 3014, **49**, 1976

10) M. Kobayashi, H. Kobayashi, _Bull. Chem. Soc. Japan,_ 3018, **49**, 1976

11) F.H.M. Dekker, G. Klopper, A. Bliek, F. Kapteijn, J.A. Moulijn, _Chem. Eng. Sci.,_ 4375, **49**, 1994.

12) D. Perti, R.L. Kabel, _Aiche J.,_ 1420, **31**, 1985

13) D. Perti, R.L. Kabel, _Aiche J.,_ 1427, **31**, 1985

14) D. Perti, R.L. Kabel, G.J. McCarthy, _Aiche J.,_ 1435, **31**, 1985

15) H. Knözinger, P. Ratnasamy, _Catal-Rev.-Sci. Eng.,_ 31, **17**, 1978

16) M.J. Sterba, V. Haensel, _Ind. Eng. Chem. Prod. Res. Dev.,_ 2, **15**, 1976.

17) T. Engel, G. Ertl, in D.P. Woodruff, ed., _The Chemical Physics of Solid Surfaces and Heterogeneous Catalysis,_ Elsevier, Amsterdam, 73, **4**, 1982.

18) G.K. Boreskov, _Kin. Kat.,_7, **14**, 1973.

19) C.S. Heneghan, G.J. Hutchings, S.R. O'Leary, S.H. Taylor, V.J. Boyd, I.D. Hudson, _Catal. Today,_ 3, **54**, 1999.

20) G.J. Hutchings, C.S. Heneghan, I.D. Hudson, S.H. Taylor, _Nature,_ 341, **384**, 1996.

21) G.J. Hutchings, C.S. Heneghan, I.D. Hudson, S.H. Taylor, _ACS Symp. Ser. 638,_ p58, 1996.

22) H. Collette, V. Deremince-Matthieu, Z. Gabelica, J.B. Nagy, E.G. Derouane, J.J. Verbist, _J. Chem. Soc. Faraday Trans.2,_ 1263, **83**, 1987.

23) K.J. Laidler, _Chemical Kinetics,_ 2nd ed., Tata McGraw-Hill, New York, p22, 1973.

24) I. Langmuir, _Trans. Faraday Soc._ 621, **17**, 1922.

25) M. Boudart, G. Djega-Mariadassu, _Kinetics of Heterogeneous Catalytic Reactions,_ Princeton University Press, Prinston, p124, 1984.

26) B. Loopstra, _J. Appl. Crystallogr.,_ 94, **3**, 1970

27) R.J Ackerman, A.T. Chang, C.A. Sorrell, *J. Inorg. Nucl. Chem.*, 75, **39**, 1977.

28) G.C. Bond, *Heterogeneous Catalysis: Principles and Applications*, Oxford University Press, Oxford, p81, 1987

Chapter 6. Catalytic Selective Reduction of Nitrogen Monoxide

This chapter is an investigation of the activity and selectivity of supported uranium materials with respect to the catalytic selective reduction of NO to N_2, using CO as a reductant. This work is inspired by results describing the activity of bulk U_3O_8 for this reaction[1], and an investigation of an alumina supported uranium oxide system, which have been published previously.[2] The data obtained from these systems will be used for direct comparison with the findings obtained from this work. As described in Chapter 5, two precursors; uranium tetrachloride, UCl_4, and uranyl nitrate hexahydrate, $UO_2(NO_3)_2.6H_2O$, were supported on three different inorganic oxide supports: mesoporous silica, amorphous silica, and amorphous alumina. This provides a total of six different supported uranium systems, deposited at 30wt% U, and allows the activity dependence of precursor and support to be investigated. Systems will be denoted in an abbreviated form for convenience, e.g. $Nit/800/H_1SiO_2$ for uranyl nitrate supported on mesoporous silica pre-treated at 800°C, or $Cl/nc/\gamma$-Al_2O_3 for uranium tetrachloride supported on alumina and not calcined prior to reaction. For comparison with industrially relevant materials, the performance of a conventional 5wt% Pt/γ-Al_2O_3 catalyst has been investigated, and these results will also be presented here.

The overall stoichiometry of the desired reaction is given below:

$$CO + NO \longrightarrow \tfrac{1}{2} N_2 + CO_2$$
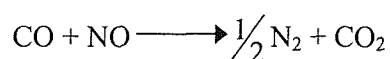
However, 100% selectivity of the reduction towards the formation of N_2 is not always apparent, and previous studies of this reaction using a variety of different catalysts, such as Cu/TiO_2,[3] $LaFeO_3$,[4] CuO-MnO_x,[5] La_2CuO_4,[6] as well as supported noble metal materials,[7,8,9] report the undesirable formation of nitrous oxide under certain conditions, i.e.

$$CO + 2NO \longrightarrow N_2O + CO_2$$
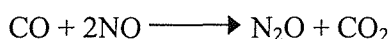
The N_2O formed may then persist, and be found in the exhaust gas from the reactor, or it may undergo further reaction:

$$CO + N_2O \longrightarrow N_2 + CO_2$$

N_2O is generally considered to have an even higher environmental impact than NO, and therefore the selectivity of the catalyst towards N_2 is of equivalent importance to the NO decomposition activity that it demonstrates.

6.1 Experimental

The synthesis, where appropriate, and pre-treatment of oxide supports has been discussed in Chapter 3, and the methodology used in the deposition of the uranium material in Chapter 4. The general microreactor configuration for continuous flow, and pulsed flow experiments has been previously documented in Chapter 5. However, due to the slightly different gas flow conditions involved for this reaction, each type of experiment will be briefly described. The experimental features common to both are initially detailed. Samples were ground to a particle size of 5-50μm using a pestle and mortar. 20mg of sample was packed into a quartz capillary, and held in place by plugs of quartz wool. The capillary was then mounted in the reactor, and thoroughly purged with a helium flow of 40ml/min.

6.1.1 Continuous Flow Experiments

For each of the six precursor/support systems, the effect of catalyst pre-treatment on the activity and selectivity of the NO reduction reaction has been investigated, and five sets of experiments have been performed for this purpose. In the first set, the supported uranium material was not subjected to any pre-treatment prior to its reaction with CO and oxygen. The sample was subjected to a continuous flow of 10ml/min 5%CO in He, and 10ml/min 5%NO in He, giving a total flow of 20ml/min (20°C). A total pressure of 2bar (20°C) was used throughout. It is important to note that this results in neither net oxidising, nor net reducing conditions, with a pCO:pNO ratio of 1:1. The sample was then heated to 600°C at a linear ramp rate of 10K/min, with the exhaust gases constantly monitored by mass spectrometry. The second, third and fourth sets of experiments were performed under identical flow conditions and heating rate, but samples had previously been calcined _ex situ_. In this calcination, the sample was subjected to a continuous flow of 20ml/min O_2. The sample was heated to either 450, 600 or 800°C at 10K/min, and held at this temperature for a period of two hours, before being allowed to cool to room temperature. The fifth set of experiments were performed on samples that had been previously calcined _ex situ_ at 800°C, followed by _ex situ_ reduction in a continuous flow of 20ml/min 10%H_2 in N_2. The sample was heated to 523°C at 10K/min, where it was held for ten hours.

Due to the character of the microreactor, extended time-on-line studies were not possible. However, eight-hour tests at constant temperature were performed, and the constant activity observed confirms the catalytic nature of the reaction.

6.1.2 Pulsed Gas Experiments

Samples that had either not been previously calcined, or had been pre-treated at 600°C in oxygen for 3 hours, were heated under a CO/NO/He mixture in continuous flow conditions, as described above. The sample was then held at 600°C, and flow conditions altered to a pulse configuration. Two sets of experiments were performed; firstly, a constant flow of 5%CO in He was periodically interrupted with a pulse of 5%NO in He, i.e. net oxidising conditions, and secondly the reverse procedure was performed with 5%CO in He used as the pulse gas, i.e. net reducing conditions. A total flow of 40ml/min was maintained throughout, and only the composition of this flow was varied during the pulse sequence. This sequence of a 2-second pulse in every 300 seconds is detailed below:

1) NO pulse

between pulses:-40ml/min 5%CO/He, 0ml/min 5%NO/He   duration 298s

during pulse:-0ml/min 5%CO/He, 40ml/min 5%NO/He   duration 2s

2) CO pulse

between pulses:-40ml/min 5%NO/He, 0ml/min 5%CO/He   duration 298s

during pulse:-0ml/min 5%NO/He, 40ml/min 5%CO/He   duration 2s

These pulse sequences were carried out under isothermal conditions at selected temperatures for each sample.

6.2 Results and Discussion

6.2.1 Continuous Flow Experiments

A description of the normalisation process applied to the mass spectrometry data is appropriate. As has been previously stated, in the investigation of this reaction it is very important to be able to distinguish both the activity, in terms of %NO conversion, and the selectivity of the reaction to the formation of N_2. Where a mass spectrometer is to be used as the exhaust gas analyser, this introduces a high level of complexity to the processes involved in the normalisation of the data obtained. Both CO and N_2 have a molecular mass of 28amu, and so the isolation of the contributions of each to the observed m/z = 28 intensity requires detailed analysis. This situation also applies to the m/z = 44 signal, which may be expected to exhibit contributions from both CO_2 and N_2O.

In order to achieve this analysis, a set of simple experiments using pure gases was performed to gain the cracking patterns of all reactants and likely products. All such experiments were carried out at an identical total pressure, to simultaneously obtain a measure of the sensitivity of the mass spectrometer to different species. Once this information is obtained, a number of assumptions and relationships must be used to gain a measure of NO consumption and N_2 selectivity at any point in the reaction. These are detailed below.

1) The intensity of the m/z = 12 signal was shown to be due only to CO and CO_2. This is shown by the above experiments to be valid. The same experiments also provide ratios of m/z = 28 (CO) to m/z = 12 (CO), and m/z = 44 (CO_2) to m/z = 12 (CO_2). Assuming that the only product of reaction of CO is CO_2, then the above ratios may be used to calculate the ratio of CO to CO_2 at any point. This is illustrated in Figure 6.1:
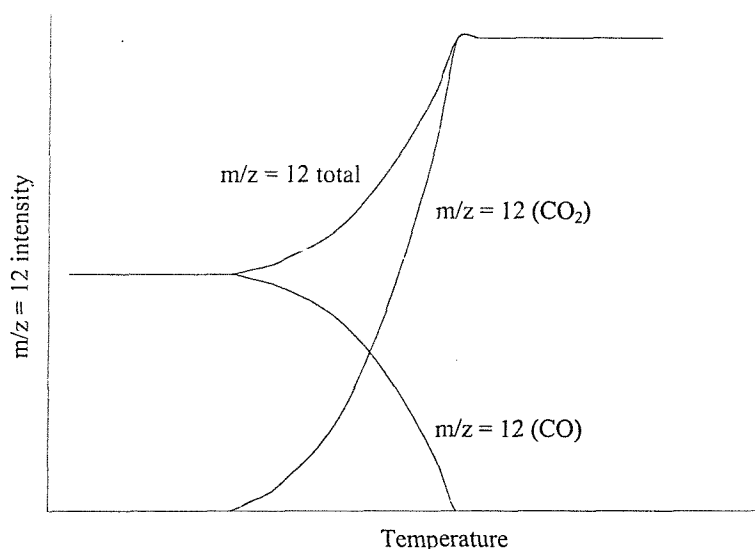
Figure 6.1 Variation of m/z = 12 intensity with CO:CO_2 ratio

2) Sensitivity measurements allow the concentration of CO and CO_2 to be determined from this ratio.

3) Also from the calibration experiments, the m/z = 28 to m/z = 29 ratios for CO and N_2 are determined. The contribution to the m/z = 29 from NO, CO_2 and N_2O is shown to be negligible.

4) The concentration of N_2 may then be determined from the m/z = 29 signal less the contribution known to be due to CO.

5) The N_2O concentration may be calculated from the m/z = 44 signal less the contribution known to be due to CO_2. If the concentration of N_2 is also known, then the selectivity of the reaction may be determined

6) The NO concentration may then be found from the m/z = 30 signal less that due to N_2O, although in practice the contribution from N_2O is significant only when the NO concentration is very low. From this, the extent of NO conversion may be gained.

The assumptions stated above will obviously introduce some supplementary sources of error to the values obtained for NO conversion and N_2 selectivity. At very low conversions these errors may be considered large, and the values associated with the selectivity at these points should be considered as only an estimate. At higher conversions, quoted selectivities are ~⊛5%, and quoted conversions ~⊛3%.

6.2.1.1 Materials Calcined Prior to Reaction

Initially, the results from samples calcined at 800°C *ex situ* will be used to introduce many of the important points in the analysis and interpretation of this data. These results provide a means of comparison with previously published work, as the pre-treatment conditions used here match those of the reportedly most active systems. The table below gives the temperature at which 25% NO conversion is achieved for each system, along with surface areas calculated with the use of the BET adsorption isotherm and the temperature at which U_3O_8 has been observed to form *ex situ*:

System	T 25%/°C	Surface Area /m^2g^{-1}	T U_3O_8 formation/°C
Nit/800/H_1SiO_2	>600	195	490
Nit/800/SiO_2	583	82	560
Nit/800/γ-Al_2O_3	565	33	590
Cl/800/H_1SiO_2	594	205	460
Cl/800/SiO_2	544	80	620
Cl/800/γ-Al_2O_3	517	31	600
U_3O_8	>600	16	-
5%Pt/γ-Al_2O_3	332	142	-
H_1SiO_2/800	488	602	-
SiO_2/800	>600	219	-
γ-Al_2O_3/800	432	90	-

Table 6.1 25% NO conversion temperature dependence on uranium precursor and support.

From Table 6.1 it is immediately obvious that the supported uranium materials prepared under these conditions are greatly inferior in activity compared to the standard platinum catalyst. This is illustrated in Figure 6.2, where the extent of NO conversion is plotted against reaction temperature for the three supported uranium tetrachloride derivative materials, as well as the 5wt%Pt/γ-Al$_2$O$_3$ sample.
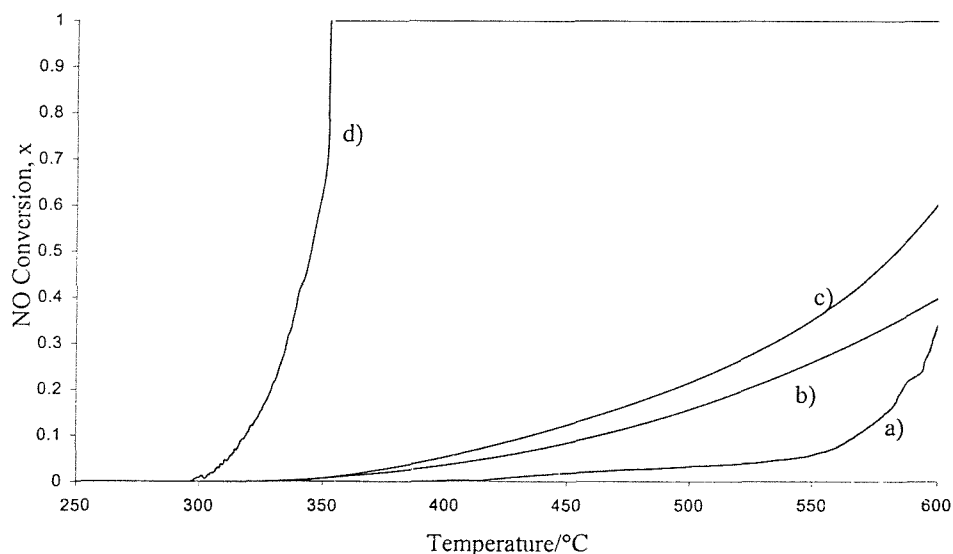

Figure 6.2 Effect of catalyst support on NO conversion activity, a) Cl/800/H$_1$SiO$_2$, b) Cl/800/SiO$_2$, c) Cl/800/γ-Al$_2$O$_3$, d) 5wt% Pt/γ-Al$_2$O$_3$

It should also be noted that, in terms of NO conversion, the supported materials listed above are in fact less active than the pure support oxides γ-Al$_2$O$_3$ and H$_1$SiO$_2$. The performance of these is illustrated in Figure 6.3:
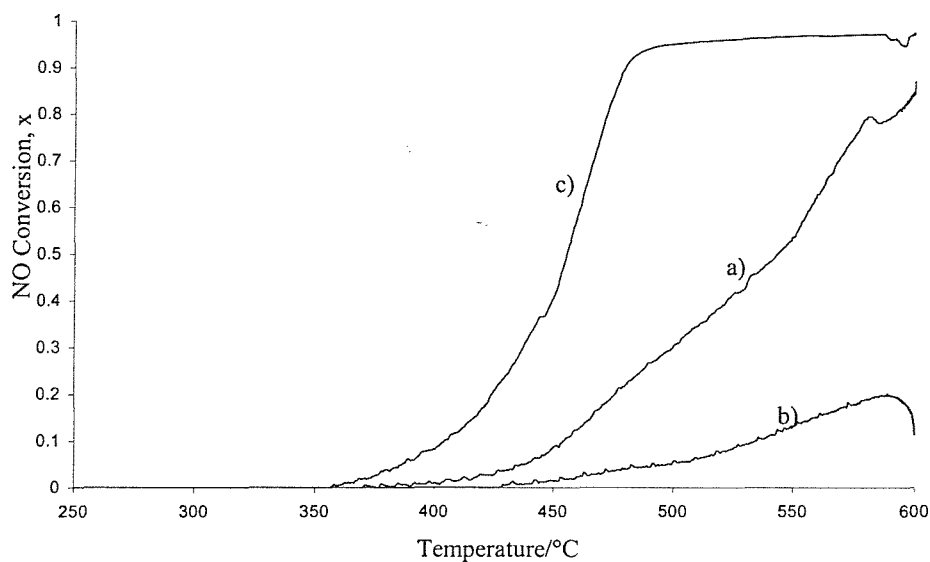
Figure 6.3 NO conversion vs. temperature for oxide support materials, a) H$_1$SiO$_2$, b) SiO$_2$, c) γ-Al$_2$O$_3$

These results suggest that the deposition of the uranium oxide precursor, and subsequent thermal treatment at 800°C, actually inhibits the catalytic conversion of NO. However, it is important to recall that the selectivity of the reaction is of greater significance than the absolute NO consumption. The selectivity towards N_2 and N_2O have been calculated for all these systems, and this behaviour is illustrated below for the 5wt%Pt/γ-Al_2O_3 material (Fig. 6.4) and Cl/800/γ-Al_2O_3 (Fig. 6.5)
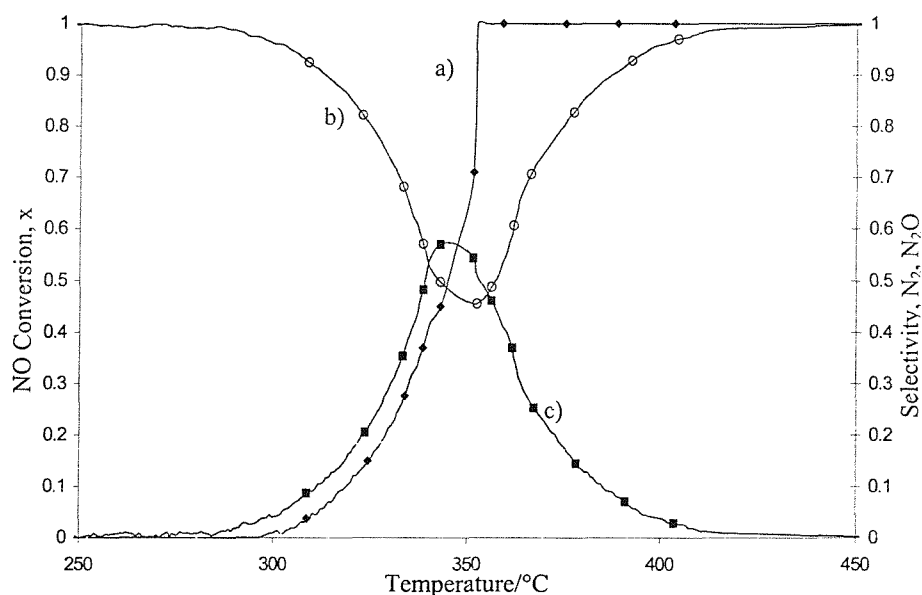
Figure 6.4 5wt%Pt/γ-Al_2O_3, a)NO conversion, b)N_2 selectivity, c)N_2O selectivity.
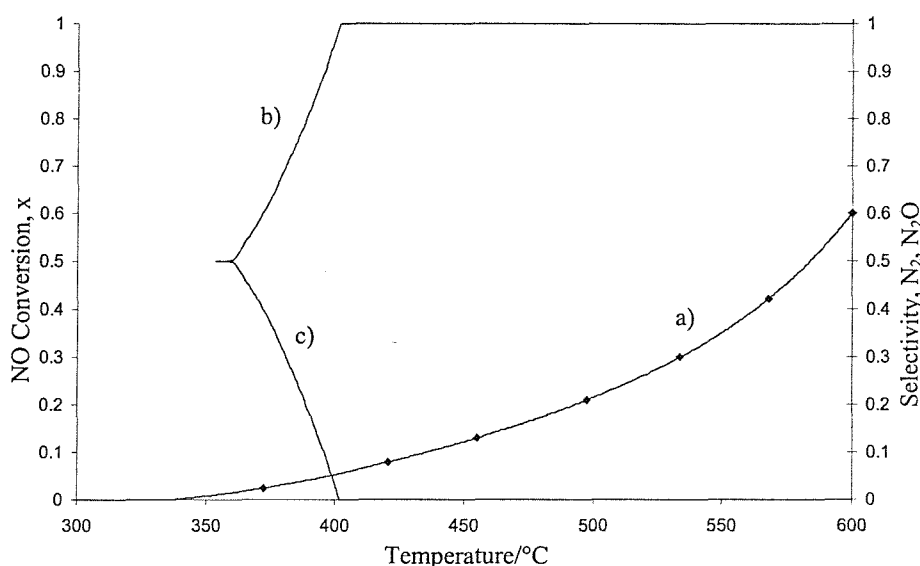
Figure 6.5 Cl/800/γ-Al_2O_3 a)NO conversion, b)N_2 selectivity, c)N_2O selectivity.

The figures 6.4 and 6.5 demonstrate that, despite the lower activity of the supported uranium material, Cl/800/γ-Al$_2$O$_3$, 100% N$_2$ selectivity is achieved at ~400°C. This behaviour is very typical of all the supported uranium materials. The supported platinum system exhibits 100% NO conversion at ~360°C, but total selectivity towards N$_2$ is not achieved until slightly greater than 400°C. The flow conditions for these experiments include a GHSV of 90000h^{-1}, which is large due to the small amount of catalyst used. The previously reported results describing the activity of a supported uranium material, derived from uranyl nitrate supported on alumina, towards this reaction showed that 100% NO conversion was achieved at 400°C, which is much lower than that found in this investigation.[2] However, although catalyst pre-treatment conditions are identical, the space velocity used by Pollington *et al* was much lower, with a GHSV of 2300h^{-1}. The extent of NO conversion at a given temperature would be expected to increase on reduction of the space velocity and increase in the contact time, and this may lead to greater agreement between the results reported here, and those previously. Indeed, this will be investigated in a later section. The pure alumina, and mesoporous silica exhibit N$_2$ selectivities at 600°C of 50% and 30% respectively.

A direct comparison of the supported uranium materials reveals that the activity decreases with choice of support in the order γ-Al$_2$O$_3$>SiO$_2$>H$_i$SiO$_2$, and with the choice of precursor, UCl$_4$>UO$_2$(NO$_3$)$_2$.6H$_2$O. The low activity of the mesoporous silica supported materials, especially considering their enhanced surface areas, has been observed in the previous chapter for samples calcined prior to reaction. It is reasonable to assume that the arguments proposed in the discussion of CO oxidation activity may also be relevant in this instance, i.e. that pre-treatment at elevated temperatures leads to the sintering of uranium oxide particles formed, and extrusion from the pore structure, resulting in a low active surface area. The similarity in activity between amorphous alumina and amorphous silica supported samples suggests that the chemical nature of the support material is not of great importance for this reaction. It was shown in chapter 4 that the U$_3$O$_8$ formation temperature and subsequent particle growth varies little between these two support materials, and it appears that this is the most important factor for materials calcined at high temperature prior to reaction. The uranium tetrachloride derivative materials are shown to be slightly more active than the uranyl nitrate analogues, but differences between the two systems are small and selectivity curves are identical within experimental error. The

calcination at 800°C appears to have removed much of the activity dependence on precursor.

Given the arguments above, the next logical step is to decrease the temperature of pre-treatment. This should provide an insight into the effect of calcination conditions on activity, and may introduce a greater level of precursor dependence on the properties exhibited. For this reason, the reaction was then performed with materials previously calcined at 600°C. The results of this investigation are summarised below in Table 6.2, with the temperature at which 25% NO conversion is achieved and the surface area of the materials prior to reaction. The T 25% values for the analogous materials pre-treated at 800°C are included for convenient comparison:

System	T 25%/°C(600)	Surface Area /m²g⁻	T 25%/°C(800)
Nit/600/H₁SiO₂	565	215	>600
Nit/600/SiO₂	555	80	583
Nit/600/γ-Al₂O₃	527	25	565
Cl/600/H₁SiO₂	572	218	594
Cl/600/SiO₂	504	76	544
Cl/600/γ-Al₂O₃	430	23	517

Table 6.2 25% NO conversion temperature dependence on uranium precursor and support.

The first point to note is that all the T 25% values are reduced in temperature with respect to those of the materials calcined at 800°C prior to reaction, so a reduction in pre-treatment temperature has resulted in a higher degree of activity. This is an important result, and for analogous precursor/support systems the only likely difference that may provide an explanation of this phenomenon is in the size of the uranium oxide particles formed on the support surface during calcination, i.e. the magnitude of the active surface area. A second result that is evident from the values above is that the activity dependence on precursor, where $UCl_4 > UO_2(NO_3)_2.6H_2O$, observed for the 800°C analogues is retained on reduction of the pre-treatment temperature. A notable exception to this is for the mesoporous silica supported materials, where the relative activity is reversed, with the uranyl nitrate derivative having a slightly lower T 25% value. This result may actually help to provide an explanation for the precursor dependence, and will be referred to below. The support dependence on activity, where $\gamma\text{-}Al_2O_3 > SiO_2 > H_1SiO_2$, is maintained without exception under these pre-treatment conditions, and indeed seems to be magnified by calcination at the lower temperature of 600°C. This is illustrated in Figure 6.6.
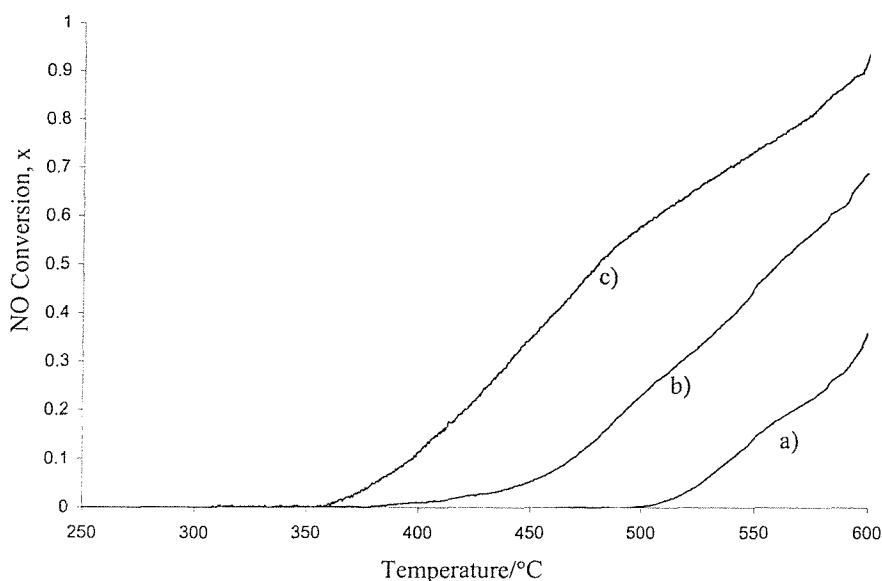
Figure 6.6 Effect of catalyst support on NO conversion activity, a) Cl/600/H₁SiO₂, b) Cl/600/SiO₂, c) Cl/600/γ-Al₂O₃

Table 6.2, along with the plot above, shows the Cl/600/γ-Al₂O₃ system to be the most active of the six studied, with a T 25% value ~75°C lower than that of any other. In chapter 5, it was demonstrated that this system is by far the most active of the pre-calcined supported uranium materials for the catalytic oxidation of carbon monoxide. This suggests that there is a correlation between the two reactions. This commonality is perhaps not surprising, as both processes require the formation of CO_2 from CO, and it may be an indication that the two reactions require similar surface sites for adsorption. The reason for the enhanced activity of this particular system remains unclear, but it must include a combination of effects from both precursor and support in the formation of the active surface.

As has been stated, the results for the materials pre-treated at 600°C, compared to those at 800°C, provide evidence for increasing activity with decreasing calcination temperature. For this reason, a similar investigation involving a pre-treatment temperature of 450°C was conducted in an attempt to establish the nature and strength of this trend. The results of this work are summarised in table 6.3, and compared with those found for materials pre-treated at 600 and 800°C. Also given are the observed surface areas post reaction, and the calculated U_3O_8 crystallite thickness estimated from X-ray powder diffraction prior to reaction.

system	T 25% NO conversion/°C			Surface Area/m^{2}g^{-1}			U$_3$O$_8$ crystallite thickness/nm		
	450	600	800	450	600	800	450	600	800
Nit/H$_1$SiO$_2$	530	565	>600	242	215	195	N/A	65	130
Nit/SiO$_2$	530	555	583	72	80	82	N/A	12	33
Nit/γ-Al$_2$O$_3$	506	527	565	24	25	33	N/A	20	71
Cl/H$_1$SiO$_2$	>600	572	594	232	218	205	41	62	156
Cl/SiO$_2$	532	504	544	70	76	80	N/A	14	36
Cl/γ-Al$_2$O$_3$	562	430	517	20	23	31	23	29	65

Table 6.3 The pre-treatment temperature dependence of NO conversion activity
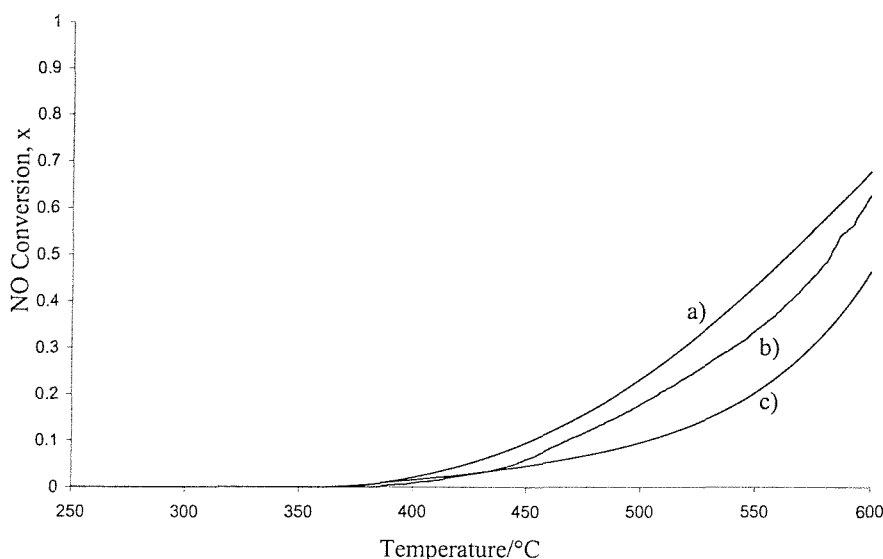
Figure 6.7 NO conversion activity dependence on pre-treatment temperature for uranyl nitrate supported on alumina, a) 450°C, b) 600°C, c) 800°C
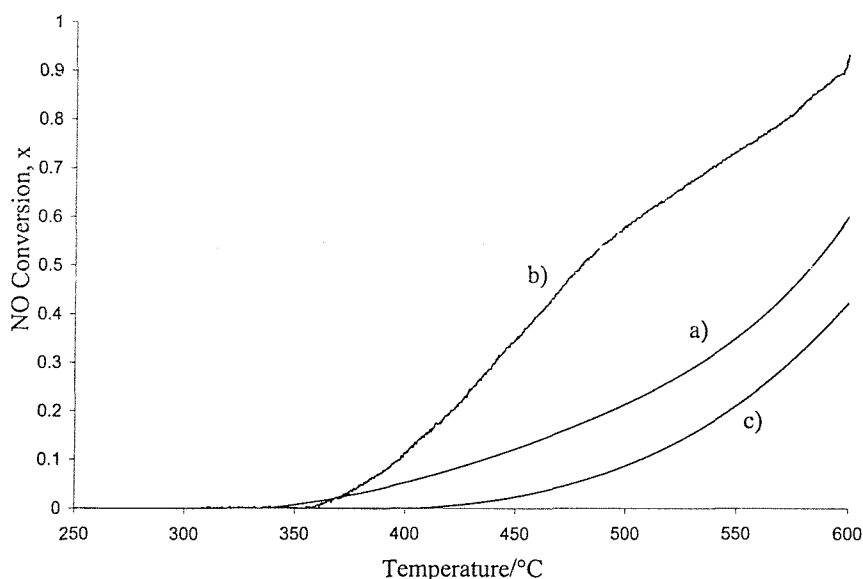

Figure 6.8 NO conversion activity dependence on pre-treatment temperature for uranium tetrachloride supported on alumina, a) 450°C, b) 600°C, c) 800°C

Figures 6.7 and 6.8 allow a direct comparison of the alumina supported uranyl nitrate and uranium tetrachloride derivative materials. It may be noted that for the nitrate precursor the trend of increasing activity with decreasing pre-treatment temperature continues as the calcination conditions become progressively less harsh. Notably, the reverse is observed for the uranium tetrachloride materials, and the activity appears to go through a maximum value at a pre-treatment temperature of 600°C. This phenomenon is independent of the support material, as the same trends are observed for mesoporous and

amorphous silica analogues. For the $UCl_4/\gamma-Al_2O_3$ system this has been investigated more extensively, and the results are shown in figure 6.9:
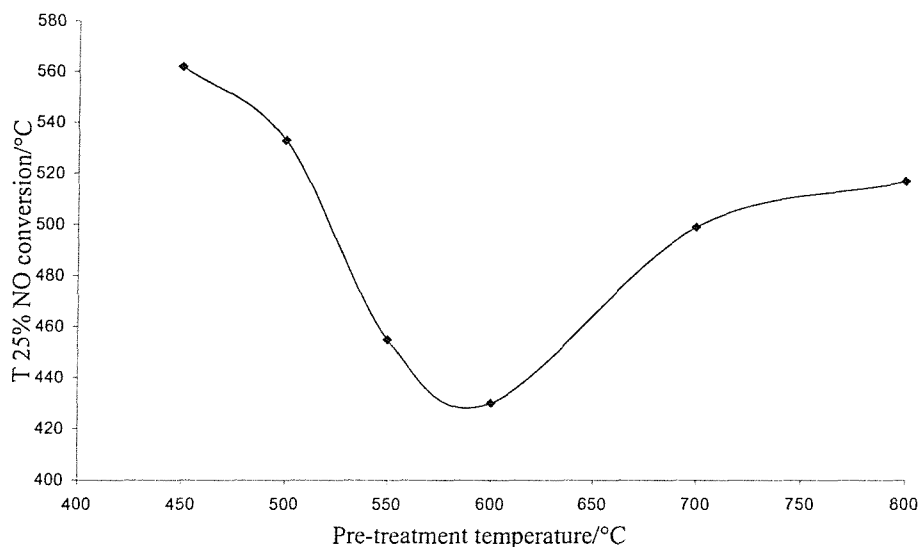

Figure 6.9 NO conversion activity dependence on pre-treatment temperature for $UCl_4/\gamma-Al_2O_3$

One explanation for the observed relationship is a combination of two factors. The first is an increase in uranium oxide particle size with increasing pre-treatment temperature, which would be expected to result in a decrease in active surface area and lower activity. The second factor is that of chlorine retention measured by X-ray fluorescence as detailed in chapter 5, which may actually inhibit the reaction. This would be expected to decrease with increasing calcination temperature. This is illustrated in figure 6.10:
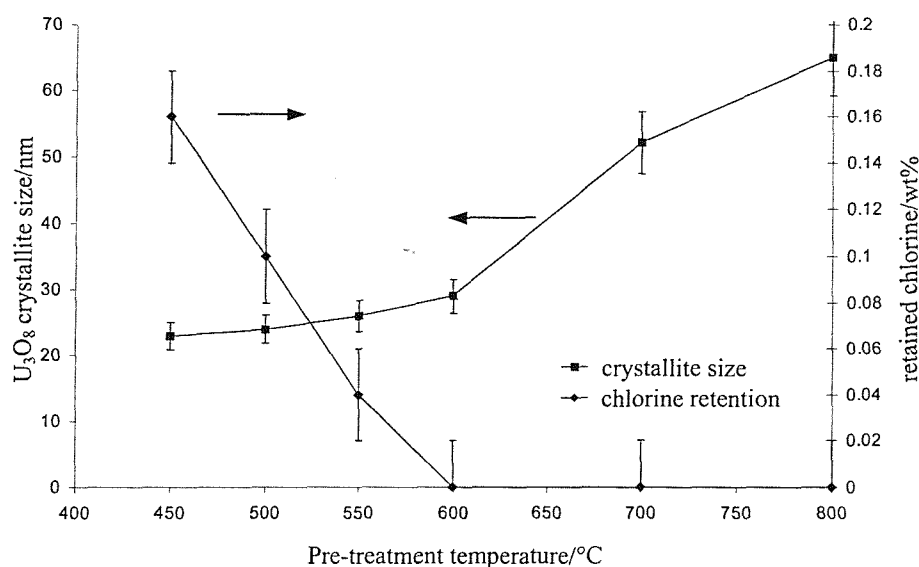

Figure 6.10 U_3O_8 crystallite size and chlorine retention dependence on pre-treatment temperature

A combination of the two properties plotted in figure 6.10 does indeed agree well with the observed activity, and this provides further evidence for the validity of the arguments given. The exact reason for the effect of retained chlorine on activity is not known, but it is probable that it relates to an electronic effect on surface sites. A similar study has been conducted on a ceria/zirconia supported rhodium system, where, as in this work, the effect of using the nitrate or the chloride as the catalyst precursor has been investigated.[10,11] This revealed that after low temperature pre-treatment, the presence of chloride decreased the extent of vacancy creation compares to the nitrate, leading to lower activity.[10] This was not apparent after high temperature treatment, although the activities of the materials towards the reduction of NO by CO still demonstrated some precursor dependence.[11] It would not be expected that the uranium oxide surface is analogous to a rhodium metal surface, but it is possible that the effect of chlorine retention is broadly similar in the creation of active surface sites available for reaction

The equation which describes the rate constant dependence on contact time in a flow system for a 1st order reaction was discussed in chapter 6, and is given below:

$$-\ln\frac{c_f}{c_i} = \frac{kV_o}{u}$$

Eq. 6.1

Where

c_f is the final concentration of reactant

c_i is the initial concentration of reactant

V_o/u is the contact time

k is the rate constant

When the order of the reaction is other than unity, the functional form of this equation is then:[12]

$$\frac{1}{n-1}\left[\frac{1}{c_f^{n-1}} - \frac{1}{c_i^{n-1}}\right] = \frac{kV_o}{u}$$

Eq. 6.2

The validity of equations 6.1 and 6.2, and a value for n, may be tested by variation of the contact time. This has been performed by alteration of the total flow rate for the system Nit/600/γ-Al$_2$O$_3$, and the NO conversion curves are shown in figure 6.12:
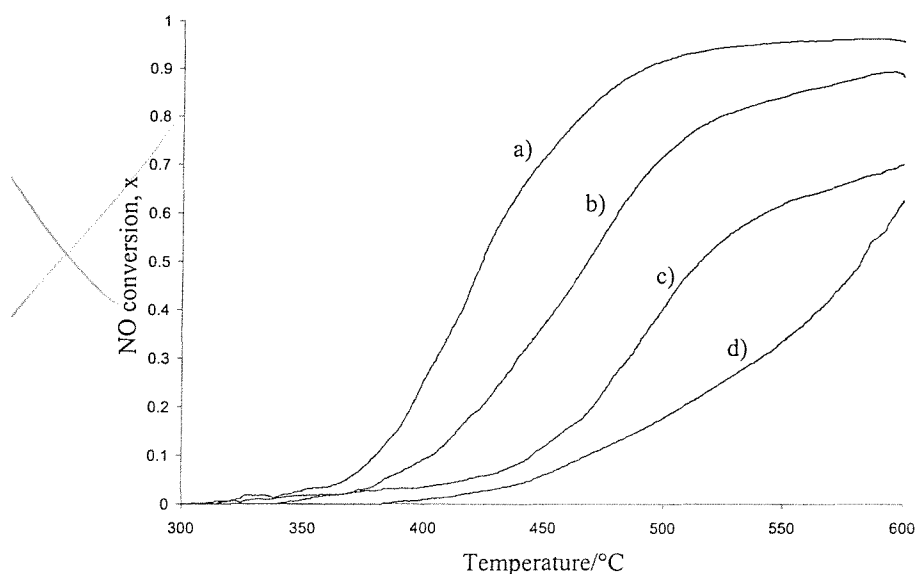
Figure 6.11 Flow rate dependence of NO conversion, a) 4ml/min, b) 6.4ml/min, c) 12ml/min, d) 20ml/min

The plot above is interesting, in that it shows a very large variation in NO conversion with flow rate, but this extreme dependence also implies great difficulty in further analysis. The calculated value of k at a given temperature should be constant between experiments for the correct choice of n. However, if the extent of NO conversion, x, varies greatly from one experiment to another at a given temperature, as is evident in figure 6.11, then a number of problems may be apparent in the analysis. For instance, at very high conversions it may be that there are some mass transport limitations to the rate of reaction, whereas at low conversions the variable selectivity may introduce other complications. Unfortunately, these considerations infer great uncertainty in the observed reaction order, and, despite attempts to verify the dependence on NO and CO concentration, no definitive statement regarding the value of n can be made by this method. An alternative route to determine the order of reaction has been employed, and this will be referred to in a section 6.2.1.3.

6.2.1.2 Materials Calcined and Reduced Prior to Reaction

Samples previously calcined at 800°C in oxygen were then reduced in 10% H_2 in N_2 at 523°C for 10 hours *ex situ*. These systems are denoted precursor/support/H_2. The purpose of this treatment is to reduce the supported U_3O_8 to UO_2, which has been reported as the active phase in the NO reduction reaction.[2] The results obtained from the use of

these materials are summarised in table 6.4, along with T25% values for the samples prior to reduction:

System	T 25%/°C	Surface Area /m²g⁻¹	UO₂/nm	T 25%/°C(800)
Nit/H₁SiO₂/H₂	>600	212	65	>600
Nit/SiO₂/H₂	558	83	16	583
Nit/γ-Al₂O₃/H₂	524	24	35	565
Cl/H₁SiO₂/H₂	>600	217	71	594
Cl/SiO₂/H₂	556	78	18	544
Cl/γ-Al₂O₃/H₂	530	23	39	517

Table 6.4 25% NO conversion temperature dependence on uranium precursor and support.

A comparison with the data from non-reduced samples yields an interesting result. The activity of the supported uranium tetrachloride derivatives is decreased on reduction, whereas that of the uranyl nitrate analogues is enhanced. The result is that the values from both precursors are almost identical. The inference is that the extended thermal treatment under a reducing atmosphere has eliminated the residual precursor dependence. The fact that it was required to calcine materials at 800°C in oxygen, and then to reduce at 523°C in hydrogen in order to achieve this precursor independence highlights the importance of the uranium source when synthesising the catalysts. This relationship between pre-treatment conditions, precursor, and activity is illustrated below, where the ratio of T 25% values uranyl nitrate:uranium tetrachloride is plotted against thermal history.
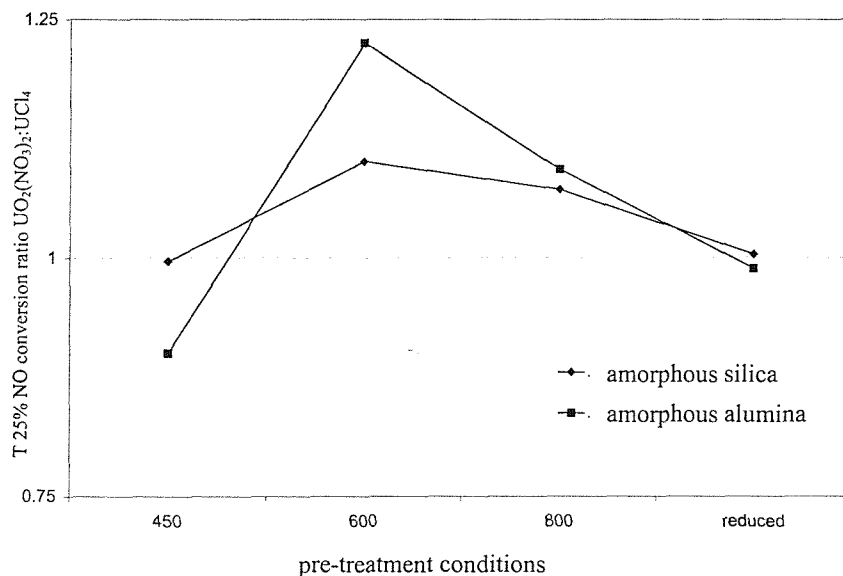

Figure 6.12 The relationship between precursor activity ratio $UO_2(NO_3)_2:UCl_4$ and catalyst pre-treatment temperature.

For both of the supports, the ratio returns to ~1 for the reduced materials. Interestingly, the observed effect is greater for the alumina supported materials than the amorphous or mesoporous silica analogues. Alumina does not appear to promote the retention of chloride over silica, so it must be that the chloride present has an exaggerated effect for this support in terms of the interaction with the active phase. Unfortunately, it is difficult to be more specific than this, as it is not known whether the chloride is initially retained in the uranium phase or in the support. Also, recall that there is no measurable level of chlorine in materials calcined at 600°C or above, so it is a latent effect that perturbs the activity in samples pre-treated beyond this temperature.

6.2.1.3 Materials not Calcined Prior to Reaction

An identical investigation to those described in the previous sections was performed using the supported uranium materials with no pre-treatment. The details of these results, with surface areas determined prior to reaction, and also a comparison of the T 25% NO conversion values obtained for samples pre-treated at 800°C are given in table 6.5.

System	T 25%/°C	Surface Area /m^2g^{-1}	T 25%/°C(800)
Nit/nc/H_1SiO_2	376	320	>600
Nit/nc/SiO_2	402	65	583
Nit/nc/γ-Al_2O_3	507	22	565
Cl/nc/H_1SiO_2	492	301	594
Cl/nc/SiO_2	476	61	544
Cl/nc/γ-Al_2O_3	537	26	517

Table 6.5 25% NO conversion temperature dependence on uranium precursor and support.

Curves of NO conversion versus temperature for the mesoporous silica, amorphous silica, and amorphous alumina supported uranyl nitrate systems are shown in figure 6.13, and those of the tetrachloride analogues in figure 6.14
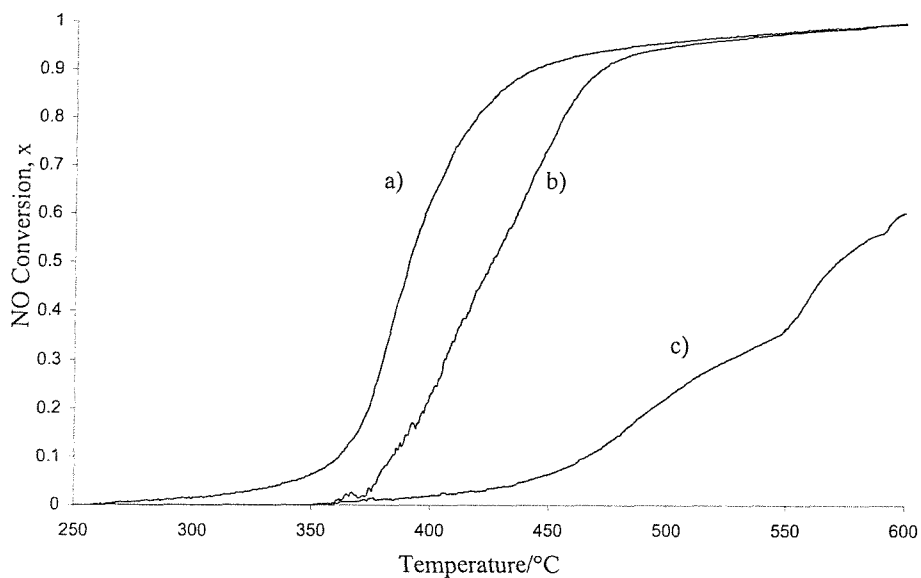
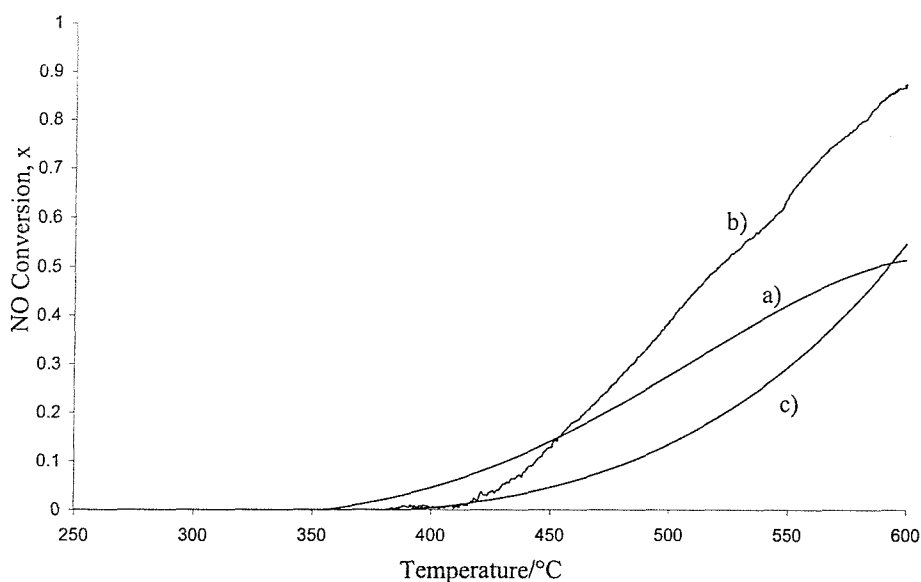Figure 6.13 Effect of catalyst support on NO conversion activity, a) Nit/nc/H$_1$SiO$_2$, b) Nit/nc/SiO$_2$, c) Nit/nc/Al$_2$O$_3$

Figure 6.14 Effect of catalyst support on NO conversion activity, a) Cl/nc/H$_1$SiO$_2$, b) Cl/nc/SiO$_2$ c) Cl/nc/γ-Al$_2$O$_3$

From the trend graphs in figure 6.13 it is immediately obvious that a lack of pre-treatment has a profound effect on the activity of these materials with respect to the NO reduction reaction. The most active system is uranyl nitrate supported on mesoporous silica, where 95% conversion is achieved at 450°C. The analogous amorphous silica

system is also highly active, although the light-off temperature is approximately 30°C lower. Interestingly, the support dependence of activity for the nitrate materials is $H_1SiO_2 > SiO_2 > \gamma\text{-}Al_2O_3$, which is the opposite of that observed for all the materials that had been pre-treated. This is possibly due to the effect of prior calcination on the area of the active surface, as the order given above is also the order of measured surface area. It is known that pre-treatment at high temperature leads to the formation of large uranium oxide particles, so the surface area that is measured by isothermal nitrogen adsorption is not necessarily representative of the dispersion of the active phase. However, in the instance where there is no prior calcination and dispersion is relatively high, then the intrinsic surface area of the support may be reasonably expected to become an important factor. The selectivity of the uranium materials towards N_2 formation appears unaffected by the lack of pre-treatment, and this is illustrated in figure 6.15.
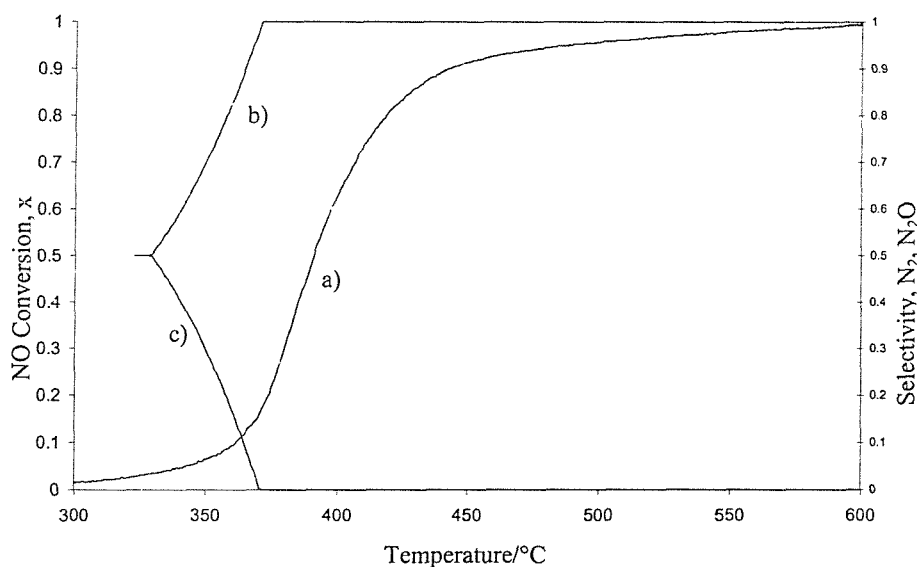

Figure 6.15 Nit/nc/H_1SiO_2 a)NO conversion, b)N_2 selectivity, c)N_2O selectivity.

A direct comparison of the selectivity of displayed by Nit/nc/H_1SiO_2 with that of the 5 wt% Pt/γ-Al_2O_3 material is given in figure 6.16.
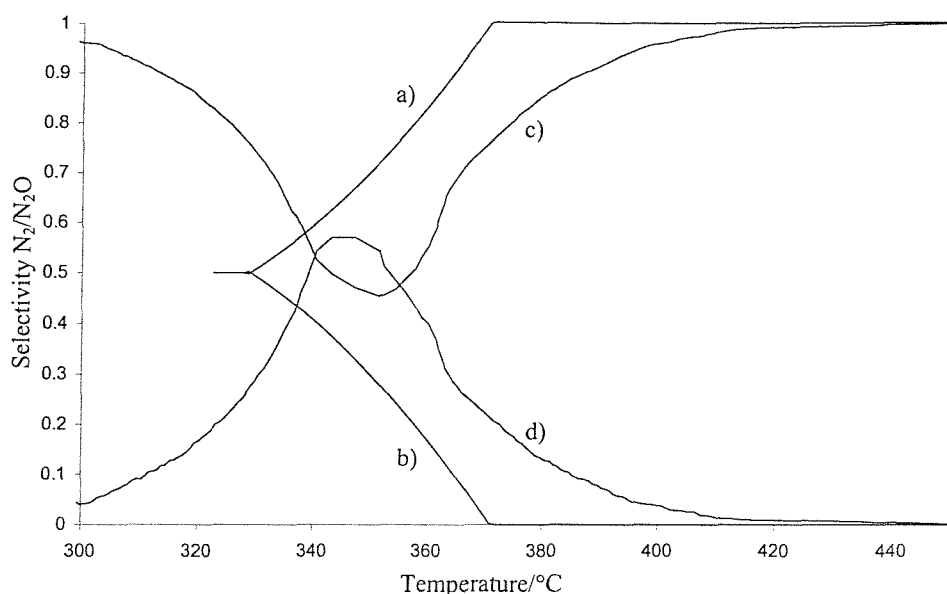
Figure 6.16 The selectivity of Nit/nc/H_1SiO_2, a) N_2, b) N_2O, and 5 wt% Pt/γ-Al_2O_3 c) N_2, d) N_2O

In contrast to the uranyl nitrate derivative materials, the activity of the supported uranium tetrachloride analogues, as illustrated in figure 6.14, is not so advantageously affected by a lack of pre-treatment. It should be noted that T 25% NO conversion values for the mesoporous and amorphous silica materials are lower than that found for any of the same samples previously calcined, so it appears that the same arguments given above with regard to the nitrate systems do apply to some extent. However, the effect is reduced, and indeed the Cl/nc/γ-Al_2O_3 material displays lower activity than Cl/600/γ-Al_2O_3 and Cl/800/γ-Al_2O_3 systems. The residual chlorine content after reaction does not depend on the nature of support, and was found at the level of 0.3wt% in all systems. From figure 6.10, where a relationship between uranium oxide particle size, chlorine retention, and activity is demonstrated, the behaviour of the alumina supported chloride system might be predicted. This also highlights the effect that the chemical nature of the support has on the relative importance of these factors. For the silica-based materials, the advantageous nature of smaller uranium oxide particles appears to dominate over the deleterious effect that chlorine retention has on activity, whereas for the alumina system the situation is reversed. The full relationship between precursor, support, pre-treatment temperature, and activity is summarised in Figures 6.17 a) and b):
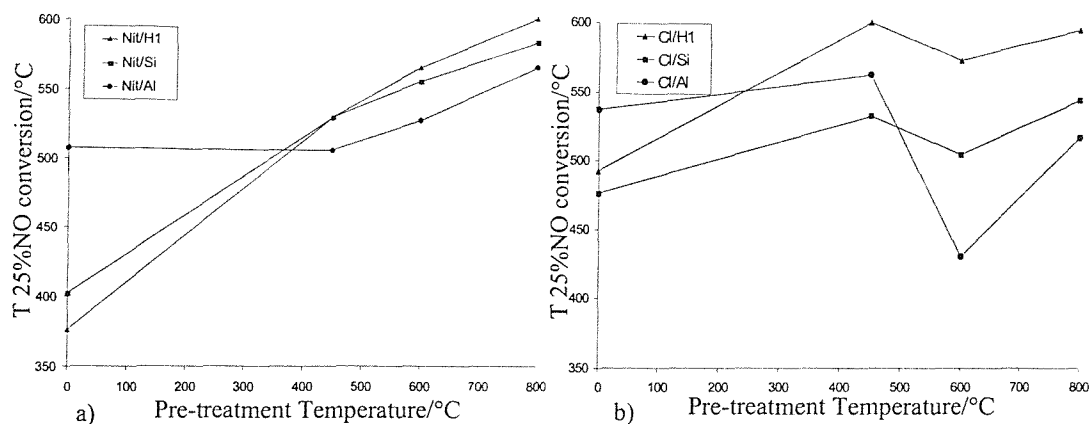
Figure 6.17 The dependence of T 25% NO conversion on precursor, support, and pre-treatment temperature a) uranyl nitrate derivatives b) uranium tetrachloride derivatives.

The flow rate dependence of NO conversion has been investigated for the Nit/nc/H_1SiO_2 system, as well as the standard 5wt% Pt/γ-Al_2O_3 material for comparison. The ratio of CO:NO was held constant throughout these sets of experiments. The results of this work are illustrated in figures 6.18 and 6.19.
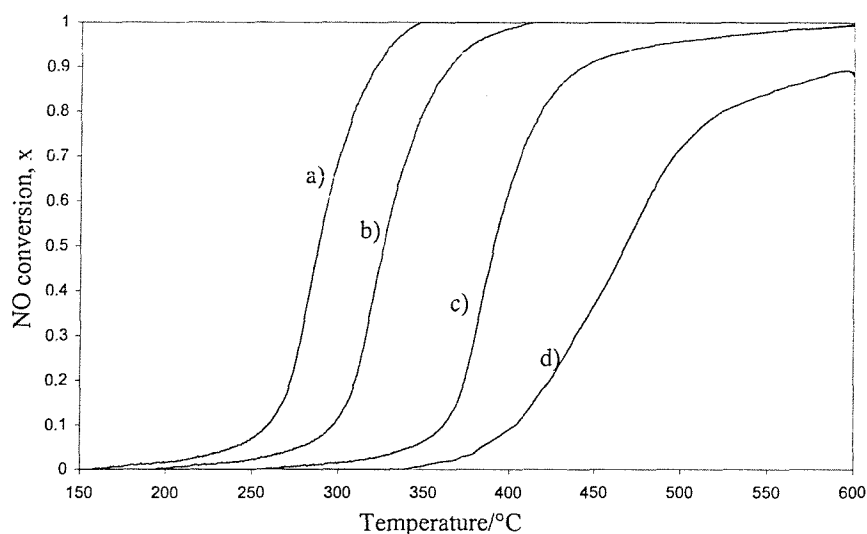

Figure 6.18 Flow rate dependence of NO conversion for Nit/nc/H_1SiO_2 system, a) 2ml/min, b) 6.4ml/min, c) 20ml/min, d) 40ml/min
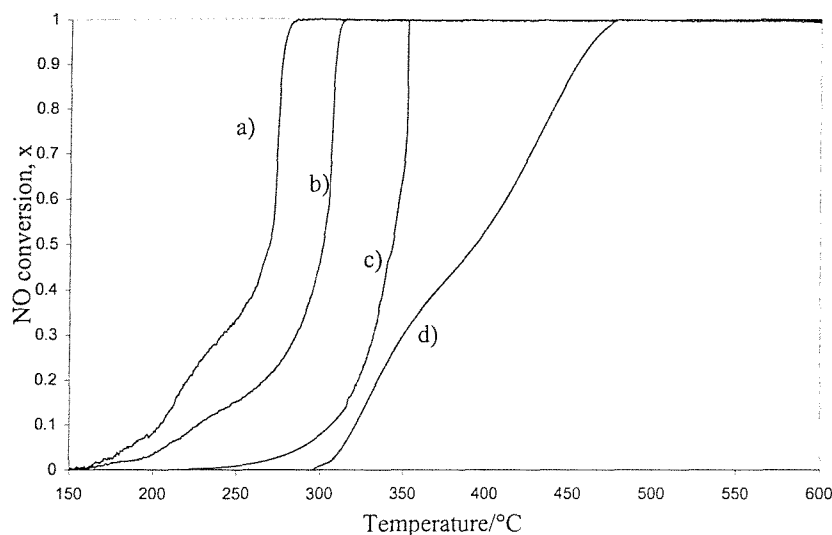
Figure 6.19 Flow rate dependence of NO conversion for 5wt% Pt/γ-Al$_2$O$_3$ system, a) 2ml/min, b) 6.4ml/min, c) 20ml/min, d) 40ml/min

The two graphs above show that, although the platinum system is more active than the supported uranium material, the Nit/nc/H$_1$SiO$_2$ system achieves 100% NO conversion at ~320°C at a total flow rate of 2ml/min (corresponding to GHSV = 9000h^{-1}). With consideration of the improved N$_2$ selectivity for the uranium materials, this suggests that supported uranium oxide may offer a viable alternative to platinum group metals in this process. A direct comparison of the two systems is perhaps better illustrated in figure 6.20, where the temperature at which 50% NO conversion is achieved is plotted against contact time.
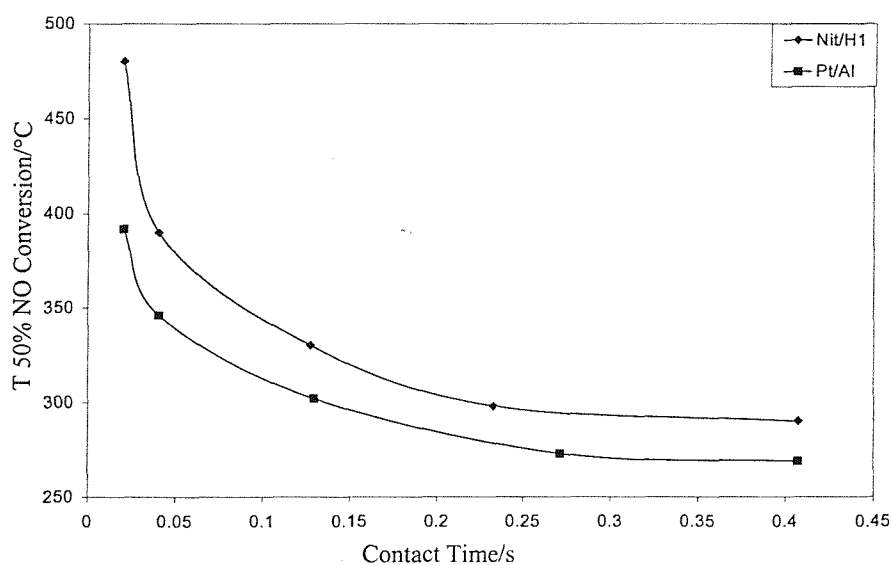

Figure 6.20 T 50% NO conversion dependence on contact time for Nit/nc/H$_1$SiO$_2$ and 5wt% Pt/γ-Al$_2$O$_3$.

Once again it is observed that, for both systems, there exists a very significant dependence of the extent of NO conversion at a given temperature on the contact time. This makes the data above unsuitable for testing equation 6.2, and an alternative route to the determination of reaction order has been employed. This involves the effect on reaction rate with a variation of the relative concentration of reactants. In practical terms, this is done by maintaining the concentration of one reactant, e.g. CO, whilst systematically varying the concentration of another, in this case NO, and then the reverse. The experiments are performed at a constant temperature, chosen for an NO conversion value of approximately 20% for a 1:1 reaction mixture, and a constant overall space velocity, maintained by a variation in flow of pure helium. This was achieved for the Nit/nc/H_1SiO_2 system at a temperature of 410°C and a total gas flow of 40ml/min. The details of flow conditions used are given in table 6.6

CO:NO ratio	5%CO/95%He	5%CO/95%He	100%He
1:1	20ml/min	20ml/min	0 ml/min
1:0.8	20ml/min	16ml/min	4ml/min
1:0.6	20ml/min	12ml/min	8ml/min
1:0.4	20ml/min	8ml/min	12ml/min
1:0.2	20ml/min	4ml/min	16ml/min
0.8:1	16ml/min	20ml/min	4ml/min
0.6:1	12ml/min	20ml/min	8ml/min
0.4:1	8ml/min	20ml/min	12ml/min
0.2:1	4ml/min	20ml/min	16ml/min

Table 6.6 Details of flow conditions for reaction order determination for the Nit/nc/H_1SiO_2 system

From the equation

$$r = kc^n \qquad\qquad \text{Eq. 6.3}$$

and taking common logarithms,

$$\log r = \log k + n \log c \qquad\qquad \text{Eq. 6.4}$$

a double-logarithmic plot of rate against concentration may give a straight line with gradient n and intercept $\log k$. This is illustrated in figure 6.21:
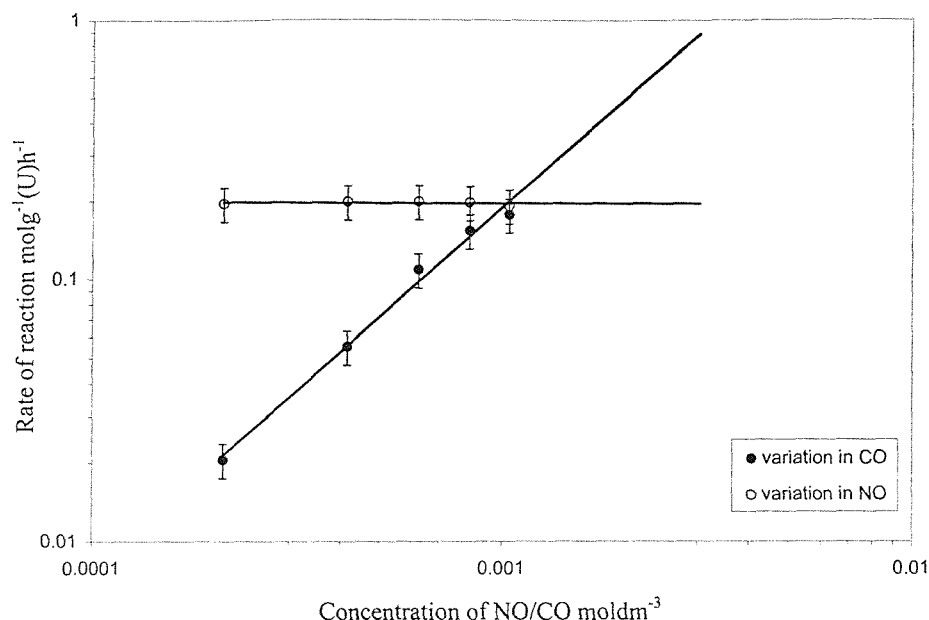
Figure 6.21 A double-logarithmic plot of NO/CO concentration against reaction rate for the Nit/nc/H₁SiO₂ system.

From the plot above it is possible to obtain a value for the order with respect to both NO and CO. The reaction is shown to be <u>zero</u> order with respect to the concentration of NO, and to have a value of $\underline{n = 1.4(2)}$ with respect to CO, which may be expressed as

$$r = kP_{CO}^{1.4}$$ Eq. 6.5

The value of $\log k$ obtained from the rate dependence on CO concentration at 410°C is 3.2(2), and this is within experimental error of the value achieved by the calculation of $\log k$ at 410°C using an overall order of 1.4, and the data obtained from the linear ramp rate experiment performed on the same system at an NO:CO ratio of 1:1, i.e. it is internally consistent. A value of 1.4 for the overall reaction order is in agreement with that found for bulk uranium oxide by Nozaki *et al.*[1] However, they reported the following rate expression:

$$r = kP_{CO}^{1.0}P_{NO}^{0.4}$$ Eq. 6.6

The major difference between the two expressions above is obviously the displayed absence of an NO concentration dependence in the results reported here. The temperatures at which the experiments were performed are within 10°C of each other, so it is unlikely that any temperature-dependence of the order, which is not unknown, is responsible on this occasion. It suggests that the dispersion of the active phase on a support results in a situation where the dissociation of NO on the surface is so rapid that this step in the reaction does not affect the rate in the conditions used. This may be simply a result of

increased active surface area leading to a greater ease of surface re-oxidation, or it may have a contribution from the nature of the support. This observation may also provide an explanation for the excellent selectivity towards N_2 of supported uranium oxide, noted here and by Pollington et al,[2] as N_2O formation may be expected to proceed via competing associative/dissociative adsorption of NO. Further experiments would be required to confirm this. A non-integral value greater than unity for the order with respect to CO concentration suggests an added complexity to the mechanism of the reaction. Possibly there are a number of competing processes; for example one mechanism may involve reaction of surface oxygen with gas phase carbon monoxide (Eley-Rideal mechanism), and a second may involve the surface physisorption of CO in a precursor state, with subsequent reaction (Langmuir-Hinshelwood mechanism). It is quite possible that the rate expression given in Eq. 6.5 is not complete, and that there is a contribution from the rate of removal of products from reaction sites. The CO concentration may have an effect on the adsorption/desorption of weakly interacting N_2/CO_2, which might inhibit the availability of surface sites for reaction. Fractional orders are frequently found in surface reactions,[13,14,15] and this observation is often linked to the non-uniformity of the surface on which the reaction proceeds. However, even on a surface with many sites of variable activity, the kinetic results obtained may not reflect this inhomogeneity, as the vast proportion of reaction will occur at the most active sites.[16] Further speculation on this point requires a greater knowledge of both the nature of the surface, and the relative importance of the processes occurring on it.

Assuming an overall order of 1.4, activation energies and frequency factors have been obtained from Arrhenius plots of ln k against 1/T, for the range of 10-20% NO conversion. The kinetic parameters for all the systems studied in this work, as well as the respective T 25% NO conversion temperatures, are given in table 6.7

System	$E_a/kJmol^{-1}$	$A/L^{0.4}mol^{-0.4}s^{-1}$	T 25% NO conversion
Nit/nc/H$_1$SiO$_2$	202	3.3x10^{17}	376
Nit/nc/SiO$_2$	142	1.5x10^{12}	402
Nit/nc/γ-Al$_2$O$_3$	134	3.9x10^9	507
Cl/nc/H$_1$SiO$_2$	95	2.8x10^7	492
Cl/nc/SiO$_2$	235	6.1x10^{14}	476
Cl/nc/γ-Al$_2$O$_3$	117	2.6x10^8	537
Nit/450/H$_1$SiO$_2$	49	1.1x10^5	530
Nit/450/SiO$_2$	105	5.7x10^7	530
Nit/450/γ-Al$_2$O$_3$	140	3.2x10^{10}	506
Cl/450/H$_1$SiO$_2$	55	1.0x10^4	>600
Cl/450/SiO$_2$	96	2.3x10^7	532
Cl/450/γ-Al$_2$O$_3$	86	1.7 x10^6	562
Nit/600/H$_1$SiO$_2$	68	2.5x10^6	565
Nit/600/SiO$_2$	95	4.3x10^7	555
Nit/600/γ-Al$_2$O$_3$	101	3.3x10^8	527
Cl/600/H$_1$SiO$_2$	186	3.3x10^{12}	572
Cl/600/SiO$_2$	155	2.3x10^{11}	504
Cl/600/γ-Al$_2$O$_3$	178	2.3x10^{14}	430
Nit/800/H$_1$SiO$_2$	72	1.2x10^5	>600
Nit/800/SiO$_2$	69	1.1x10^5	583
Nit/800/γ-Al$_2$O$_3$	76	3.6x10^5	565
Cl/800/H$_1$SiO$_2$	75	1.3x10^5	594
Cl/800/SiO$_2$	61	5.7x10^4	544
Cl/800/γ-Al$_2$O$_3$	59	4.2x10^4	517
U$_3$O$_8$	62	3.6x10^4	>600

Table 6.7 Calculated Arrhenius parameters and T25% NO conversion temperatures for supported uranium systems.

The statistical errors associated with the values for kinetic parameters in the table above are estimated in the same way as in section 5.2.1.1 of the previous chapter. Activation energies should be considered correct ± 10%, and frequency factors ± 20%. The plot of ln k against 1/T for the systems Nit/nc/H$_1$SiO$_2$ and Nit/800/H$_1$SiO$_2$, shown in figure 6.22, illustrates the effect of high temperature calcination prior to reaction for this material. The 1/T axis is unmarked, as one set of data has been shifted in the x-direction to allow comparison of the gradients:
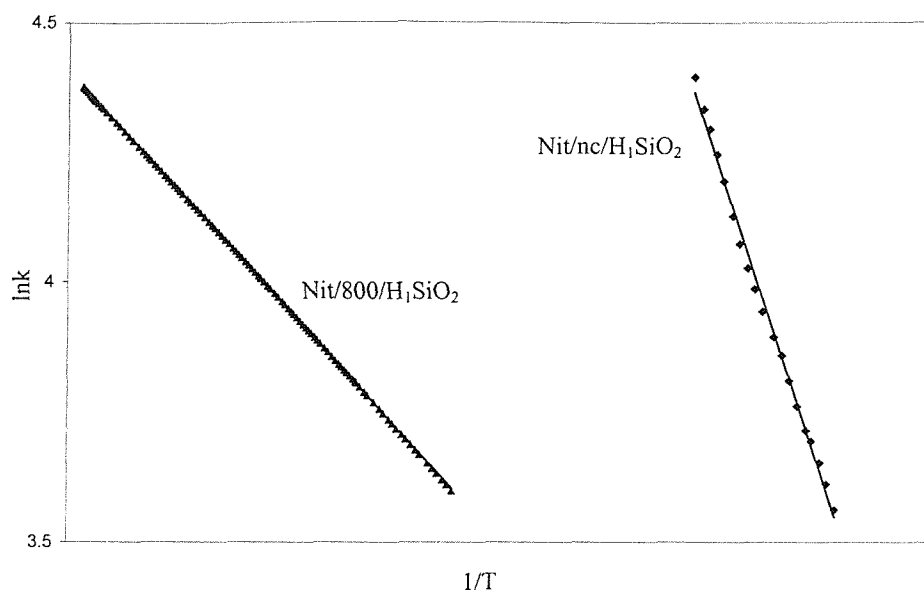
Figure 6.22 Arrhenius plot for systems $Nit/nc/H_1SiO_2$ and $Nit/800/H_1SiO_2$

The large extent of variation from one system to another in the Arrhenius parameters detailed in table 6.7 is another indication of the complex dependence of activity on support, precursor, and pre-treatment conditions. The activation energy of 62 $kJmol^{-1}$, found for the unsupported U_3O_8 material, is in agreement with that found in the literature.[1] This compares with values reported for the same reaction using a Pd/Al_2O_3 catalyst of 80-90 $kJmol^{-1}$,[17,18,19] a Rh/Al_2O_3 system of 87 $kJmol^{-1}$,[20] and, for a Pt/Al_2O_3 analogue, of 89 $kJmol^{-1}$.[7] As for the CO oxidation catalysts discussed in the previous chapter, the most active supported uranium systems have, in general, the highest activation energies and frequency factors. This is typified by the $Cl/600/\gamma\text{-}Al_2O_3$ and $Nit/nc/H_1SiO_2$ materials, which demonstrate activation energies of 178 and 202$kJmol^{-1}$, and frequency factors of $2x10^{14}$ and $3x10^{17}L^{0.4}mol^{-0.4}s^{-1}$ respectively. This compares with values of 157$kJmol^{-1}$ and $1.7x10^{14}$ for CO oxidation on the same mesoporous silica supported uranyl nitrate material, and indeed the trends between systems, if not the absolute values of activity, activation energy, and frequency factor are broadly the same for the NO reduction reaction as for the CO oxidation. This is another indication that in the reduction of NO with CO with these supported materials, the re-oxidation of surface sites by NO dissociation is not rate-limiting, and instead the rate with which these active sites are regenerated by reaction and reduction with CO is of the greater importance. A second general point is that the wide variation in activity between the six systems studied here, indicates that there is a high probability of further improvement of the performance of these materials by extended variation of precursor, support, and pre-treatment conditions.

The effect of metal loading on activity has also been investigated, using the Nit/H$_1$SiO$_2$ system as model material. Samples with a range of uranium loadings were prepared by exactly the same route as previously described, with the only variation in the amount of uranyl nitrate deposited on the support. Figure 6.23 demonstrates the dependence of 50% NO conversion temperature on wt% U in the sample:
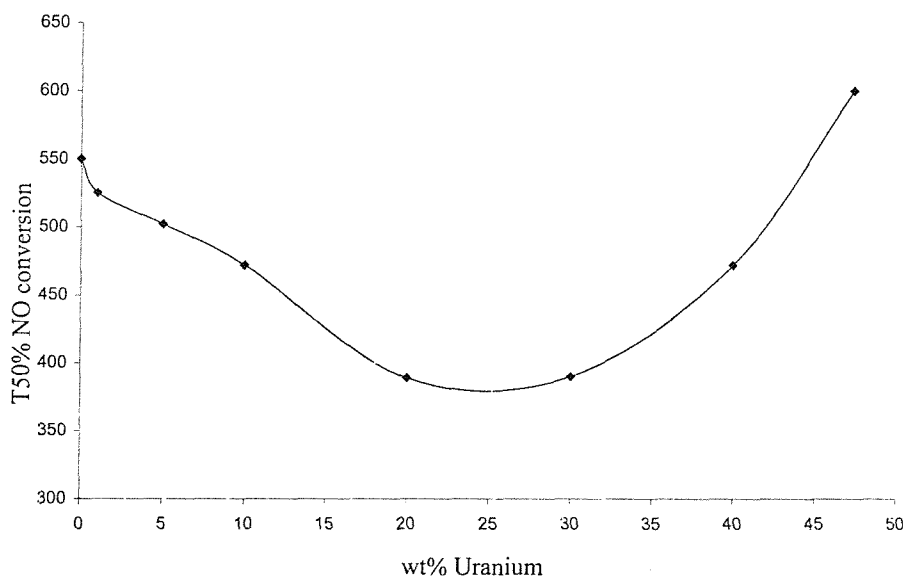

Figure 6.23 The dependence of NO conversion activity on uranium loading

The value obtained for a sample with 0wt% U obviously relates to solely the activity of the mesoporous silica support, and the value associated with the 47.5wt% U is the activity of pure, unsupported, uranyl nitrate. The plot above indicates a minimum in T 50% NO conversion at 20-30wt% U, with a similar decrease in activity at either 10 or 40wt% metal. Above 40wt%, the limit of bulk uranium material is approached, whereas at 10wt% or below it would appear that the number of active sites is not sufficient to maintain the level of NO reduction activity. The trend in N$_2$/N$_2$O selectivity, which is not shown here, demonstrates that at levels of 5wt% U and below, the contribution of reaction on the support material is significant, and at these low loadings selectivity towards N$_2$ is reduced.

6.2.2 Pulsed Flow Experiments

These experiments afford an alternative method of comparing the activity of the supported materials, and their transient response to a rapid change in feed gas composition, using the slightly different conditions of higher space velocity, lower contact times, and a net reducing/oxidising atmosphere. The normalisation process applied to this data is

initially very similar to that described in the previous chapter. The m/z = 4 signal was used in order to account for any variation in leak rate to the mass spectrometer during the isothermal experiment. This was also used to facilitate normalisation between experiments on the same system at different temperatures. Following this, these experiments are then normalised with the blank response to a pulse recorded at room temperature. The activity with regards to NO conversion, and the selectivity of the reaction towards N_2/N_2O has been calculated in a similar way as that described for the continuous flow experiments in this chapter. However, instead of just the calculation of ratios at each temperature, as for the linear ramp rate continuous flow configuration, to gain a real measure of conversion for each pulse it is necessary to integrate over the entire pulse for each component contributing to a particular m/z signal. It should be noted that the errors associated with these values are increased in the pulse flow configuration, due simply to decreased signal levels in the mass spectrometer for some of the m/z values. Realistic statistical errors are ~10% for selectivities at >5% conversion, and ~5% for conversions. Experiments performed under net oxidising, and net reducing conditions will, initially, be dealt with separately.

6.2.2.1 Net Reducing Conditions

These experiments were performed by the regular introduction of a pulse of 5%NO in He in place of a flow of 5%CO in He, as described in section 6.1.2. The result is a net reducing atmosphere in the reactor for a large majority of the time. The appearance of the data, after the experiments at each temperature have been normalised with respect to each other and contributions from N_2O removed, is illustrated in figure 6.24:
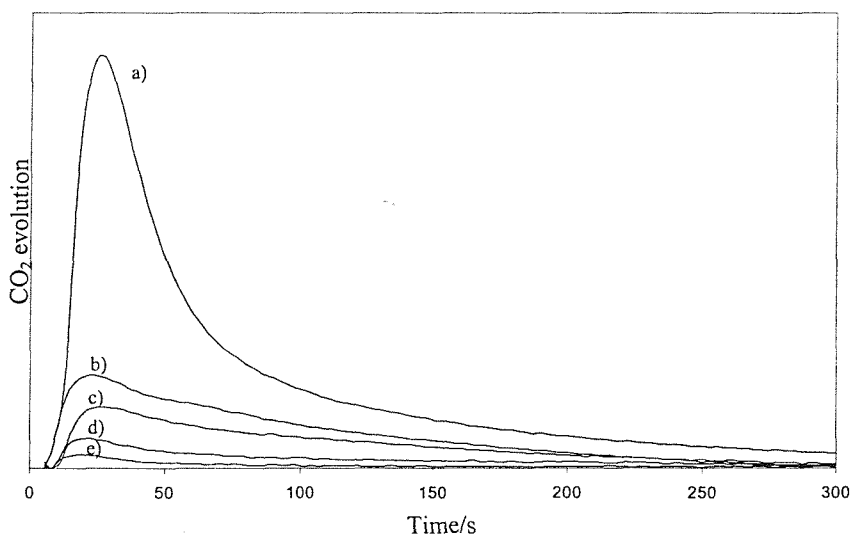

Figure 6.24 The temperature dependence on the extent of CO_2 evolution for the $UCl_4/nc/\gamma\text{-}Al_2O_3$ system at a) 600°C, b) 500°C, c) 450°C, d) 400°C, e) 350°C

The selectivity of the reaction at each point in time after a pulse may be evaluated by the same procedures as described in the previous chapter. This is illustrated in figure 6.25, where the total m/z = 44 signal is separated into contributions from CO_2 and N_2O, and these are plotted in arbitrary units with respect to time, along with the calculated percentage selectivity with respect to N_2.
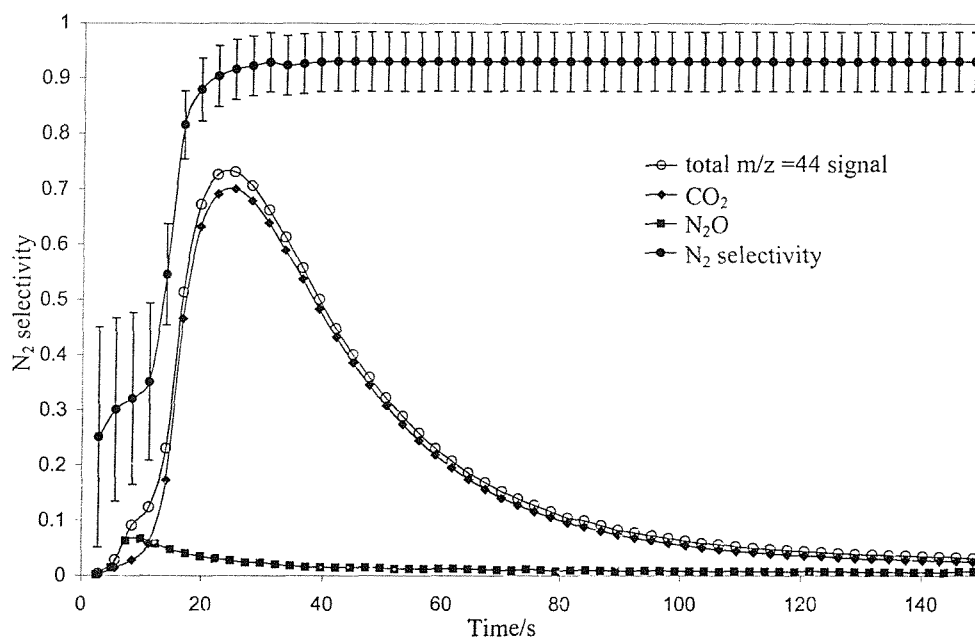

Figure 6.25 The time after pulse dependence of N_2 selectivity for the $UCl_4/nc/\gamma-Al_2O_3$ system at 600°C

From figure 6.25 it is possible to observe the formation of a relatively small amount of N_2O, and that this occurs immediately after the introduction of the pulse of NO. This contrasts with the continuous flow experiments, where, at 600°C, 100% selectivity towards N_2 is achieved. It is unlikely that this difference is a result of the increased flow rate for the pulse flow experiments, and more possible that this observation is caused by the nature of the adsorbed surface species or the type of uranium oxide phase formed under the reducing CO atmosphere. The most probable explanation is that the way in which the pulse experiment is performed, with switching between gases, leads to a highly NO rich and CO lean atmosphere over the reactor bed immediately after the introduction of the NO pulse. This oxidising feed gas results in the formation of N_2O instead of N_2 due to a greater amount of adsorbed O on the surface, and this occurs until the reintroduction of CO reverses this situation. There is obviously some mixing of the gases prior to entry to the reactor bed, and this distribution in the composition of the feed gas would intuitively result

in the shape of the N_2O evolution curve observed. The same selectivity trends were observed for all the supported uranium systems studied

The N_2O contribution to the $m/z = 30$ curves may then be removed, and the residual signal integrated with respect to time, and normalised with respect to the integrated response of an NO pulse at room temperature. This provides an accurate measure of the percentage conversion for each pulse. Figures 6.26 and 6.27 illustrate the extent of NO conversion for the supported uranyl nitrate and uranium tetrachloride systems that had not been calcined prior to the reaction.
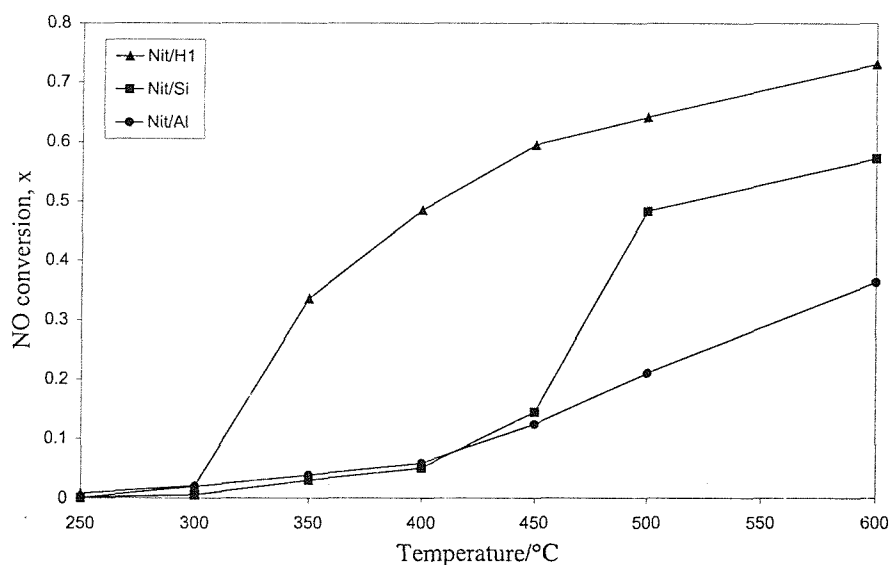

Figure 6.26 The NO conversion dependence on reaction temperature for the supported uranyl nitrate systems not calcined prior to reaction
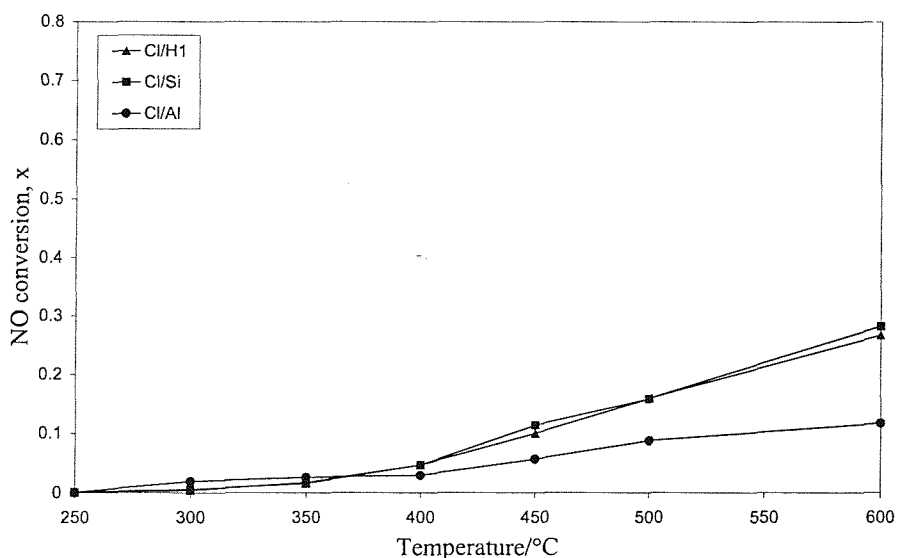

Figure 6.27 The NO conversion dependence on reaction temperature for the supported uranium tetrachloride systems not calcined prior to reaction

The results illustrated in figures 6.26 and 6.27 are similar to that found by continuous flow experiments, with the $Nit/nc/H_1SiO_2$ system being the most effective, and with the nitrate derivative materials generally performing better than the uranium tetrachloride analogues. 100% NO conversion is not achieved for any of the systems, and this is presumably to the high flow rates, as well as a possible contribution from the differing nature of the uranium oxide phase prior to the introduction of the pulse compared to that present under 1:1 NO:CO conditions. A further observation concerning all of the materials is that, prior to the commencement of the pulsing experiment, at which time the reactor bed is exposed to a solely reducing atmosphere of CO/He, the continued production of a significant amount of CO_2 is observed. It has been discussed in the previous chapter that the source of O in the oxidation of CO is likely to be labile lattice oxygen, and the production of carbon dioxide in the absence of an oxidant seems to provide some evidence for this. After a period of time this evolution of CO_2 in the absence of NO reduces to zero as the lattice oxygen is diminished and not replaced, and the uranium oxide phase is no longer further reduced. The results achieved for analogous systems that had been calcined at 600°C in oxygen prior to the reaction were also very similar to those obtained by continuous flow experiments, and will not be discussed further.

Identical experiments have been performed using the conventional 5wt% $Pt/\gamma-Al_2O_3$ catalyst, and the results of this investigation are illustrated in figure 6.28. The extent of NO conversion is plotted, as well as the normalised CO_2 evolution.
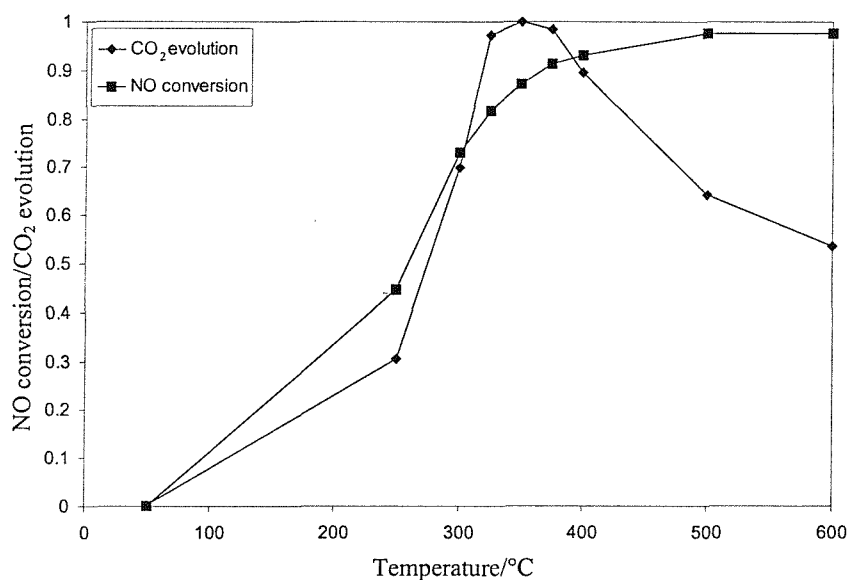

Figure 6.28 NO conversion, and CO_2 production dependence on reaction temperature for the 5wt% $Pt/\gamma-Al_2O_3$ system.

Figure 6.28 shows that, although ~100% NO conversion is achieved at 500°C, interestingly the level of CO_2 production reaches a maximum at ~375°C before falling with further increase in temperature. This is due to the formation of dioxygen from adsorbed O at higher temperatures, as opposed to CO_2 from CO and adsorbed O. This further evidence of the involvement of surface adsorbed oxygen in the catalytic reaction rather than oxygen dissolved in the bulk metal. This observation has been previously reported,[21] and further highlights the differences between the metal and metal oxides as catalysts for this process.

6.2.2.2 Net Oxidising Conditions

These experiments were performed by the regular introduction of a pulse of 5%CO in He in place of a flow of 5%NO in He, as described in section 6.1.2. The result is a net oxidising atmosphere in the reactor. The data obtained was analysed in exactly the same way as described in the previous section. Several differences between the results obtained under oxidising conditions, compared to those found under CO excess have been observed. Firstly, the absence of a reductant leads to the formation of, initially, N_2 as the sole product, then after a period of time the NO reacts with the surface of the uranium oxide or the support to form almost exclusively N_2O. After a further time the extent of N_2O production falls slowly to zero. In this instant, as the CO pulse replaces NO as the feed gas, the result is 100% selectivity towards N_2, in contrast to that observed above for the reverse procedure. The results of these experiments for the supported uranyl nitrate and uranium tetrachloride materials previously calcined in oxygen at 600°C are given in figures 6.29 and 6.30 respectively.
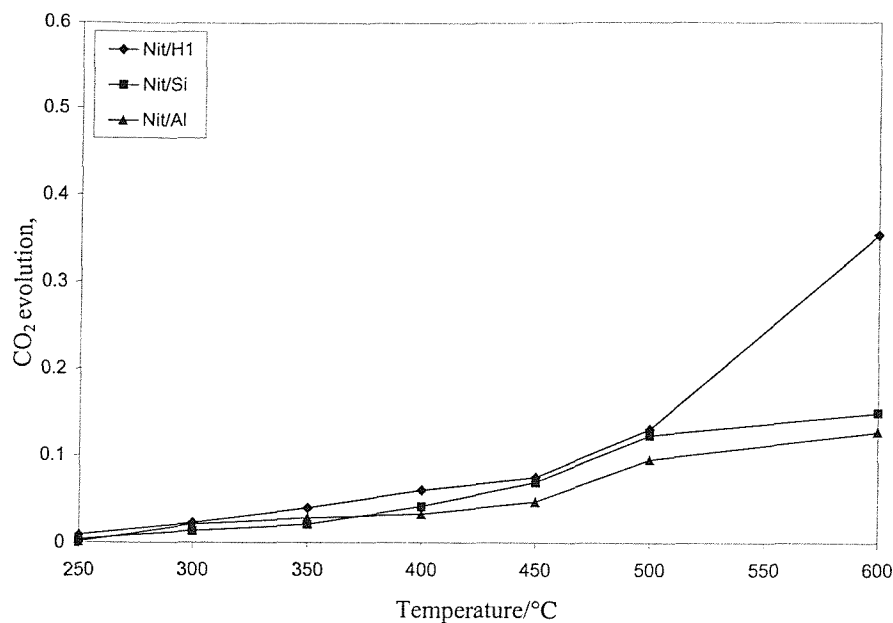
Figure 6.29 The NO conversion dependence on reaction temperature for the supported uranyl nitrate systems calcined at 600°C in oxygen prior to reaction
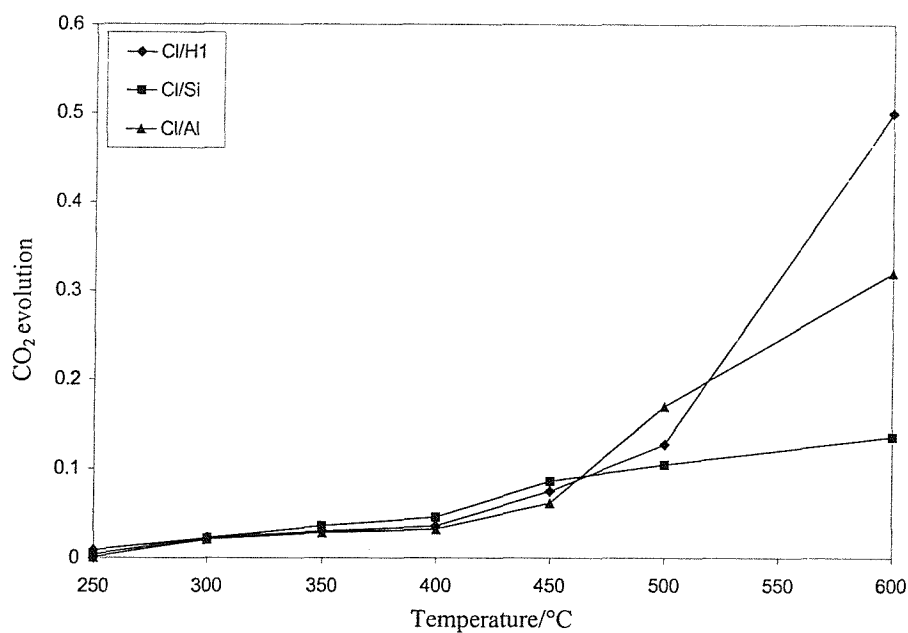
Figure 6.30 The NO conversion dependence on reaction temperature for the supported uranium tetrachloride systems calcined at 600°C in oxygen prior to reaction

It may be observed that the mesoporous silica supported materials are shown to perform better, at least at high temperatures, than the amorphous silica and alumina analogues. Indeed, the order of activity found for the nitrate materials is mesoporous silica> alumina ≈ amorphous silica, and mesoporous silica> alumina > amorphous silica for

the chloride derivatives. This is not similar to the continuous flow experiments, where the amorphous alumina supported uranium tetrachloride derivative was found to be the most active system of those calcined prior to reaction. The most active of the uranyl nitrate derivatives under a 1:1 NO:CO ratio is also the alumina supported material. It is likely that these differences are a result of the excess NO conditions in this set of experiments, which may have an effect on the nature of the uranium oxide phase that is present. The origin of this effect will be discussed in the next section of this chapter.

An interesting observation from the results of both sets of the pulsed flow experiments is illustrated in figure 6.31
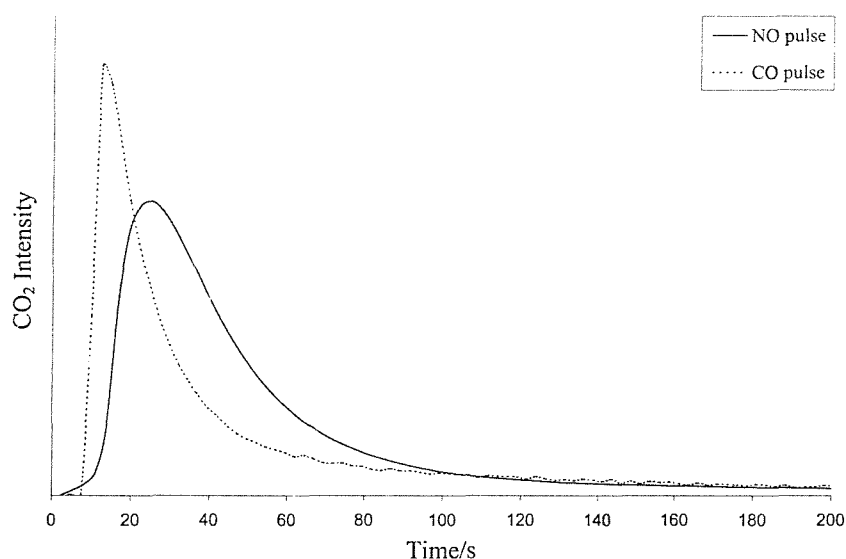
Figure 6.31 The effect of pulse gas on the time dependence of CO_2 evolution for the system Nit/nc/H_1SiO_2

It is possible to observe that CO_2 evolution with time for the NO pulse is much broader than for the analogous CO pulse experiment. Presumably this is an indication of the processes that occur on the surface for CO_2 evolution to take place. For the CO pulse experiment, the sample is under an atmosphere of NO for much of the time, and the uranium oxide surface is oxidised. CO then very quickly reduces the surface, with the formation of CO_2. For the NO pulse experiment, the oxide surface may be considered reduced as a result of the CO rich atmosphere. The NO pulse oxidises the surface very quickly, and then it must be reduced again to lead to the formation of CO_2. It has been shown earlier in this chapter that oxidation of the surface by NO is very fast, and under the continuous flow experiment may be considered an unimportant step in terms of the overall rate. If the oxide is considered fully reduced under the CO atmosphere prior to the pulse,

then the oxidation by NO may be expected to result in a still partially reduced oxide. The further reduction of this phase may be difficult, making the evolution of CO_2 somewhat slower in this configuration.

6.2.3 Characterisation of Materials Post-Reaction

X-ray powder diffraction was used in order to characterise the uranium oxide phase present in the sample on removal from the microreactor. The samples produced under a net oxidising atmosphere i.e. CO pulsed into an NO flow, displayed diffraction patterns consistent with a U_3O_8 phase, with peaks at 21.5, 26.1 and 34.1 $^\circ 2\theta$ indexed respectively as the (001), (110) and (111) reflections.[22] The low signal to noise ratio of these diffraction patterns, due to the small amounts of sample used, disallows the exact determination of the type of U_3O_8 phase present. The existence of this oxidised phase of uranium oxide is as expected given the reaction conditions to which the sample is subjected.

The samples removed from the microreactor after reaction in net reducing conditions, i.e. NO pulsed into a CO flow, displayed diffraction patterns with peaks at 28.2 and 32.3 $^\circ 2\theta$ which have been indexed as the (111) and (200) reflections of a UO_2 phase.[23] Once again, this result is as may be predicted for a material produced in the reducing atmosphere described. Reduction of uranium oxide to a stoichiometry of lower oxygen composition than UO_2 is very unlikely under the type of conditions given here, and it may be reasonably suggested that this represents the most reduced phase that could be formed.

The structure of the uranium oxide phase formed after reaction in a 1:1 CO:NO gas composition has also been determined with the use of X-ray powder diffraction. One such diffraction pattern for the system $Nit/600/H_1SiO_2$ is shown in figure 6.32, and has been identified as $UO_{2.2}$, alternatively termed U_5O_{11}.[24]
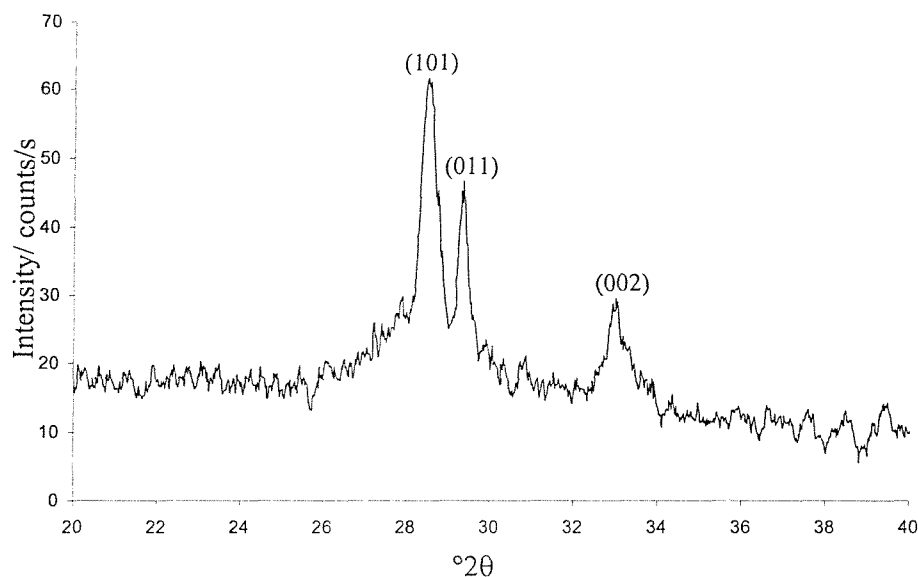
Figure 6.32 X-ray powder diffraction pattern of an ex-reactor sample of the Nit/600/H_1SiO_2 system treated under a 1:1 CO:NO gas mixture, indexed as $UO_{2.2}$.

The identification of a partially reduced phase after reaction is an important result. The active uranium oxide phase in the selective reduction of NO with CO has been previously reported as UO_2,[2] but, as has already been stated above, it is not expected that this would be easily reducable, even to a small extent.[25] The presence of a partially reduced phase, $UO_{2.2}$, as the catalytically active material is intuitively more sensible, as it may be considered as an intermediate between UO_2 and U_3O_8, and as such, may be readily partially oxidised or reduced in the course of the reaction. A second possibility, that of a mixture of phases, is also eliminated by this observation. All the systems studied displayed a similar diffraction pattern to that shown above, although, for the materials that had not been calcined prior to reaction, peak broadening is shown to be more extensive. As described in Chapter 4, the full diffraction peak width at half height was used to gain an estimate of the uranium oxide crystallite thickness with the Scherrer formula. In this instance the (101) reflection has been used to perform the analysis. Isothermal nitrogen adsorption has also been performed on these samples, and the BET isotherm used to obtain a measure of the surface area. These results are summarised in table 6.8

Supported Material	Crystallite Thickness/nm	Surface Area/m^2g^{-1}
Nit/nc/H_1SiO_2	3	300
Nit/nc/SiO_2	2	65
Nit/nc/γ-Al_2O_3	2	22
Cl/nc/H_1SiO_2	2	310
Cl/nc/SiO_2	1	64
Cl/nc/γ-Al_2O_3	2	22
Nit/450/H_1SiO_2	59	282
Nit/450/SiO_2	10	72
Nit/450/γ-Al_2O_3	17	28
Cl/450/H_1SiO_2	53	293
Cl/450/SiO_2	14	79
Cl/450/γ-Al_2O_3	22	29
Nit/600/H_1SiO_2	65	221
Nit/600/SiO_2	12	71
Nit/600/γ-Al_2O_3	17	32
Cl/600/H_1SiO_2	62	253
Cl/600/SiO_2	14	78
Cl/600/γ-Al_2O_3	20	29
Nit/800/H_1SiO_2	130	195
Nit/800/SiO_2	33	82
Nit/800/γ-Al_2O_3	71	33
Cl/800/H_1SiO_2	156	205
Cl/800/SiO_2	36	80
Cl/800/γ-Al_2O_3	65	31

Table 6.8 Post reaction $UO_{2.2}$ crystallite size and surface area dependence on precursor, support, and pre-treatment conditions.

The table above demonstrates similar trends to those observed in the previous chapter. The lower the pre-treatment temperature, the smaller the particles of uranium oxide formed. This reaches a limit at the materials that have not been calcined prior to reaction, which results in very small $UO_{2.2}$ crystallites. At this limit, the supported oxide particles are of the same order of magnitude as the pore size of the mesoporous silica. The errors associated with the given crystallite sizes are large for smaller particles, and must considered as $\pm$ 50%.[26] This increase in active surface area is the proposed explanation for the greater activity of these materials over the analogous systems pre-treated at high temperatures. Indeed, many of the arguments that may be used to interpret the trends

observed in table 6.8, and to link these trends to the observed activity for different systems, have been fully discussed in section 5.2.3 in the previous chapter.

6.3 Summary

After high temperature pre-treatment the mesoporous silica supported materials display low activity compared to the amorphous silica and alumina analogues. This is the same behaviour as that observed for the CO oxidation reaction over the same systems, and is probably due to the fact that, during the pre-treatment, the uranium oxide particles formed are extruded from the pore structure and sinter to form very large particles analogous to bulk uranium oxide. The most active system for the selective reduction of NO with CO after high temperature calcination pre-treatment is the uranium tetrachloride on alumina system treated at 600°C. The uranyl nitrate on mesoporous silica system is the most active material when samples are not subjected to calcination prior to reaction. Even the most active supported uranium system does not perform as well, in terms of NO conversion as the conventional $Pt/\gamma-Al_2O_3$ catalyst studied for comparison. However, the supported uranium oxide materials show greater selectivity towards N_2 than the platinum catalyst at lower temperatures. All the supported uranyl nitrate derivative materials display increased activity with respect to the NO reduction reaction as the pre-treatment temperature, and coincident uranium oxide particle size, is decreased. For the uranium tetrachloride derivative materials, the activity reaches a maximum at a pre-treatment temperature of 600°C, with activity decreasing as this temperature is increased or decreased. The decrease in activity with increasing calcination temperature is proposed to occur for the same reason as that discussed for the uranyl nitrate materials, whereas at lower temperatures the fall off in performance is considered to be due to an inhibiting effect resulting from observed retained chloride. The active phase in all systems is identified by X-ray powder diffraction as $UO_{2.2}$.

Systematic variation of the flow rates of NO and CO yielded an order of reaction for both species; the reaction being zeroth order with respect to NO, and to have an order of 1.4 with respect to CO. As for the CO oxidation reaction, the most active systems display the highest activation energies for the process, with coincidentally high frequency factors. An investigation of the activity dependence on the supported uranium loading was shown to yield a maximum in activity between 20 and 30 wt%U.

Pulse flow experiments yielded some similar information to the continuous flow studies regarding the activity of the supported uranyl nitrate derivative materials. However, concerning the uranium tetrachloride analogues, the activity of the $Cl/600/H_1SiO_2$ and $Cl/600/SiO_2$ are reversed compared to that observed for the continuous flow studies, with the mesoporous material demonstrating higher activity under the pulse flow conditions. This was also noted in the study of the CO oxidation reaction. Indeed, in the higher space velocity experiment, the mesoporous silica supported material is shown to have higher activity than even the amorphous alumina analogue.

6.4 References

1) F. Nozaki, F. Matsukawa, Y. Mano, *Bull. Chem. Soc. Japan,* 2674, **48**, 1975.

2) S.D. Pollington, A.F. Lee, T.L. Overton, P.J. Sears, P.B. Wells, S.E Hawley, I.D. Hudson, D.F. Lee, V. Ruddick, *Chem. Commun.* 725, 1999.

3) F. Boccuzzi, A. Chiorino, M. Gargano, N. Ravasio, *J. Catal.,* 140, **165**, 1997.

4) S.D. Peter, E. Garbowski, V. Perrichon, M. Primet, *Catal. Lett.,* 27, **70**, 2000.

5) I. Spassova, M. Khristova, D. Panayotov, D. Mehandjiev, *J. Catal.,* 43, **185**, 2000.

6) S.D. Peter, E. Garbowski, N. Guilhaume, V. Perrichon, M. Primet, *Catal. Lett.,* 79, **54**, 1998.

7) E. Seker, E. Gulari, *J. Catal.,* 4, **194**, 2000

8) S.S.C. Chuang, C-D. Tan, *J. Catal.,* 95, **173**, 1998

9) J.H. Holles, R.J. Davis, T.M. Murray, J.M. Howe, *J. Catal.,* 193, **195**, 2000

10) P. Fornasiero, N. Hickey, J. Kašpar, C. Dossi, D. Gava, M. Graziani, *J. Catal.,* 326, **189**, 2000.

11) P. Fornasiero, N. Hickey, J. Kašpar, T. Montini, M. Graziani, *J. Catal.,* 339, **189**, 2000.

12) K.J. Laidler, *Chemical Kinetics,* 2nd ed., Tata McGraw-Hill, New York, p23, 1973.

13) S.H. Oh, *J. Catal.,* 477, **124**, 1990.

14) N.T. Pande, A.T. Bell, *J. Catal.,* 7, **98**, 1986.

15) D.R. Rainer, S. M. Vesecky, W.S. Oh, D.W. Goodman, *J. Catal.,* 234, **167**, 1997.

16) H.S. Taylor, S.C. Liang, *J. Am. Chem. Soc.,* 1306, **69**, 1947.

17) G. Xi, J. Bao, S. Shao, S. Li, *J. Vac. Sci. Technol. A,* 2351, **10**, 1992.

18) G.W. Graham, A.D. Logan, M. Shelef, *J. Phys. Chem.* 5445, **97**, 1993.

19) S.M. Vesecky, P. Chen, X. Xu, D.W. Goodman, *J. Vac. Sci. Technol. A,* 1539, **14**, 1995.

20) J.H. Holles, M.A. Switzer, R.J. Davis, *J. Catal.,* 247, **190**, 2000.

21) R. Burch, P. Fornasiero, B.W.L. Southward, *J. Catal.,* 234, **183**, 1999.

22) B. Loopstra, *J. Appl. Crystallogr.,* 94, **3**, 1970

23) S.A. Barrett, *Acta Cryst. B,* 2775, **38**, 1982.

24) L. Zvezdinskaya, L. Dubronivskiy, *Dokl. Acad. Sci. USSR, Earth Sci-Sec (Engl. Transl.),* 319, **197**, 1993.

25) C. Muggelberg, M.R. Castell, G.A.D. Briggs, D.T. Goddard, *Surf. Sci.,* 673, **402**, 1998.

26) G.C. Bond, *Heterogeneous Catalysis: Principles and Applications,* Oxford University Press, Oxford, p81, 1987.

Chapter 7. Characterisation of Supported Organouranium

Materials

This chapter is an investigation of the structure and stability of mesoporous silica supported organouranium complexes. The materials used for this study include examples of tripodal amino(triamido)uranium compounds, and (tris)cyclopentadienyluranium chloride. The structures of these complexes are illustrated in figure 7.1.
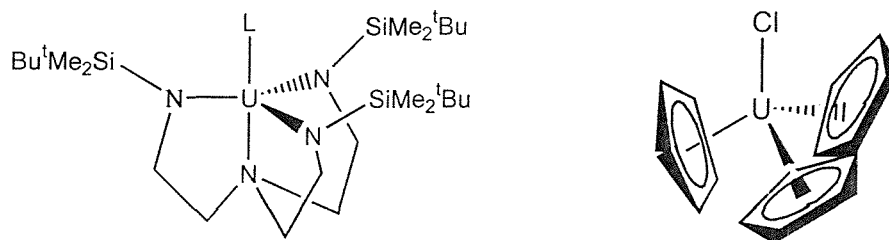
Figure 7.1 a) {N[CH$_2$-CH$_2$N(SiMe$_2$^{t}Bu)]$_3$}UL [L= O^{t}Bu, NEt$_2$]   b)Cp$_3$UCl

For convenience, the {N[CH$_2$-CH$_2$N(SiMe$_2$^{t}Bu)]$_3$} ligand will be denoted as [N'$_3$N], and the (C$_5$H$_5$) ligand as (Cp).

7.1 Experimental

The amino(triamido)uranium complexes were provided by the research group of Dr. Scott.[1,2,3,4] A brief description of the synthetic procedure used is appropriate. The [N'$_3$N] ligand was synthesised as the lithium salt by methods described in the literature.[5,6] To a mixture of equimolar amounts of this ligand and uranium tetrachloride, was added cold tetrahydrofuran, and this was allowed to warm slowly to room temperature to give a clear green solution. Evaporation of the solvent, and recrystallization of the residue from pentane afforded the air and water sensitive [UCl(N'$_3$N)(thf)$_n$], which were sublimed (ca 150°C, 10^{-6} mbar) to give the solvent-free complex [UCl(N'$_3$N)]$_2$.[1] Further reaction with K[OBu^t] in cold tetrahydrofuran yielded the butoxide derivative.[3] The diethylamide compound was synthesised either from reaction of lithium diethylamide with [UCl(N'$_3$N)]$_2$, or from [{U(NEt$_2$)$_4$}$_2$] and (N'$_3$N)H$_3$ in pentane.[7]

The support used was a Brij76 surfactant templated mesoporous silica that had been pre-treated at 800°C. Dry pentane was added to a mixture of the silica, and an amount of organometallic calculated to give a maximum loading of 6wt% U. The uranium complexes dissolved readily in pentane to give a solution of the organometallic over a silica slurry. This mixture was stirred for twenty minutes, during which time no discolouration of the solution was observed The solvent was then removed *in vacuo*, and the sample further dried for two hours, to give the deposited organouranium materials.

The (tris)cyclopentadienyluranium chloride complex was synthesised by the method of Marks *et al*,[8] from uranium tetrachloride and thallium cyclopentadienylide. One molar equivalent of uranium tetrachloride (2.70g)was dissolved in dimethoxyethane (100ml) under an inert atmosphere, and to this was added three molar equivalents of thallium cyclopentadienylide (5.75g). The resulting milky tan suspension was stirred at room temperature for 36h, after which time the mixture was Schlenk-filtered under vacuum. The filtration residue was washed with dimethoxyethane, and then the dark red-brown filtrate was stripped of solvent via trap-to-trap distillation to yield a golden brown solid as the product. This is then washed with 20ml of dry hexane and dried for 12h under high vacuum. Yield 1.17g (35%). The ^{1}H nmr spectrum in $CDCl_3$ showed a singlet at δ–2.88ppm (ref TMS), corresponding to the hydrogens on the cyclopentadienyl rings. This is in agreement with that reported in the literature.[8] Cp_3UCl was evaporation deposited on mesoporous silica at 6wt% U from a tetrahydrofuran solution.

7.2 Characterisation of Supported Organometallic Materials

7.2.1 As Made Supported Materials

EXAFS analysis has been extensively used in an attempt to characterise the supported materials, and the first stage in this process is to obtain a reliable model of the organometallic compound prior to deposition. For this reason, U L(III) EXAFS spectra of the pure material diluted to 10wt% U in boron nitride have been recorded. A fit obtained for this EXAFS data for the [NEt₂U(N'₃N)] system is given in figure 7.2. The parameters used to define this fit, and the calculated correlation matrix of these parameters are shown in tables 7.1 and 7.2.
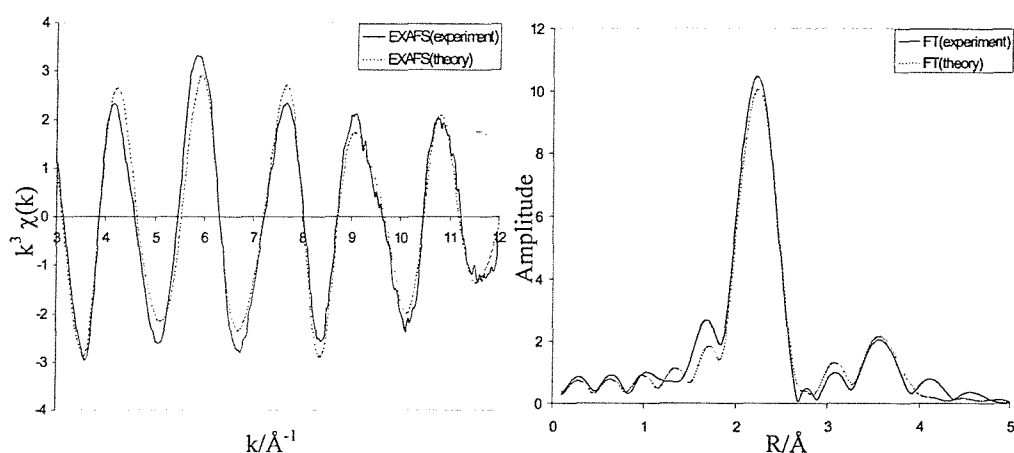

Figure 7.2 The U L (III)-edge k^3 weighted EXAFS spectrum and phase shift corrected Fourier transform of [NEt₂U(N'₃N)], diluted to 10wt% U in a boron nitride matrix.

$$EF = -11.2 \qquad R = 19.79 \qquad F.I = 2.3 \times 10^{-4}$$

Shell(n)	Tn	Cn	$Rn(\text{Å})_{EXAFS}$	$Rn(\text{Å})_{XRD(ave)}$[9]	$a\ (2\sigma^2/\text{Å}^2)_{EXAFS}$
1	N	4.0(1)	2.27(1)	2.271	0.006(1)
2	N	1.0(1)	2.71(5)	2.709	0.025(8)
3	C	3.1(4)	3.15(3)	3.162	0.022(9)
4	C	6.2(9)	3.48(3)	3.456	0.026(9)
5	Si	3.0(9)	3.63(8)	3.594	0.024(10)
6	C	3.2(8)(	3.76(8)	3.701	0.017(11)

Table 7.1 EXAFS derived structural parameters for [NEt$_2$U(N'$_3$N)], diluted to 10wt% U in a boron nitride matrix. Statistical errors are given in brackets. Also given are parameters from previously reported single crystal X-ray diffraction data.

	EF	A1	A2	A3	A4	A5	A6	R1	R2	R3	R4	R5	R6
EF	1												
A1	.05	1											
A2	.51	.04	1										
A3	.17	.06	.52	1									
A4	.19	.13	.44	.66	1								
A5	.52	.05	.84	.40	.37	1							
A6	.09	.15	.17	.39	.71	.25	1						
R1	.81	.01	.35	.06	.08	.36	.10	1					
R2	.30	.06	.13	.41	.23	.07	.15	.29	1				
R3	.59	.06	.45	.08	.02	.47	.17	.46	.06	1			
R4	.50	.04	.85	.21	.30	.88	.18	.37	.04	.51	1		
R5	.25	.12	.30	.64	.92	.22	.82	.15	.18	.07	.17	1	
R6	.55	.03	.82	.51	.48	.81	.02	.38	.10	.46	.73	.44	1

Table 7.2 Calculated Correlation matrix of EXAFS derived structural parameters for [NEt$_2$U(N'$_3$N)]. (negative values given in bold type)

The fit described above has a good R factor of 19.79, and a low fit index, 2.3×10^{-4}. More importantly, there is agreement, within experimental error, between the distances found from the EXAFS experiment, and those found from previous X-ray diffraction studies.[9] Extensive calculations to include the possibility of multiple scattering pathways

were performed, but there was no evidence that these contributions were statistically significant in this system. The first shell of 4 nitrogen atoms at 2.27 Å includes the three amido nitrogens of the tripodal ligand, as well as that of the apical NEt_2 group. The second shell of a single nitrogen atom at 2.71 Å relates to the amino nitrogen at the apex of the tripodal co-ordination set. The third and fourth shells, comprising of 3.1 and 6.2 carbon atoms at 3.15 and 3.48 Å respectively, include carbon from the backbone of the tripodal ligand, as well as some from the $SiMe_2Bu^t$ group. Further statistical analysis suggests that the inclusion of the 6th shell, comprising of 3.2 carbon atoms at 3.76 Å, is perhaps not significant, but for the purposes of defining a structural model it is retained in this instance. The correlation matrix is used to give a measure of how one parameter relates to, and depends on, another, and helps to provide an indication of possible problems with the fit. Unless there are exceptional circumstances, correlation coefficients should not be greater than 0.85. It may be seen from the matrix in table 7.2 that this figure is only exceeded in the relationship between parameters for shells 4 and 5, which may suggest that the contributions from these shells are not completely resolved. This is perhaps reflected in the uncertainty in co-ordination numbers shown in table 7.1. One possible explanation is that the nature of the refinement in PAXAS, where the program seeks to fit contributions from the EXAFS as Gaussian peaks in the Fourier transform, causes the contribution from two shells at similar distances to be highly correlated.

This procedure has also been performed for the butoxide analogue, and the fit obtained, along with the parameters that define it is given in figure 7.3, and table 7.3.
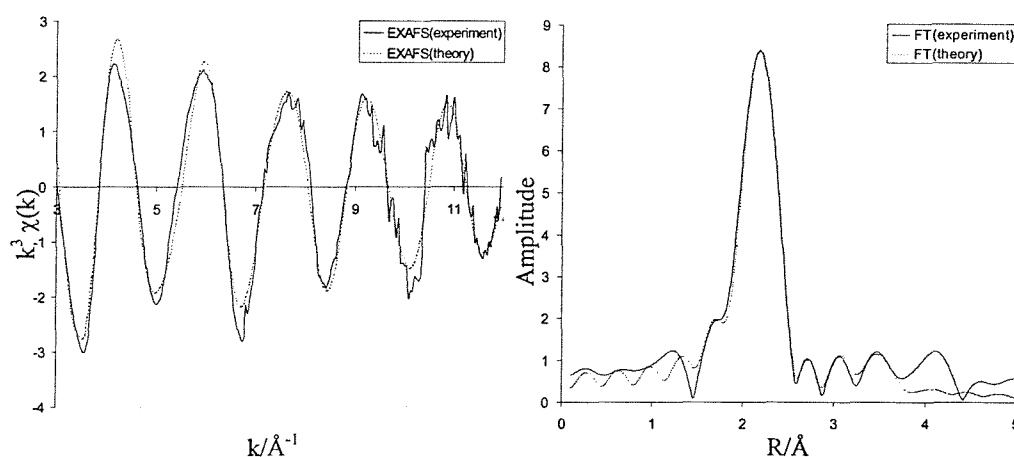

Figure 7.3 The U L (III)-edge k^3 weighted EXAFS spectrum and phase shift corrected Fourier transform of [Bu^{t}OU(N'$_3$N)], diluted to 10wt% U in a boron nitride matrix.

$$EF= -12.8 \qquad R= 19.88 \qquad F.I= 2.6 \times 10^{-4}$$

Shell(n)	Tn	Cn	Rn(Å)$_{EXAFS}$	Rn(Å)$_{XRD(ave)}$[3]	a (2σ²/Å²)$_{EXAFS}$
1	O	1.0(1)	2.24(7)	2.208	0.023(2)
2	N	3.0(3)	2.27(4)	2.235	0.006(1)
3	N	1.0(2)	2.58(5)	2.623	0.019(8)
4	C	3.1(4)	3.21(5)	3.182	0.029(5)
5	Si	3.0(6)	3.58(5)	3.540	0.016(6)
6	C	6.3(9)	3.60(6)	3.543	0.016(7)

Table 7.3 EXAFS derived structural parameters for [Bu^{t}OU(N'$_3$N)], diluted to 10wt% U in a boron nitride matrix. Statistical errors are given in brackets. Also given are parameters from previously reported single crystal X-ray diffraction data.

Once again, there is an agreement within experimental error between the EXAFS derived parameters, and those previously published from single crystal diffraction data.[3] The first shell of one oxygen at 2.24 Å relates to that of the butoxide group, and shells two and three comprise of the amido and amino nitrogens of the tripodal ligand.

A similar procedure has been performed for the (tris)cyclopentadienyluranium chloride compound. Analysis of the U (LIII) EXAFS data acquired from a pure sample diluted to 10wt% U in boron nitride firstly required the construction of a model. In order to do this, the parameters derived from single crystal X-ray diffraction data for this material were used to locate the cyclopentadienyl rings in three-dimensional space. Secondly, all three Cp rings were assumed to be equivalent to allow the number of parameters that required refining to be reduced. This is desirable, as if the number of parameters is too high, then the number of independent data points in the original spectrum is not sufficient to allow justification of the statistical significance of any fit obtained. Thirdly, in the model, a hydrogen atom was placed at the centroid of each ring in a plane with the five carbon atoms. This was done to allow the ring to tilt and rotate as a unit during refinement. A hydrogen atom was chosen because it is a low z atom, and as such a poor X-ray scatterer. Its contribution to the theoretical EXAFS generated may therefore be assumed to be negligible. An illustration of this model is shown in figure 7.4. In figure 7.5, three fits obtained to the U L (III)-edge k^3 weighted EXAFS spectrum and phase shift corrected Fourier transform of [Cp$_3$UCl] are shown. The first is a single scattering model, the second includes multiple scattering calculations, and the third incorporates the possibility of partial oxidation of the sample.
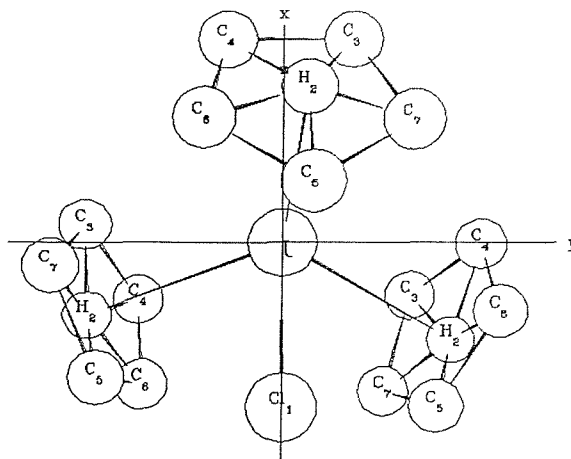
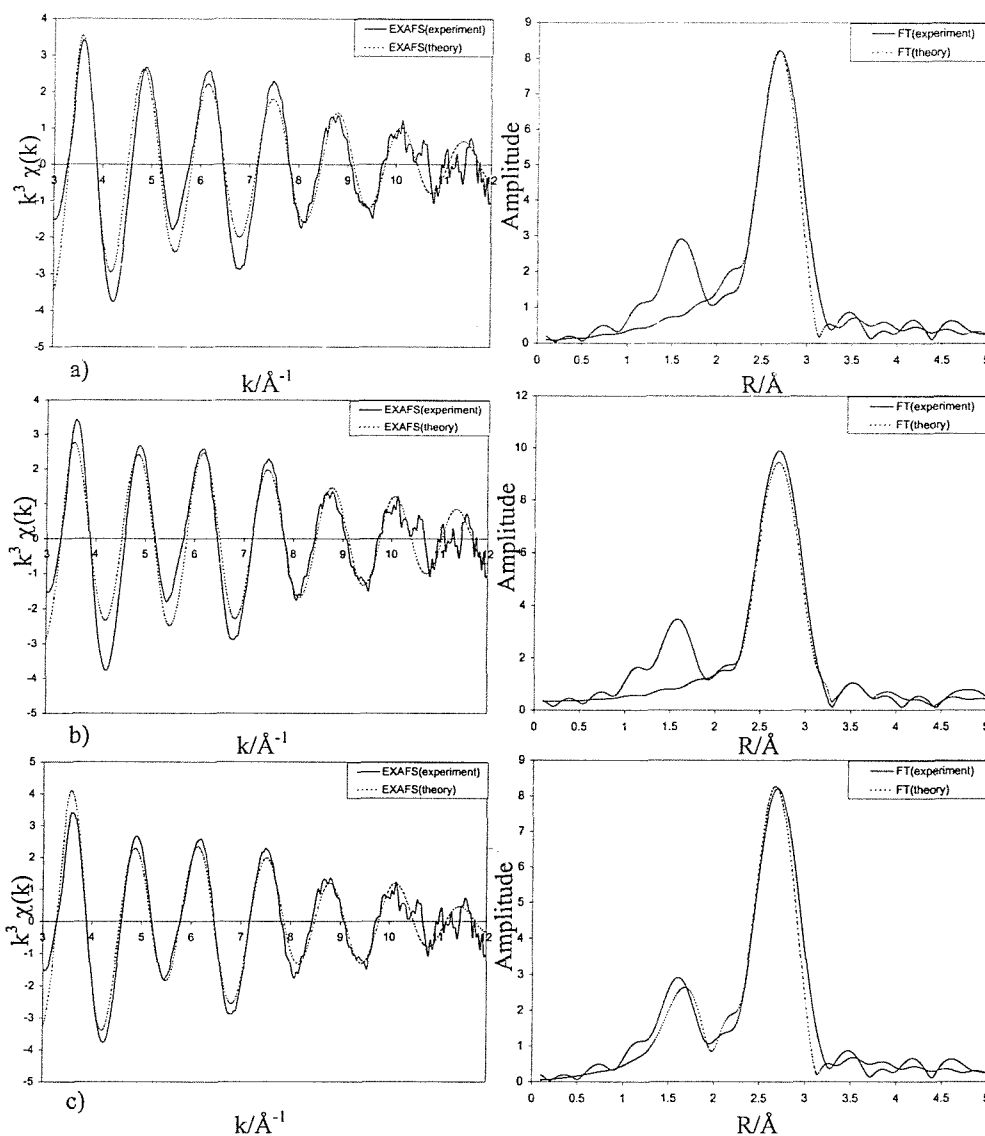Figure 7.4 The three-dimensional model of Cp$_3$UCl used for U (LIII) multiple scattering EXAFS analysis.

Figure 7.5 The U L (III)-edge k^3 weighted EXAFS spectrum and phase shift corrected Fourier transform of [Cp$_3$UCl], diluted to 10wt% U in a boron nitride matrix. a) single scattering calculation, b) multiple scattering calculation, c) partial oxidation model.

The parameters derived from these three models are summarised in table 7.4.

Fit	R	Shell(n)	Tn	Cn	Rn(Å)$_{EXAFS}$	Rn(Å)$_{XRD(ave)}$[10]	a $(2\sigma^2/Å^2)_{EXAFS}$
a)	34.3	1	Cl	1.0(1)	2.59(4)	2.56	0.022(3)
		2	C	15.3(23)	2.74(1)	2.74	0.020(2)
b)	31.3	1	Cl	1	2.58(5)	2.56	0.019(8)
		2	H	3	2.48	-	0.03
		3	C	3	2.69	2.74	0.023
		4	C	3	2.72	2.74	0.018
		5	C	3	2.74	2.74	0.025
		6	C	3	2.78	2.74	0.023
		7	C	3	2.79	2.74	0.019
c)	26.2	1	O	0.25(5)	1.78(2)	-	0.008(1)
		2	Cl	1.1(2)	2.58(3)	2.56	0.021(2)
		3	C	14.5(9)	2.74(1)	2.74	0.015(4)

Table 7.4 EXAFS derived structural parameters for [Cp₃UCl] diluted to 10wt% U in a boron nitride matrix. a) single scattering calculation, b) multiple scattering calculation, c) partial oxidation model. Statistical errors, where appropriate, are given in brackets. Also given are parameters from previously reported single crystal X-ray diffraction data.

The single scattering model consists of only two shells. The first consists of a single chlorine at 2.59 Å. This is within experimental error of the structure reported by Wong et al,[10] and also that given in other investigations of this structure.[11,12,13] The second shell is of 15 carbon atoms, relating to the three cyclopentadienyl rings, at 2.74 Å, and again this is in agreement with previously published data. The R factor for this fit was found as 34.3, and the fit index as 8.4×10^{-3}.

The model incorporating multiple scattering calculations comprises of seven shells of atoms. The first shell is the same as for the single scattering model, and the second shell is of three hydrogen atoms representing the centroids of the cyclopentadienyl rings. The other five shells of three carbon atoms each relate to the Cp rings, and it may be shown from the slight variation in U-C distance between these shells that the rings are slightly tilted with respect to the plane perpendicular to the U-H vector. Again, this is in agreement with the published X-ray and neutron diffraction studies. Due to the symmetry requirements, and the correlated refinement of the carbon atoms within each ring, no

estimate of statistical errors associated with the derived parameters for these shells may be given. From the calculations it is possible to identify multiple scattering pathways with a significant contribution to the observed EXAFS. These pathways involve two adjacent carbon atoms in the same Cp ring, to give a total path length of ~7.0 Å. The associated contribution in the Fourier transform would be expected at ~3.5 Å, and indeed it is observed that the fit to the experimental feature centred at this value is improved for the multiple scattering model. However, the R factor after these calculations is only reduced to 31.3 from 34.3 for the single scattering model. This means that, despite the fact that the multiple scattering model is more thorough, the large increase in the number of parameters required to gain a small increase in the goodness of fit cannot be statistically justified. The statistical test employed to check whether the addition of a shell is significant is that proposed by Joyner et al.[14], which suggests that if a reduction in the fit index is satisfied by $FI_{n+1}/FI_n < 0.96$ for a data set of 200 points, then the new shell is significant within a 95% confidence limit, and may be statistically justified. The number of independent data points from this experiment is approximately 40.

The third model that was used considered the possibility that partial oxidation of the sample had occurred prior to, or during, the analysis. The most likely oxidation pathway of this material, as for all uranium (IV) systems, is via a uranium (VI) species with linear, $O=U=O$, uranyl type bonding. For this reason, a shell of oxygen at 1.78 Å is included in this model. For a completely oxidised material a co-ordination number of 2 would be expected, but for the fit shown in figure 7.5 this was refined to 0.25. Qualitatively, this suggests that approximately $\frac{1}{8}$ of the sample has undergone some oxidation. This is disappointing, as, although this compound is known to be highly hygroscopic, it is not as sensitive to air and moisture as the triamidoamine complexes. This model provided an R factor of 26.2, which is a significant improvement in goodness of fit on those detailed above. Attempts were made to fit the data as two separate clusters; one with the [Cp₃UCl] symmetry, and the second with a uranyl type group. The relative proportions of these species may then be refined, and multiple scattering calculations performed on both clusters simultaneously. However, this produced a negligible effect on the fit index obtained.

U (LIII) EXAFS spectra of the 6wt% U mesoporous silica supported samples were also recorded, and the fit obtained for [NEt₂U(N'₃N)]/H₁SiO₂ material, along with the parameters used to define it, is given in figure 7.6.
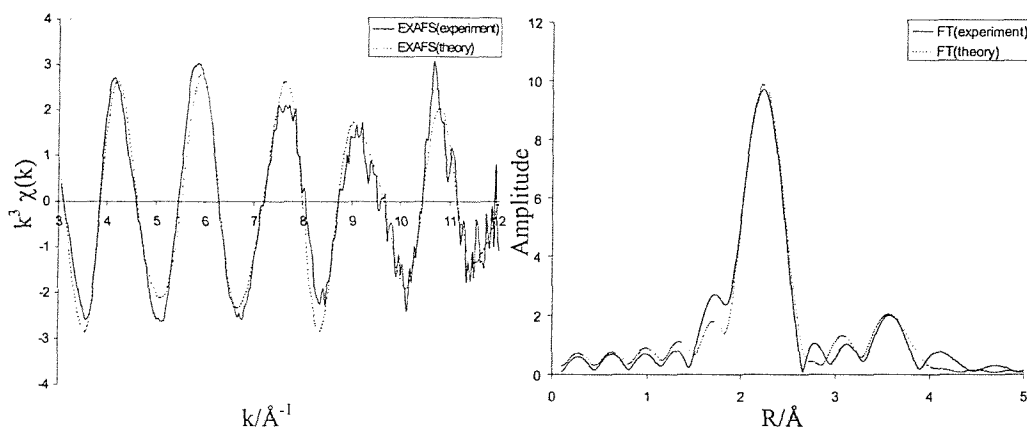
Figure 7.6 The U L (III)-edge k^3 weighted EXAFS spectrum and phase shift corrected Fourier transform of [NEt$_2$U(N'$_3$N)]/H$_1$SiO$_2$.

$$EF = -9.8 \qquad R = 24.45 \qquad F.I = 3.6 \times 10^{-4}$$

Shell(n)	Tn	Cn	Rn(Å)$_{EXAFS/SiO2}$	Rn(Å)$_{EXAFS/BN}$	Rn(Å)$_{XRD(ave)}$[9]	a $(2\sigma^2/Å^2)_{EXAFS}$
1	N	4	2.27(1)	2.27(1)	2.271	0.006(1)
2	N	1	2.81(7)	2.71(5)	2.709	0.027(16)
3	C	4	3.16(5)	3.15(3)	3.162	0.025(18)
4	C	4	3.51(7)	3.48(3)	3.456	0.012(8)
5	Si	3	3.65(8)	3.63(8)	3.594	0.028(20)

Table 7.5 EXAFS derived structural parameters for [NEt$_2$U(N'$_3$N)]/H$_1$SiO$_2$. Statistical errors are given in brackets. Also given are parameters from the unsupported material, and the previously reported single crystal X-ray diffraction data.

It may be observed that the values obtained for the supported material with no further treatment are within experimental error of those derived from both the EXAFS spectrum of the pure sample, and single crystal X-ray studies. This strongly suggests that the triamidoamine complex is unchanged as a result of evaporation deposition, and that the surface silanol species of the silica are not sufficiently reactive to cause any structural alteration or chemisorption interaction. This is an important result, and indicates that further treatment of the supported material is required to initiate any reaction with the surface. The same result was found using the butoxide analogue of this compound, and the derived EXAFS parameters will not be detailed here.

The U L(III) EXAFS spectrum of the mesoporous silica supported cyclopentadienyl complex was also obtained. The fit achieved is given in figure 7.7, and the parameters used to define it in table 7.6.
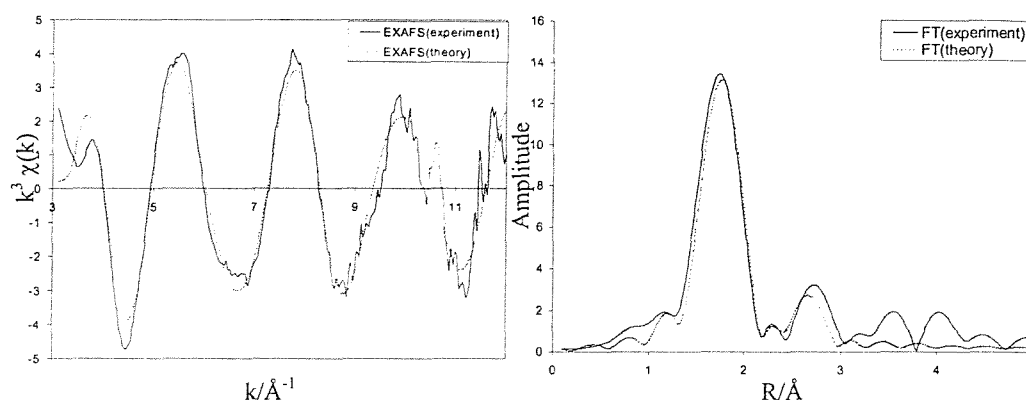

Figure 7.7 The U L (III)-edge k^3 weighted EXAFS spectrum and phase shift corrected Fourier transform of [Cp$_3$UCl]/H$_1$SiO$_2$.

$$EF = -10.1 \qquad R = 24.1 \qquad F.I = 4.5 \times 10^{-4}$$

Shell(n)	Tn	Cn	Rn(Å)$_{EXAFS}$	a (2σ^2/Å^2)$_{EXAFS}$
1	O	2.0(2)	1.79(1)	0.004(1)
2	O	2.0(3)	2.35(2)	0.023(6)
3	C	3.0(5)	2.60(3)	0.016(3)

Table 7.6 EXAFS derived structural parameters for [NEt$_2$U(N'$_3$N)]/H$_1$SiO$_2$. Statistical errors are given in brackets.

It is immediately obvious from the above fit that the (tris)cyclopentadienyluranium chloride has decomposed on deposition. The exact nature of this decomposition product is difficult to ascertain. The first shell comprises of two oxygen atoms at 1.79Å, and this is a clear indication of oxidation to uranium (VI), and of O=U=O uranyl bond formation.[15] The remainder of the co-ordination sphere is less distinct. In the fit illustrated in figure 7.7, the second shell consists of two oxygen atoms at 2.35 Å, and the third shell of three carbon atoms at 2.60 Å. 2.35 Å is a reasonable distance for equatorially co-ordinated oxygen in uranate materials,[15] and 2.60Å is a sensible length for a U^{IV}-C bond.[16] However, uranium-carbon bond formation is rare, and is very unlikely to occur for U(VI), so it is quite possible that the supported species is a mixture of U(IV) and U(VI). The third co-ordination shell may well have a contribution from associated oxygen donors, possibly from surface oxygen or retained tetrahydrofuran from the deposition process. One of the

limitations of the EXAFS technique is that differentiation between elements of similar mass can be difficult, particularly for low mass scatterers. A second limitation has already been alluded to, and this is that the EXAFS spectrum is the result of a sum over all of the absorbing uranium atoms within the sample, and as such it provides an average representation of local structure. It is quite probable that in this example there is a mixture of uranium species present, and this leads to added complexity in the interpretation of the results of analyses.

The effect of the deposition of the organometallic on the pore structure of the mesoporous silica has been investigated with the use of isothermal nitrogen adsorption. From the adsorption data obtained, a measure of the surface area, and pore size distribution has been calculated. This information is summarised in table 7.7.

System	Surface Area/m^2g^{-1}	Pore Diameter/Å	Pore Volume/mlg^{-1}
H_1SiO_2	700	30	0.43
[$NEt_2U(N_3N)$]/H_1SiO_2	580	27	0.35
[$Bu^tOU(N_3N)$]/H_1SiO_2	590	27	0.34
[Cp_3UCl]/ H_1SiO_2	570	26	0.31

Table 7.7 The effect of organometallic deposition on the mesoporous silica structure

This effect on pore size distribution for the systems [$NEt_2U(N_3N)$]/H_1SiO_2 and [Cp_3UCl]/ H_1SiO_2 is illustrated in figure 7.8. The butoxide analogue is omitted, as the result is indistinguishable from the amide.
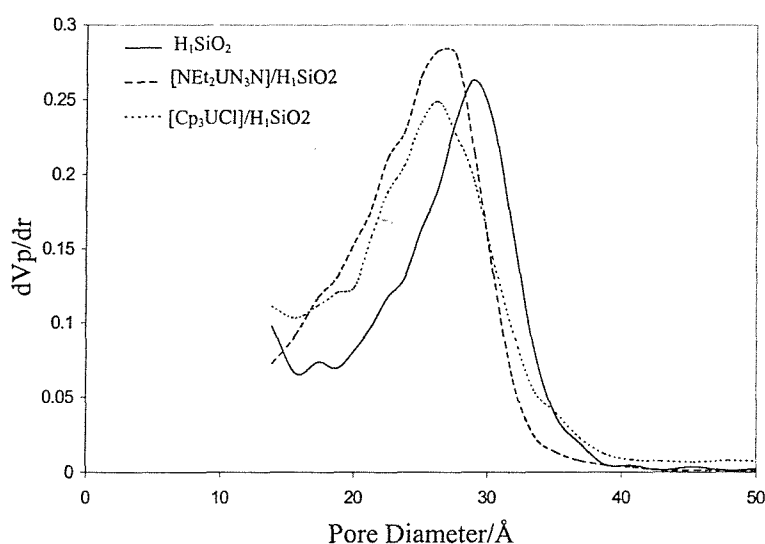

Figure 7.8 The effect of organometallic deposition on pore size distribution

The reduction in the pore size maximum on deposition is as expected. The exact chemical nature of the adsorbed organouranium complex does not seem to have a large effect, and it is reasonable to conclude that it is the physical size of the complex and the metal loading, 6wt% U in all cases, that are the factors responsible for the noted change in pore dimension.

The mesoporous silica supported organometallics have also been investigated with the use of X-ray powder diffraction. There was no evidence of high angle diffraction relating to a uranium phase with long range order, but at the low metal loading this is as expected. The low angle diffraction pattern of the supported $[Bu^tOU(N_3N)]/H_1SiO_2$ system, compared to that of the pure silica, is illustrated in figure 7.9.
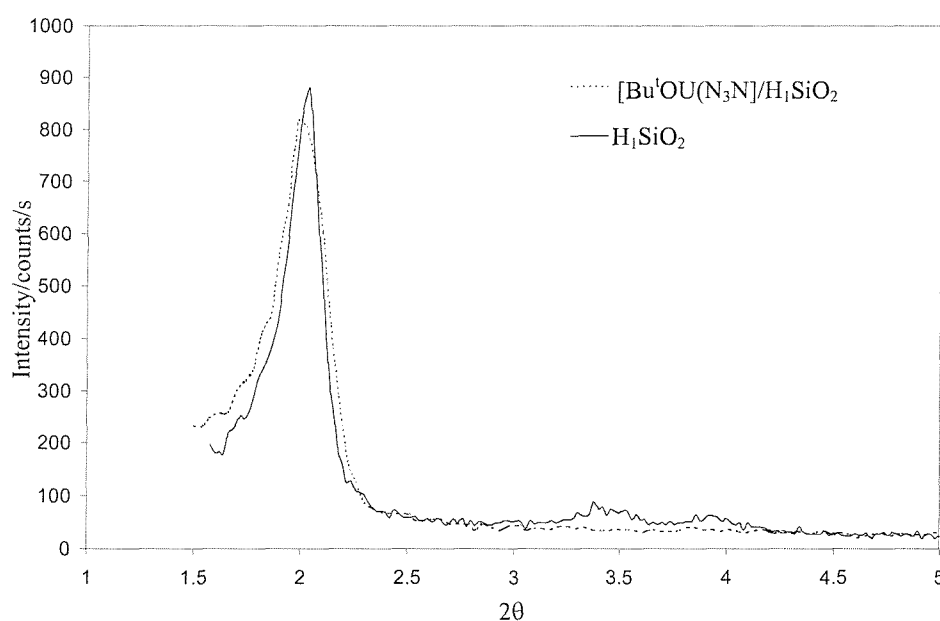

Figure 7.9 The effect of $[Bu^tOU(N_3N)]$ deposition on the low angle X-ray diffraction pattern of mesoporous silica.

It may be observed that there is a slight broadening of the (001) reflection on deposition, and an absence of secondary diffraction peaks in the pattern of $[Bu^tOU(N_3N)]/H_1SiO_2$. This may be an indication of some structural collapse of the porous framework, but it is more likely that this is simply a result of increased disorder on adsorption of the uranium complex. This behaviour is maintained for the other two supported organometallic systems.

Diffuse reflectance UV/vis spectroscopy has also been used in an attempt to characterise the structure of the supported materials. Due to the complex nature of f-element electronic spectra, a direct comparison of the spectrum of the pure material with

that of the supported sample has been employed. For the triamidoamine complexes, once the contribution from the support was accounted for, the spectra of the supported materials were identical to those of the pure compound. The spectra of these supported materials are shown in figure 7.10.
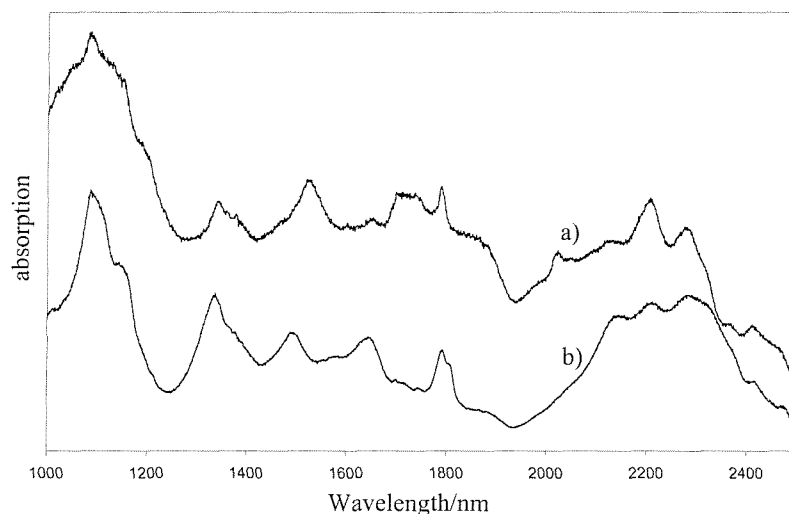
Figure 7.10 The diffuse reflectance UV/vis spectra of a) [Bu^{t}OU(N$_3$N)]/H$_1$SiO$_2$, b) [NEt$_2$U(N$_3$N)]/H$_1$SiO$_2$

This was not the case for the [Cp$_3$UCl] sample, and this is illustrated in figure 7.11.
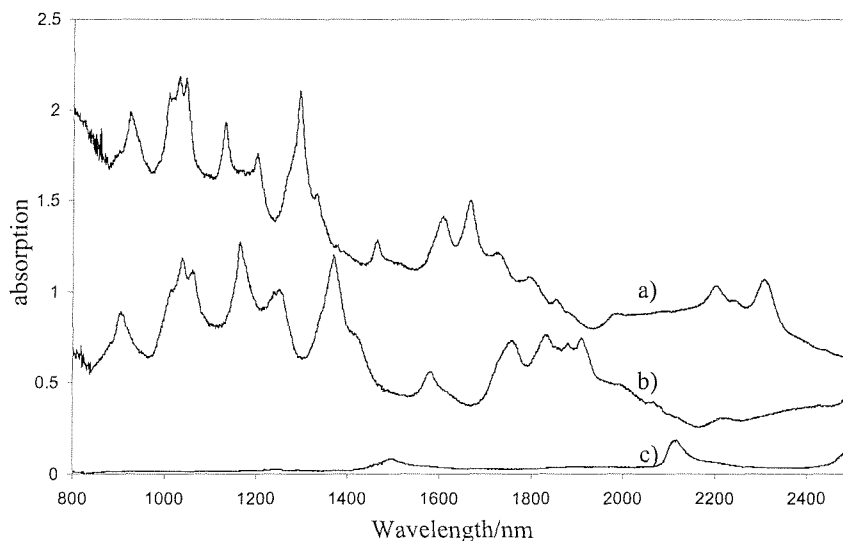
Figure 7.11 The diffuse reflectance UV/vis spectra of a) [Cp$_3$UCl], b) [Cp$_3$UCl]/H$_1$SiO$_2$, c) H$_1$SiO$_2$

Figure 7.11 demonstrates that, although the spectra of pure and supported material have some common features, there is a clear change in the electronic structure of the material on deposition. It has already been noted that this complex is oxidised on deposition, and so it might be expected that the [Cp$_3$UCl]/H$_1$SiO$_2$ sample would have a

much simpler spectrum due to the lack of f-electrons in uranium (VI). In fact, a very complex spectrum is observed, suggesting the continued presence of f-electrons and a uranium oxidation state less than (VI), and this highlights the difference between this technique and that of EXAFS. The uranium is probably present mostly as the oxidised form, and this is what is observed by analysis of EXAFS spectra, but if this oxidation is not complete throughout the sample, then the electronic spectrum may only reflect the unoxidised minority of uranium species. It would appear that this is the case for the supported [Cp$_3$UCl] system.

For the triamidoamine complexes, which demonstrated no structural change or surface interaction on deposition, the next logical step is to attempt to determine the conditions under which such a reaction may be induced. The technique employed to achieve this was a temperature programmed reaction (TPR) in the microreactor described in chapter 2. The reaction was performed under a flow of pure helium at 20ml/min, and the sample was subjected to linear temperature ramp of 10°C/min to 450°C. The results of this experiment for the [NEt$_2$U(N$_3$N)]/H$_1$SiO$_2$ system is illustrated in figure 7.12.
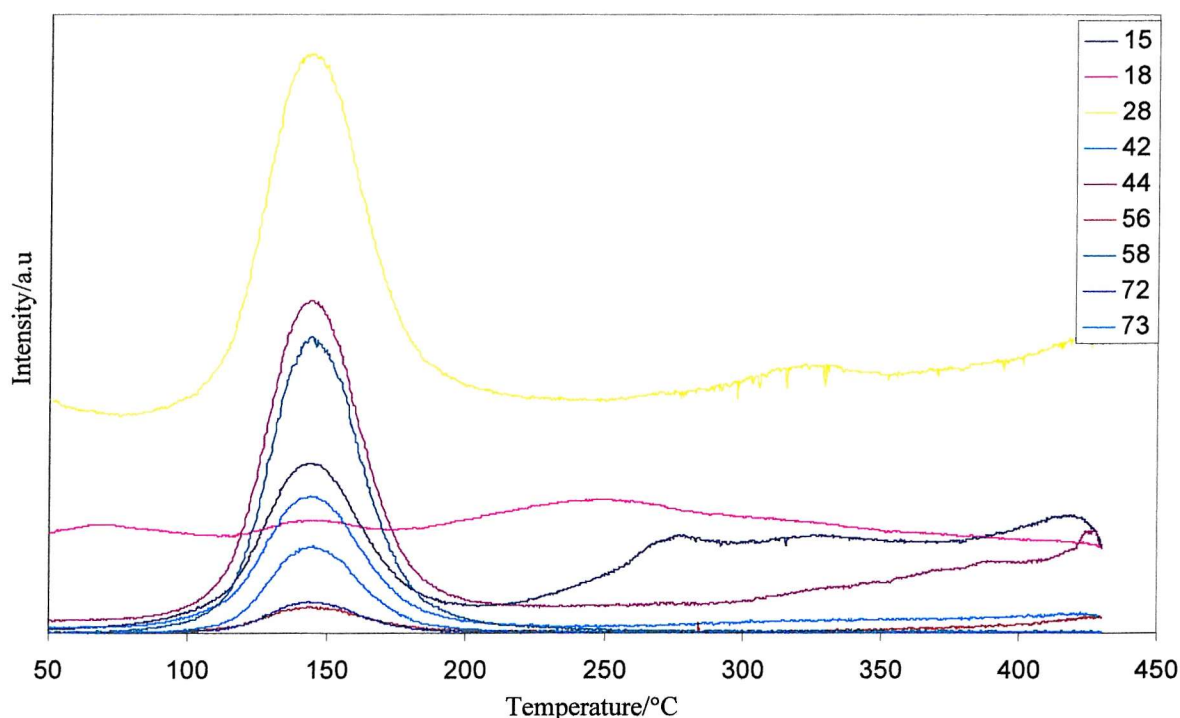
Figure 7.12 Mass evolution as a function of temperature for [NEt$_2$U(N$_3$N)]/H$_1$SiO$_2$ under a helium flow.

The major feature of this TPR experiment is the evolution of a range of masses between 100 and 200°C. The origin of this feature may reasonably be the evolution of one

of two species. One possibility is the desorption of adsorbed pentane ($m/z = 72$) persisting from the evaporation deposition. However, it may be expected that this would occur at lower temperature than that observed, and this option can be eliminated by comparison of the relative intensity of mass signals in figure 7.12 with the known cracking pattern of pentane.[17] The second possibility is the formation and evolution of diethylamine ($m/z = 73$), and this has been confirmed by analysis and comparison of the fragmentation pattern of this compound. A reasonable explanation for the presence of diethylamine in the reactor effluent is given in figure 7.13.
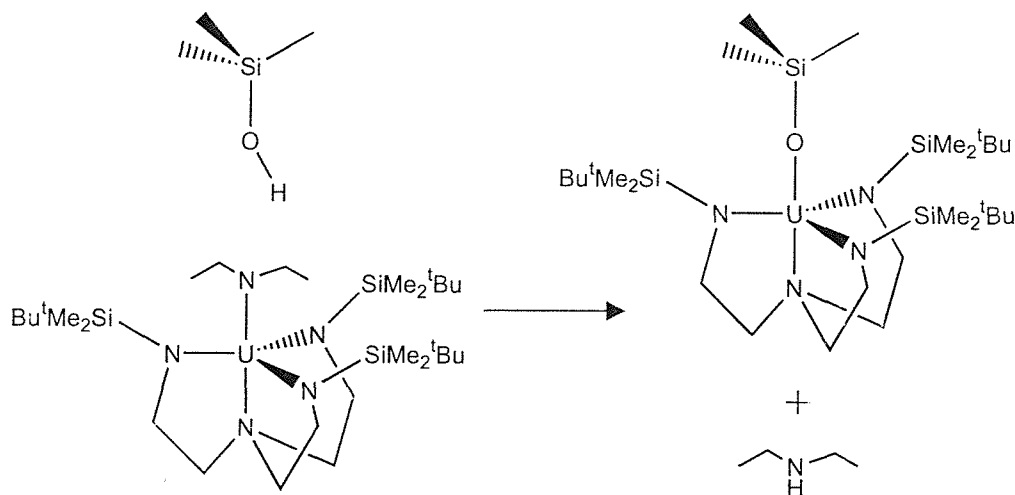
Figure 7.13 The proposed reaction between the silica surface and $[NEt_2U(N_3N)]/H_1SiO_2$

The same experiment has been performed on the butoxide analogue, and figure 7.14 illustrates the results obtained.

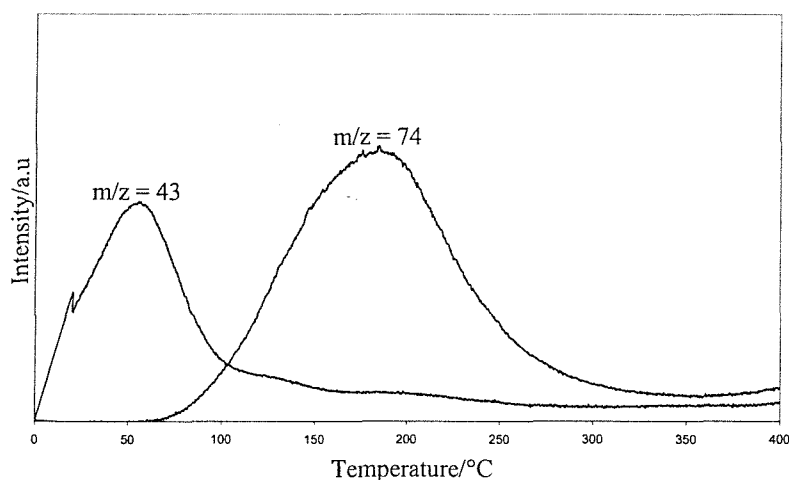Figure 7.14 Mass evolution as a function of temperature for $[Bu^tOU(N_3N)]/H_1SiO_2$ under a helium flow.

The peak in the m/z = 43 signal at ~50°C relates to the desorption of residual pentane, and confirms the assumption made previously. The peak in the mass 74 trend curve centred at approximately 200°C may reasonably be assigned as due to the evolution of *tert*-butanol, and the origin of this species is attributed to a similar process to that suggested in figure 7.13 for the amide analogue. However, the evolution of the alcohol/amine does not provide any information regarding the nature of the uranium species that remains on the surface.

7.2.2 Thermally Treated Supported Materials

The next logical step is then to attempt to gain information on this structure, and this was achieved by recording EXAFS spectra of supported samples that had been pre-treated at 125°C in helium for 30 minutes. The fit that was obtained for $[NEt_2U(N_3N)]/H_1SiO_2/125°C$ is given in figure 7.15, and the parameters used to define this fit are given in table 7.8.

Figure 7.14 The U L (III)-edge k^3 weighted EXAFS spectrum and phase shift corrected Fourier transform of $[Cp_3UCl]/H_1SiO_2/125°C$.

$$EF= -14.3 \qquad R= 26.2 \qquad F.I= 5.2 \times 10^{-4}$$

Shell(n)	Tn	Cn	Rn(Å)$_{EXAFS}$	a $(2\sigma^2/Å^2)_{EXAFS}$
1	O	2.0(2)	1.84(1)	0.004(1)
2	O	2.0(3)	2.23(3)	0.026(10)
3	O	2.0(5)	2.48(5)	0.027(10)

Table 7.8 EXAFS derived structural parameters for $[NEt_2U(N'_3N)]/H_1SiO_2/125°C$. Statistical errors are given in brackets.

It is immediately possible to observe from the parameters of this fit that the surface uranium species has oxidised from U(IV) to U(VI) with evidence of uranyl bonding. The

first shell of two oxygen atoms is found at 1.84 Å, and this comprises the linear O=U=O unit. This distance is within the limits previously found for the uranyl bond. Two further shells of two oxygens have also been fitted, at 2.23 and 2.48 Å. These are reasonable distances for U-O bonds, but the exact nature of the donor species cannot be determined from the EXAFS data. Nominally associating the linear uranyl group with the molecular *z*-axis, the location of the other four oxygen atoms was assigned as within the equatorial *xy* plane. This unit was then used as a D_{2h} model for multiple scattering calculations. The only significant contribution from these calculations was derived from a four-legged path involving the absorbing atom and the two uranyl oxygens, which led to a slight increase in intensity of the Fourier transform at ~3.6 Å. The fit index decrease was negligible, and the result is not shown here. A very similar result was obtained for the butoxide analogue. The fact that these materials have oxidised following this thermal treatment is disappointing. It was predicted that chemisorption may occur with the loss of the apical ligand following reaction with surface silanol groups, and that the uranium (IV) species may be stable on the silica surface with potential as centres for catalytic activity. It may be that oxygen or water was not as rigorously excluded during treatment and handling as would be required to prevent oxidation. A second possibility is that the loss of the apical ligand and reaction with the pore surface causes the decomposition of the tripodal ligand set and subsequent oxidation of the metal centre. The possibility that this may be a mixed species, as was found for the $[Cp_3UCl]/H_lSiO_2$ system, was investigated using diffuse reflectance UV/vis spectroscopy, but no evidence of residual f-electrons, and therefore U(IV) species, was observed. It would appear that total oxidation of the supported uranium complex has occurred.

U (LIII) EXAFS spectra of samples of the supported triamidoamine materials on their removal from the microreactor, after treatment in helium at 450°C, have also been recorded. The fit obtained for $[NEt_2U(N_3N)]/H_lSiO_2/450°C$ is shown in figure 7.16, and the parameters used to define it are given in table 7.9.
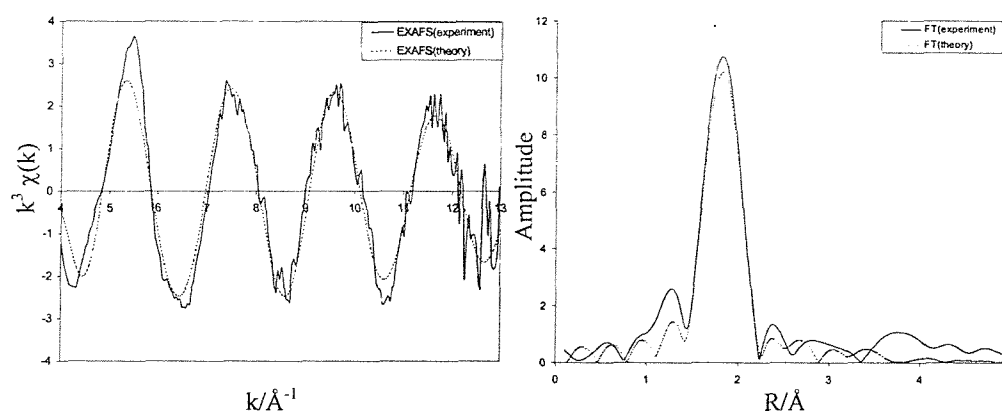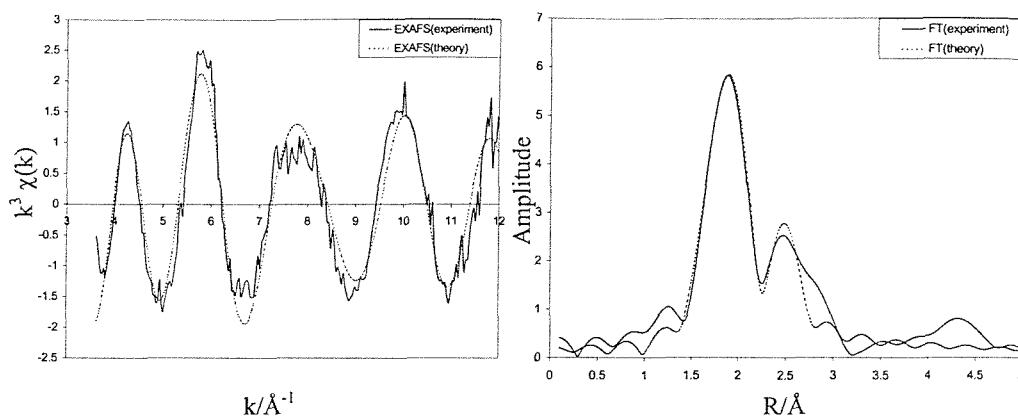
Figure 7.16 The U L (III)-edge k^3 weighted EXAFS spectrum and phase shift corrected Fourier transform of [Cp$_3$UCl]/H$_1$SiO$_2$/450°C

$$EF= -1.1 \qquad R= 29.8 \qquad F.I= 6.1 \times 10^{-4}$$

Shell(n)	Tn	Cn	Rn(Å)$_{EXAFS}$	a $(2\sigma^2/Å^2)_{EXAFS}$
1	O	2.0(2)	1.81(1)	0.010(1)
2	O	4.0(10)	2.12(1)	0.014(2)
3	O	3.1(9)	2.33(2)	0.015(2)

Table 7.9 EXAFS derived structural parameters for [NEt$_2$U(N'$_3$N)]/H$_1$SiO$_2$/450°C. Statistical errors are given in brackets.

This fit must be compared with that found for the material treated at 125°C. The first shell once again comprises of two oxygen atoms at a short distance of 1.81 Å. This must be assigned as the uranyl group, and it must be noted that the bond length given is slightly shorter than for the same sample calcined at 125°C (1.84 Å). This trend of bond length reduction continues for the second and third shells of oxygen at 2.12 and 2.33 Å, compared to 2.23 and 2.48 Å for the analogue treated at lower temperature. Also, the average total co-ordination number of the uranium has increased from ~6 to ~9 with increasing treatment temperature. This highlights the variety of U-O bond lengths that may occur in these uranate type materials, and the large range co-ordination numbers that are possible.[15] Once again, the results achieved for the butoxide analogue are very similar, and this suggests little dependence on the exact nature of the precursor complex. Thermal treatment of the supported materials appeared to have a negligible effect on the pore structure, long range order, or surface area of the samples. Diffuse reflectance UV/vis spectra of these materials have been recorded, and compared with those of UO$_3$ and UO$_2$(NO$_3$)$_2$.6H$_2$O, but no common features are present.

7.3 Summary

The organometallic complexes $[(C_5H_5)_3UCl]$, $\{N[CH_2\text{-}CH_2N(SiMe_2{}^tBu)]_3UOBu^t\}$, and $\{N[CH_2\text{-}CH_2N(SiMe_2{}^tBu)]_3UNEt_2\}$, were deposited on mesoporous silica at 6wt% U. The (tris)cyclopentadienyluranium chloride is shown to oxidise on deposition from U(IV) to U(VI). The triamidoamine complexes are unchanged on deposition, but thermal treatment at 125°C, which causes loss of the apical ligand as diethylamine or _tert_-butanol, also results in the decomposition of the remaining ligand set and oxidation of the uranium centre. The structure of the resulting material is approximately six co-ordinate, and this increases to approximately nine co-ordinate with further thermal treatment at 450°C

7.4 References

1) P. Scott, P.B. Hitchcock, *Polyhedron*, 1651, **13**, 1994.

2) P. Scott, P.B. Hitchcock, *J. Chem. Soc. Dalton Trans.*, 603, 1995.

3) P. Roussel, P. B. Hitchcock, N.D. Tinker, P. Scott, *Inorg. Chem.*, 5716, **36**, 1997

4) P. Roussel, P. Scott, *J. Am. Chem. Soc.*, 1070, **120**, 1998.

5) D. Gudat, J.G. Verkade, *Organometallics*, 2772, **8**, 1989.

6) C.C. Cummins, R.R. Schrock, W.M. Davis, *Organometallics*, 1452, **11**, 1992.

7) P. Roussel, N.W. Alcock, R.Boaretto, A.J. Kingsley, I.J. Munslow, C.J. Sanders, P. Scott, *Inorg. Chem.*, 3651, **38**, 1999.

8) T.J. Marks, A.M. Seyam, W.A. Wachter, *Inorganic Syntheses,* 300,**28**, 1990.

9) P.Scott, A.Kingsley, University of Warwick, unpublished results.

10) C-H. Wong, T-M. Yen, T-Y. Lee, *Acta Cryst.*, 340, **18**, 1965.

11) P. Raison, J. Rebizant, C. Apostolidis, G.H. Lander, A. Delapalme, J.M. Kiat, P. Schweiss, B. Kanellakopulos, A. Gonthier-Vassal, P.J. Brown, Z. Kristallogr. 720, **209**, 1994.

12) A. Delapalme, P. Raison, G.H. Lander, J. Rebizant, P. Schweiss, B. Kanellakopulos, Z. Kristallogr. 727, **209**, 1994.

13) A. Delapalme, P Schweiss, P. Spirlet, J. Rebizant, *Mat. Sci. For.*, 211, **27**, 1988.

14) R.W. Joyner, K.J. Martin, P. Meehan, *J.Phys.C:Solid State Phys.*, **20**, p4005, **1987.**

15) P.C. Burns, R.C. Ewing, F.C. Hawthorne, *Can. Mineral.,* 1551, **35**, 1997.

16) A.G. Orpen, L. Brammer, F.H. Allen, O. Kennard, D.G. Watson, R. Taylor, *J. Chem. Soc. Dalton Trans.,* S1, 1989.

17) NIST Standard Reference Database 69 - February 2000 release: NIST Chemistry WebBook.

Chapter 8. Conclusions

8.1 The Synthesis and Characterisation of Mesoporous Silica

In chapter 3 it was shown that mesoporous silica with a regular hexagonal array of pores has been synthesised by a liquid crystal templating route, using a variety of surfactants. The template is removed by calcination in nitrogen at 470°C for 4h, followed by treatment in oxygen at the same temperature for a further 8h. The mesostructure in all cases is retained on surfactant removal. The structure of these materials is typified by the Brij76 surfactant-templated silica, for which the nitrogen adsorption data showed a type IV isotherm with no hysteresis, giving a specific surface area of $870 m^2 g^{-1}$, a pore volume of $0.7 cm^3 g^{-1}$ and an average pore diameter of 3.6nm. X-ray powder diffraction patterns for this silica show an intense peak at low 2θ value corresponding to a d_{100} value of 4.9nm, as well as secondary peaks indicative of a hexagonal array of pores and extended long range order. The hydroxyl concentration is found to be 1.21 $OHnm^{-2}$ for the material calcined at 470°C. Further degassing in dioxygen at temperatures up to 950°C reveals a very slow, steady decline in surface area and pore size up to 800°C, whereafter these values fall sharply to $300 m^2 g^{-1}$, and 2.2nm, respectively at 850°C. A similar effect on the (100) reflection intensity is noted by X-ray powder diffraction. The surface hydroxyl concentration undergoes a similar non-linear reduction with calcination temperature, but this occurs between 700 and 800°C, suggesting that extensive dehydroxylation occurs before rapid structural collapse.

8.2 The Characterisation of Supported Uranium Materials

The supported uranyl nitrate hexahydrate derivative materials, deposited from aqueous solution at 30wt% U have been identified, prior to calcination, as $[UO_2(NO_3)_2.2H_2O]$/support material. The analogous uranium tetrachloride derivatives, which were prepared from evaporation of a tetrahydrofuran solution, have been characterised as predominantly a $UOCl_2$-type phase on deposition, although only the mesoporous silica provides a supported phase with sufficiently long-range order to give an X-ray diffraction pattern. The decomposition of these supported materials occurs at reduced temperatures compared to the pure, unsupported materials. This phenomenon has a support dependence which is the same for both precursors, where the temperature of initial decomposition increases in the order amorphous silica ≤ amorphous alumina < mesoporous silica < unsupported bulk material. For the nitrate materials, this decomposition proceeds via dehydration and $deNO_x$ steps, whereas for the chloride

materials, chlorine loss in the form of HCl is observed. These decomposition processes have been followed with the use of thermogravimetric analysis, differential thermal analysis, and temperature programmed reaction, and for both precursors the result is the formation of an oxygen rich uranium material, such as aUO_3-type phase, which converts to U_3O_8 at higher temperatures. The temperature at which this U_3O_8 formation process occurs also has a support dependence, and this is opposite to that given above for the initial decomposition, i.e. mesoporous silica < amorphous alumina ≤ amorphous. This has been followed by *in situ* X-ray powder diffraction, and occurs at lower temperatures for the tetrachloride derivative materials compared to the nitrate analogues. It has been shown by X-ray powder diffraction pattern analysis, and transmission electron microscopy, that the U_3O_8 particle size formed at a given temperature is larger for materials that promote U_3O_8 formation at lower temperatures, i.e. a sintering process occurs. The U_3O_8 particles formed on the mesoporous silica support at elevated temperatures are much larger than the dimensions of the pores, and the majority of the uranium oxide is present on the external surface of the silica.

In chapter 7, it was described how the organometallic complexes [(C$_5$H$_5$)$_3$UCl], {N[CH$_2$-CH$_2$N(SiMe$_2$^{t}Bu)]$_3$UOBu^t}, and {N[CH$_2$-CH$_2$N(SiMe$_2$^{t}Bu)]$_3$UNEt$_2$}, were deposited on mesoporous silica at 6wt% U. The (tris)cyclopentadienyluranium chloride is shown by U(LIII) edge EXAFS analysis and diffuse reflectance UV/vis spectroscopy to partially oxidise from U(IV) to U(VI) as a result of deposition. The triamidoamine complexes are unchanged on deposition, but thermal treatment at 125°C causes loss of the apical ligand as diethylamine or *tert*-butanol, shown by temperature programmed reaction, and also results in the decomposition of the remaining ligand set and oxidation of the uranium centre. The structure of the resulting uranium (VI) material is shown by EXAFS analysis to be approximately six co-ordinate, with two short U-O distances consistent with the formation of a uranyl species and four longer U-O/U-C bonds. This increases to approximately nine co-ordinate with further thermal treatment at 450°C

8.3 The Catalytic Oxidation of Carbon Monoxide

The systems tested were derived from two precursors; uranium tetrachloride, UCl$_4$, and uranyl nitrate hexahydrate, UO$_2$(NO$_3$)$_2$.6H$_2$O, which were supported on three different inorganic oxide supports; mesoporous silica, amorphous silica, and amorphous alumina. This provided a total of six different supported uranium systems, deposited at 30wt% U,

and allowed the activity dependence of precursor and support to be investigated. The results of this work have been detailed in chapter 5.

The most active system after pre-treatment at 600°C for two hours *in situ* is uranium tetrachloride on alumina. This material achieves 90% CO conversion to CO_2 at 400°C under continuous flow conditions, which is significantly more active than the other five systems. Under these conditions, the mesoporous silica supported materials display low activity, and fail to achieve 50% CO conversion at 600°C. This is probably mainly due to the fact that during the pre-treatment, the uranium oxide particles formed are shown by scanning electron microscopy to be extruded from the pore structure and to sinter to form very large particles analogous to bulk uranium oxide. The uranyl nitrate on mesoporous silica system is the most active material when samples are not subjected to calcination prior to reaction, with conversions similar to that found for $Cl/600/Al_2O_3$. The lack of pre-treatment increases the activity of most systems with respect to the CO oxidation reaction. The exception is the $Cl/nc/Al_2O_3$ system, where pre-calcination enhances activity. The most active systems display the highest activation energies for the process ($\sim150kJmol^{-1}$), with coincidentally high frequency factors.

Pulse flow experiments yielded similar information regarding the activity of the supported materials. An exception was noted for the $Cl/600/H_1SiO_2$ and $Cl/600/SiO_2$ systems, where the relative activity was shown to be the reverse of that displayed under continuous flow conditions. The pulse flow experiments also confirmed the character of the reactor as suitable for following this type of reaction.

Characterisation of materials post-reaction with the use of X-ray powder diffraction suggested that the active phase is U_3O_8, and confirmed that pre-treatment at 600°C serves to sinter this phase to form large particles, especially with regard to the mesoporous silica supported materials where this oxide material is extruded from the pore structure. Where pre-treatment is avoided, analysis of isothermal nitrogen adsorption data suggests that material is retained within the pore structure throughout the course of the reaction.

8.4 The Selective Catalytic Reduction of Nitric Oxide

In chapter 6 the activity and selectivity dependence on the nature of precursor and support has been described with respect to the NO reduction reaction. After high temperature pre-treatment, the mesoporous silica supported materials displayed low activity for this reaction compared to the amorphous silica and alumina analogues. Once again this

highlights the importance of uranium oxide particle size, and the associated surface area, on activity. The most active system for the selective reduction of NO with CO after high temperature calcination pre-treatment is the uranium tetrachloride on alumina system treated at 600°C. The uranyl nitrate on mesoporous silica system is the most active material when samples are not subjected to calcination prior to reaction. These results are equivalent to those found for the CO oxidation reaction. Even the most active supported uranium system does not perform as well, in terms of NO conversion, as the conventional $Pt/\gamma-Al_2O_3$ catalyst studied for comparison. However, the supported uranium oxide materials show greater selectivity towards N_2 than the platinum catalyst at lower temperatures. All the supported uranyl nitrate derivative materials display increased activity with respect to the NO reduction reaction as the pre-treatment temperature, and coincident uranium oxide particle size, is decreased. For the uranium tetrachloride derivative materials, the activity reaches a maximum at a pre-treatment temperature of 600°C, with activity decreasing as this temperature is increased or decreased. The decrease in activity with increasing calcination temperature is proposed to occur for the same reason as that discussed for the uranyl nitrate materials, whereas at lower temperatures the fall off in performance is considered to be due to an inhibiting effect resulting from observed retained chloride. The active phase in all systems is identified by X-ray powder diffraction as $UO_{2.2}$.

Systematic variation of the flow rates of NO and CO yielded an order of reaction for both species; the reaction being zeroth order with respect to NO, and to have an order of 1.4 with respect to CO. As for the CO oxidation reaction, the most active systems display the highest activation energies for the process, with coincidentally high frequency factors. An investigation of the activity dependence on the supported uranium loading was shown to yield a maximum in activity between 20 and 30 wt%U.

Pulse flow experiments yielded some similar information to the continuous flow studies regarding the activity of the supported uranyl nitrate derivative materials. However, concerning the uranium tetrachloride analogues, the activity of the $Cl/600/H_1SiO_2$ and $Cl/600/SiO_2$ are reversed compared to that observed for the continuous flow studies, with the mesoporous material demonstrating higher activity under the pulse flow conditions. This was also noted in the study of the CO oxidation reaction. Indeed, in the higher space velocity experiment, the mesoporous silica supported material is shown to have higher activity than even the amorphous alumina analogue.

8.5 General Conclusions and Further Development

The supported uranium oxide materials demonstrate great potential as effective catalysts for the selective reduction of NO with CO. The work reported here implies a high level of importance on the pre-treatment conditions to which these systems are subjected prior to reaction. The particle size of the active uranium oxide phase must remain smaller than the dimensions of the mesopores if the extremely high surface area of the support is to be fully utilised. It has also been shown that the nature of the uranium precursor has a profound effect on the final activity of the catalyst. The retention of chlorine within the supported sample has been demonstrated to have a detrimental effect on the catalytic performance of materials, but total removal of this chlorine by treatment at higher temperature does not result in identical activity for systems analogous in every other way. It should be concluded that the complex nature of the uranium oxide system implies a subtle, but significant, dependence of eventual UO_x phase formation on the nature of the original precursor.

It should be noted that this project constitutes only an initial investigation of these systems as catalysts for the selective reduction of NO, and considerable further work is required to establish whether or not these materials may offer a viable, or even preferable, alternative to the platinum group metal based catalysts currently used industrially. The stability of the uranium oxide materials over long periods of use must be established, as must their resistance to poisoning, or inhibition, by the large number of other chemicals commonly found in gas exhaust streams. In automotive applications, reductants other than carbon monoxide, such as hydrocarbons and hydrogen (from the water-gas shift reaction) are found in the gas feed, and the ability of uranium oxide catalysts to selectively reduce NO with these as the reductant must be measured. The catalytic reactor used in the work reported here is a highly idealised system, with a 1:1 CO:NO ratio and an absence of gas phase oxygen and water, and there is a requirement that the performance of supported UO_x catalysts should be tested over a wide range of experimental conditions.

The body of work required to satisfy the reservations given above is substantial, but it should also be noted that the scarcity of work reported on these systems implies that there are a large number of methods by which the performance of uranium oxide catalysts might possibly be improved.

1. The preparation of materials where the uranium is fully incorporated into the framework of the support, or more likely into the amorphous matrix, by methods

similar to those proposed in section 1.1.3.1 might yield systems with highly dispersed uranium species, which may improve the catalytic activity.

2. It may be possible to incorporate other metals into the support material, which in turn may have an effect on the catalyst performance.

3. Mixed oxides of uranium with antimony, bismuth and molybdenum are known to be very effective selective oxidation catalysts, and it may be that supporting these materials on a high surface area silica or alumina could produce a very active catalyst for the selective reduction of NO.

4. The inclusion of ceria in commercial platinum group metal catalysts for its oxygen storage properties is well established, and from the studies of uranium oxide catalysts that have been performed it may be expected that they would have similar properties. The synthesis of a system where platinum is supported on uranium oxide, which in turn is supported on a mesoporous silica may yield a very interesting catalyst.